

Development of a New In Situ X-ray Diffraction Technique for Characterising Embedded Nanoparticles

Nadia Alexandrovna Zatsepin
B.Sc.(Sci.Schol.Prog.)(Hons), A.Mus.A.



School of Physics • Monash University

November 2010

Copyright © Nadia Zatsepin 2010, 

For your convenience, the PDF edition of this thesis has linked internal references.

This work is licenced under the Creative Commons Attribution-Non-Commercial-No Derivative Works 2.5 Australia License. To view a copy of this licence, visit <http://creativecommons.org/licenses/by-nc-nd/2.5/au/> or send a letter to Creative Commons, 171 Second Street, Suite 300, San Francisco, California 94105, USA.

You are free to copy and distribute this work provided it is not altered, not used for commercial purposes and attribution is given to the author.

PDF EDITION

Copyright Notices

Notice 1

Under the Copyright Act 1968, this thesis must be used only under the normal conditions of scholarly fair dealing. In particular no results or conclusions should be extracted from it, nor should it be copied or closely paraphrased in whole or in part without the written consent of the author. Proper written acknowledgement should be made for any assistance obtained from this thesis.

Notice 2

I certify that I have made all reasonable efforts to secure copyright permissions for third-party content included in this thesis and have not knowingly added copyright content to my work without the owner's permission.

Errata

p 4 para 1 first sentence: "...scanning electron microscopy (SEM)," for "...scanning TEM (STEM),"

p 16 para 3 first sentence: "...are fundamentally limited to very thin samples (TEM) or surface studies (SEM)." for "...are fundamentally limited to very thin samples or surface studies."

p 85 para 2 of Section 5.2.1

"This corresponds to sampling at a spacing finer than the Nyquist frequency, i.e. sufficient oversampling (Bates, 1982; Miao *et al.*, 2000)." for "This corresponds to sampling at a spacing finer than the Nyquist frequency, or oversampling (Bates, 1982; Miao *et al.*, 2000)."

p 112 line 1, "inevitable decrease" for "natural decrease"

p 132 para 3, 4th sentence: "... where we carried out a preliminary study..." for "... where we carried out an essential preliminary study..."

p 187 Bibliography:

"Robinson, I. K., Vartanyants, I. A., Williams, G. J., Pfeifer, M. A. & Pitney, J. A. Reconstruction of the shapes of gold nanocrystals using coherent X-ray diffraction. *Phys. Rev. Lett.* **87** (19), 195505 (2001). (Cited on pages 10 and 12.)"

For

"Robinson, I. K., Vartanyants, I. A., Williams, G. J., Pfeifer, M. A. & Pitney, J. A. Reconstruction of the shapes of gold nanocrystals using coherent X-ray diffraction. *Phys. Rev. Lett.* **87** (2001). (Cited on page 10.)"

Addendum

p 12 para 2, add comment after 2nd sentence: "However, CDI does allow the measurement of diffraction from individual crystal particles, benefitting from the enhanced signal due to the crystalline nature of the sample (Robinson *et al.*, 2001)."

p 105 add comment to fig. 5.20 caption: "The fluctuations seen in these figures stem from the numerical nature of the calculations of dynamical diffraction (described in Section 5.3.1), where their magnitude strongly depends on the step size of the 1D beam along the surface of the analyzer crystal (2nm in this case). The arrays used for these simulations were not sufficient to adequately smooth the simulated diffraction profile. A finer step size along the surface of the beam does decrease these fluctuations but the dramatic increase in calculation time is impractical and the smoother profiles do not provide more information about the sample in this context."

p114 fig. 6.3 Add to the end of caption:

The arbitrary units are scaled intensity measurements where the maximum intensity is set to 1.0. The extracted line (along the monochromator pseudo streak direction) is obtained in the same way as in the simulated data in section 5.3.3. This extraction was used for all data in this chapter.

p 122 eqs. 6.1 and 6.2: "265" should read "265 nm"

p 124 eqs. 6.3 and 6.4: "199" should read "199 nm"

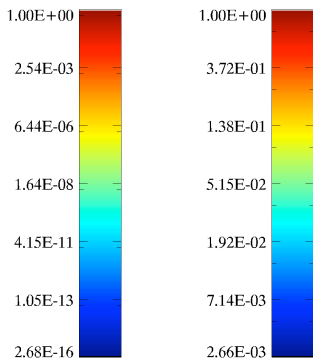
p 117 para 2: add footnote to "boxcar": "In this thesis we use "boxcar" averaging/smoothing to refer to averaging over the neighbouring pixels (in two dimensions)."

p 140 para 4 line 1 add footnote after "naturally": "Natural ageing is ageing of the alloy at room temperature, as was defined in section 2.2.0 on page 21."

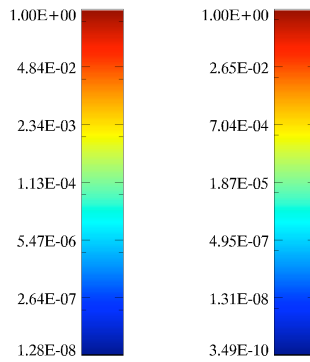
p 194 (List of Abbreviations) insert into line 3: "SEM Scanning electron microscopy"

Please refer to the following intensity scale bars when viewing the reciprocal space maps throughout this thesis. The corresponding page and figure numbers are included.

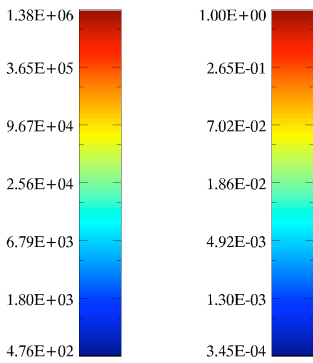
p 96 fig. 5.14(a) fig. 5.14(b)



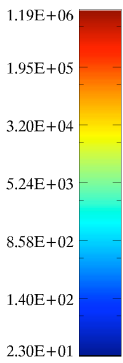
p 100 fig. 5.17(a) fig. 5.17(b)



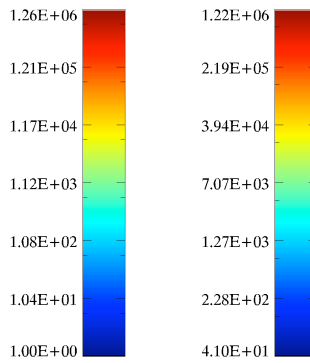
p 112 fig. 6.1 and fig. 6.1 normalised intensity for easier comparison with simulated RSMs



p 113 fig. 6.2(a)



p 116 fig. 6.4(a) fig. 6.4(b)



p 118 fig. 6.6(a)

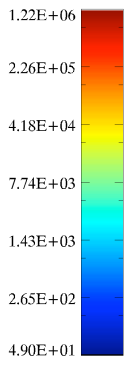
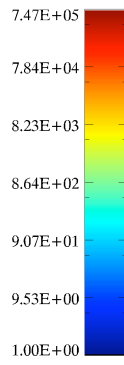


fig. 6.6(b)



p 119 fig. 6.7(a)

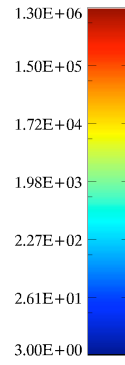
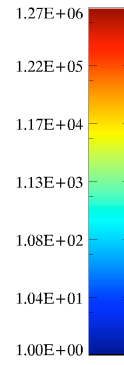


fig. 6.7(b)



p 123 fig. 6.9(a)

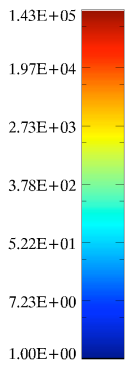
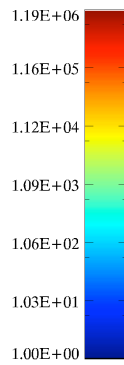


fig. 6.9(b)



p 126 fig. 6.11(a)

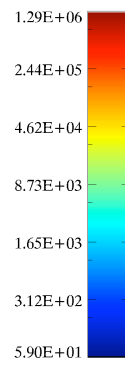
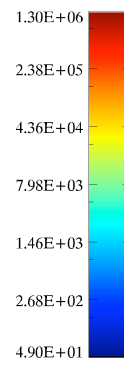
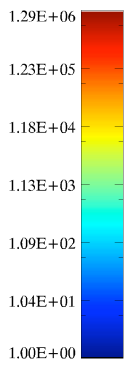


fig. 6.11(b)



p 128 fig. 6.13



p 145 fig. 6.20(a)

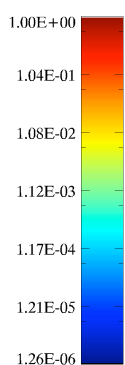


fig. 6.20(b)

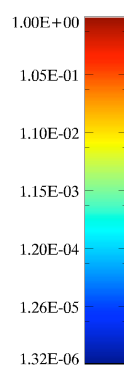


fig. 6.20(c)

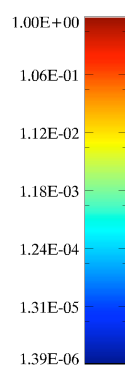
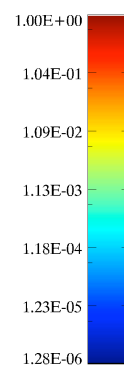


fig. 6.20(d)



p 146 fig. 6.21(a)

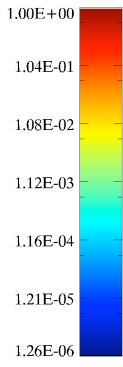


fig. 6.21(b)

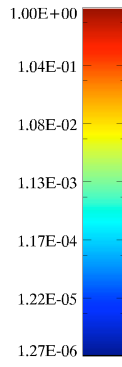


fig. 6.21(c)

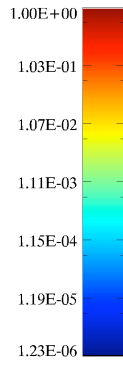
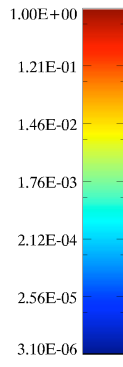


fig. 6.21(d)



p 160 fig. 7.1(a)

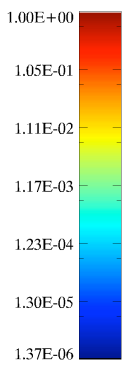


fig. 7.1(b)

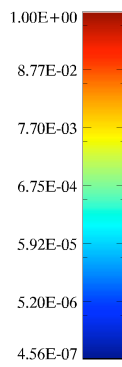


fig. 7.1(c)

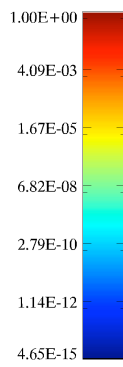


fig. 7.1(d)

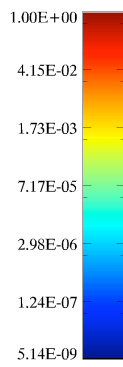


fig. 7.1(e)

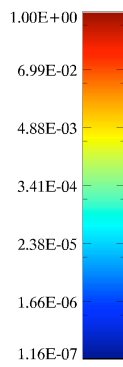
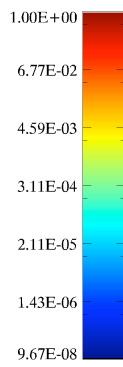


fig. 7.1(f)



p 164 fig. 7.4(a)

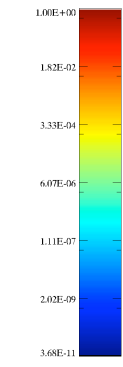


fig. 7.4(b)

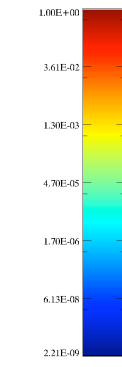


fig. 7.4(c)

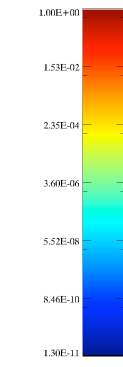
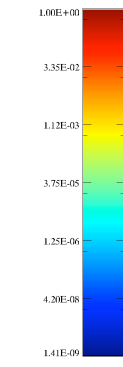


fig. 7.4(d)



Contents

Contents	i
List of Figures	v
List of Tables	ix
Abstract	xi
Disclosure	xiii
Acknowledgements	xiv
1 Introduction	1
1.1 Characterising nanomaterials	3
1.1.1 Electron microscopy	4
1.1.2 Probing matter with X-rays	5
1.1.3 Crystallographic methods	5
1.1.4 Non-crystallographic methods	7
1.1.5 Triple axis diffractometry	13
1.2 Imaging large ensembles of embedded nanoparticles	16
2 Nanomaterials with ensembles of embedded nanoparticles	19
2.1 Introduction	19
2.2 Age hardenable Al-Cu alloys	20
2.2.1 Al-Cu nanoprecipitate composition, shapes and dimensions	21
2.2.2 Preparation of a suitable sample microstructure	24
2.2.3 Preparation of a suitable sample size	28
2.3 Summary	29
3 X-ray diffraction theoretical background	31
3.1 Interaction of X-rays with matter	32
3.1.1 First Born approximation	33

3.1.2	Fraunhofer diffraction	34
3.2	Diffraction from crystals	40
3.2.1	Kinematical diffraction	41
3.2.2	Dynamical diffraction	42
3.2.3	Summary	47
4	Experimental setup for reciprocal space mapping with an analyser crystal	49
4.1	Synchrotron X-ray sources	50
4.1.1	Beam characteristics from bending magnets and insertion devices	50
4.1.2	Brightness and coherence	54
4.2	Triple axis diffractometry setup	57
4.2.1	Crystal monochromators and analysers	58
4.2.2	Reciprocal space mapping geometry	60
4.3	Information content of triple axis diffractometry reciprocal space maps	62
4.3.1	Triple axis diffractometry instrumental function	62
4.3.2	Fraunhofer diffraction from the sample in the reciprocal space map	64
4.4	Sample holder and heater	65
4.5	X-ray detectors for reciprocal space mapping with an analyser crystal	68
4.6	Summary	69
5	Simulations of X-ray diffraction from ensembles of nanoparticles	71
5.1	Simulation methodology for X-ray diffraction from embedded nanoparticle ensembles	73
5.1.1	Limits of the first Born approximation for embedded Al-Cu nanoparticles	74
5.1.2	Limits of the projection approximation for embedded Al-Cu nanoparticles	75
5.1.3	Simulating Fraunhofer diffraction patterns from large ensembles of weakly diffracting Al-Cu nanoparticles	77
5.1.4	Simulations of Al-Cu nanoparticle ensembles with various size distributions	81
5.1.5	Practical considerations for computing Fraunhofer diffraction patterns from large sample volumes	82
5.2	Nanoparticle reconstructions from simulated Fraunhofer diffraction patterns of polydisperse nanoparticle ensembles	83

5.2.1	The hybrid input-output iterative image reconstruction algorithm	85
5.2.2	Reconstruction results and discussions	87
5.3	Simulating analyser based reciprocal space maps	93
5.3.1	Simulating reciprocal space maps with XDC	93
5.3.2	Simulation and measurement of the triple axis diffractometry instrumental function	94
5.3.3	Simulations of RSMs with various nanoparticle size distributions and nanoparticle rotation	97
5.4	Summary	106
6	Experimental development of an X-ray nanoparticle characterisation technique	109
6.1	Introduction	109
6.2	Establishing the sensitivity of the reciprocal space mapping technique to nanoparticle size and orientation: a feasibility study	110
6.2.1	Introduction	110
6.2.2	Experimental setup and sample details	110
6.2.3	Results	111
6.2.4	Nanoparticle reconstruction	128
6.2.5	Further discussions and conclusions	131
6.2.6	Summary	135
6.3	A phenomenological study of diffraction changes during <i>in situ</i> nanoparticle growth using triple axis diffractometry	136
6.3.1	Introduction	136
6.3.2	Experimental setup and sample details	136
6.3.3	Results and discussions	139
6.4	<i>In situ</i> reciprocal space mapping of the initial stages of nanoparticle growth in an Al-Cu alloy	142
6.4.1	Introduction	142
6.4.2	Experimental setup and sample details	143
6.4.3	Results and analysis	144
6.4.4	Conclusions	152
6.5	Summary	153
7	Conclusions	155
7.1	Overview	155

7.2	Limitations of this study and suggested future work	157
7.2.1	Extensions of the technique to laboratory X-ray sources	157
7.2.2	Suggested further development of the method for simulating two dimensional RSMs	158
7.2.3	Implications of the 2D diffraction plane of the analyser	159
7.2.4	Current work on nanoparticle reconstruction based on outcomes discussed in the thesis	165
7.2.5	Retrospective considerations regarding the samples	167
7.3	Summary	168
	Bibliography	171
A	Publications arising from this thesis	195
A.1	Real-time in situ nanoclustering during initial stages of artificial aging of Al-Cu alloys	197
A.2	Early detection of nanoparticle growth from x-ray reciprocal space mapping	203
A.3	3D X-ray diffraction imaging of nanoparticles using incoherent radiation	206

List of Figures

1.1	Coherent diffractive imaging	11
1.2	Triple axis and triple crystal diffractometry	14
2.1	Model of nanoprecipitates in an Al-Cu single crystal	23
2.2	Simulated structure of GP and GP2 zones in Al-Cu alloys	24
2.3	Solubility of Cu in Al	25
2.4	Hardness curves for Al-Cu alloys	26
2.5	TEM micrograph of nanoprecipitation in an Al-5.0wt% Cu sample, after 10 hours at 220°C	27
3.1	Ewald sphere	34
3.2	Projection approximation	36
3.3	Fraunhofer diffraction on the Ewald sphere	38
3.4	Fraunhofer diffraction on the Ewald sphere for a shorter wavelength	39
3.5	Ewald sphere with reciprocal lattice	42
3.6	Bragg diffraction geometry for dynamic diffraction	44
3.7	Simulated rocking curve from a Si(400) crystal with 1.0Å X-rays	46
4.1	Spectra of various X-ray sources compared	51
4.2	Wiggler/Undulator: Alternating periodic dipole magnets	52
4.3	Photograph of "BigDiff" at ANBF, Photon Factory	54
4.4	Experimental setup at BL29XU, SPring-8	55
4.5	Experimental setup at BL13XU, SPring-8	56
4.6	Non dispersive TAD with channel cut monochromator and analyser	58
4.7	Monochromator and analyser in the non-dispersive setting	59
4.8	Collation of various 1D scans to assemble a 2D RSM	62
4.9	TAD instrumental function schematic	63
4.10	Ewald shell: finite thickness of the Ewald sphere surface	64
4.11	Reciprocal space map content: Instrumental function and Fraunhofer diffraction from the sample	65
4.12	Specimen sandwich	66

4.13	Sample holder and heater	67
5.1	X-ray optical path from source to detector in five stages	71
5.2	TEM micrograph of nanoprecipitation in an Al-2.0wt% Cu sample, after 48 hours at 200°C	75
5.3	Model of three orthogonal Al ₂ Cu nanoparticles in an Al-Cu alloy	76
5.4	Volume of sample contributing coherently to the diffraction pattern	78
5.5	Compromise between sample thickness and number of diffracting nanoparticles	80
5.6	Simulated Al ₂ Cu nanoparticles in an Al-Cu sample	82
5.7	Simulated Fraunhofer diffraction patterns from an Al-Cu sample	84
5.8	Hybrid input-output algorithm: an iterative phase retrieval method	86
5.9	Reconstruction of Al-Cu nanoparticles from simulated Fraunhofer diffraction patterns	88
5.10	Reconstructed nanoparticle profiles as a function of the standard deviation of polydisperse nanoparticle ensembles	90
5.11	Reconstructed nanoparticle size vs. standard deviation of simulated diameters	91
5.12	Reconstructions from Fraunhofer diffraction of periodically arranged nanoparticles	92
5.13	Geometry of reciprocal space mapping as simulated by XDC	94
5.14	Simulated and experimentally measured TAD instrumental functions	96
5.15	Projected nanoparticle diameter as a function of azimuthal rotation	98
5.16	Projected nanoparticle diameter as a function of azimuthal rotation	99
5.17	Simulated 2D RSMs from ensembles of Al-Cu nanoparticles where $S_m = 250\text{nm}$	100
5.18	Simulated monochromator pseudo streak profiles from various azimuthal orientations where $S_m = 250\text{nm}$	101
5.19	Simulated monochromator pseudo streak profiles from various diameter distributions	103
5.20	Simulated monochromator pseudo streak profiles from various diameter distributions where $\theta_z = 5^\circ$	105
6.1	Experimental TAD instrumental function 2	112
6.2	Experimental RSM from sample 0	113
6.3	Experimental monochromator pseudo streaks from the instrumental function and sample 0	114

6.4	Experimental RSMs of sample 1a and 2b using two beam sizes	116
6.5	Experimental monochromator pseudo streaks from the instrumental function and samples 1a and 1b	117
6.6	Experimental RSMs of sample 2a in two orientations	118
6.7	Experimental RSMs of sample 2a in two orientations with a smaller beam	119
6.8	Experimental monochromator pseudo streaks from the instrumental function and sample 2a in two orientations with two beam sizes scaled for comparison	120
6.9	Comparison of experimental RSMs from sample 2b in two orientations	123
6.10	Experimental monochromator pseudo streaks from the instrumental function and sample 2b in two orientations	124
6.11	Experimental RSM from sample 3a	126
6.12	Experimental monochromator pseudo streaks from the instrumental function and sample 3a in two orientations	127
6.13	Experimental RSM from sample 3b	128
6.14	Comparison of experimental RSMs from sample 2b, 3a and 3b in one orientation	129
6.15	Reconstruction of modal nanoparticle from experimental RSM	130
6.16	Comparison of monochromator pseudo streaks from all samples, symmetrised and scaled	131
6.17	Experimental RSM showing where 2D scans were collected for preliminary <i>in situ</i> nanoparticle growth investigations	138
6.18	Experimental results from preliminary <i>in situ</i> real-time nanoparticle growth	139
6.19	Al-Cu hardness curves for Cu concentrations and heat treatments similar to samples S1-S5 (Gable, 2006a)	141
6.20	Experimental RSMs collected during <i>in situ</i> nanoparticle growth, 1-4 of 8	145
6.21	Experimental RSMs collected during <i>in situ</i> nanoparticle growth, part 2 of 2	146
6.22	Experimental RSM from an Al-4.0wt% Cu sample after 75 minutes at 220°C	147
6.23	Time dependent variation of the diffracted intensity profile during artificial ageing of an Al-4.0wt% Cu sample	147
6.24	Strain field modulation parameter <i>vs.</i> time	150
6.25	TEM micrographs of Al-4.0wt% Cu after a total of 136 minutes at 220°C	151
7.1	Simulated RSMs with 2D sample functions	160
7.2	Simulated monochromator pseudo streak from two orientations of 3D Al ₂ Cu nanoparticle ensembles	161
7.3	Schematic of incident beam on the analyser crystal	162

7.4	Fraunhofer diffraction patterns from 3D nanoparticle ensembles	164
7.5	Reconstructed Al ₂ Cu nanoparticles from experimental RSMs	165
7.6	TEM micrographs of Al-4.0wt% Cu aged at 220° for 8.5 hours	166

List of Tables

2.1	Nanoprecipitates in an Al-Cu alloy	22
4.1	Beamline characteristics: BL20B (Photon Factory), BL13XU and BL29XU (SPring-8)	53
4.2	Characteristics of silicon crystals used as monochromators and analysers	59
4.3	Scan types in triple axis diffractometry	61
6.1	Al-Cu alloy sample details for experimental part 1: Feasibility study	111
6.2	Al-Cu alloy sample details for experimental part 2: Real-time <i>in situ</i> nanoparticle growth	137

Abstract

A new non-destructive, high resolution X-ray diffraction technique is developed for the characterisation of ensembles of embedded nanoparticles. The method is based on reciprocal space mapping using an analyser crystal, making it sensitive to very low diffraction contrast between nanoparticles and their surrounds, and capable of encompassing a large volume, representative of the bulk material. The robustness of the technique is demonstrated by its lack of dependence on the X-ray coherence volume and optical stability. In addition, the use of a counting detector provides the necessary high dynamic range, and avoids the restrictions imposed by the finite pixel size of a direct space detector and loss of information due to a beamstop.

We review the most widely used techniques for imaging on the nanometre scale and highlight their unique capabilities. We then demonstrate that no single technique alone is sufficient for model independent, non-destructive, nanoscale characterisation of embedded nanoparticles in a bulk material sample. *In situ* and real-time investigations are imperative for the understanding, and ultimately the control of nanoparticle nucleation and growth in technologically important alloys, colloidal suspensions and various nanomaterial specimens. In this thesis we make significant progress in addressing this crucial omission.

We begin by presenting the particulars of scalar diffraction theory that enable us to mathematically describe kinematic diffraction from large ensembles of nanoparticles embedded in a matrix. The requirements of X-ray optics are then discussed, from the pertinent properties of synchrotron X-ray sources through high quality analysing and monochromating crystals.

A method of simulating Fraunhofer diffraction and reciprocal space maps from a large, sparse ensemble of weakly diffracting Al-Cu nanoparticles is deduced from elementary coherence considerations. We then demonstrate that quantitative information regarding the nanoparticle ensemble polydispersity can be extracted from the reconstructions of nanoparticles from the Fraunhofer diffraction patterns of numerous such ensembles. In simulated reciprocal space maps we examine the effects of nanoparticle ensemble polydispersity and nanoparticle orientation with respect to the diffraction plane. Experimentally obtained reciprocal space maps of diffracted

intensity from nanoparticles in an Al-Cu alloy are then presented, demonstrating the sensitivity of the technique to weakly diffracting embedded nanoparticles and their orientation relative to the diffraction plane. Here we also present the results of an iterative algorithm applied to reconstruct, with <10nm resolution, a two dimensional nanoparticle, representative of the ensemble.

Practical considerations for an *in situ*, real-time X-ray diffraction investigation of the initial growth dynamics of embedded nanoparticles in a bulk material sample are explored in a pilot experiment. Finally, the results from an experimental demonstration of the first, real-time, *in situ* X-ray diffraction investigation of the early stages of nanoparticle growth (in Al-Cu alloys) are then presented and analysed in the context of clustering and dynamic strain in the sample. Simulations involving a simplified model of local strain are shown to be well correlated with the X-ray diffraction data, and a modal, representative nanoparticle size is determined, which agrees with data from transmission electron micrographs of the sample.

In conclusion, current ongoing nanoparticle reconstruction efforts are discussed alongside the future directions suggested as an extension of the nanoparticle characterisation technique.

Disclosure

I declare this thesis:

- (i) contains no material which has been accepted for the award of any other degree or diploma in any university or other institution,
- (ii) to the best of my knowledge contains no material previously published or written by another person, except where due reference is made in the text of the thesis,
- (iii) includes work which is based on joint research and publications. Where such work is presented a statement declaring the relative contributions of the respective authors has been included.

Nadia Zatsepin: _____ 5 November 2010

Acknowledgements

I am very grateful to my supervisors A/Prof. Andrei Nikulin, Dr. Karen Siu and Dr. Ruben Dilanian. I really admire Andrei's experimental expertise and creativity and in addition to his support and encouragement, I am deeply thankful to him for nurturing me into an independent researcher. To Karen, who bravely stepped into the role of my co-supervisor at a later stage, I am grateful for the exposure to the light at the end of the tunnel. Without her patience, expertise, support, and endless proof-reading, I would not be finished now. To Ruben, for many helpful discussions, as well as much encouragement and support. Thank you to Ruben, also, for the nanoparticle reconstruction and for the basis of the analysis of *in situ* experimental results in chapter 6.

I owe a debt of gratitude to David Paganin, whose selfless dedication to students, positivity, guidance, encouragement and wisdom were invaluable during my years at Monash University.

During my candidature I had the privilege to work with some incredible researchers and would like to thank them for their contributions.

This work would not have been possible without the generosity and expertise of Barry Muddle. Not only did he introduce me to the fascinating, dynamic world of light metal alloys, he also provided me with much encouragement, many ideas and invaluable advice.

I am especially thankful to Victor Matveev, who overcame the challenge nobody else could and made our unique, single-crystal Al samples. Thank you again to Matveev for his contribution to our published work.

Thank you to Brian Gable for his constant readiness to help and pass on knowledge. Of course, I am also very grateful for his sample preparation training and the Al-Cu hardness curves used in this thesis. Many other people also helped with sample preparation and/or obtaining transmission electron micrographs of our samples, so my gratitude goes out to them too: Colleen Bettles, Sam (Xiang) Gao, Laure Bourgeois, from Monash University, and Andrew Sullivan at Deakin University. Thanks also goes to Yury Kryvasheyev for advice on and proof reading of the chapter on samples.

Our experiments at the Photon Factory and SPring-8 would not have been possible

without the attentive support of James Hester, Osami Sakata and Tetsuya Ishikawa. Thanks also to Yoshinori Nishino, Aliaksandr Darahanau, Alexeiy Souvorov and Garry Foran.

I'd also like to extend my sincere thanks to a number of other researchers who freely gave their time to help me. First and foremost, I am very grateful to Tim Gureyev, especially for the XDC code used for reciprocal space map simulations. For sharing their expertise in reciprocal space mapping, I would like to thank Konstantin Pavlov and Andrew Stevenson. Thank you again to Andrew, and Laure Bourgeois, for their encouraging comments and useful advice during my confirmation of candidature. Thanks also to Imants Svalbe and Lincoln Turner for their kind advice.

Thanks to the School of Physics Mechanical Workshop, in particular to Alan Holland and Roger Bucknell, for aiding my design of, and machining, the sample holder and careful sectioning of our ridiculously expensive monocrystalline aluminium samples. Thank you, papa, for helping immensely with the sample heater. I'd like to thank Rod Mackie too, who in addition to helping with sample preparation, shared many humorous tales with me over the years.

I am very grateful to the staff at the School of Physics, headed by Michael Morgan, for all the assistance they have provided over the years, on a professional and personal level, with special thanks to Jean Pettigrew, James Gibbons, Tracey Lawrence and Julia Barnes.

It was a pleasure to be a physics demonstrator in the undergraduate labs. I am grateful to have been trained and supervised by Susan Feteris, who was an exemplary employer, mentor and an inspiration. A big thank you also to Jenny McCabe, Lincoln Turner and the laboratory tech staff for their support in my laboratory teaching endeavours.

Throughout my candidature I have been the recipient of several scholarships and would like to acknowledge the following funding bodies: the Australian Postgraduate Awards scheme, the Australian Research Council, the Australian Synchrotron Radiation Program, the Access to Major Research Facilities Program, Monash Research Graduate School, Monash University Faculty of Science and School of Physics, as well as support from RIKEN and SPring-8 synchrotron facility. I would also like to thank SPIE and the organisers of XMNP 2009 for financial aid that enabled my participation in their respective conferences.

I would like to thank Philip Chan at the eResearch Centre at Monash University and Mike Kuiper at the Victorian Partnership for Advanced Computing. I am very grateful to Philip for patiently sharing his expertise, for discussions and shell scripts,

and especially for the plethora of borrowed nodes he afforded me on the Monash Sun Grid. To Mike, I'm grateful for all his help in trying to get IDL working on the cluster, but more importantly, for sharing with me his unjaded, inspirational love of science and science education.

Thank you to my fellow postgraduates, who have made my postgrad life very enjoyable: Sally Irvine, David Vine, Gary Ruben, Kaye Morgan, Kathryn Spiers, Shakes Chandra, Naomi Schofield, John Gillam, Ivan Williams, Toby Beveridge, Marcus Kitchen, Shane Kennedy, and John Daniels; thanks for the coffees and Friday drinks. To the newer kids on the block, Katie Auchettl, Elliot Hutchison, Martijn Jasperse, Jeremy Brown, Brad Murnane, David Palamara, thanks for keeping the coffee train alive. I must single out Gary Ruben and Shakes Chandra for, among many things, their help with \LaTeX and other technical things.

I enjoyed sharing not only an office but many laughs, frustrations, and chocolate with Sally and Kathryn. Nothing can replace the mutual understanding we have for each others' PhD journeys. To my new office mates, Jay, Elliot and Katie, thanks for the shared humour and our communal creative pursuits – you've made the last few months of writing up really fun.

I am immensely grateful to David Vine for patiently discussing aspects of my work *ad infinitum*, and for ensuring our conferences are very enjoyable and educational. Sally and Kaye, I hope we can repeat our incredible conference trip to Positano.

Thank you to my friends outside of work: Mark Fisher, who introduced me to Feynman and whose passion for physics made me realise my own, Rachel Lee, for her refreshing humour and our delicious catch-ups, Steve Homolya, for our shared love of music (and for my physics office guitar), Sasha Grubman, David Treeby, Julian Giordani and Suralini Fernando, for our rare (sorry!) but cherished catch-ups.

To my dear Veniamin, Rosa, Taya, Mum and Dad, thank you for your boundless love and support. Mama, Papa, thank you for seeding my curiosity and love of nature and education, and for your endless hard work that enabled my comfortable postgraduate life.

Jayden, thank you for your wicked humour, for keeping me sane, for cooking for me and for being so effortlessly patient and understanding. You inspire me. I dedicate this thesis to you.

Introduction

This thesis describes a non-destructive, high resolution X-ray diffraction technique developed for the characterisation of ensembles of weakly diffracting embedded nanoparticles. The method combines high resolution triple axis X-ray diffractometry (TAD) and an iterative image reconstruction algorithm also used in coherent diffracting imaging (CDI). Significant advantages of the technique are its ability to overcome the low diffraction contrast between nanoparticles and their surrounding material, and the ability to encompass a large volume, representative of the bulk material. The lack of strict dependence on either a large X-ray coherence volume or a high degree of experimental optics stability attests that such bulk material, high resolution, systematic investigations are not restricted to high end synchrotron X-ray sources, but can be extended to laboratory sources.

We formulate the theoretical considerations and experimental conditions necessary for the observation of X-ray diffraction from static intermetallic nanostructures. Experimentally, we focus on the problem of characterising the bulk material: age-hardenable Al-Cu alloys that contain weakly diffracting embedded nanoparticles. These alloys are representative of a family of technologically important nanomaterials that obtain their mechanical properties, such as strength, hardness and plasticity, from the embedded precipitate morphology, composition, volume fraction and/or spatial distribution. An *in situ*, real-time¹ method of observing the formation and growth of nanoparticles in these kinds of samples is important because the conditions (heat or pressure, for example) at the initial stages of nanoparticle formation, and consequential dynamic behavior, determine the resultant microstructure, and hence the properties of the final product.

¹In this thesis we will use *real-time* to describe dynamics that occur over time scales of tens of minutes to hours, as is appropriate for the nanomaterials we investigated and data collection time, as detailed in chapters 2 and 4, respectively.

Outline of thesis

In the first chapter we review the most relevant techniques for imaging on the nanometre scale, and compare their successes and limitations in relation to embedded nanoparticle characterisation. We begin with electron microscopy, as it is arguably the most common approach to nanoparticle characterisation. X-ray crystallographic and non-crystallographic approaches are discussed next. The second chapter describes the samples of interest, motivation for their selection, and the relevant characteristics of nanoparticle formation and morphology.

In chapter 3 the background theory regarding the interaction of X-rays with matter is presented, including an outline of Fraunhofer diffraction from inhomogeneous matter, as well as kinematic and dynamical theories of diffraction from crystals. The experimental particulars pertinent to analyser based reciprocal space mapping of diffraction from embedded nanoparticle ensembles are presented in chapter 4. In this chapter we discuss the ideal X-ray source characteristics and optical elements, and then describe the geometry of reciprocal space mapping. We outline the design of a dedicated sample holder/heater that enabled us to carry out *in situ* real-time nanoparticle growth investigations. The chapter concludes with a brief discussion of X-ray detectors suitable for reciprocal space mapping of diffraction from weakly diffracting nanoparticle ensembles.

Chapter 5 describes the most pertinent considerations for imaging large ensembles of weakly diffracting embedded nanoparticles, which enable us to simulate the diffracted X-ray intensities. These simulations are presented in the second half of chapter 5, including Fraunhofer diffraction patterns from ensembles of nanoparticles, and the nanoparticles reconstructed from these diffraction patterns by the iterative hybrid input-output (HIO) algorithm. In addition to clarifying our understanding of the interactions that take place, the simulations show a quantitative relationship between the reconstructed representative nanoparticle and the size distribution of the diffracting nanoparticles. Simulated reciprocal space maps of the TAD instrumental function and diffraction from various nanoparticle size distributions and orientations are explored in an effort to understand the experimentally observed diffraction effects presented in chapter 6.

In chapter 6 we present the results of the experimental development of the technique. We begin with a feasibility study investigating the sensitivity of the technique to nanoparticle size and orientation, as well as sample thickness. A demonstration of a high resolution (less than 10nm) reconstruction of the shape and size of a nanoparticle, representative of the ensemble, is also included. We then establish the technique's

ability to measure diffraction changes during *in situ* nanoparticle growth (sample heating), from a variety of samples. This experiment is a necessary predecessor to the first experimental study of the initial growth dynamics of nanoprecipitates in a bulk material Al-Cu sample using X-rays, which closes the experimental chapter.

The thesis concludes with an overview of the main results, including technique successes and limitations. We close with a discussion of current ongoing extensions and suggested future work necessary to further the non-destructive, *in situ*, real-time, nanoparticle characterisation technique.

1.1 Characterising nanomaterials

Novel materials are emerging whose properties are governed increasingly by their structure on nanoscale dimensions. At such small scales, in one, two, or three dimensions, physical and chemical properties arise that differ greatly from their bulk material counterparts (Schmid, 2004; Wagner, 2007). Nanomaterials may be single nanoparticles such as quantum dots or nanocrystals in colloidal suspensions, or materials containing ensembles of nanoparticles or nanoprecipitates that govern the physical properties of the bulk material (Schmid, 2004). These materials have new applications in materials engineering, energy generation and storage, electronics and biotechnology.

Any progress in the ability to create and manipulate on the nanometre scale can only be made with detailed understanding of the physical and chemical behaviours of the material, and the influence of the size of its constituents on its properties. Consequently, progress in nanofabrication is in need of specialised non-destructive metrology techniques, especially those that allow imaging in three dimensions (3D) on the nanometre scale, and offer the possibility of real-time, *in situ* characterisation of the bulk material.

There are a number of techniques using X-rays, electrons or neutrons, dedicated to the characterisation of nanomaterial morphology with high resolution (on the order of nanometres). However, for an important class of nanomaterials, those which include embedded nanoparticles, no single technique suffices. We will now provide a brief overview of the commonly available techniques, loosely grouped into crystallographic and non-crystallographic methods. The discussion will focus on the techniques' accomplishments and limitations in determining physical properties like size, form, and spatial distribution of nanoparticles.

1.1.1 Electron microscopy

Electron microscopy methods, in particular transmission electron microscopy (TEM) and scanning TEM (STEM), are the most commonly applied tools to study nanomaterials at the atomic level, including embedded nanoparticles (Liu, 2005; Williams and Carter, 2009). A transmission electron microscope can explore both crystallographic or non-crystallographic samples, and can image in real-space or diffraction mode.

By virtue of the short wavelength of electrons when accelerated by high voltages (e.g. $\sim 0.02\text{\AA}$ at 300 keV), TEM offers very high resolution information about samples, for example sub-50pm resolution of atomic spacing in a Germanium crystal (Erni *et al.*, 2009). Multiple scattering effects, penetration depth and possible radiation damage restricts TEM applicability, by necessitating a sample thickness of less than $\sim 0.3\mu\text{m}$. Consequently, preparation of suitable specimens is often time consuming, costly, destructive and prone to the introduction of artifacts. Such thin samples complicate the observation of nanoparticles with very high aspect ratios, and impose an artificial environment for nanoprecipitate nucleation and growth, which means real-time, *in situ* experiments (such as those by Alani and Pan (2001) and Chen *et al.* (2006)) may not be representative of bulk material dynamical behavior. It is also difficult to obtain 3D information on such materials, or on nanoparticles contained within them, by TEM, without serial sectioning of the sample or a complicated tomographic approach (Midgley, 2007; Bárcena and Koster, 2009).

However, when the necessary conditions are met, TEM and other electron microscopy techniques are complementary to X-ray imaging, as their currently available resolution (on the nanometre scale) is an excellent reference for X-ray imaging. Also, electron microscopy methods can be combined with X-ray coherent diffractive imaging (CDI, §1.1.4) to achieve sub-Ångström resolution for non-crystallographic samples (for example Zuo *et al.* (2003); Huang *et al.* (2009)). Nonetheless, such single-particle approaches are not suitable for bulk-material analysis where characterisation requires quantitative morphological information about a very large number of nanoprecipitates. Indeed, the analysis of many TEM micrographs, including thousands of particles, is necessary in order to obtain sufficient statistics about the size and size distribution of the bulk material ensemble.

Scanning probe techniques, such as atomic force microscopy or scanning tunnelling microscopy can image surfaces or very thin structures with sub-Ångström resolution, but are insensitive to strain in the crystal lattice (Cowley, 1975; Zhuang *et al.*, 1999). Thus these techniques are also not directly applicable to thick samples with embedded nanoparticles, nor to the observation of strain dynamics during

the growth of nanoparticles, which is pertinent to the final microstructure of the nanoprecipitate-containing material.

1.1.2 Probing matter with X-rays

Hard X-rays (~ 5 to ~ 120 keV) are also very suitable for high-resolution material analysis, due to their short wavelengths ($\sim 2.5 - 0.01\text{\AA}$). However, in contrast to transmission electron microscopy, X-ray methods are generally non-destructive, and their high penetration allows bulk material analysis. The ability to characterise the internal structure of a material is a result of X-ray scattering and absorption by the material (Bonse, 2008), the theoretical details of which are presented in chapter 3. For a specimen of unknown composition, comprehensive phase-amplitude contrast characterisation requires knowledge of both absorption and scattering phenomena as expressed by the real and imaginary parts of the complex refractive index of the material. The desire for comprehensive characterisation of a material is a statement of the inverse problem (Kress, 1999) – the process of obtaining detailed information about the structure of the object from the scattered and/or absorbed radiation.

In the discussion that follows we describe X-ray techniques used for nanoscale material characterisation. We begin with the well established X-ray crystallography, and then review non-crystallographic methods such as small angle X-ray scattering, CDI and TAD, the last of which forms the basis of the technique developed in this thesis.

1.1.3 Crystallographic methods

X-ray crystallography is widespread and well developed, having had a tremendous impact on chemistry, structural biology (Helliwell, 2005) and materials sciences (for a historical review see Bragg (1975)). The diffraction pattern, arising from X-rays elastically scattered by the electrons in the sample, is measured in order to calculate the atomic positions in the unit cell of a crystal lattice (for example, see Zachariassen (1945); Pauling (1946); Borchardt-Ott and Gould (1995)).

X-ray crystallographic methods are ideal for anything that can be forced into arrays of periodically repeated unit cells. This real space symmetry leads to constructive interference of diffracted X-rays in discrete directions. An infinite, ideal crystal would lead to very sharp, measurable diffraction peaks, the positions of which are related to the crystal lattice spacing by Bragg's law (Bragg, 1913a,b), discussed in §3.2. In order to solve the phase problem of reconstructing the crystalline sample structure, given

only the magnitude of the diffracted field, further sample information is often needed to supplement the discretely probed diffracted X-ray intensities. Widely used in macromolecular crystallography, for example, is a method that exploits the difference in diffraction contrast near an element's absorption edge, called multi-wavelength anomalous dispersion (MAD) (Fourme and Hendrickson, 1990; Hendrickson, 1991).

Structural information, in particular the unit cell, can be reconstructed with real space resolution on the order of $\sim 0.1 - 100 \text{ \AA}$. Any deviation from the ideal crystal, whether by crystal defects, misalignment of unit cells, or small crystal sizes (insufficient number of unit cells) would diminish the accuracy of the reconstructed structure.

Powder diffraction is a closely related, widely used technique where the sample consists of thousands of randomly oriented crystals, leading to smooth, symmetric rings in the diffraction pattern, as opposed to the discrete Laue (transmission geometry) diffraction points observed for single crystals (Jenkins and Snyder, 1996). This rapid, non destructive technique can shed light on constituent materials, their phases² and concentrations, and is also widely used for crystal structure determination.

However conventional crystallographic reconstruction approaches are not valid for samples which cannot be crystallised, such as amorphous and disordered materials (including some inorganic nanostructures), polymers, or crystals with defects or strain. This limitation also extends to many important biological samples, whose crystalline form is significantly different from the native state, or those where the functional behaviour of a material is dependent on a wet environment. Similarly, crystallographic methods are inappropriate for obtaining quantitative morphological information about an ensemble of embedded nanoparticles, such as their size, shape and spatial distribution. This is because often the nanoparticles are too weakly diffracting, nor is the requirement satisfied for a large number of identical effective "unit cells". Moreover, the nanoparticles are rarely identical, identically oriented and/or strictly periodic. Crystallographic methods can be useful to explore the crystal structure within nanoparticles though, in which case the problem becomes analogous to powder diffraction.

²In this materials science context, the term *phase* refers to the chemical composition, crystal structure (if applicable) and physical state of a material. Throughout this thesis we will mostly use the usual definition of *phase* in wave optics, and the meaning (optical or materials) will be clear from the context.

1.1.4 Non-crystallographic methods

Non-crystallographic methods are those aimed at characterising non-periodic (non-Bragg diffracting) samples, which have continuous reciprocal space representations, i.e. their diffracted intensities are not concentrated around isolated points in reciprocal space. In this section we will discuss two related non-crystallographic techniques that are used in nanoscale characterisation, small angle X-ray scattering and coherent diffractive imaging. We should mention that there is a vast number of other X-ray methods, which we will not be discussing in detail as they are not readily applicable to nanoscale characterisation of ensembles of nanoparticles. These include in-line holography (Gabor, 1948), off-axis holography (Leith and Upatnieks, 1962, 1963, 1964) and phase contrast (PC) imaging techniques, such as propagation based PC (Snigirev *et al.*, 1995; Wilkins *et al.*, 1996; Cloetens *et al.*, 1996), analyser based PC or diffraction enhanced imaging (Förster *et al.*, 1980; Somenkov *et al.*, 1991; Ingal and Beliaevskaya, 1995; Davis *et al.*, 1995b,a; Chapman *et al.*, 1997) and interferometry (Bonse and Hart, 1965; Hart, 1975). As we will argue in this thesis, the direct space, micrometre resolution techniques just mentioned are not well suited, and the most appropriate approach to characterisation of large ensembles of nanoparticles is via diffraction measurements in reciprocal space.

Small angle X-ray scattering

Small angle X-ray scattering (SAXS) and small angle neutron scattering (SANS) are the most widely used non-crystallographic approaches to nanoscale characterisation. Their primary advantage is the ability to characterise amorphous systems, including in solution. Hence SAXS, in particular, has been extensively used in biological applications, such as analysing macromolecules, porous media, micelles, proteins and polymers (see Putnam *et al.* (2007) and references therein). An advantage of SANS over SAXS is the ability to manipulate contrast by deuteration. When complemented by electron microscopy, SAXS and SANS are some of the most powerful methods to characterise nano-sized precipitates in alloys (see Preston (1938a); Williams *et al.* (1999); Deschamps *et al.* (2001); Fratzl (2003) and references therein).

SAXS involves the measurement of small angle scattering data using X-rays with wavelengths of several Ångströms to determine nanoscale structural information with $\sim 1 - 5$ nm resolution (Guinier *et al.*, 1955; Glatter and Kratky, 1982). It is suited to length scales of tens to thousands of nanometres, giving "ultrastructural" information, i.e. secondary and tertiary order structure. SAXS is non-destructive and capable of

investigating a relatively large volume simultaneously ($\sim 10 - 100\mu\text{m}$ thick samples, and up to 1mm at synchrotron sources, depending on attenuation/energy). Enhanced elemental diffraction contrast in SAXS is achieved by using anomalous scattering near absorption edges, similar to that used in MAD (see [Goudeau *et al.* \(1986\)](#); [Materlik *et al.* \(1994\)](#); [Haubold *et al.* \(1996\)](#) and references therein).

For sufficiently dilute monodisperse solutions, the diffracted intensities of the individual particles are added incoherently, while at higher particle concentrations the interparticle interference effects dominate, complicating the analysis. Average particle dimensions and size distributions are commonly derived by fitting experimental data to an established model ([Feigin and Svergun, 1987](#); [Fratzl *et al.*, 1993](#); [Brumberger, 1993](#)), which may lead to ambiguity as particles with very similar diffracting properties are indistinguishable. Many metallic alloys are anisotropic with polydisperse embedded nanoprecipitates, which SAXS cannot easily distinguish. Nanoparticles randomly oriented in an amorphous matrix or colloidal suspension result in spherical averaging of the scattering curve's intensity, which makes the analysis and shape resolution of anisotropic systems/particles much more dependent on *a priori* information ([Ramos *et al.*, 1996](#)). Although SAXS data analysis techniques of increasing complexity are being developed ([Svergun, 1991](#); [Hansen and Pedersen, 1991](#); [Förster *et al.*, 2005](#); [Saldin *et al.*, 2010](#)), the success of SAXS in nanoparticle shape analysis fundamentally relies on modelling, fitting and *a priori* knowledge.

Grazing incidence small angle X-ray scattering (GISAXS) couples SAXS with diffuse X-ray reflectivity ([Als-Nielsen and McMorrow, 2001](#)), a quantitative surface roughness analysis technique based on kinematic diffraction. The approach is good for investigating density correlations and/or the shape of nanoscopic objects (in 1D or 2D) on surfaces (e.g. islands and quantum dots), at buried interfaces, or in thin films. The sensitivity of GISAXS for surface studies suggests it is not well suited to investigating a large ensemble of nanoparticles embedded throughout a thick sample.

Notwithstanding the limitations and difficulties just described, SAXS and GISAXS have been used in determining the morphology and dispersion of nanoscale particles in colloidal systems, quantum dots and colloidal suspensions ([Thiyagarajan, 2003](#)). The techniques are also capable of time resolved, *in situ* studies of nanoparticles ([Renaud *et al.*, 2003](#); [Shinohara *et al.*, 2005](#); [Sakamoto *et al.*, 2006](#); [Zickler *et al.*, 2008](#); [Revenant *et al.*, 2009](#); [Odén *et al.*, 2009](#); [Lazzari *et al.*, 2009](#); [Eymery *et al.*, 2009](#)) and ([Yefanov *et al.*, 2009](#)), where it was combined with coherent diffraction tomography to recover the 3D structure of nanoislands.

Applications of small angle scattering to characterisation of embedded nanoparticles in an Al-Cu alloy

We chose to focus on a particular type of sample that contains embedded nanoparticles for the development of our technique, viz. an Al-Cu alloy. One of the reasons for choosing these samples was the simplicity of the platelet like shape of the naturally growing embedded nanoprecipitates and the moderate ease of sample preparation (further details will be presented in chapter 2). It behooves us to briefly review the use of SAXS/SANS to specifically characterise this and closely related materials.

SANS, combined with TEM, was used to explore *in situ* kinetics of the growth of nanoprecipitates in a single crystal Al-4.0wt% Cu alloy (Czeczor *et al.*, 2000). Czeczor *et al.* made use of *a priori* knowledge of the shape and orientation of the platelet-like precipitates (details in §2.2), to characterise the platelet thickness from SANS data, and used TEM to measure the platelet diameters. So while the investigation was quantitative with high resolution for these simple shaped precipitates, it is not generalisable to all materials containing embedded nanoparticles.

More recently SAXS has been applied to quantitative, *in situ* characterisation of the state of precipitation (including their size and volume fraction) in an Al-8.4Zn-2.1Mg-1.8Cu-0.1Zr (wt%) alloy (Deschamps *et al.*, 2006), where *a priori* knowledge of the shape of the precipitates was, again, beneficial. The study focused on stable phase precipitates (details in §2.2.1), and so was not designed to access the region in reciprocal space that contained information about the initial stages of nanoparticle formation, which often play a pivotal role in determining the microstructure and properties of the final material (Muddle and Nie, 2006).

Marlaud *et al.* (2006) combined SAXS with differential scanning calorimetry and TEM to observe the microstructural evolution of spherical precipitates in an aluminium alloy (7000 series). In the work of Marlaud *et al.* (2006) the aluminium alloy samples were very thin ($\sim 70\mu\text{m}$), risking an imprecise representation of bulk material behavior; the precipitate sizes were evaluated using the Guinier approximation³, involving the radius of gyration (Guinier, 1952), and the nanoparticle volume fraction was evaluated from the integrated scattered intensity. Such calculations, as in the works of Deschamps *et al.* (2006) and Marlaud *et al.* (2006), require assumptions about the composition of the precipitates (Fribourg *et al.*, 2006), and for anisotropic systems containing asymmetric nanoparticles (such as the Al-Cu alloys used in the

³The Guinier approximation expresses the SAXS intensity at very small scattering angles as a function of the radius of gyration of the particle, where the radius of gyration is a distribution of the mass of an object about its centre of mass (or electron density distribution). The Guinier approximation can generally be applied to a particle of any shape.

development of our technique), the commonly used Guinier approximation has no use (Sequeira *et al.*, 1995).

Coherent Diffractive Imaging

X-ray coherent diffractive imaging (CDI) is a lensless imaging technique based on the premise that the Fourier inversion of a specimen's complex far-field diffraction pattern can be used to reconstruct an object's real space structure (see for example van der Veen and Pfeiffer (2004); Nugent (2009) and references therein).

The experimental setup for CDI is very similar to the setup used in SAXS, as shown in Figure 1.1. The specimen is illuminated with coherent X-rays (defined in §4.1.2), and the diffraction pattern is recorded by an area detector, such as a charge coupled device (CCD) coupled with a scintillator and/or image intensifier. Successful phase retrieval from periodic and non-periodic objects by oversampling⁴, coupled with iterative phase retrieval based on the Gerchberg and Saxton (1972) algorithm, and Fienup's improvements thereof (Fienup, 1982) (§5.2.1), was demonstrated computationally by Miao *et al.* (1998); Sayre *et al.* (1998) and Millane (1990), and experimentally demonstrated in transmission geometry by Miao *et al.* (1999) and in reflection geometry by Robinson *et al.* (2001). We have used the same kind of iterative approach to our reciprocal space data to reconstruct average nanoparticles as is commonly used in CDI. Similar to the technique developed here, the resolution in CDI is only limited by the ability to collect data over a large range in reciprocal space. The phase-retrieval/image reconstruction algorithm is discussed in detail in §5.2.1.

CDI is very promising, but is not yet routine. Some of the more recent successful demonstrations of CDI include reconstructions of nanostructures in two dimensions (2D) (Miao *et al.*, 1999; Chapman *et al.*, 2006), in 3D (Larson *et al.*, 2002; Miao *et al.*, 2002; Kohmura *et al.*, 2005; Vartanyants *et al.*, 2005; Juul Jensen *et al.*, 2006; Miao *et al.*, 2006), with 3D imaging of the internal microstructure within a gold nanocrystal (Williams *et al.*, 2003), direct imaging of 3D strain fields and deformations within a lead nanocrystal (Pfeifer *et al.*, 2006), and biological specimens in 2D (see Kirz *et al.* (1995) and references therein, Miao *et al.* (2003); Shapiro *et al.* (2005)).

The technique requires a very stable optical setup as the intensity is measured in direct space and any vibration or drift of an optical component would smear the diffraction pattern. In other words the optical wavefront must be stable with

⁴Oversampling the diffraction pattern, as suggested by Sayre (1952), provides sufficient information to solve the phase problem. The term *oversampling* refers to measuring the diffraction pattern at a frequency higher than the Nyquist frequency (twice the highest spatial frequency of the smallest feature of the sample to be characterised). This corresponds to the isolation of the object in real space.

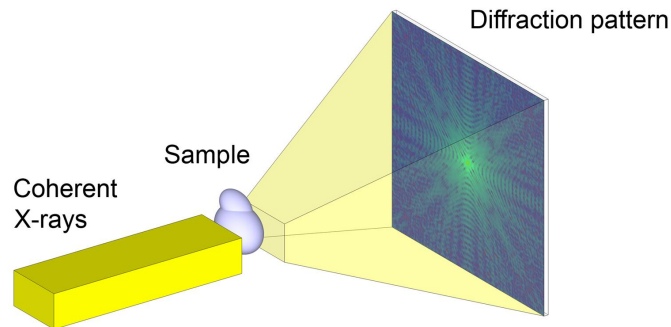


FIGURE 1.1: **Coherent diffractive imaging.** The main experimental principle of coherent diffractive imaging involves an isolated sample illuminated by coherent X-rays and its Fraunhofer (far field) diffraction pattern is recorded in direct space, for example with an area detector.

respect to the single area detector being used. It also requires a coherence volume greater than the sample volume of interest (discussed in §4.1.2), which limits the volume of material that can be explored at a given time. Restrictions imposed by the requirement of complete isolation of the specimen in real space can be avoided by alternative techniques currently being developed, such as the scanning aperture approach (ptychography), originally invented for electron microscopy (Rodenburg and Bates, 1992; Nellist *et al.*, 1995; Chapman, 1996; Nellist and Rodenburg, 1998; Faulkner and Rodenburg, 2004; Rodenburg and Faulkner, 2004; Rodenburg *et al.*, 2007) and Fourier holography (McNulty *et al.*, 1992; Eisebitt *et al.*, 2004).

The diffracted intensities in CDI applications have a wide dynamic range (~ 6 orders of magnitude), requiring a detector system that has a linear response, or at least a well characterised, nonlinear one-to-one response, over this wide range. In addition, nanoscale imaging requires large detector areas and small pixel sizes in order to resolve high spatial frequencies. As CCD systems do not offer the necessary dynamic range nor a very large area, a high number of frames needs to be summed (Nugent, 2009). A new generation of 2D hybrid pixel counting detectors, such as the Medipix (Ballabriga *et al.*, 2006) or PILATUS (DECTRIS Ltd. (Henrich *et al.*, 2009)), offers no read-out noise, single photon counting, a superior signal-to-noise ratio, and a dynamic range spanning six orders of magnitude, compared to 3 – 4 orders for a CCD. However, the currently available pixel sizes (e.g. $172 \times 172 \mu\text{m}^2$ in PILATUS detectors, $75 \times 75 \mu\text{m}^2$ for the upcoming EIGER detector (EIGER, 2009) and $55 \times 55 \mu\text{m}^2$ for the Medipix3 detector (Ballabriga *et al.*, 2006)) are too large for most applications

([Marchal *et al.*, 2009](#); [Nugent, 2009](#)). The necessary use of a beamstop (to protect the detector from the extremely bright central beam that could damage it and/or result in extended dead time) corresponds to a loss of low frequency information. This could result in stagnation of the reconstruction algorithm ([Dilanian and Nikulin, 2005](#)), as the magnitude of the transmitted beam is determined by the total number of electrons involved in the scattering process. The data in this region needs to be estimated by other experimental means (for example soft X-ray microscopy in [Miao *et al.* \(1999\)](#)), which leads to additional constraints becoming necessary ([Nishino *et al.*, 2003](#); [Dilanian and Nikulin, 2005](#)), and requires careful modification of the iterative reconstruction algorithms ([Spence, 2007](#)).

The stringent requirements on optics quality, stability, as well as X-ray brightness and coherence restrict the use of CDI to high end synchrotron sources. However, for samples with low refractive index contrast (i.e. weakly scattering samples) such as biological specimens or some nanoprecipitates embedded in host matrices, as compared to gold ([Williams *et al.*, 2003](#)) or lead ([Pfeifer *et al.*, 2006](#)), even the most powerful existing synchrotrons do not produce the high brilliance that would permit detection of individual particles when using CDI. The next generation of synchrotron sources, i.e. the emerging X-ray free electron lasers (XFELs), will provide a more brilliant X-ray source, which will decrease data collection time and improve the signal to noise ratio ([Chapman, 2009](#)). The femtosecond X-ray pulses will enable dynamics on unprecedented time scales to be probed, in addition to being beneficial to biological experiments where radiation damage (Coulomb explosion) typically completely destroys the specimen shortly after a single exposure ([Neutze *et al.*, 2000](#); [Chapman *et al.*, 2006](#); [Chapman, 2009](#); [Kirian *et al.*, 2010](#)). However, for relatively slow time resolved studies, the shot-to-shot variation in an XFEL will need to be averaged over time, and so will imitate a partially coherent data set ([Nugent, 2009](#)). We will see in §5.1.1 that an increased coherence volume (defined in §4.1.2) is not necessarily beneficial to bulk material investigations of embedded nanoprecipitates.

In summary, the critical advantages of CDI are its ability to obtain 2D and 3D nanoscale structural information about non-crystallographic samples, the potential to work in a wet environment, and that it is relatively easily implemented, with moderate computational demands.

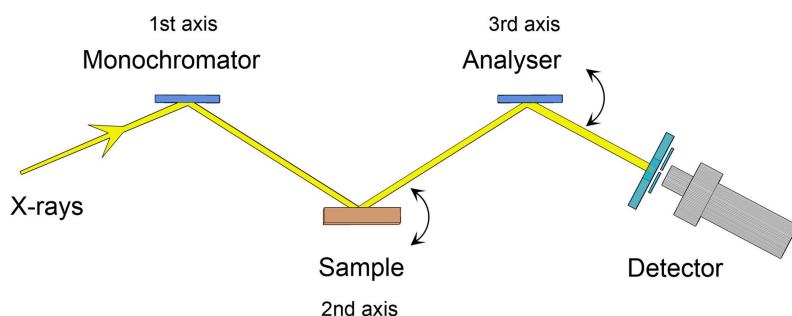
1.1.5 Triple axis diffractometry

Triple axis diffractometry⁵ is an extension of high resolution diffractometry, in which an analyser crystal is used to probe the angular distribution of diffracted X-rays from the sample (Bowen and Tanner, 1998). The setup, shown in Figure 1.2, allows quantitative, high-resolution measurements, separately, of diffraction from different sources, such as perfect crystallinity, defects, mosaic spread and tilt (Eisenberger *et al.*, 1972; Iida and Kohra, 1979; Fewster, 1989). Two dimensional, high angular resolution reciprocal space maps (RSM) in the vicinity of a reciprocal lattice point (Bragg reflection of the 2nd crystal) are obtained by rotation of the second and third axes, defining the reciprocal space coordinate being probed (Iida and Kohra, 1979; Zaumseil and Winter, 1982b). RSMs are discussed in detail in §4.2.2.

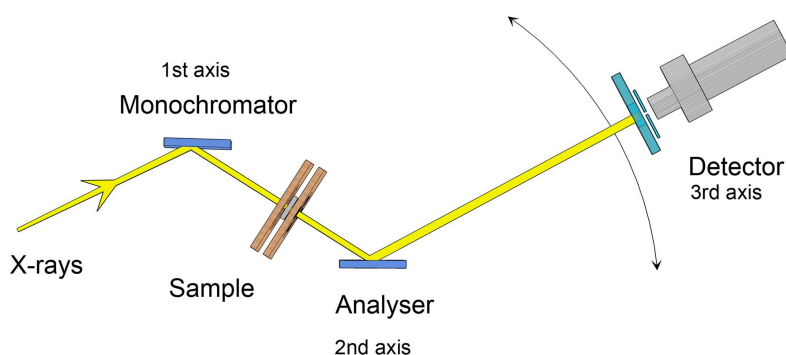
Double crystal diffractometry (DCD) preceded TCD and offered faster, simpler data acquisition, with no loss of intensity since there was no analyser crystal. However, the lack of discrimination of the angle at which the diffracted X-rays impinge on the detector resulted in a large loss of information that limited the quantitative use of DCD to laterally homogeneous crystals (Aristov *et al.*, 1992). The shift from DCD to TCD accompanied the availability of brilliant synchrotron radiation sources, which meant that experiments with higher angular resolution were now practical, with the concomitant decrease of absolute intensity, due to reflection(s) from the crystal on the third axis.

Some advantages of TAD are its ability to measure the radius of curvature of crystals (Bubakova and Szmíd, 1965), separate the elastic Bragg and thermal diffuse scattering in studies of phonon phenomena (Eisenberger *et al.*, 1972), see clear proof of diffuse scattering (and its distribution in reciprocal space) due to crystal lattice defects, calculate the depth profile of lattice strain and disorder (Zaumseil and Winter, 1990; Zaumseil *et al.*, 1990), obtain two dimensional (2D) strain profiles of crystals with inhomogeneities (Aristov *et al.*, 1992), where the effects of defects acting along or perpendicular to the scattering vector are rigorously separated (Fewster, 1993), as well as explore bent, mosaic crystals, or those with a rough surface (Iida and Kohra, 1978; Bowen and Tanner, 1998). TAD is also effective for investigating lattice distortions in a crystal or its subsurface layers (Larson and Schmatz, 1974; Pick *et al.*, 1977; Haubold and Martinsen, 1978; Iida and Kohra, 1978, 1979; Larson and Schmatz, 1980; Zaumseil

⁵Triple axis diffractometry (TAD) is referred to in the literature as triple crystal diffractometry (TCD) when the three axes correspond to the beam conditioning crystal, the sample, and the analyser crystal, as shown in Figure 1.2. We will use the term TAD to mean both TAD and TCD unless the context requires more specificity. As TAD forms the basis of the technique discussed in this thesis, it is explained in detail in chapter 4.



(a) The conventional triple axis diffractometry setup, usually called triple crystal diffractometry



(b) The particular triple axis diffractometry setup used for the technique in this thesis

FIGURE 1.2: Triple axis and triple crystal diffractometry. Conventional triple axis diffractometry is called triple crystal diffractometry as it involves three crystals (one on each axis): monochromator, sample and analyser. In triple axis diffractometry the sample (not necessarily crystalline) is in transmission mode between the monochromator and analyser, the latter of which sits on the 2nd axis. The detector sits on the 3rd axis, which is coupled to the 2nd axis. Rotation of the 2nd and 3rd axes in either setup probes the same area of reciprocal space about a Bragg reflection from the crystal on the 2nd axis (further details in §4.2).

and Winter, 1982a; Afanas'ev *et al.*, 1984; Afanas'ev and Fanchenko, 1988; Nikulin *et al.*, 1994, 1995a,b, 1996a, 1997a).

A significant improvement in resolution was achieved by Nikulin *et al.* (1995a), where the authors demonstrated the measurement of lattice distortions perpendicular to the sample surface with 16nm resolution. To reconstruct the strain map, the authors used the 1D phase recovery method of Petrashen' and Chukhovskii (1989), based on a logarithmic dispersion relation (Hilbert transform) (Burge *et al.*, 1976), which Goureev *et al.* (1992) extended to 2D distortions involving periodic superlattice modulations in the lateral direction. Model-independent determination of lattice strain was then demonstrated on thin SiGe/Si multilayers (Nikulin *et al.*, 1996a) with 25Å resolution, and later demonstrated on annealed, ion-implanted silicon crystals (Nikulin *et al.*, 1997a) with 100Å resolution.

The problem of the localisation of zeros of the complex diffraction amplitude complicates phase retrieval based on a logarithmic dispersion relation (Burge *et al.*, 1976; Petrashen' and Chukhovskii, 1989; Nikulin, 1998b), which may lead to a non-unique solution. This ambiguity was overcome by Nikulin *et al.* (1996b, 1997b), where the authors introduced a practical procedure to distinguish between real and virtual zeros, thereby unambiguously calculating the physical dimensions of multilayer structures with 27Å and 15Å resolution, respectively. Dubbed Phase Retrieval X-ray Diffractometry (PRXRD), this experimental-analytical TAD based technique offers non-destructive, model-independent, unambiguous characterisation of Bragg diffracting structures (Nikulin, 1998a,b,c; Nikulin *et al.*, 2000, 2001).

The first quantitative analysis of SAXS data from a homogeneous, non-crystalline sample, with PRXRD, was demonstrated by Siu *et al.* (2001a,b), where *a priori* knowledge was necessary to identify an acceptable solution. Siu *et al.* (2003) reconstructed the complex scattering amplitude (with submicron spatial resolution) of a weakly diffracting amorphous sample, where the use of two X-ray energies ensured a unique solution. Recently Darahanau *et al.* (2005) demonstrated the possibility of nano-resolution profiling of micro-structures (a series of weakly diffracting, thickness-modulated samples) using quantitative PRXRD, demonstrating the ability to map the thickness profile with a spatial resolution of 100nm. Darahanau *et al.* (2007) followed this work with an X-ray diffraction investigation into a metal-metal interface, with resultant resolution of ~40nm. In this paper, the authors suggest a practical algorithm of experimental data collection for future detailed examination of internal interfaces, supported by computer simulations of various configurations of interfaces. They conclude that the PRXRD technique can be readily applied to reconstruct 50–100nm

interface modulations in bimetals from TAD data (Darahanau *et al.*, 2007).

1.2 Imaging large ensembles of embedded nanoparticles

Attempting to investigate and reconstruct images of nanoparticles from large ensembles of embedded nanoparticles is not without its difficulties. Nanoprecipitates grown inside their host matrix, for example, often have low diffraction contrast compared to their surrounding material, so a large number of similar particles is required in order to produce a sufficiently strong signal. A compromise must be reached between the number of diffracting nanoparticles, proportional to sample thickness, and minimisation of loss of intensity due to attenuation through the surrounding matrix, which favours a thinner sample. Also, it is useful if the sample has some degree of symmetry such as crystallographic orientation of the nanoparticles, or similar nanoparticle sizes and/or shapes that can be used as *a priori* knowledge to aid technique development.

In order to put the work that follows into context, we have presented the major techniques currently used in nanoscale material characterisation. We have briefly reviewed electron microscopy methods, X-ray crystallography, small angle X-ray scattering, coherent diffractive imaging, triple axis diffractometry and phase retrieval X-ray diffractometry.

We noted that the widely used electron microscopy techniques for nanoparticle characterisation, which provide very high resolution and are capable of *in situ* studies, are fundamentally limited to very thin samples or surface studies. The use of X-ray diffraction is thus necessitated by the requirement that an experimental technique to characterise materials with embedded nanoparticles needs to be non-destructive, applicable to bulk material (thick) samples, and capable of high resolution nanoparticle image reconstruction in 3D. It should also be easily extendible to real-time, *in situ* investigations.

We discussed that the non-Bragg diffracting nature of ensembles of embedded nanoparticles requires a non-crystallographic X-ray diffraction technique. The desire for a technique capable of model independent 2D or 3D image reconstruction excluded SAXS, and the requirement of an isolated nanoparticle and very high intensity source, among other restrictions, rendered CDI techniques unsuitable or impractical for investigating large nanoparticle ensembles simultaneously.

In this thesis we provide an alternative that overcomes some of the disadvantages

of the conventional techniques outlines here by exploiting the non-destructive, high resolution characterisation ability of TAD (with a sample in transmission mode), akin to the triple axis Bonse-Hart camera used in SAXS by [Lambard and Zemb \(1991\)](#). In [chapter 4](#) we will present the pertinent experimental particulars such as X-ray beam properties, monochromator and analyser crystals and detectors.

We determine the sensitivity of a particular optical setup to the presence and crystallographic orientation of the nanoparticles, and extend the technique to *in situ* nanoparticle formation and growth investigations ([chapter 6](#)). With this technique we are able to investigate thick samples ($\sim 1\text{mm}$), collect diffraction data with resolution ultimately limited only by data collection time (and possibly radiation damage, for some samples). By employing an iterative image reconstruction algorithm we reconstructed nanoparticles representative of thousands of embedded nanoprecipitates in the bulk-material sample. The details of this development, including supporting simulations, will be presented in [chapters 5 and 6](#).

Prior to formulating the relevant theory required to approach the forward problem (simulation and measurement of diffraction data), we first present a discussion of the samples chosen to develop this emerging technique in the following chapter.

Nanomaterials with ensembles of embedded nanoparticles

2.1 Introduction

In the previous chapter we spoke of the motivation for developing a non-destructive, high-resolution, bulk material, nanoparticle characterisation technique, and reviewed numerous experimental techniques that satisfy some of these criteria.

For the development of the emerging analyser based, reciprocal space mapping technique presented in this thesis, we focussed the experimental work on light metal alloys of the Al- x Cu family, where $x = 2.0$ – 5.0% by weight. As well as being technologically important, the relatively simple morphology of embedded nanoprecipitates in these samples rendered them suitable for our technique development studies. In addition, the nucleation and growth of these nanoparticles is a good example of a naturally slow process¹ that is well suited to the extension of our technique to probe “real-time” nanoparticle growth dynamics (chapter 6).

At this point, let us emphasise that the emergence and development of this technique based on these samples is by no means a limitation. The technique is aimed at any sample containing embedded nanoparticles, where the non-destructive characterisation of the sample probes volumes containing thousands of nanoparticles. The ability to obtain ensemble characteristics of the nanoparticle population with nanometre resolution, in two or three dimensions, coupled with time-resolved *in situ* analysis, has applicability even broader than the large field of light metal alloys.

This chapter is dedicated to a discussion of the morphological details of nanoparticles grown embedded within the Al-Cu matrix, and the age-hardening process, which

¹As specified in the previous chapter, by the terms “slow process” and “real-time” we refer to dynamics on time scale of tens of minutes to a few hours. In this chapter we discuss that nanoparticle growth in our samples can be expedited or significantly slowed, depending on the Cu concentration and temperature. The particulars of this dependence were used to design a real-time *in situ* experiment to investigate nanoparticle growth over this experimentally measurable time scale.

allows us to prepare samples with a suitable microstructure.

2.2 Age hardenable Al-Cu alloys

Aluminium is intrinsically soft, with a yield strength of 7–11 MPa. It can be strengthened by the addition of small amounts of alloying elements, on the order of ~1–5 wt%, which have low solid solubility in the Al matrix. Aluminium alloys are an essential part of the light metal alloys industry, accounting for the bulk of applications, from commercial aircraft (Starke Jr. and Staley, 1996), to building construction and machine components. Following the serendipitous discovery of age-hardened aluminium by Wilm (1911), Merica *et al.* published the fundamental understanding and basis for the age-hardening technique (Merica *et al.*, 1919a,b,c, 1921; Martin, 1968), quickly establishing it as one of the most widely used mechanisms, to this day, for the strengthening of metal alloys (Lloyd, 1998; Williams and Starke, 2003). The Al-Cu family of age-hardenable alloys is the prototypical and most famous example of technologically important, precipitation hardened alloys (Esmaeili *et al.*, 2001).

Age-hardenable alloys obtain their strength from an ensemble of nanoprecipitates grown within the bulk matrix. Understanding the precipitation microstructure in such alloys, as well as its evolution during annealing, is important when optimising the hardness or yield strength of an alloy system. Other mechanical properties, such as plastic behaviour, also depend strongly on the microstructure of the precipitates, i.e. the precipitate morphology, volume fraction, and spatial distribution (Martin, 1968; Hirth *et al.*, 2001; Bastow and Celotto, 2003; Muddle and Nie, 2006). In particular, the study of the initial stages of nanoprecipitate formation would significantly aid in the understanding of their nucleation and growth kinetics, leading to improved control and design of light-metal alloys. However, despite the growing body of work on aluminium and other precipitation hardened alloys (Hatch, 1998; Müller *et al.*, 1999; Lokker *et al.*, 2000; Alani and Pan, 2001; Williams and Starke, 2003; Deschamps *et al.*, 2006; Chen *et al.*, 2006), the crucial early stages of nucleation and growth kinetics have eluded systematic *in situ* study, especially in bulk material samples, as there is no single, non-destructive technique available for this purpose.

Age-hardening is a three-step process involving solution heat treatment, quenching, and ageing. Solution heat treating is a process during which the solute elements are (re)dissolved (back) in(to) the host matrix. Rapid quenching forces the solute elements into supersaturated solid solution, which is homogeneous in ideal, monocrystalline Aluminium. The samples used here were solution heat treated for an hour

at 525–530°C, followed by rapid quenching in water, at ~20°C. Ageing, which can be natural (at room temperature), or artificial (at higher temperatures), is the controlled decomposition of the supersaturated solid solution to form a fine dispersion of precipitates.

The nucleation and kinetics of the growth of Cu and Al₂Cu nanoprecipitates in an Al matrix are complex, depending non-trivially on the concentration of Cu and annealing parameters such as temperature and pressure (Murray, 1985; Konno *et al.*, 2001). Generally, a higher Cu concentration and lower ageing temperature create a greater driving force for precipitate nucleation. A higher temperature, however, is more conducive to atom migration, so the precipitate growth rate is increased. Ongoing annealing and the resultant growth of the nanoscale precipitates leads to further localisation of the strain field in short-range regions and to depletion of Cu atoms in the Al matrix (Zatsepin *et al.*, 2010). Numerous dedicated studies demonstrate the complexity of interplay between nucleation and growth dynamics during the early stages of the ageing process (Martin, 1968; Matsubara and Cohen, 1983; Kanadani and Sakakibara, 1989; Barlat and Liu, 1998; Esmaeili and Lloyd, 2006).

2.2.1 Al-Cu nanoprecipitate composition, shapes and dimensions

Precipitation in an Al-Cu alloy takes the form of platelets that grow along the orthogonal <100> planes of the face-centred cubic Al lattice (Figure 2.1). The chemical composition of the precipitation changes with continued annealing (and increase in precipitate size), as shown in Table 2.1 and described below.

It is well established that the formation of the precipitate equilibrium phase (θ phase) is preceded by a series of metastable phases of decreasing coherence² with the Al matrix: Guinier and Preston zones (GP zones, after Guinier (1938); Preston (1938b)), θ'' (GP2 zones) and θ' precipitates (Kou, 2003). Coherent precipitates are those with the same underlying lattice structure as the bulk matrix and with crystallographic planes continuous through precipitate and matrix, producing significant strain fields around the precipitate (Wolverton, 2000). The precipitates and their surrounding strain fields act as obstacles for dislocation motion, hence strengthening the alloy (Martin, 1968; Wolverton, 2000).

Due to their small size and their coherence with the Al matrix, the atomic structure of GP zones was historically rather difficult to determine. This led to much discussion

²In this chapter the terms coherence and phase are used in their materials science meaning.

	GP zones	θ''	θ'	θ
Unit cell				
Composition	Single or double layer of Cu atoms	Pure Cu layers separated by 3 layers of Al (Al_3Cu)	Tetragonal (Al_2Cu)	Body centred tetragonal (Al_2Cu)
Nanoprecipitate thickness (approx.)	a few Å	a few nm	3–10nm	>10nm
Nanoprecipitate diameter (approx.)	1–10nm	<100nm	~100–500nm	>500nm

TABLE 2.1: **Nanoprecipitates in an Al-Cu alloy** in order of increasing size and decreasing crystalline coherence with the Al matrix, which typically corresponds to the order of their appearance in the sample during age-hardening (Russell and Aaronson, 1975; Wolverton, 1999; Ravi *et al.*, 2006). θ'' particles are also called GP2 (Guinier-Preston) zones. Generally the peak hardness of an age-hardened Al-Cu alloy is achieved with a distribution of θ'' nanoparticles, or a combination of θ'' and θ' nanoparticles.

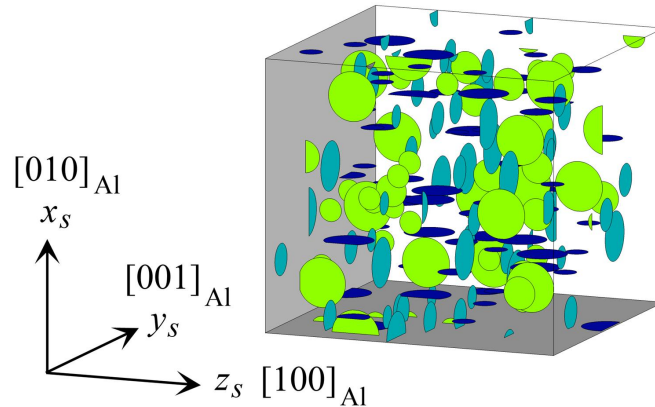


FIGURE 2.1: **Model of nanoprecipitates in an Al-Cu single crystal.** The Cu, Al_3Cu and Al_2Cu nanoprecipitates can be approximated by platelets with a Gaussian distribution of diameters. An example of a transmission electron micrograph of θ'' phase surrounding much larger θ' nanoparticles is shown in Figure 2.5.

between solid state physicists and metallurgists (see for example [Khachaturyan \(1983\)](#); [Gerold \(1988\)](#); [Wolverton \(1999\)](#)), but GP zones have since been unambiguously determined to consist of single-layer (and occasionally double layered) platelet-like zones of copper atoms ([Wang *et al.*, 2004](#); [Konno *et al.*, 2001](#)). GP zones are a few Ångströms thick, about 10nm in diameter, and form in very high number densities (up to $10^{18}/\text{cm}^3$ for an Al-4.0wt% Cu alloy). Simulations of precipitate shapes by [Wolverton \(1999\)](#) place the size dependent transition between GP zones and the θ'' phase at about 15nm in diameter (see Figure 2.2). The θ'' phase precipitates are traditionally accepted to be two pure Cu layers separated by three Al atomic layers (Al_2Cu), with diameters up to $\sim 100\text{nm}$. The θ' precipitates (Al_2Cu particles) can have diameters up to $\sim 500\text{nm}$, with very high aspect ratios.

One of the primary factors controlling the strength of a precipitation-hardened alloy is the volume fraction of the metastable precipitates. The maximum volume fraction is determined by the metastable phase boundaries (Figure 2.3), which unfortunately are very difficult to ascertain experimentally ([Murray, 1985](#)), and yet are very important for controlling the final microstructure of the alloy ([Zandbergen, 1997](#); [Ravi *et al.*, 2006](#)). A higher Cu concentration results in higher maximum hardnesses since larger volume fractions of precipitate are possible. The maximum hardness of an Al-Cu alloy is usually achieved with a microstructure comprising a large number of θ' phase particles, so this phase is of primary interest for materials engineering applications. A sample is considered over-aged when the incoherent (θ phase) precipitates

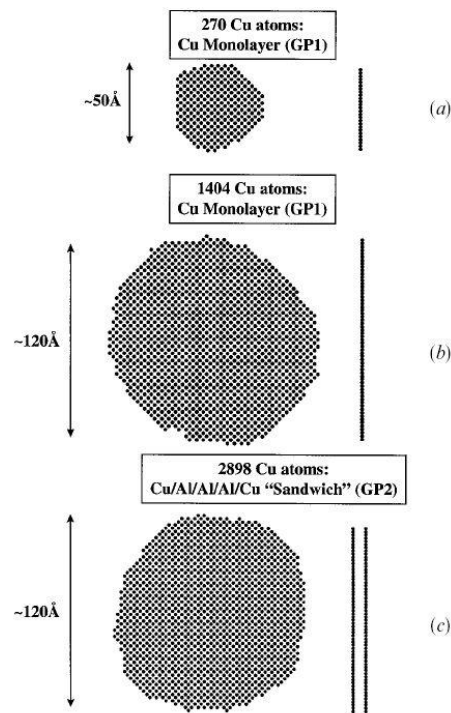


FIGURE 2.2: **Simulated structure of shapes and dimensions of initial precipitation in Al-Cu alloys.** The top two are GP zones, i.e. pure Cu platelets, and the third particle is a GP2 zone, with Al_3Cu composition. This simulation image is taken from [Wolverton \(1999\)](#).

form and begin to dominate. These equilibrium phase particles can have thicknesses of $\sim 50\text{nm}$ ([Parrini and Schaller, 1996](#)), but their decreased aspect ratios compared to preceding phases lead to a decrease in their ability to block the migration of defects effectively.

2.2.2 Preparation of a suitable sample microstructure

In order to simulate and design experiments appropriately, specific samples must be prepared taking into consideration the details presented above. As the hardness is primarily determined by the size of the precipitates, in addition to their volume fraction and spacing ([Starke Jr. and Staley, 1996](#)), Al-Cu hardness curves can be used as an estimate of the mean diameter of precipitates grown during heat treatments. Figure 2.4 shows an example of hardness curves for three Al-Cu alloys with different Cu concentrations, age-hardened at various temperatures ([Gable, 2006a](#)). The gradient of increasing hardness indicates the rapidity of microstructural changes, such as particle formation and growth. This suggests which Cu concentration and anneal-

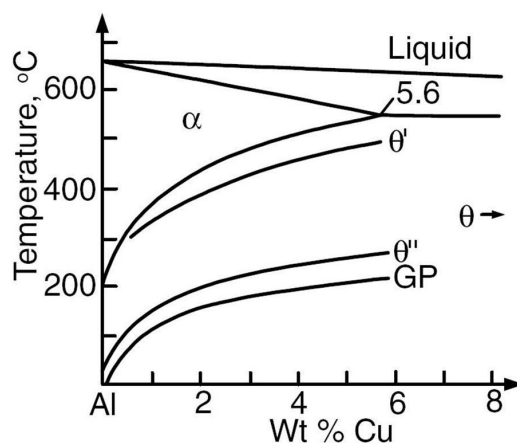


FIGURE 2.3: **Solubility of nanoprecipitates in an Al-Cu alloy.** This Figure shows the solvi, or solubility limits, of the precipitate phases described in Table 2.1. Annealing for a sufficient amount of time at a temperature higher than the solvus for a particular precipitate phase ensures it is dissolved and a sample more closely resembling a monodisperse ensemble of nanoparticles can be achieved. This figure is reproduced from Russell and Aaronson (1975), after Hornbogen (1967).

ing temperature would show the most change in real-time *in situ* X-ray diffraction experiments over a reasonable number of hours. In addition, the solid solubility of various precipitate phases at various temperatures (Figure 2.3) can also be used as a reference for estimating the concentrations of each phase. We can ensure, for example, a population of only θ' phase with an insignificant number of θ'' phase precipitates in an Al-4.0wt% Cu sample at $>250^{\circ}\text{C}$, so as to simulate the composition (Al_2Cu), and hence the refractive index, appropriately.

The reversal of the precipitation sequence is thermodynamically impossible (Russell, 1980), so cooling the sample after annealing it for some time, for example at 220°C , slows down precipitation growth considerably, yielding a relatively stable microstructure. This allowed us to carry out real-time *in situ* X-ray diffraction experiments to observe the sample's dynamic behaviour during annealing, with sufficient time between annealing periods for a complete 2D scan to be collected (presented in chapter 6).

As will be discussed in detail in the following chapter, X-rays are sensitive to changes in the refractive index of a sample. Pure Cu precipitates (GP zones) embedded in an Al crystal thus diffract X-rays more strongly than Al_2Cu precipitates embedded therein. However, GP zones are simply too small to diffract significantly enough to create a measurable signal, despite the high nanoparticle number densities achievable. The potentially lengthy transition in precipitate phase, from θ'' to θ' , corresponds to

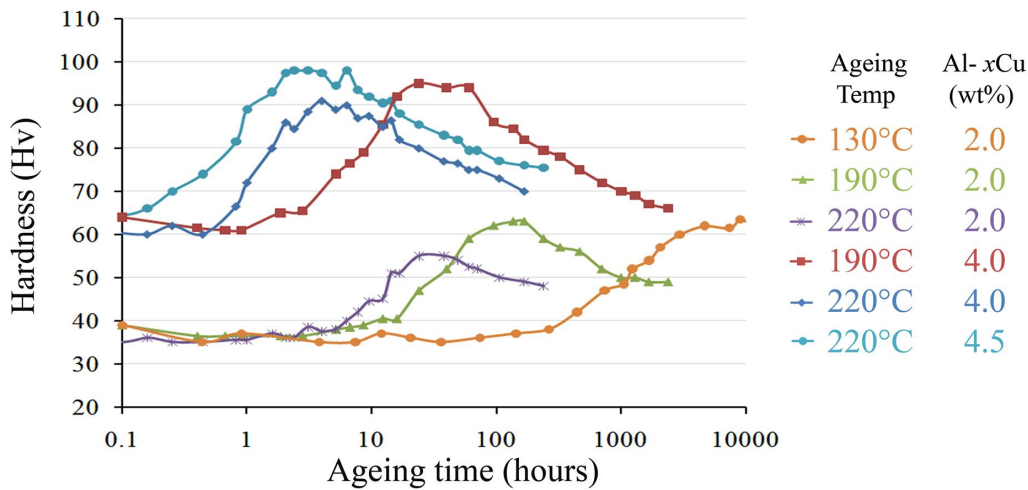


FIGURE 2.4: **Hardness curves for Al-Cu alloys** (Gable, 2006a). Ageing temperatures and Cu concentrations (wt%) are listed in the legend. The samples used for these Vickers hardness tests (Smith and Sandland, 1922) were a good representation of samples prepared for our experiments as they had similar, and in some cases identical, composition and heat treatments. The units of hardness are Hv (Vickers Pyramid Number), a measure of force over area, where the yield strength, σ (in MPa), can be obtained from $\sigma = 9.807Hv$. Peak hardness is determined approximately by the size of nanoprecipitates in the sample (Starke Jr. and Staley, 1996) and the gradient of the hardness curves serves as a good estimate for the time scale of dynamic changes in the microstructure.

a change from X-rays being diffracted by a high number of small nanoparticles to X-rays being diffracted by larger, but more weakly diffracting, nanoparticles, possibly with a lower number density. The uncertainty in this transitional stage significantly complicates simulations of real-time, *in situ* nucleation and early stages of nanoparticle growth in such a sample.

Indeed, as will be discussed further in chapter 5, the main difficulty of seeing individual nanoscale objects with X-rays stems from insufficient diffracting volume, i.e. the nanoparticle volume. Higher concentrations of Cu would lead to a higher number density of GP zones, but a truly homogeneous, random spatial distribution of such small particles and their surrounding strain fields is a good approximation to a homogeneous material with an effective combined refractive index of the Cu atoms and Al matrix. In sufficient numbers, the slightly bigger precipitates, θ'' phase, may ameliorate the weakness of the diffracted X-rays by constructive interference, which is increased by the preferred orientation of the nanoparticles in the Al crystal.

However, when even larger precipitates grow at the expense of smaller ones,

in a process called coarsening, or Ostwald ripening (Martin, 1968; Hatch, 1998), the precipitate number density decreases. Again, there is a compromise between a decreased number of similarly diffracting nanoparticles, and an increase in diffracting volume. In chapter 5 we will discuss in more detail how the number of particles affects the visibility of the diffraction signal from the ensemble.

~

A monodisperse distribution of sizes and identical orientations would be ideal for the development of the technique in this thesis, as it improves the signal to noise ratio of the resulting diffraction pattern (details in §5.1), but this is often unattainable. An annealing temperature of 220°C for an Al-5.0wt% Cu sample, as shown in the transmission electron microscopy (TEM) micrograph in Figure 2.5, is insufficient to dissolve the smaller θ'' particles. This results in a bimodal distribution of diameters, which is not uncommon.

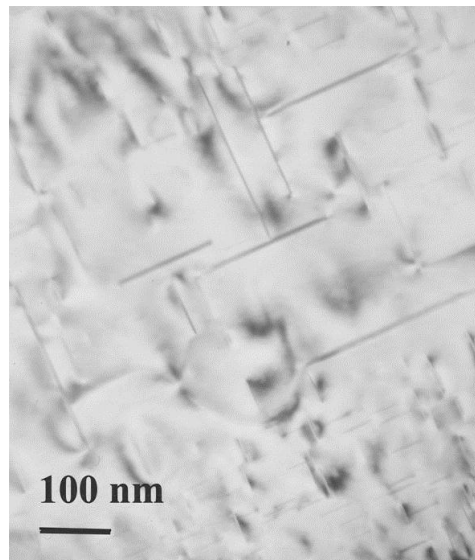


FIGURE 2.5: **Bimodal precipitation in an annealed Al-5.0wt% Cu crystal.** $\langle 100 \rangle_{\alpha}$ zone-axis TEM micrograph of θ'' and θ' nanoprecipitates in Al-5.0wt% Cu, as a result of annealing for 10 hours at 220°C. As the temperature is below the solvus of the θ'' phase, the resultant microstructure is bimodal. TEM was carried out on a Philips CM20 instrument operated at 200 keV.

TEM micrographs of the samples prior or subsequent to the X-ray experiments (or TEM micrographs of identically prepared samples) were used to validate the size and shape of the nanoparticles. Figure 2.5 shows a $\langle 100 \rangle_{\alpha}$ zone-axis micrograph of

an Al-5.0wt% Cu sample with a bimodal distribution of diameters. One should note that the high coherence of the precipitates results in a high degree of strain contrast (surrounding the precipitates) visible with a transmission electron microscope. This complicates the analysis of nanoparticle shape and size. To improve visibility of just the precipitates we must always look slightly off a major zone axis, rendering some orientations with increased visibility. Also, as discussed in §1.1.1, TEM micrographs are limited to very thin regions of the sample, resulting in truncation of the nanoparticles perpendicular to the electron-optical axis. This introduces ambiguity into the analysis of nanoprecipitate diameters, as it is not clear if the truncation represents the diameter or some other chord of the platelet shaped nanoparticle. Coupled with the narrow transverse field of view, the TEM sample thinness also makes statistical number density analysis a slow manual task, requiring a large number of sections to collect sufficient statistics. TEM is also unable to give absolute 3D information without tomographic reconstruction, or serial slicing, therefore requiring some amount of *a priori* information about the particles, both in order to obtain accurate, well aligned micrographs and to interpret them correctly.

2.2.3 Preparation of a suitable sample size

As will be discussed in detail in chapter 6, the experimental development of our novel nano-characterisation technique was done in three stages. The first stage was a feasibility study investigating the sensitivity of the technique to nanoparticle sizes and orientation, as well as thickness. The second stage was a preliminary experiment for the *in situ* real-time investigation of nanoparticle growth in various Al-Cu alloys in order to confirm the most suitable candidate for the third stage. The third stage was the first analyser based, reciprocal space mapping investigation of the nucleation and growth of embedded nanoparticle ensembles.

For the first stage we required samples with a high degree of crystallinity to ensure the orientation of the nanoparticles could be controlled. It is important to reiterate, however, that we were not investigating the crystalline structure of the aluminium matrix surrounding the nanoprecipitates, nor that of the nanoprecipitates themselves. The growth of almost pure Aluminium single crystals is challenging, and thus expensive. Indeed, it took our first suppliers³ 11 months to successfully grow a cylindrical (1.0cm diameter and <2 cm in length) single-crystal Al-2.0wt% Cu, which was used in the feasibility study that will be presented in §6.2. This meant the number

³MaTeck GmbH, Germany.

of samples was limited and the selection of sample sizes and heat treatments was crucial.

For uniformity, in particular for the second stage of the experimental technique development, all Al-Cu samples were prepared with the consideration of potentially being heat-treated *in situ*. Thus samples were required to be relatively small in order to be able to be heated rapidly and uniformly (details in §4.4). As such, samples were prepared in the shape of small discs, with 3mm diameters. Sample thicknesses of 0.3–1.6mm were chosen initially, as much thinner samples may not be representative of the bulk material when undergoing heat treatment, whereas thicker samples risk too much beam attenuation (details in §6.2). In addition, the dimensions of the samples made them ideal for preparation as TEM specimens following our experiments.

2.3 Summary

We have discussed the samples containing embedded nanoparticles that were used in the development of the X-ray diffraction based, nanoparticle characterisation technique in this thesis. The technological importance of light metal alloys and other age-hardenable materials, containing ensembles of nanoparticles, was presented. We described the main physical characteristics of the Al-Cu nanoprecipitates, including their platelet shape (with very high aspect ratios), and specific crystallographic orientation in the Al matrix. We outlined how the nanoparticle composition and sizes differ, depending on annealing conditions, and how this knowledge allowed us to prepare samples with estimated microstructures, including suitable candidates for *in situ*, real-time studies of nanoparticle growth.

In the following chapter we will present the theoretical background necessary to describe the interaction of X-rays with matter, both crystalline and non-crystalline, ultimately developing an appropriate picture of X-ray diffraction from large ensembles of embedded nanoparticles.

X-ray diffraction theoretical background

In the first chapter we reviewed the experimental techniques available to approach the problem of characterising materials containing embedded nanoparticles. We established the need to develop a single, non-destructive, nanoscale resolution, bulk material technique, and chose the advantages of triple axis X-ray diffractometry as an appropriate starting point.

In this chapter we present the relevant theoretical framework of the interaction of X-rays with matter. Firstly, we define the nature of X-rays, followed by an exposition of their interaction with weakly diffracting, non-Bragg diffracting, inorganic matter, which forms the basis of the theoretical/computational side of this project. We begin with the single-scattering scenario expressed by the first Born approximation, introduce the useful geometrical concept of the Ewald sphere, and finish with Fraunhofer diffraction. We then move on to X-ray diffraction from crystals, as the triple axis diffractometry setup (§4.2) involves the use of perfect crystals for beam conditioning and analysing. This section involves a discussion of kinematical diffraction from crystalline matter, and a brief sojourn to the domain of X-ray dynamical diffraction, as well as an overview of where both theories break down in the context of studying ensembles of embedded nanoparticles.

The following chapter presents the experimental elements of triple axis diffractometry, including a description of analyser based reciprocal space mapping. By drawing on the theory presented in this chapter and experimental considerations in the next chapter, we will outline an appropriate approach for simulating diffraction from dispersions of embedded nanoparticles, including Fraunhofer diffraction patterns and analyser based reciprocal space maps (chapter 5).

3.1 Interaction of X-rays with matter

X-rays obey Maxwell's equations, which describe the temporal and spatial evolution of electromagnetic waves (Born and Wolf, 1999). We will not repeat the derivations here but will cite only the most relevant results. From Maxwell's equations one can derive the vacuum field equation for the electric field, the d'Alembert equation, and an analogous one obeyed by the magnetic field. In vacuum the three spatial components of each field are uncoupled from each other and thus obey a scalar version of the same equation (Nieto-Vesperinas, 1991).

A single monochromatic component of the electric field can be expressed as

$$\psi(\mathbf{r}, t) = \psi(\mathbf{r}, \omega) \exp(-i\omega t), \quad (3.1)$$

where we will henceforth only consider the spatial component, $\psi(\mathbf{r}, \omega)$. Here $\mathbf{r} = (x, y, z)$, t is time and ω is the angular frequency. Assuming a static, dielectric and non-magnetic material and negligible depolarisation, the behaviour of all monochromatic components of the electric and magnetic field can be summarised with a single scalar, time-independent (Helmholtz) inhomogeneous wave equation (see for example Nieto-Vesperinas (1991); Attwood (2000); Goodman (2005) or Paganin (2006)):

$$\nabla^2 \psi + k^2 n^2(\mathbf{r}) \psi = 0, \quad (3.2)$$

where $\nabla = (\partial/\partial x, \partial/\partial y, \partial/\partial z)$, $k = |\mathbf{k}| = \omega/c = 2\pi/\lambda$ is the wavenumber and the magnitude of the wavevector, \mathbf{k} , which is in the local direction of X-ray propagation, λ is the radiation wavelength and $n(\mathbf{r}) = n(x, y, z)$ is the spatially dependent complex refractive index of the material (in vacuum, $n = 1$). This is valid for the propagation of a spatially coherent (see §4.1.2), monochromatic X-ray wavefield. For X-rays with energies $\gtrsim 3$ keV interacting with metals, the refractive index differs only slightly from unity (by factors directly proportional to the electron density if one is sufficiently far from absorption edges). It can be written as

$$n = 1 - \delta + i\beta, \quad (3.3)$$

where it is expressed in terms of δ , the refractive part, and β , the absorptive part. For hard X-rays, δ is on the order of 10^{-5} and β is on the order of 10^{-7} . The linear absorption coefficient, μ , in Beer's law of absorption (Born and Wolf, 1999) is related to β via $\mu = 2k\beta$.

The measurable quantity experimentally is the wavefield intensity, or its squared amplitude, while the phase is not directly measurable. The inability to measure the

phase corresponds to a loss of half the information about the diffracted wavefield. It is the recovery of this lost information in order to gain further insight into the diffracting medium that constitutes the phase problem in optics.

3.1.1 First Born approximation

When X-rays are scattered by an inhomogeneous medium, the total outgoing wave after the scatterer obeys the integral eq. (3.4), which is the sum of the incident wave and the integral of wave amplitudes elastically scattered by all points within the scatterer,

$$\psi(\mathbf{r}) = \psi^0(\mathbf{r}) + \frac{k^2}{4\pi} \int G(\mathbf{r} - \mathbf{r}') [n^2(\mathbf{r}') - 1] \psi(\mathbf{r}') d\mathbf{r}'. \quad (3.4)$$

Here $\psi(\mathbf{r})$ is the resultant wave, $\psi^0(\mathbf{r})$ is the incident wave, $G(\mathbf{r} - \mathbf{r}')$ is the outgoing Green function and $[n^2(\mathbf{r}') - 1]$ is the scattering potential (Born and Wolf, 1999). The Green function is a solution to eq. (3.2) in vacuum ($n = 1$), with a three dimensional (3D) Dirac delta function source at \mathbf{r}' , i.e. a point scatterer. A convenient choice for $G(\mathbf{r} - \mathbf{r}')$ is an outgoing spherical wave, i.e.

$$G(\mathbf{r} - \mathbf{r}') = \frac{\exp(ik|\mathbf{r} - \mathbf{r}'|)}{|\mathbf{r} - \mathbf{r}'|}. \quad (3.5)$$

For a weakly scattering object, i.e. $|\delta|, |\beta| \ll 1$, the amplitude of the scattered wave is much less than that of the incident wave, so $\psi(\mathbf{r}')$ in the integral of eq. (3.4) can be well approximated by $\psi^0(\mathbf{r}')$, the unscattered wave,

$$\psi(\mathbf{r}) = \psi^0(\mathbf{r}) + \frac{k^2}{4\pi} \int G(\mathbf{r} - \mathbf{r}') [n^2(\mathbf{r}') - 1] \psi^0(\mathbf{r}') d\mathbf{r}'. \quad (3.6)$$

This single-scattering scenario is the first Born approximation. It is an example of kinematical diffraction theory, and forms the basis of most of our subsequent considerations of the interaction of X-rays with matter. The first Born approximation is most useful to us as it gives an accurate description of diffraction of hard X-rays by materials containing weakly diffracting, embedded nanoparticles.

Higher order Born approximations can be derived recursively by the using the previous approximation as the incident wave for the next iteration. This describes multiple scattering events, which we will briefly look at in §3.2.2 in the context of dynamical diffraction of X-rays by crystals. Dynamical diffraction is necessary for an accurate description of the strong scattering interaction of X-rays with (nearly) perfect crystals.

3.1.2 Fraunhofer diffraction

In this section we derive the Fraunhofer diffraction integral from the first Born approximation in eq. (3.4), by applying the approximations germane to the far field. We also explore the limitations of using the projection approximation, which describes the effect of a weakly diffracting object on the incident wavefield.

Ewald sphere

The Ewald sphere is a very useful geometrical construct, closely related to the first Born approximation, for both crystalline and non-crystalline diffraction. In reciprocal space, consider an incident plane wave, $\psi^0(\mathbf{r}) = \exp(i\mathbf{k}_0 \cdot \mathbf{r})$, whose wavevector, \mathbf{k}_0 , has its tip at the origin, as shown in Figure 3.1. A sphere is then constructed centered on $(0, 0, -\mathbf{k}_0)$, with a radius of $k = |\mathbf{k}| = 2\pi/\lambda$ (cf. eq. (3.2)). This sphere represents the locus of possible directions of elastically scattered waves (\mathbf{k}_h) from $(0, 0, 0)$. The scattering vector, $\mathbf{Q} = \mathbf{k}_h - \mathbf{k}_0$, describes the momentum change of the incident X-rays upon scattering, and can be considered as a reciprocal space probe for reasons that will become clear shortly.

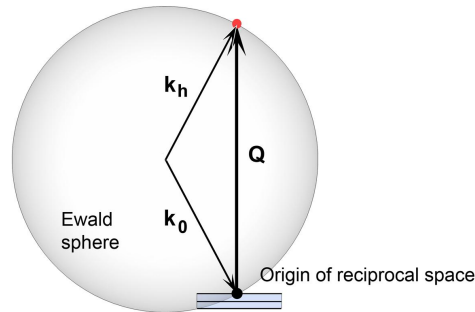


FIGURE 3.1: **Ewald sphere construct**, shown simplified in two dimensions. The incident and diffracted X-ray directions are denoted \mathbf{k}_0 and \mathbf{k}_h , respectively, and $\mathbf{Q} = \mathbf{k}_h - \mathbf{k}_0$ is the scattering vector. The Ewald sphere defines the locus of all possible elastically diffracted wavevectors.

First Born approximation in the far field

Suppose the outgoing wavefield in eq. (3.6) is allowed to propagate sufficiently far downstream such that $|\mathbf{r}'| \ll |\mathbf{r}|$, and the Fresnel number, N_F , meets the stringent far

field condition, $N_F \ll 1$, where N_F is defined as (Born and Wolf, 1999)

$$N_F = \frac{b^2}{\lambda r_z}. \quad (3.7)$$

Here b is defined as the largest dimension characterising the scatterer, which is the most slowly diffracting and therefore requires the longest propagation distance, r_z , to allow for the spatial separation of diffracted waves. We will not be considering Fresnel diffraction, or the near field region, for which $N_F \geq 1$, where the smallest dimension is used for b (Born and Wolf, 1999; Gureyev *et al.*, 2004).

These conditions allow the Green function in eq. (3.6) to be approximated as

$$\frac{\exp(ik|\mathbf{r} - \mathbf{r}'|)}{|\mathbf{r} - \mathbf{r}'|} \approx \frac{\exp(ikr\sqrt{1 - 2r^{-2}\mathbf{r} \cdot \mathbf{r}'})}{r} \approx \frac{\exp(ikr)}{r} \exp(-ikr^{-1}\mathbf{r} \cdot \mathbf{r}'), \quad (3.8)$$

where $r \equiv |\mathbf{r}|$ is the distance from the origin of coordinates in the diffracting sample ($\mathbf{r}' = [0, 0, 0]$), to the observation point \mathbf{r} . The binomial approximation has been used for the second step in eq. (3.8). Thus the resultant wavefield becomes a superposition of the incident plane wave with a modulated outgoing spherical wave,

$$\psi(\mathbf{r}) = \exp(i\mathbf{k}_0 \cdot \mathbf{r}) + \frac{\exp(ikr)}{r} f(\mathbf{Q}), \quad (3.9)$$

with scattering amplitude

$$f(\mathbf{Q}) \equiv \frac{k^2}{4\pi} \int [n^2(\mathbf{r}') - 1] \exp(-i\mathbf{Q} \cdot \mathbf{r}') d\mathbf{r}', \quad (3.10)$$

where $\mathbf{Q} = k\mathbf{r}/r = \mathbf{k}_h - \mathbf{k}_0$ (Paganin, 2006). Eq. (3.10) indicates that to calculate $\psi(\mathbf{r})$ for a particular incident plane wave, the three dimensional (3D) Fourier transform (FT) of $[n^2(\mathbf{r}') - 1]$ need only be evaluated on a two dimensional (2D) subset of reciprocal space, i.e. for all the possible directions of \mathbf{Q} . These points, by definition, lie on the Ewald sphere (or rather, they define the Ewald sphere). This is an important result, so let us emphasise that under the first Born approximation, only the values of the 3D FT of $[n^2(\mathbf{r}') - 1]$ that intersect the Ewald sphere contribute to the detectable intensities for a fixed object position and orientation.

Fraunhofer diffraction under the projection approximation

Consider a weakly diffracting, non-periodic object whose entrance and exit surfaces along the optical axis, which we have chosen to be along z , are $z = 0$ and $z = z_{ES}$, as shown in Figure 3.2. The exit surface wavefield, $\psi(x, y, z = z_{ES})$, can be expressed as

a product of the wavefield at the entrance surface, $\psi(x, y, z = 0)$, and the 2D complex transmission function of the object, $t(x, y)$ (Paganin, 2006):

$$\psi(x, y, z = z_{ES}) = t(x, y) \psi(x, y, z = 0). \quad (3.11)$$

Derived from the object's electrostatic potential and expressed in terms of accumulated phase and amplitude shifts in the propagation direction, z , (Warren, 1969; Cowley, 1975; Born and Wolf, 1999), the complex transmission function for non-Bragg diffracting samples under the projection approximation, is (Born and Wolf, 1999):

$$t(x, y) = \exp \left[ik \int_{z=0}^{z=z_{ES}} [n(\mathbf{r}) - 1] dz \right]. \quad (3.12)$$

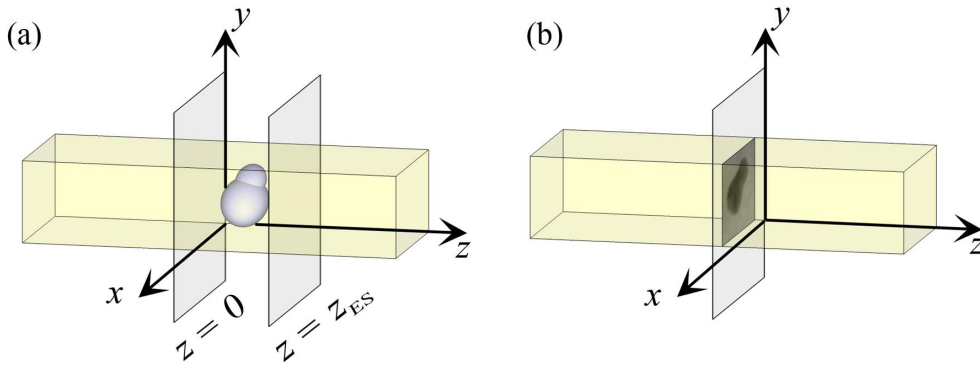


FIGURE 3.2: **Projection approximation.** (a) An object with complex refractive index $n(\mathbf{r})$ that interacts weakly with hard X-rays sits between $z = 0$ and $z = z_{ES}$. (b) Under the projection approximation the X-ray are considered to be diffracted at the plane onto which the object's refractive index has been projected.

Let us now consider the resultant wavefield in eq. (3.9) under the projection approximation. Firstly, by keeping in mind that the refractive index decrement for hard X-rays is very small (cf. eq. (3.3)), we can apply the binomial approximation to the scattering potential (Born and Wolf, 1999; Attwood, 2000):

$$n^2 - 1 = (1 - \delta + i\beta)^2 - 1 \approx -2(\delta - i\beta). \quad (3.13)$$

Secondly, we can rewrite eq. (3.10) explicitly in terms of the transverse components of the scattering vector, \mathbf{Q}_\perp , and object spatial coordinate vector, \mathbf{r}'_\perp ,

$$\begin{aligned} f(\mathbf{Q}) &\equiv \frac{2k^2}{4\pi} \iiint [-\delta(\mathbf{r}') + i\beta(\mathbf{r}')] \exp[-i(\mathbf{Q}_\perp \cdot \mathbf{r}'_\perp + Q_z z')] dx' dy' dz' \\ &= \iint \exp[-i(\mathbf{Q}_\perp \cdot \mathbf{r}'_\perp)] \left[\int (-\delta(\mathbf{r}') + i\beta(\mathbf{r}')) \exp(-iQ_z z') dz' \right] dx' dy'. \end{aligned} \quad (3.14)$$

For a paraxial wave, we can set $\exp(-iQ_z z') = 1$. We can also linearise the transmission function (eq. (3.12)) for a weak object,

$$\begin{aligned} t(x, y) &\approx 1 + ik \int (n(\mathbf{r}) - 1) dz \\ &\equiv 1 + ik \int (-\delta(\mathbf{r}) + i\beta(\mathbf{r})) dz, \end{aligned} \quad (3.15)$$

and then discard the undiffracted beam. By doing this we see that the integral term inside the square brackets in the second line of eq. (3.14) is proportional to the 2D transmission function of a weakly diffracting object, $t(x, y)$.

Now eq. (3.9) can be rewritten in a form equivalent to the Fraunhofer diffraction integral, in which the wavefield in the far field is proportional to the 2D FT of the transmission function (see e.g. Paganin (2006)):

$$\psi(\mathbf{r}) \rightarrow -\frac{ik \exp ikr_z}{2\pi r_z} \exp\left[\frac{ik}{2r_z}(x^2 + y^2)\right] \tilde{\psi}\left(k_x = \frac{kx}{r_z}, k_y = \frac{ky}{r_z}, z = z_{ES}\right), \quad (3.16)$$

where $\tilde{\psi}$ represents the 2D FT of $\psi(x, y, z = z_{ES})$ in eq. (3.11), when $N_F \ll 1$.

For reference, we will use the following definition of the transverse FT and its inverse (Bracewell, 2000):

$$\tilde{\psi}(\mathbf{k}_\perp) = \widetilde{\mathcal{F}}_\perp \{\psi(\mathbf{r}_\perp)\} = \frac{1}{2\pi} \int \psi(\mathbf{r}_\perp) \exp(-i\mathbf{k}_\perp \cdot \mathbf{r}_\perp) d\mathbf{r}_\perp, \quad (3.17)$$

$$\psi(\mathbf{r}_\perp) = \widetilde{\mathcal{F}}_\perp^{-1} \{\psi(\mathbf{k}_\perp)\} = \frac{1}{2\pi} \int \tilde{\psi}(\mathbf{k}_\perp) \exp(i\mathbf{k}_\perp \cdot \mathbf{r}_\perp) d\mathbf{k}_\perp. \quad (3.18)$$

Projection slice theorem

If the X-ray wavelength is very small compared to the object being investigated, then the Ewald sphere can be considered planar in a small region near the origin of reciprocal space (the small purple square in Figure 3.3). In this region, the 2D slice of reciprocal space on which we probe the 3D FT of $[n^2(\mathbf{r}') - 1]$, as in eq. (3.10), all the scattered vectors, \mathbf{Q} , have a negligible Q_z component, which is precisely the assumption made when we set the term $\exp(-iQ_z z')$ to unity in eq. (3.14).

According to the projection slice theorem (also called the Fourier slice theorem) (Wolf, 1969), this slice (purple square) is equal to the 2D FT of the projection of the object, or in other words, proportional to the 2D FT of the transmission function.

It is important to know when the Ewald sphere curvature is negligible, or when the conditions for the validity of the projection approximation are met, as the interpretation of experimental data is greatly simplified, especially for 3D reconstruction (Spence, 2007). Exploiting the projection approximation to calculate the Fraunhofer diffraction pattern via a 2D fast FT (Press *et al.*, 2007) avoids the significant computational burden of calculating the entire 3D FT of the scattering potential.

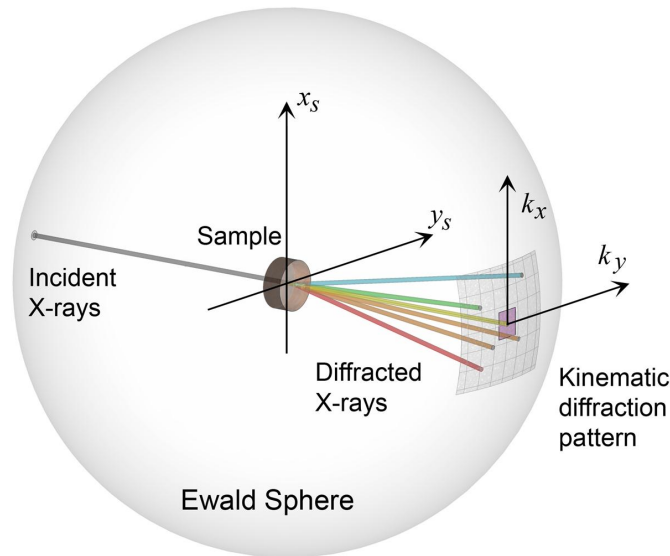


FIGURE 3.3: **Fraunhofer diffraction on the Ewald sphere.** The diffraction angles of the emerging X-rays are exaggerated for clarity. The small purple square at the centre of the diffraction pattern (origin of reciprocal space) demonstrates that for small diffraction angles the Ewald sphere can be considered flat in the vicinity of the origin of reciprocal space

Fourier diffraction theorem

The projection slice theorem is extended to include diffraction effects under the first Born or Rytov approximation (Rytov, 1937; Born and Wolf, 1999) by the Fourier Diffraction Theorem (FDT) (also called the generalised projection slice theorem). The FDT is a statement of eq. (3.14), that the FT of a diffracted projection corresponds to the 2D FT sampled on a curved Ewald sphere (Wolf, 1969; Iwata and Nagata, 1975; Mueller *et al.*, 1980). In Figure 3.3 the colored wavevectors represent elastically (kinematically) diffracted X-rays (with tips lying on the Ewald sphere). The diffraction angles are exaggerated to clearly demonstrate the difference between a curved 2D slice through the 3D FT of $[n^2(\mathbf{r}) - 1]$ (albeit shown only at discrete points of the Ewald sphere), and the “flat region” near the origin of reciprocal space (the purple square) where the projection approximation is applicable.

If a smaller wavelength is used, the Ewald sphere and its corresponding “flat region” in the purple square in Figure 3.3 are increased in size, as shown in Figure 3.4. In other words, using harder X-rays decreases the diffraction angles so values of \mathbf{Q} which lay outside the purple square in the original experimental scenario (for which the projection approximation was inapplicable), are now within the new purple square,

thus demonstrating how the Fourier diffraction theorem approaches the Fourier slice theorem when the wavelength is decreased.

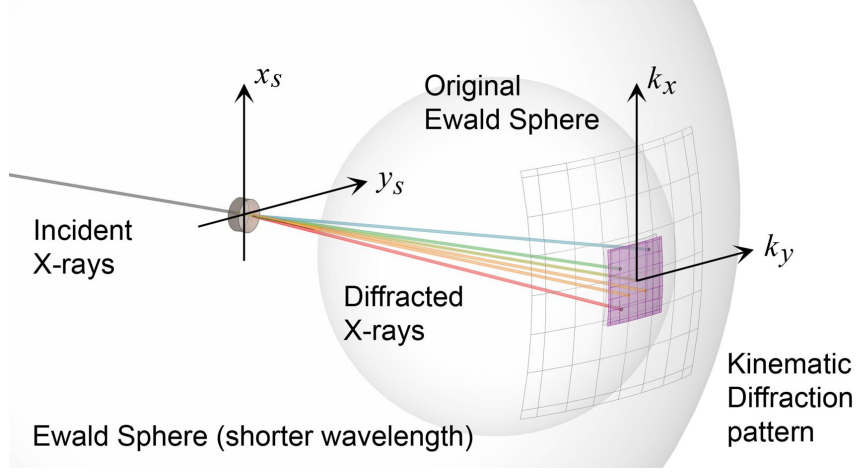


FIGURE 3.4: **Fraunhofer diffraction on the Ewald sphere with a shorter X-ray wavelength.** The effect of a decreased wavelength on the flatness of the Ewald sphere in the region encompassing the sample (k_x, k_y) space as in Figure 3.3. The smaller Ewald sphere corresponds to the original experiment, whose curvature needs to be taken into account in the (k_x, k_y) region of interest.

A number of authors have analysed the effect of Ewald sphere curvature on electron diffraction patterns (see for example [Cohen *et al.* \(1984\)](#); [Bamler \(1988\)](#); [DeRosier \(2000\)](#); [Wolf *et al.* \(2006\)](#)). [DeRosier \(2000\)](#) described the corrections needed to mitigate the failure of the projection approximation in terms of sample thickness, tilt and wavelength, in electron microscopy. In X-ray diffraction experiments, the projection approximation is valid when the following condition is satisfied ([Spence, 2007](#)):

$$L_{PA} < d, \quad (3.19)$$

where

$$L_{PA} = \sqrt{\frac{\lambda T}{2}}, \quad (3.20)$$

d is the desired resolution and T is the thickness of the object. If we make the substitutions $T = r_z$ and $d = b$ and compare this expression to the Fresnel number in eq. (3.7), then eq. (3.19) is equivalent to the requirement $N_F > \frac{1}{2}$. This is also analogous to the column approximation¹.

¹The column approximation was introduced by [Hirsch *et al.* \(1960\)](#) for electron diffraction calculations. In the column approximation, the structure of a column with diameter D , parallel to the electron beam and centred on some point on the exit surface, A , determines the amplitudes of the

We close this introduction to kinematic X-ray diffraction by emphasising that the 3D kinematical diffraction description in eq. (3.10) is accurate regardless of whether the region explored on the Ewald sphere is curved or flat (Cowley, 1975). Furthermore, in order to probe the values of the FT of $[n^2(\mathbf{r}') - 1]$ that do not lie on the Ewald sphere for a particular experimental configuration, the sample can be rotated around an axis transverse to the optical axis, or equivalently, the radiation incidence angle, θ , can be rotated around the sample. Another approach is to change the wavelength, as discussed above, thereby changing the size and curvature of the Ewald sphere, allowing a different 2D surface embedded within the 3D FT to be probed.

We are almost ready to discuss Fraunhofer diffraction patterns of samples containing embedded dispersions of nanoparticles, however in triple axis diffractometry the analyser crystal determines which part of the Fraunhofer diffraction pattern can be measured, so we will briefly digress to discuss X-ray diffraction from crystals.

3.2 Diffraction from crystals

In this section we describe diffraction from crystals as these are used to condition and analyse the X-ray beam in high resolution X-ray diffractometry. Crystalline structures are well suited to a description by discrete spatial frequencies because of their long range spatial periodicity. Theories describing X-ray diffraction from crystals are generally either kinematical or dynamical (Zachariasen, 1945; von Laue, 1960; Cowley, 1975; Authier, 2003). For a general picture of diffraction from crystals we will briefly describe the former, and then present the main results of the latter as it describes diffraction from perfect crystals very accurately in the vicinity of the Bragg reflection.

In a subsequent chapter, we will specifically consider X-ray diffraction from nanoparticle ensembles embedded within a host matrix (§4.3.1 and §5.1), as measured in triple axis diffractometry, by incorporating the theory presented in (§3.1), and in this section.

waves emerging from the specimen at A (Cowley, 1975). Owing to the high energy and thus very small wavelength of the accelerated electron, it will scatter at an angle smaller than that required for it to leave the column laterally. Naturally the column diameter depends on the thickness of the sample and neighbouring columns do not interact.

3.2.1 Kinematical diffraction

Kinematical theories work well for weakly diffracting objects where the X-rays can be considered to be singly scattered. They do not take multiple scattering into account, and violate the conservation of energy principle by ignoring absorption effects. Despite these omissions, this approximation is accurate for very thin crystals, surface and diffuse scattering, and as a general rule, it is valid for rather imperfect systems and small scattering volumes.

The kinematical approach has been successfully applied to describe, for example, diffraction from polycrystalline materials, powder diffraction, and diffraction from soft matter (Guinier, 1952). For systems with increasing levels of perfection (symmetry/periodicity), the kinematical scattering theory approaches its limitations (Schmidbauer, 2004).

Let us introduce a coordinate system that corresponds to the crystal of interest, with the surface normal along the z_c direction (where we use the subscript c to differentiate between the optical axis z and the crystalline axis, z_c), and with the crystal surface parallel to the (x_c, y_c) plane. The 3D FT of the scattering potential of a semi-infinite crystal is embodied by its reciprocal space lattice. In the Ewald sphere construction (Figure 3.5), when the origin of reciprocal space is coincident with the origin of the crystal reciprocal space lattice, each reciprocal lattice point that intersects the sphere corresponds to a family of parallel planes (with Miller indices hkl) whose interplanar spacing, d_{hkl} , satisfies the Bragg equation (Bragg, 1913a,b):

$$2d_{hkl} \sin \theta_B = \lambda, \quad (3.21)$$

where λ is the wavelength of radiation incident on the crystal at an angle of θ_B . The scattering vector for this reflection, \mathbf{Q}_{hkl} is related to d_{hkl} via

$$d_{hkl} = \frac{2\pi}{|\mathbf{Q}_{hkl}|}. \quad (3.22)$$

The above formalism assumes a plane, monochromatic incident wave on the sample, which means the Ewald sphere is unique (one incident direction, i.e. no divergence) and infinitely thin. However, in experimental realisations, the monochromator has a finite bandpass and hence the Ewald sphere surface on which the 3D FT of the scattering potential of the sample is probed has a finite thickness determined by the energy resolution of the monochromator. For a perfect monochromator, commonly used for monochromating hard X-rays, the energy resolution can be derived from eq. (3.21) as:

$$\frac{\Delta E}{E} = \frac{\Delta \lambda}{\lambda} = \Delta \theta \cot \theta_B. \quad (3.23)$$

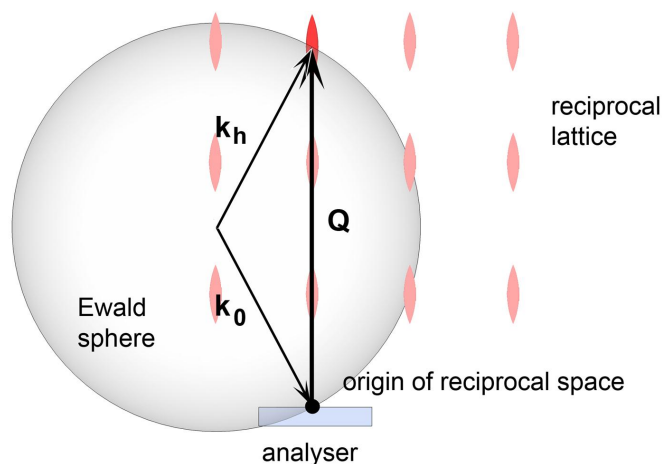


FIGURE 3.5: **Ewald sphere with reciprocal lattice.** Each reciprocal lattice point that intersects the Ewald sphere corresponds to a family of planes that satisfy the Bragg condition. The crystal truncation rods, shown here as elongated reciprocal space points perpendicular to the surface of the analyser, are due to the abrupt change in electron density at the surface of the crystal.

This will be discussed in more detail later, in §4.3.

The reciprocal space representation of a physically realisable crystal, finite in one or more dimensions, is the FT of the infinite crystal lattice convolved with the crystal shape function (Ewald, 1962; Cruickshank *et al.*, 1996; Authier, 2003). For the aforementioned semi-infinite perfect crystal, the abrupt change of electron density at the surface results in the elongation of the reciprocal space lattice point, normal to this direction, which is known as the crystal truncation rod (CTR) (Robinson, 1986). The analyser's CTR plays a prominent role in the characteristic instrumental function of triple axis diffractometry, which will be described in §4.3.1.

3.2.2 Dynamical diffraction

Dynamical theories do take multiple scattering into account and provide excellent agreement with experimental intensities around Bragg peaks, for perfect or nearly perfect, thick crystals, such as those used to monochromate and analyse the X-rays in the triple axis technique developed here.

The integrated reflected intensities calculated using kinematical theory are proportional to the crystal thickness, t_{cryst} , and the square of the structure factor, F_{hkl} ,

$$I \propto t_{\text{cryst}} |F_{hkl}|^2, \quad (3.24)$$

where the structure factor is the FT of the electron density. The corresponding expressions calculated using dynamical theory, for an infinite perfect crystal, are proportional to the modulus of the electron density (Authier, 2003). Consequently, the intensity around a Bragg peak is much higher, in general, when calculated using kinematical theory, than with dynamical theory. However when the scattered intensities are sufficiently low, i.e. either the Bragg reflection is very weak, or the crystal is sufficiently thin, kinematical and dynamical diffraction theories give the same results very close to the Bragg peaks.

In the framework of dynamical theory, the exact theoretical treatment of X-ray diffuse scattering from mesoscopic structures is excessively complicated and impractical (Schmidbauer, 2004). When a system is too distorted to treat the scattering in the framework of dynamical theory, but on the other hand, too perfect to be treated in conventional kinematical scattering theory, it is possible to separate the descriptions into a perfect, periodic part and an aperiodic part (Schmidbauer, 2004). The former requires dynamical theory for an accurate description, while the latter, (mesoscopic structures such as islands grown on a surface, embedded defects or nanoprecipitates), can be described using kinematical diffraction (Schmidbauer, 2004). In our case, where nanoparticles are embedded in an amorphous matrix, the kinematical description presented in §3.1.1 and §3.1.2 suffices, provided the approximations discussed therein are valid for the nanoparticles in questions (which will be described in detail in chapter 5).

The first dynamical X-ray diffraction theory, developed by Darwin (1914a,b), gave the correct expressions for reflected intensities by solving recurrence equations describing the transmittance and reflectance at each lattice plane. An alternative dynamical diffraction theory introduced by Ewald (1916, 1917, 1969), and later developed by von Laue (1931, 1960), represents the exact solution of Maxwell's equations for electromagnetic wavefields inside and outside the crystal, which was considered to be a periodic distribution of dipoles (Ewald) or triply periodic continuous distribution of dielectric susceptibility (von Laue). This Ewald-Laue theory is regarded as the general two-beam X-ray dynamical theory for a perfect crystal.

Over the last several decades, a great quantity of theoretical work has been carried out on dynamical theory (see e.g. Pinsker (1978); Authier (2003)), among which we shall highlight the independent work of Takagi (1962, 1969) and Taupin (1964). The Takagi-Taupin equations are two coupled, second-order partial differential equations expressed in terms of the forward (K_0) and diffracted beam (K_h) directions (Afanasev and Kohn, 1971). For the two-beam case, the Takagi equations describing diffraction

from a perfect crystal in Bragg geometry reduce to (Authier, 2003),

$$\frac{\partial D_0(\mathbf{r})}{\partial x_0} = -i\pi k C \chi_{\bar{h}} D_h(\mathbf{r}) \quad (3.25)$$

$$\frac{\partial D_h(\mathbf{r})}{\partial x_h} = -i\pi k [C \chi_h D_0(\mathbf{r}) - 2\beta_h D_h(\mathbf{r})] \quad (3.26)$$

where $D(\mathbf{r})$ is the electric displacement, x_0 and x_h are coordinates in direct space along K_0 and K_h , respectively (Figure 3.6), K_0 and K_h are the wavevectors in the crystal and k_0 is the wavevector in vacuum. χ_h and $\chi_{\bar{h}}$ are the Fourier components of the dielectric susceptibility; the polarisation factor $C = 0$ for σ polarisation (perpendicular to the (K_0, K_h) plane), and $C = \cos 2\theta_B$ for π polarisation, (parallel to that plane); and β_h is the resonance error, which represents the deviation of the incident wave from the exact Bragg condition, where

$$\beta_h = \frac{K_h^2 - k^2(1 + \chi_0)}{2k^2} = \frac{K_h^2 - K_0^2}{2k^2} \simeq \frac{K_h - K_0}{k}. \quad (3.27)$$

The crystal's reflectivity as a function of angle, also known as the rocking curve (Figure 3.7), is expressed as a function of this parameter, β_h . A strict requirement, and thus a severe limitation of the above equations, is that the deviation from the Bragg condition is very small, i.e. $|\theta_B - \beta_h| \ll 1$. An obvious consequence is that this dynamical description describes reflectivity well only in the vicinity of the Bragg peaks.

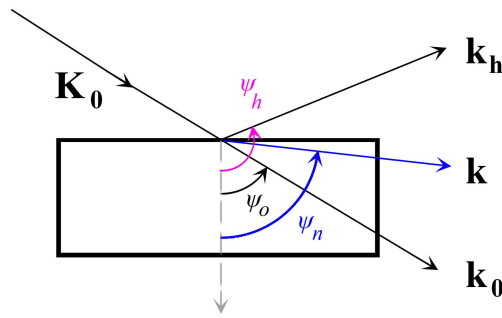


FIGURE 3.6: **Bragg geometry explained:** $-\pi/2 - 2\theta_B < \psi_h < -\pi/2$; $-\pi/2 < \psi_0 < -\pi/2 + 2\theta_B$, after (Authier, 2003).

Figure 3.6 shows that in Bragg (reflection) geometry the reflected wave is directed

towards the outside of the crystal, with the following angular relationships:

$$-\frac{\pi}{2} < \psi_0 < -\frac{\pi}{2} + 2\theta_B, \quad (3.28)$$

$$-\frac{\pi}{2} - 2\theta_B < \psi_h < -\frac{\pi}{2}, \quad (3.29)$$

$$-\frac{\pi}{2} - \theta_B < \psi_n < -\frac{\pi}{2} + \theta_B. \quad (3.30)$$

The rocking curve, $\xi(\eta)$, of a perfect crystal is expressed as the ratio of the amplitudes of exit wave, Ψ_h , to incident wave, Ψ_0 , (Authier, 2003)

$$\xi(\eta) = \frac{\Psi_h}{\Psi_0} = \frac{S(\gamma_h)}{\sqrt{|\gamma|}} \frac{\sqrt{\chi_h \chi_h^-}}{\chi_h^-} \left[\eta \pm \sqrt{\eta^2 + S(\gamma_h)} \right]. \quad (3.31)$$

Here S is the sign of γ_h , which is +1 in transmission geometry, and -1 in reflection geometry. The asymmetry ratio, γ , is expressed as

$$\gamma = \frac{\gamma_h}{\gamma_0} = \frac{\cos(\psi_n - \theta_B)}{\cos(\psi_n + \theta_B)}, \quad (3.32)$$

where ψ_n is the angle between the normal to the crystal surface and the incident wavevector (cf. Figure 3.6). The deviation parameter, η is defined as

$$\eta = \frac{\Delta\theta \sin 2\theta_B + \chi_0(1 - \gamma)/2}{|C| \sqrt{|\gamma|} \sqrt{\chi_h \chi_h^-}} = \frac{(\Delta\theta - \Delta\theta_{os})}{\delta_{os}} \quad (3.33)$$

where

$$\Delta\theta_{os} = -\frac{\chi_0(1 - \gamma)}{2 \sin 2\theta_B}, \quad (3.34)$$

$$\delta_{os} = \frac{C \sqrt{|\gamma|} \chi_h \chi_h^-}{\sin 2\theta_B}, \quad (3.35)$$

$$\chi_h \chi_h^- = |\chi_{rh}|^2 (1 - \kappa^2 + 2i\kappa \cos \phi), \quad (3.36)$$

$$\kappa = \left| \frac{\chi_{ih}}{\chi_{rh}} \right|. \quad (3.37)$$

Here χ_{rh} is the real part of the Fourier coefficient of the polarisability and ϕ is the difference between the real and imaginary components of the phase factor of the structure factor, F_h . The Darwin width, $2\delta_{os}$, is the full width at half-maximum (FWHM) of the rocking curve. As it determines the wavelength/energy resolution (cf. eq. (3.23)), where $\Delta\theta = 2\delta_{os}$, the Darwin width is one of the key characteristics one considers when choosing appropriate monochromator and analyser crystals. In the Bragg case, $\gamma < 1$ and $\Delta\theta_{os}$ is never zero, due to refraction.

Far from the total reflection domain (within half the Darwin width from the perfect Bragg condition), the rocking curve can be approximated by the function $I_h \approx 1/(4\eta^2)$ (Authier, 2003). For n reflections the rocking curve tails decrease as $1/\eta^{2n}$, since the intensity of n such successive reflections is $I^n(\Delta\theta)$, where $I(\Delta\theta)$ is the intensity of a single reflection. The theoretical rocking curve of a symmetric reflection from an ideal Si(400) crystal, with $\lambda = 1.0\text{\AA}$, is shown in Figure 3.7, where the solid black line shows the reflectivity of a single symmetric reflection, while the short-dashed red line and long-dashed blue lines shown the reflectivities from a symmetric double and triple reflection, respectively. The FWHM, however, remains constant (Authier, 2003), so the reflection's intrinsic energy resolution is unchanged. The lowering of the rocking curve tails by multiple reflections plays an important role in reducing the prominence of the instrumental function of triple axis diffractometry, which will be discussed in chapter 4.

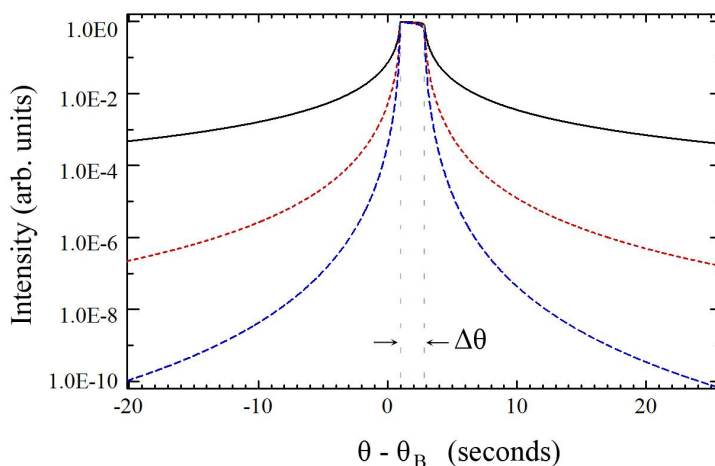


FIGURE 3.7: **Simulated, normalised rocking curves** (angular reflectivity) of a perfect Si(400) crystal using 1.0\AA X-rays. The solid black line is the single reflection, the short dashed red line is two reflections, and the long dashed blue line is three reflections, showing how multiple reflections significantly lower the tails but do not affect the Darwin width of the crystal rocking curve. The offset of the peak is due to refraction. These reflectivities were simulated using IDL 6.4 (ITT Visual Information Solutions).

In deriving eqs. (3.25) and (3.26), a number of approximations were made, such as neglecting all but two beams, neglecting terms of order χ^2 since $\chi \ll 1$ for X-rays, approximating the angular parameters (as in eq. 3.27) and approximating boundary conditions. Even despite the multitude of variations on approaches to dynamical diffraction theory, with various additional complexities and the ability to calculate

intensities from perfect and deformed crystals (Takagi, 1962; Taupin, 1964; Afanas'ev and Kohn, 1971; Härtwig, 2001), dynamical theories are generally based on the small angle approximation and hence break down far from the Bragg peaks (Grundmann, 2000; Podorov *et al.*, 2006). In order to simulate the diffracted intensities on the nanometre scale we must move away from the Bragg peaks to the tails of the crystal rocking curves, which the dynamical description presented here does not describe accurately.

3.2.3 Summary

In this chapter we introduced the theoretical background necessary to describe the interaction of X-rays with matter, both Bragg and non-Bragg diffracting. We began with identifying the basic properties of an X-ray wavefield, and its interaction with inhomogeneous media. From the single-scattering scenario described by the first Born approximation, we moved to a Fraunhofer diffraction description. Diffraction from crystalline materials, both in the kinematical and dynamical description, was presented next, as the interaction of the X-ray wavefield with crystalline matter plays a pivotal role in determining the information content of the reciprocal space maps.

We now turn to the description of the experimental setup for reciprocal space mapping with an analyser crystal.

Experimental setup for reciprocal space mapping with an analyser crystal

The previous chapter presented the theoretical framework necessary to describe the interactions of X-rays with weakly diffracting embedded nanoparticle ensembles. For the experimental development of the nano-characterisation technique described in this thesis, we need appropriate optical components to enable reciprocal space mapping of X-ray diffraction from embedded nanoparticle ensembles in a bulk material, which is the topic of this chapter. These experimental parameters are also important to reconstructions as we need to understand the contributions of the various optical components to the recorded intensities before reconstructions can be attempted.

In the discussion that follows, we start with the generation of the X-ray wavefield by the synchrotron X-ray sources we used, including a discussion of the source's pertinent properties. We then move on to discussing reciprocal space mapping with an analyser crystal, which includes the details of the monochromating and analysing crystals used, and the scanning geometry. The information content of a reciprocal space map (RSM) is presented next, which includes the triple axis diffractometry instrumental function and far field diffraction from the sample. Then we examine the considerations for building the dedicated sample holder and heater, designed to enable testing of the experimental technique's sensitivity to nanoparticle size and orientation (§6.2), as well as to enable investigations of *in situ* real-time embedded nanoparticle growth (§6.3 and §6.4). We close the experimental chapter with a brief look at the X-ray detectors suitable for reciprocal space mapping.

The three stages, X-ray generation, interaction with optical elements and sample, and detection, constitute the forward problem in X-ray optics. The fourth step is the inverse problem: retrieving (the nanoparticle) structural information from the diffraction data. Nanoparticle reconstructions from simulations are described in chapter 5 and those from experimental data are presented in chapter 6.

4.1 Synchrotron X-ray sources

The diffracted intensities from weakly diffracting embedded nanoparticles may have a range of six to eight orders of magnitude, so it is preferable to have a source with high brilliance in order to maintain a high signal to noise ratio (SNR). Likewise, the loss of intensity through optical elements such as slits and crystals, and attenuation by the sample itself (representative of the bulk material, §2.2.3), suggests that development of the emerging analyser based, reciprocal space mapping technique is most effectively carried out at synchrotrons. This development, the results of which are presented in chapter 6, was carried out over a series of dedicated experiments at the Australian National Beamline Facility on beamline BL20B, at the Photon Factory, a 2nd generation synchrotron in Tsukuba, Japan, as well as on beamlines BL13XU and BL29XU at SPring-8, a 3rd generation synchrotron in Hyogo, also in Japan.

Synchrotron radiation is emitted when relativistic charged particles are accelerated along curved trajectories (Attwood, 2000). Historically, the production of synchrotron radiation was initially considered a nuisance, as it constituted a significant energy loss from particle accelerators. Such sources were retrospectively named *first generation* synchrotrons, with *second generation* defining those purpose built as sources of tuneable electromagnetic radiation with high brilliance. *Third generation* synchrotrons include insertion devices, discussed below, which are optimised to considerably improve upon the brightness and coherence of the beam. Figure 4.1 compares the brilliance of spectra emitted from the sun, a conventional X-ray tube and synchrotron bending magnets, wigglers and undulators, showing in particular the significant increase in flux at the fundamental and harmonic frequencies of undulators.

4.1.1 Beam characteristics from bending magnets and insertion devices

The relativistic speed of the electrons in a synchrotron gives rise to the intrinsic high directionality and small transverse size of the beam, which, coupled with the long distances from source (bending magnet or insertion device) to sample (from tens of metres up to a kilometre at one beamline at SPring-8) result in a very highly spatially coherent beam (cf. eq. 4.3). Bending magnets are composed of a single magnetic dipole, which forces the electrons into circular trajectories. The continuum of light emitted is linearly polarised in the bending plane, and elliptically polarised in the transverse plane (Kim, 2001).

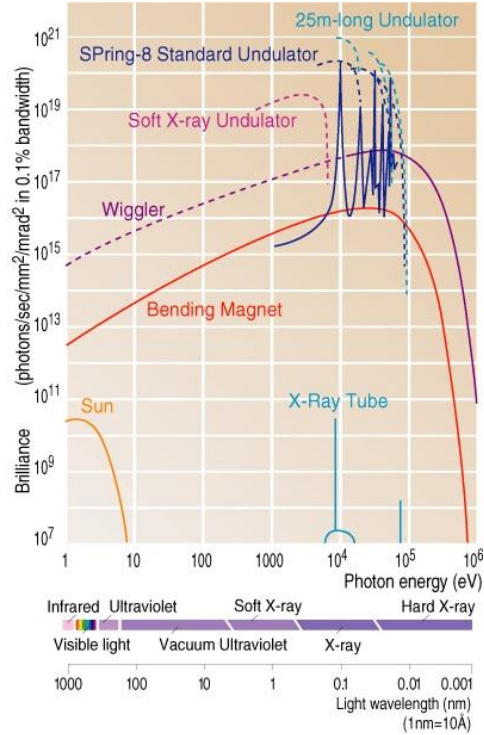


FIGURE 4.1: **Comparison of spectra from various X-ray sources** used with permission from [SPring-8 Features \(2010\)](#).

Insertion devices, called wigglers and undulators, sit in the straight sections of the storage ring between the bending magnets. These consist of periodic arrays of magnetic dipoles that force the electrons into horizontal sinusoidal motion (Figure 4.2). The maximum angular deflection of the orbit from its tangential direction is expressed in terms of the deflection parameter, K ([Moser, 2004](#)), a convenient parameter for characterising the electron motion, given by

$$K = \frac{eB_0\lambda_u}{2\pi m_e c} \approx 0.934B_0\lambda_u, \quad (4.1)$$

where B_0 is the peak magnetic field in Tesla, λ_u is the magnetic period in centimetres, m_e is the electron mass and c is the speed of light ([Kim, 2001](#)).

For wigglers, $K > 2$ ([Moser, 2004](#)) and the total divergence of the emitted beam is larger than the divergence of the radiation emitted by a point on the electron's orbit ([Authier, 2003](#)). Wigglers produce a spectrum similar to bending magnets but the beam is broader and the flux is increased by $2N$, where N is the number of magnetic poles, since the beam is the incoherent sum of beams emitted by each magnetic pole ([Authier, 2003](#)).

Radiation emitted from undulators, where $K \leq 2$, is in a very narrow cone in

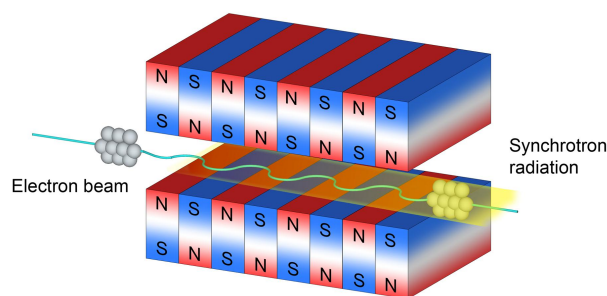


FIGURE 4.2: **Alternating dipole magnets in a wiggler or undulator.** The strong, alternating magnetic field forces the relativistic electron beam to undergo oscillatory motion in the plane of its orbit, whereby synchrotron radiation is emitted.

the direction of electron motion, with angular divergence of the same order as the diffraction width of a low order reflection from a crystal (e.g. a few arcseconds for Si(400) at 10.9 keV (Stepanov, 2008), as shown in §4.2.1) (Authier, 2003). The beams emitted by individual dipoles interfere coherently, increasing the intensity as N^2 . As a result of the interference, undulator radiation is quasi-monochromatic, consisting of the sum of the fundamental frequency (peak energy) and its harmonics (Authier, 2003). The bandwidth of the n^{th} harmonic is

$$\frac{\Delta E}{E} = \frac{\Delta \lambda}{\lambda} \approx \frac{1}{nN} \quad (4.2)$$

where E , λ , ΔE and $\Delta \lambda$ are the energy and wavelength, and their respective bandwidths.

In Table 4.1 we compare the properties of the three beamlines used, with a brief description of each below.

Australian National Beamline Facility (BL20B) at the Photon Factory

The Photon Factory is a 2.5 GeV second generation synchrotron radiation source, completed in 1992 and upgraded in 2005 (Sakanaka *et al.*, 2007), at the High Energy Accelerator Research Organization (KEK), in Tsukuba, Japan. The Australian National Beamline Facility (ANBF) is situated at beamline BL20B, a bending magnet source. The principal experimental chamber at ANBF is a large vacuum two-circle diffractometer, the “BigDiff” (Figure 4.3), which can be used in a variety of configurations such as for powder diffraction in Debye-Scherrer and Weissenberg geometries, grazing incidence diffraction and reflectometry. It can also be used as a two-circle diffractometer, a triple axis diffractometer or a Bonse-Hart small angle scattering

Beamline	BL20B Photon Factory	BL13XU SPring-8	BL29XU SPring-8
Storage ring energy	2.5 GeV	8 GeV	8 GeV
Source type	Bending magnet	Undulator	Undulator
Spectral range	4 - 21 keV	7 - 32 keV	4.4 - 37.8 keV
Primary monochromator	Si(111) channel cut	Si(111) double crystal	Si(111) double crystal
Max beam size H×V	30 × 2 mm ²	0.5 × 0.5 mm ²	0.7 × 1.6 mm ²
Source to sample distance	14 m	58 m	52 m (987 m also available)

TABLE 4.1: **Beamline characteristics.** The nanoparticle characterisation technique development in this thesis was carried out at a bending magnet source, the ANBF at the Photon Factory, and two undulator beamlines, BL13XU and BL29XU at SPring-8. Data was taken from [BL-20B \(2000\)](#); [ANBF \(2009\)](#); [BL13XU Outline \(2010\)](#); [BL29XU Outline \(2010\)](#) and [SPring-8 Features \(2010\)](#).

diffractometer. The beamline was chosen for its high resolution diffractometry capabilities, as well as the big advantage that experiments can be performed in vacuum (to 10^{-2} Torr), which greatly improves the SNR by reducing air absorption and parasitic scattering ([Barnea *et al.*, 1992](#); [Creagh *et al.*, 1998](#); [BL-20B, 2000](#)).

The primary monochromator at BL20B is a water-cooled, channel-cut Si(111) crystal that can be detuned to reject harmonics ([Creagh *et al.*, 1998](#)). A secondary monochromator was used (particular to the experiment) to further monochromate the beam (chapter 6). The key characteristics of ANBF (BL20B) are displayed in Table 4.1.

BL13XU and BL29XU at SPring-8

SPring-8 is an 8 GeV, third generation synchrotron at the Harima Science Garden City, in Hyogo, Japan. It was built in 1997 and is one of the world's brightest third-generation synchrotrons. Our experiments were performed on two undulator beamlines, BL13XU and BL29XU, the characteristics of which are shown in Table 4.1. Both beamlines are in-vacuum undulator sources with 140×32 mm magnetic periods, giving a natural energy resolution of $\Delta E/E = 0.0071$. The energy resolution is greatly improved upon by the primary monochromator (cf. eq. (3.23)), which is a liquid nitrogen-cooled Si(111) double crystal (at both beamlines), and a secondary monochromator,

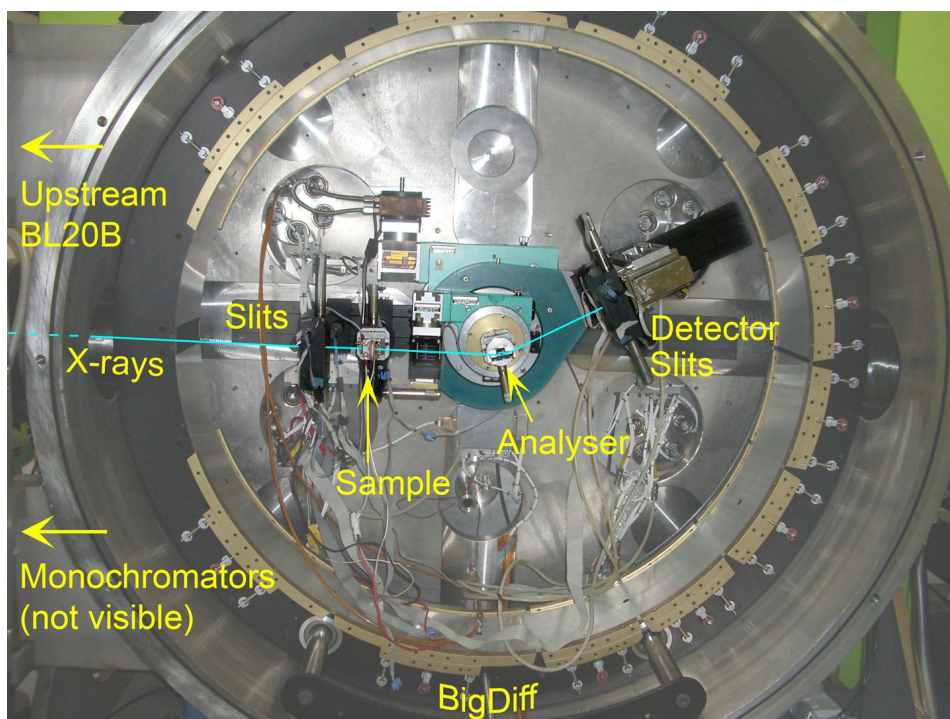


FIGURE 4.3: The “**BigDiff**”. The high resolution diffractometer at ANBF, on BL20B of the Photon Factory, Tsukuba, Japan. The entire chamber is able to be evacuated, minimising parasitic scatter and thus increasing the SNR. A preliminary study investigating the practicalities of performing *in situ* real-time X-ray diffractometry investigations of nanoparticle growth in Al-Cu alloys was carried out here, using X-rays of 8.5 keV, with a channel-cut, double reflection Si(111) monochromator (§4.2.1) and single reflection Si(111) analyser in the non-dispersive mode (§4.2.1). Also, X-rays of 15 keV were used, with the monochromator set to the Si(333) reflection. The incident beam on the sample was set to $0.4 \times 0.2 \text{ mm}^2$. The analyser was a Si(111) single reflection crystal, and the detector, a Radicon scintillation counter (§4.1.1).

as described for each experiment in chapter 6.

The first *in situ* real-time investigation of nanoparticle growth in an Al-Cu alloy with analyser based reciprocal space mapping was carried out at BL13XU (§6.4). BL13XU was ideal for this experiment as it is equipped with a multi-axis diffractometer that allows automated, high angular resolution scans to be performed (Figure 4.5).

4.1.2 Brightness and coherence

The main quantitative characteristics of an X-ray source can be summarised by its coherence and (spectral) brightness (see e.g. Kim (2001)). The diffraction theory presented in the previous chapter assumed perfectly planar, monochromatic X-rays,

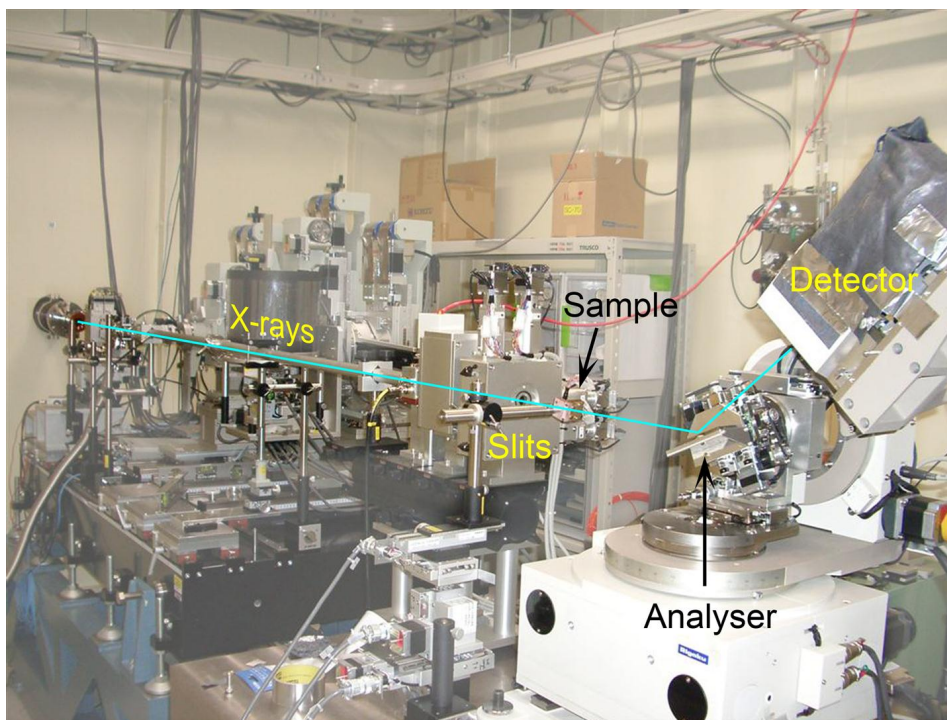


FIGURE 4.4: **Experimental setup at BL29XU, SPring-8.** This triple axis diffraction setup included a channel cut Si(400) monochromator (in addition to the primary Si(111) monochromator at the beamline), single reflection Si(400) analyser (in the non-dispersive setup (§4.2.1)), and silicon PIN diode detector. X-rays of 10.9 keV were used in this setup for a feasibility experiment investigating the sensitivity of the novel technique to Al-Cu embedded nanoparticles of various sizes and crystallographic orientations (Zatsepin *et al.*, 2008).

neither of which is possible in reality. Hence the need arises to quantify the degree of deviation from the ideal case, which is expressed by the beam coherence.

The coherence volume, Coh_V , defines a volume within which exists a fixed relationship between the phase at each point of the X-ray wavefield. It is defined as the product of transverse coherence lengths in the vertical and horizontal directions, and the longitudinal coherence length, Coh_L , described below. X-rays diffracted from within the coherence volume interfere coherently at the detector, while X-rays diffracted from sample volumes greater than the coherence volume result in the incoherent addition of intensities at the detector, in direct-space intensity measurements.

Transverse coherence length, also known as the spatial coherence, depends on beam divergence and source-to-sample distance. The vertical coherence length is defined as (Attwood, 2000)

$$Coh_{L_v} \equiv z\theta_v = \frac{z\lambda}{2\pi\sigma_v}. \quad (4.3)$$

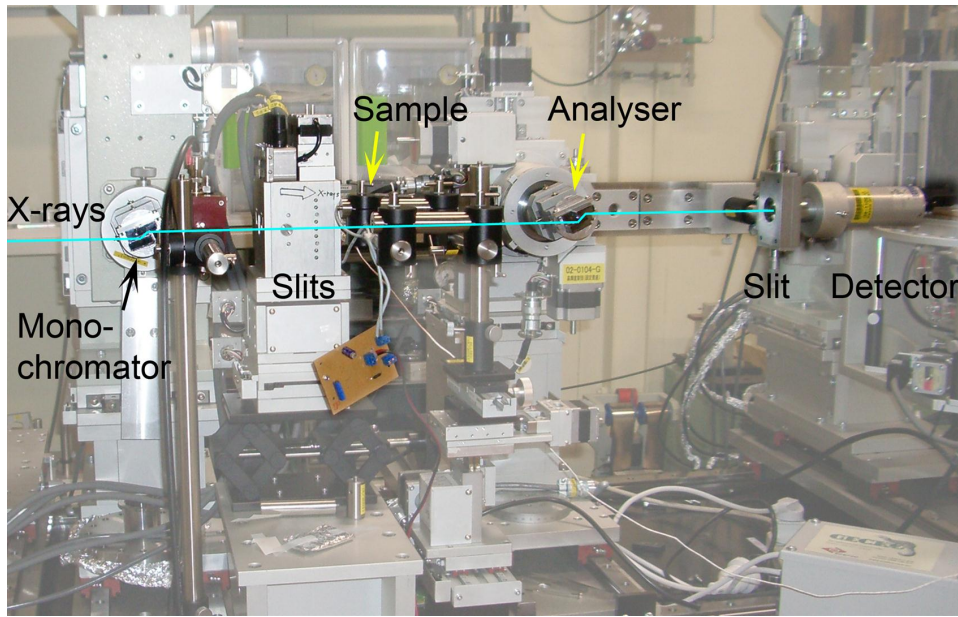


FIGURE 4.5: **Experimental setup at BL13XU, SPring-8.** The monochromator and analyser in this triple axis diffractometry setup were both channel cut, double reflection Si(400) crystals in a non-dispersive setup. The primary Si(111) double crystal is not shown. X-rays of 12.4 keV were used for the investigation of *in situ*, real-time embedded nanoparticle ensemble growth in an Al-Cu alloy, reported in §6.4 (Zatsepin *et al.*, 2010).

Here z is the distance from the source, θ_v is the root-mean-square (RMS) vertical half-angle of the divergent beam, λ is the wavelength and σ_v is the RMS height of the beam. An equivalent expression defines the transverse coherence length horizontally. Evidently, an increase in the distance from the source increases spatial coherence, or in other words, decreases the effective source size. The transverse coherence area, Coh_A , is the product of coherence lengths in vertical and horizontal directions, and can be expressed as (Demtröder, 2003)

$$Coh_A \approx \frac{\lambda^2}{d\Omega}, \quad (4.4)$$

where $d\Omega = (\sigma_h\sigma_v)/z^2$ is the solid angle subtended by the source. The source of radiation emitted by the afore described insertion devices at synchrotrons can be described as a distribution of elementary quasi-monochromatic sources of infinitesimal size, which emit spherical waves. At the position of the experimental hutches, however, Mocella *et al.* (2000) have shown that they can be approximated locally by a plane wave.

Longitudinal coherence length, or temporal coherence, is a measure of the degree

of beam monochromaticity ([Attwood, 2000](#)),

$$Coh_L = \left(\frac{1}{\lambda - \frac{1}{2}\Delta\lambda} - \frac{1}{\lambda + \frac{1}{2}\Delta\lambda} \right)^{-1} \approx \frac{\lambda^2}{\Delta\lambda}, \quad (4.5)$$

where $\Delta\lambda$ is the spectral bandwidth. In reciprocal space mapping of diffracted intensities, only the temporal coherence plays a significant role and the requirement of a large coherence volume is relaxed. This is because recording the intensity as a function of its diffraction angle does not discriminate between X-rays diffracted from different positions within the sample. Using a detector that integrates over its input window similarly does not differentiate X-rays arriving at different positions on the detector window. This is discussed in more detail with regards to diffraction from large ensembles of nanoparticles in §5.1.

As mentioned earlier, the source brightness is important as a high photon flux is necessary in order to record a statistically significant signal from very weakly diffracting specimens in an acceptably short time to construct an RSM. Brightness, or spectral brightness ([Mills *et al.*, 2005](#)) is defined as ([Kim, 2001](#)):

$$\mathcal{B}(E) = \frac{\Phi(E)}{4\pi^2 \varepsilon_h \varepsilon_v}, \quad (4.6)$$

where $\Phi(E)$ is the X-ray flux at energy E in photons per second within a 0.1% bandwidth centred at E , and the horizontal and vertical emittances, ε_h and ε_v are defined as ([Authier, 2003](#))

$$\varepsilon_h = \sigma_h \theta_h, \quad (4.7)$$

$$\varepsilon_v = \sigma_v \theta_v. \quad (4.8)$$

Brightness has units of photons \cdot s⁻¹ \cdot mrad⁻² \cdot mm⁻² \cdot (0.1% bandwidth)⁻¹. The brightness of various X-ray sources was compared in Figure 4.1.

4.2 Triple axis diffractometry setup

In this section we discuss the experimental details of triple axis diffractometry (TAD), which was reviewed in §1.1.5. Following the description of crystals typically used for monochromating and analysing the beam in §4.2.1, we discuss their role in determining the information content from the sample in the RSM in §4.3. We close the section with a look at the geometry of various scans that are used to map reciprocal space.

The three axes in our TAD setup correspond to the rotation axes of the monochromator, analyser and detector. Both single reflection and double reflection analyser

crystals were utilised in the development of the RSM technique, (Figure 4.6). Details of the crystals used are presented in §4.2.1. The sample is placed between the monochromator and analyser, oriented normal to the optical axis.

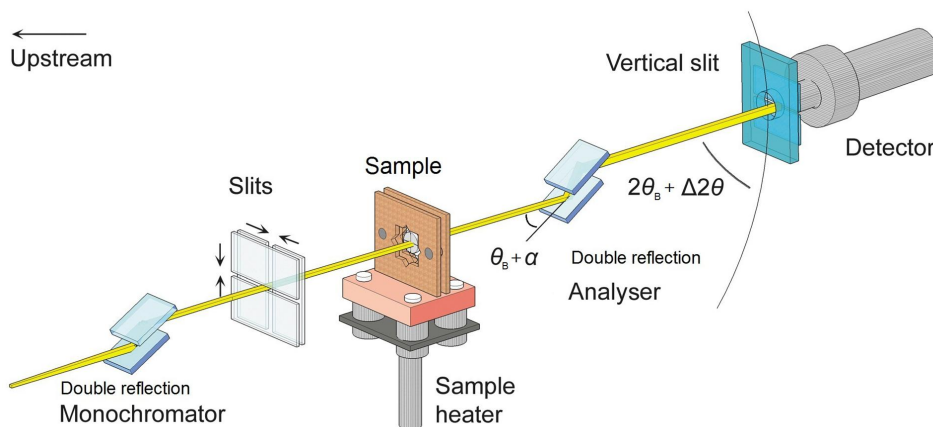


FIGURE 4.6: **Experimental setup for triple axis diffractometry.** This schematic of the experimental setup shows channel-cut, double reflection monochromator and analyser crystals in a parallel (+n, -n, +n, -n) non-dispersive setting.

4.2.1 Crystal monochromators and analysers

High quality silicon single crystals were used to achieve the extremely low angular divergence (cf. eq. (4.3)) and energy bandwidth (cf. eq. (3.23)) necessary for our high resolution X-ray diffraction studies (listed in Table 4.2. As a result of the development of the semiconductor industry, single crystal silicon is readily available in large sizes and at low cost. The only difference between a monochromator and analyser is its role (and hence position) in the optical setup, as shown in Figure 4.6.

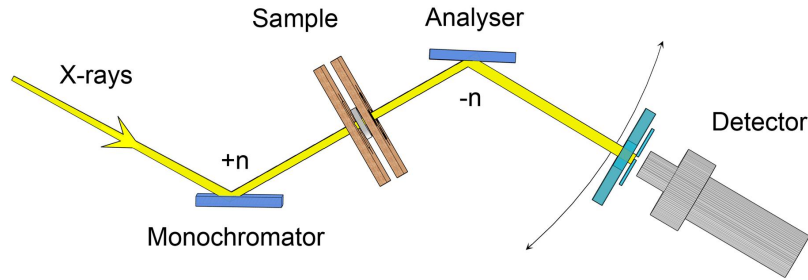
Primary monochromators at synchrotron beamlines monochromate and sometimes collimate (by sagittal focussing) the X-ray beam, providing a narrow bandwidth with high intensity. A secondary monochromator (on the 1st axis in TAD) is used to further narrow the energy spread, as determined by its rocking curve (cf. 3.2), and is not rotated during the experiment.

Using the same crystal and Bragg reflection for both the monochromator and analyser in the parallel setting (+n, -n) as in Fig. 4.7(a), or (+n, -n, +n, -n), as in Fig. 4.7(b), for the channel cut monochromator and analyser (where n is the order of reflection), ensures no wavelength dispersion. In the non-dispersive setting, the

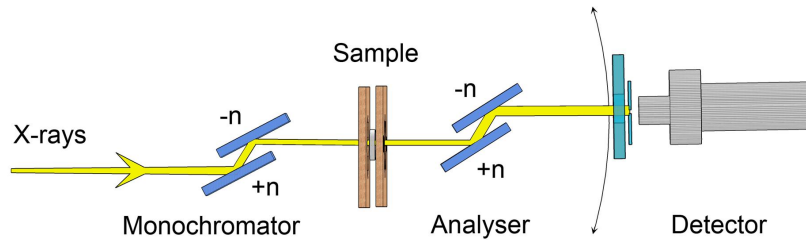
Si(hkl) reflec- tion	Energy (keV)	$\Delta\alpha_{cryst}$ (arcsec)	$\Delta\lambda/\lambda$ ($\times 10^{-6}$)	Coh_L (μm)	Coh_V (μm)
111	8.5	6.5	132.1	1.1	4.6
111	15	3.6	130.7	0.6	4.8
333	15	0.7	8.0	10.3	24.0
400	10.9	2.2	23.5	4.8	10.5
400	12.4	1.9	23.4	4.3	10.8

TABLE 4.2: **Properties of silicon crystals that were used as monochromators and analysers.** Darwin width, $\Delta\alpha_{cryst} = 2\delta_{os}$ (eq. (3.35)), bandwidth, $\Delta\lambda/\lambda$, temporal coherence length, Coh_L (eq. (4.5)), and spatial (transverse) coherence length, $Coh_V = \lambda/\Delta\alpha_{cryst}$ for the silicon crystal reflections, with corresponding energies, used for the experimental results in this thesis (chapter 6), from [Stepanov \(2008\)](#).

energy resolution depends solely on the width of the rocking curve (see eqs. 3.23 and 3.35), and is independent of the divergence of the source ([Authier, 2003](#)).



(a) Single reflection non dispersive TAD setup



(b) Double reflection non dispersive TAD setup

FIGURE 4.7: **Monochromator and analyser crystals in the non-dispersive setting.**

TAD in non-dispersive mode is very sensitive to the 2nd crystal's quality ([Iida and Kohra, 1979](#); [Afanasev et al., 1984](#); [Alexandropoulos and Kotsis, 1985](#)), showing

diffuse scattering from defects in the crystal, which complicates analysis by masking the interesting information about our sample. Hence we must ideally use a perfect analyser crystal to be able to extract information about the sample.

4.2.2 Reciprocal space mapping geometry

The distribution of X-rays diffracted by the sample is recorded as a function of the angular deviation from the exact Bragg positions of the 2nd and 3rd axes, α and $\Delta 2\theta$, indicated in Figure 4.6. When the analyser is set precisely at the Bragg condition, i.e. $\alpha = 0$, and the detector is at the corresponding position of 2θ , i.e. $\Delta 2\theta = 0$, then the scattering vector $\mathbf{Q} = (Q_x, Q_z) = 2\mathbf{k} \sin \theta_B$ (cf. Figure 3.1). The angular deviations are related to reciprocal space coordinates by (Iida and Kohra, 1979)

$$Q_x = (2\alpha - \Delta 2\theta) \frac{\sin \theta_B}{\lambda}, \quad (4.9)$$

and

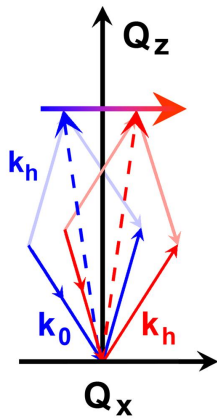
$$Q_z = \Delta 2\theta \frac{\cos \theta_B}{\lambda}. \quad (4.10)$$

There are three main types of scans in TAD that enable one to probe the diffraction plane of the analyser, (Q_x, Q_z) , (Table 4.3), depending on the region of interest. A 2D intensity distribution in reciprocal space, i.e. an RSM, around the Bragg reflection of the analyser, can be collected by collating 1D scans of one of the types described below, with shifts of an alternate scan type between subsequent scans (Iida and Kohra, 1979). The individual 1D scan types are described and illustrated in Table 4.3. Some examples of the region of reciprocal space in the (Q_x, Q_z) plane spanned by the RSMs are shown in Figure 4.8.

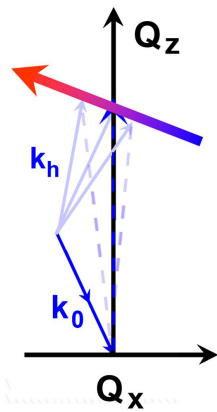
The 1D nature of our data collection is a limitation of our technique, making collecting high resolution RSMs time consuming. The total time for one 2D scan is dependent upon the diffractometer hardware and beam intensity. For example, at BL13XU (§4.1), a 250×250 point scan, spanning $Q_x = \pm 0.06 \text{ nm}^{-1}$, and $Q_z = \pm 0.4 \text{ nm}^{-1}$ (with ~ 0.5 seconds per data point) requires ~ 10 hours, and even a 50×50 point scan over $Q_x = \pm 0.03 \text{ nm}^{-1}$ and $Q_z = \pm 0.08 \text{ nm}^{-1}$ as shown in §6.4, requires 2 hours. However, provided radiation damage, and hence data collection time, is not an issue, the spatial resolution is limited only by the angular range of the RSM, as in conventional Fraunhofer diffraction (Born and Wolf, 1999),

$$\Delta_{res} = \frac{\lambda}{2 \sin \theta_{MAX}}, \quad (4.11)$$

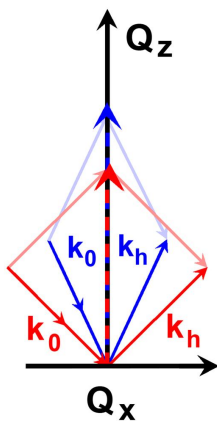
where θ_{MAX} is the maximum angular deviation of the measured intensities.



The rocking curve scan, also called the transverse or α scan, where the analyser is rotated around its Bragg condition by α . This scan is sensitive to mosaicity in the 2nd crystal (the sample, in conventional TAD, or the analyser crystal, in our TAD setup). For small angular deviations, this scan is parallel to the Q_x axis.



The detector ($\Delta 2\theta$) scan, which probes along the Ewald sphere, for a fixed $\alpha = \alpha_0$. When the conditions for a locally flat Ewald sphere are met (cf. eq. (3.19)), this scan is along a straight line inclined by θ_B anticlockwise from Q_z .



The ($\alpha/2\theta$) scan, also called the longitudinal scan: rotating the detector at twice the angular velocity as the analyser probes reciprocal space parallel to Q_z . This scan is sensitive to strain in the crystal on the 2nd axis, which, as stated in the text, is the sample in conventional TAD, or the analyser in our TAD.

TABLE 4.3: **Scan types in triple axis diffractometry.** A combination of one scan type with steps of another scan type in between is used to collate a 2D RSM, as demonstrated in Figure 4.8.

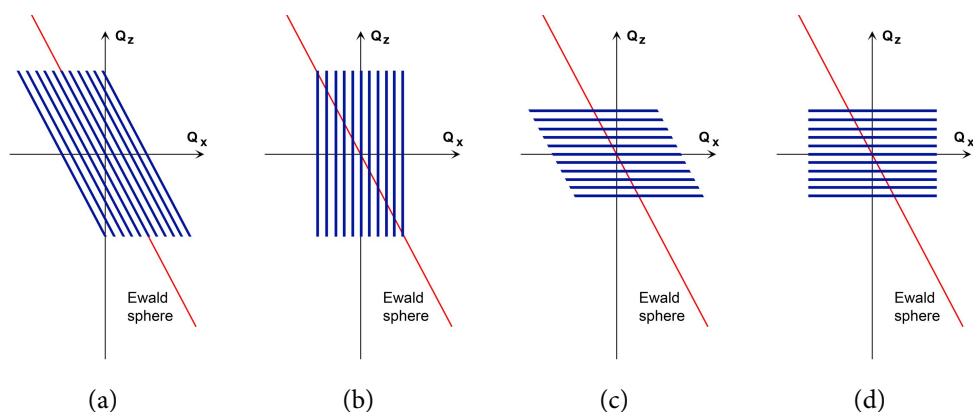


FIGURE 4.8: **Constructing a 2D RSM from 1D scans.** The lines indicate individual 1D scans and thus the order of data acquisition in reciprocal space. (a) Detector scans ($\Delta 2\theta$) at different positions of the analyser (α_0); (b) $\alpha/2\theta$ scans at different positions of the analyser; (c) Analyser scans at different positions of the detector; (d) Analyser scans at different positions of both the analyser and detector, i.e. with shifts of $\alpha/2\theta$ between individual α scans.

4.3 Information content of triple axis diffractometry reciprocal space maps

4.3.1 Triple axis diffractometry instrumental function

A key feature of RSMs obtained by triple axis diffractometry is the instrumental function that arises from the tails of the monochromator rocking curve (Figure 3.7), and a finite slit in front of the detector (Iida and Kohra, 1979; Kotsis and Alexandropoulos, 1987). The deviations of the monochromator rocking curve and the detector slit from delta functions manifest themselves as intensity pseudo streaks. As shown in Figure 4.9, the pseudo streaks are oriented at the Bragg angle of the monochromator, θ_{B_M} , clockwise, and the Bragg angles of the analyser, θ_{B_A} , anti-clockwise, from the Q_z axis, respectively. For the parallel, non dispersive setting previously described, $\theta_{B_M} = -\theta_{B_A}$ (Pietsch *et al.*, 2004).

The elongated intensity streak normal to the surface of the analyser is its crystal truncation rod (cf. §3.2.1) (Robinson, 1986). The finite wavelength bandwidth $\Delta\lambda$ results in a *wavelength streak*, which is along the diffraction vector, \mathbf{Q} , for symmetric reflections. In the non-dispersive configuration, the direction of the wavelength streak depends on the angular divergence of the X-ray source (Gartstein *et al.*, 2001).

The pseudo streaks in the TAD instrumental function can be suppressed by multiple reflections at the monochromator (and analyser, in conventional triple crystal

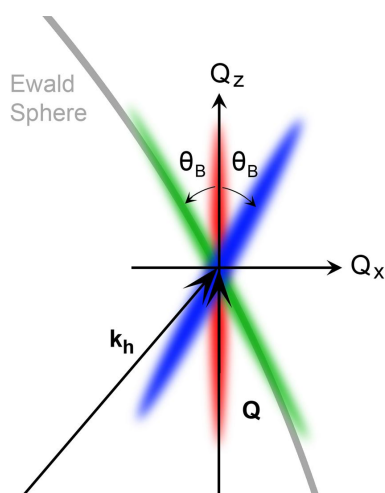


FIGURE 4.9: **TAD instrumental function schematic.** The analyser's crystal truncation rod (CTR) lies along the diffraction vector \mathbf{Q} (in red), which is along the Q_z axis for a symmetric Bragg reflection. The pseudo streak from the monochromator is oriented at θ_B clockwise from Q_z , shown in blue, while the pseudo streak from the finite window of the detector is oriented at θ_B anti-clockwise from Q_z , shown in green.

diffractometry) (§4.2.1), in order to measure diffuse diffraction or significantly simplify data analysis by obviating the need for a complicated deconvolution (DuMond, 1937; Bonse and Hart, 1965; Iida and Kohra, 1979; Zaumseil and Winter, 1982b). Iida and Kohra (1979) used a five-fold reflection from the monochromator to achieve a tailless, low-divergence beam, and Zaumseil and Winter (1982b) demonstrated that different applications required tailored reflection multiplicity at the monochromator and analyser, with correspondingly brighter sources being necessary to counteract intensity suppression.

For this reason, our synchrotron experiments involved the use of a channel cut, double reflection monochromator, and at times, a channel cut, double reflection analyser. The streak arising from the finite slit width of the detector can only be decreased by narrowing the slit, which can also decrease the SNR of the weak signal from the sample or, alternatively, increase the required scan time. Simulated and measured instrumental functions are presented in §5.3.

4.3.2 Fraunhofer diffraction from the sample in the reciprocal space map

In this section we describe the information about the sample that is obtained from the RSM. In §3.2.1 we described the energy/wavelength resolution of a perfect crystal monochromator, and briefly mentioned its critical role in determining the information content of our diffraction data, which we further develop here.

A consequence of the wavelength band pass of the monochromator, derived from the finite width of its rocking curve (cf. eq 3.23), is the finite thickness of the Ewald sphere surface (Fewster, 1991), as shown in Figure 4.10. For clarity only the diffraction plane of the analyser, (Q_x, Q_z) , is shown, and the angles are exaggerated. Recall that we established in §3.1.2, that the intersection of the Ewald sphere with the 3D FT of the scattering potential of the object defines the available region of reciprocal space in which the FT can be measured, which in this case is a spherical shell section.

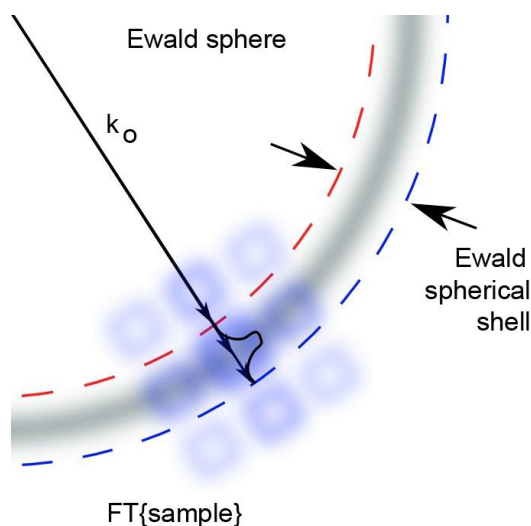


FIGURE 4.10: **Ewald sphere shell defined by the finite wavelength bandwidth of the monochromator.** This reciprocal space schematic shows how wavelength dispersion from the monochromator leads to a finite thickness of the Ewald sphere. The intersection of the Ewald shell and the 3D Fourier transform of the scattering potential of the sample is measured in our experiments.

Diffraction from the analyser can be represented by the addition of the momentum transfer vector \mathbf{Q} to each diffracted vector \mathbf{k}_d comprising the spherical shell section of the 3D FT of the scattering potential of the sample (Figure 4.10). In the RSM these intensities lie along the pseudo streak of the monochromator (Figure 4.11).

Azimuthal rotation of the sample (about the optical axis) results in the identical

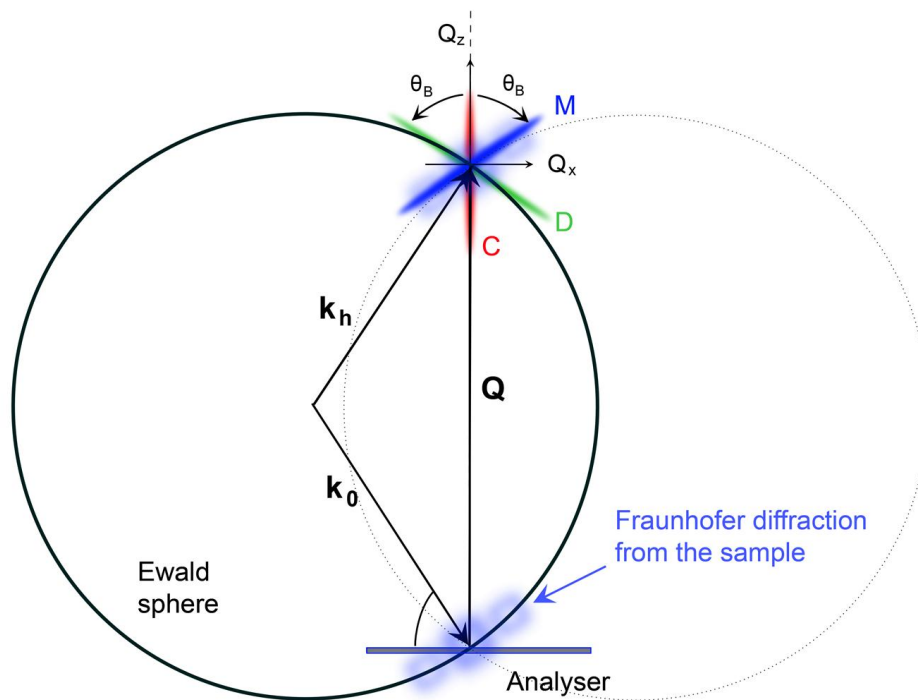


FIGURE 4.11: **Reciprocal space map content.** Diffraction from the analyser crystal results in the addition of the diffraction vector, \mathbf{Q} to the diffracted X-rays emerging from the sample, thus translating the Fraunhofer diffraction on the thick Ewald shell section, around $(0, 0, 0)$, (Figure 4.10) to \mathbf{Q} , where it lies atop the monochromator pseudo streak. The crystal truncation rod from the analyser is shown in red, labelled C. The monochromator and detector pseudo streaks are shown in blue and green, and labelled M and D, respectively.

rotation of its k_x, k_y diffraction plane. However, in reciprocal space mapping with an analyser, a different distribution of diffracted X-rays is brought into the diffraction plane of the analyser (Nikulin *et al.*, 2007). The effect of azimuthal rotation of platelet shaped Al-Cu nanoparticles is explored in the simulations presented in the following chapter.

4.4 Sample holder and heater

The development of a nano-characterisation technique based on reciprocal space mapping with an analyser crystal was carried out over three stages, the details and results of which will be presented in chapter 6. These experiments required a dedicated sample holder and heater to be built for *in situ* studies of nanoparticle development,

which forms the subject of this section.

A preliminary, qualitative study of *in situ*, real-time nanoparticle growth in various Al-Cu alloys was carried out (§6.3), in order to choose an appropriate Al-Cu sample and heat treatment, in which the heating mechanism was tested. We subsequently carried out the first investigation, based on reciprocal space mapping, of *in situ*, real-time growth of embedded nanoparticles in an Al-Cu alloy (§6.4), using the heater.

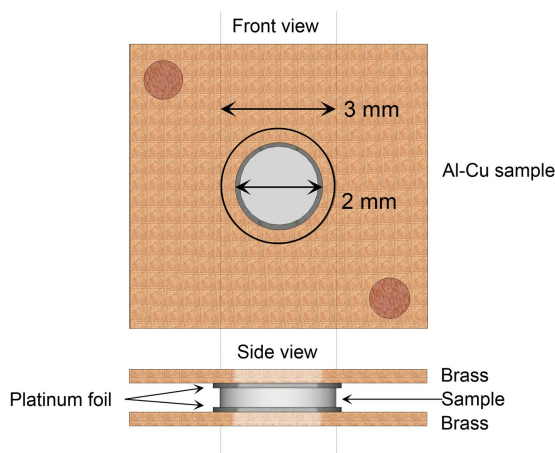


FIGURE 4.12: **Specimen sandwich.** The 3mm Al-Cu disc-shaped samples were sandwiched between two square brass slices with holes (2mm diameter) for the X-ray beam, with a Platinum foil spacer to inhibit contamination of the sample by the brass slices when heated to high temperatures (up to 530°C).

We also needed a sample holder that would allow the orientation of the Al-Cu alloy to be changed easily (see §6.2). As discussed in §2.2.3, the Al-Cu samples were prepared as discs with 3mm diameters, of various thicknesses ($0.41\text{--}1.60 \pm 0.05\text{mm}$), with $(100)_{\text{Al}}$ parallel to the surface. These Al-Cu discs were sandwiched between two slices of brass, each $1 \times 1\text{ cm}$, and $\sim 1\text{mm}$ thick, with a hole for the X-ray beam (2mm diameter) such that the X-rays are normal to the surface (Figure 4.12). The Al-Cu disks were aligned with $(010)_{\text{Al}}$ and $(001)_{\text{Al}}$ parallel to the sides of the square brass slices as reference directions. Samples prepared for the second and third stages of the experimental development were also sandwiched between square brass slices, but with the addition of Platinum foil between the sample and the brass holder in order to minimise potential contamination of the Al-Cu sample by the holder when held at temperatures of $200\text{--}250^\circ\text{C}$ (Figure 4.12), or solution heat treated at $525\text{--}530^\circ\text{C}$. The latter Al-Cu discs did not require specific alignment with the sides of the brass holder.

The holder/heater used for all experiments, shown in Figure 4.13, was built with a

cavity to fit the brass-sample sandwich (Figure 4.12) and allow easy rotation of the sample by 45° about the optical axis. The main component of the heater is a brass body, surrounded by a heating element, attached to a thermally isolating structure with a stainless steel post that can be screwed into a post-holder on the optical bench. The body was made of brass because of its high thermal conductivity, to allow rapid heating and cooling of the sample for *in situ* nanoparticle growth investigations. The sample holder was thermally isolated from the steel post by a layered structure that allowed air to circulate for convective cooling, and ceramic spacers to isolate the bolts and minimise heat conduction (Figure 4.13), also to isolate the holder and hence improve the efficiency of heating, and to help maintain a temperature of $220\text{--}250^\circ\text{C}$ on the sample.

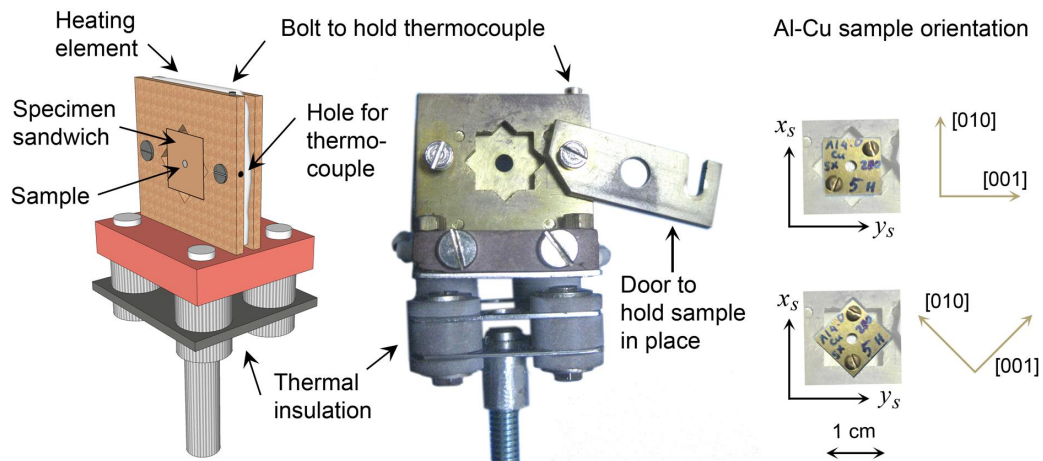


FIGURE 4.13: *In situ* sample heater. Sample holder design and photograph with a schematic showing two orientations of the Al-Cu sample (sandwiched in brass and Platinum foil as shown in Figure 4.12), with one oriented at 45° about the optical axis with respect to the other. The photograph of the heater as built has an extra layer of steel with stone spacers at its base, compared to the design schematic for improved thermal insulation.

The heating element was a Nichrome wire, threaded through an electrically isolating fibreglass and ceramic tubing and wrapped around the main holder (shown in the schematic but not visible in the photograph in Figure 4.13). The thermocouple used was type K (chromel-alumel), chosen for its linear response over a wide temperature range (-200°C to $+1350^\circ\text{C}$) as our *in situ* heat treatments (including solution heat treating) required a range of ~ 20 to $\sim 530^\circ\text{C}$. It was inserted through a $\sim 1\text{mm}$ hole drilled in the holder, and held in place with a bolt from above (labelled in Figure 4.13).

We measured the temperature at different positions on the holder and concluded that after <10 minutes of heating (from room temperature to 220°C), the entire sample holder was indeed uniformly heated by conduction from the brass body. The minute size of the Al-Cu sample itself guaranteed that it too was uniformly heated (only samples with thicknesses of >1mm allowed the thermocouple to be positioned in direct contact with the Al-Cu sample).

A simple proportional-integral-derivative (PID) controller (Ogata, 2009) was used to monitor the temperature and provide the necessary voltage across the Nichrome wire. It could hold a temperature of 220°C with $\pm 5^\circ\text{C}$ fluctuations (with a period of ~ 3 minutes), which is an insignificant fluctuation for the time scales and heat treatments involved in the Al-Cu alloy heat treatments that were investigated (§2.2.2).

4.5 X-ray detectors for reciprocal space mapping with an analyser crystal

Ionisation chambers were sometimes used to monitor the incident X-ray intensity upstream of the sample, but were removed during data collection so as to maximise incident flux. Upon entering an ionisation chamber, X-rays ionise the medium (usually a gas), whereby the resultant ions and electrons create a measurable current that is proportional to the intensity of the X-rays.

For the data collection at ANBF, a Radicon scintillation counter was placed on the 2θ axis, as described in §4.2. When an X-ray or other ionising radiation interacts with a scintillator window, the scintillator material emits visible or UV photons, the number of which is proportional to the energy deposited by the incident radiation. They offer a wide dynamic range (5–7 orders of magnitude), and crude energy discrimination is possible, though the counter was used in single channel mode for all experiments in this project. Mapping X-ray diffraction data in reciprocal space means the resolution of the RSM is determined by the total angular aperture of the detector, as in conventional Fraunhofer diffraction. The motorised movement of the detector allows very high angular resolution (arcseconds), but the data collection is relatively slow due to the need for rotation of the analyser and/or detector for each datum point as explained in §4.2.2.

Both beamlines BL13XU and BL29XU at SPring-8 have a few X-ray detectors available, including scintillation counters, ionisation chambers, and diode detectors.

A silicon PIN¹ photodiode is available at BL13XU, and a PIN diode and an avalanche photodiode are available at BL29XU. A PIN photodiode has an intrinsic dynamic range exceeding 6 orders of magnitude, making it well suited to measuring weak diffraction. An avalanche photodiode can effectively be considered as a PIN diode and photomultiplier, combined.

4.6 Summary

In this chapter we presented the particulars of the experimental setup for analyser based reciprocal space mapping of diffraction from embedded nanoparticle ensembles. We began by considering the ideal X-ray beam characteristics, in particular high brilliance, that is necessary to be able to record the weak diffraction pattern from such nanoparticles. We discussed the three synchrotron beamlines at which the availability of high angular resolution diffractometers allowed the experimental technique development to be carried out, the results of which will be presented in chapter 6. The setup of triple axis diffractometry was discussed in detail, including the ideal crystals for monochromating and analysing the beam, as well as the scanning geometry in reciprocal space. We closed the experimental setup chapter with a brief look at appropriate X-ray detectors for analyser based reciprocal space mapping.

In the following chapter we discuss the various stages of simulating diffraction from weakly diffracting nanoparticles embedded in Al-Cu samples, including Fraunhofer diffraction (and nanoparticle reconstruction) and reciprocal space mapping.

¹A PIN diode is thus named due to the intrinsic layer between the p-type and n-type semiconductors.

Simulations of X-ray diffraction from ensembles of nanoparticles

In this chapter we describe the simulation of diffraction patterns (in order of increasing complexity) from ensembles of weakly diffracting, embedded nanoparticles in a bulk material Al-Cu sample. We consider the optical path of the X-rays in five stages, as labelled in Figure 5.1.

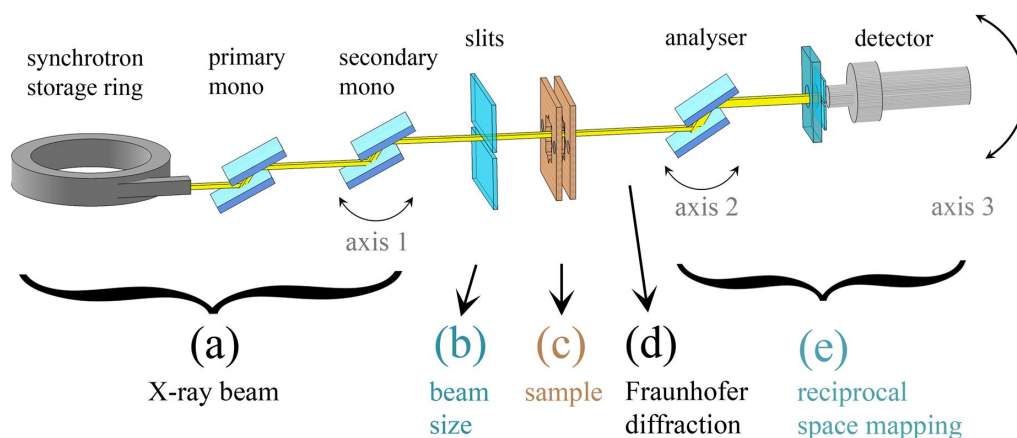


FIGURE 5.1: **X-ray optical path from source to detector in five stages.** The experimental setup is broken up into these five stages for consideration in the simulation of X-ray diffraction from embedded nanoparticle ensembles. Stage (a) includes the synchrotron X-ray source, and the primary monochromator of the beamline, as well as the secondary monochromator that rotates around the first axis in triple axis diffractometry. Stage (b) is the beam defining slit; stage (c) is the sample, which contains an ensemble of weakly diffracting embedded nanoparticles; stage (d) is a virtual stage representing the far field of the sample, and simulation stage (e) involves the reciprocal space mapping, which corresponds to the roles of the analyser and detector in our experimental setup.

The first stage, labelled (*a*) in Figure 5.1, includes the X-ray source, a synchrotron X-ray source with high brilliance as described in §4.1, the primary beamline monochromator (cf. §4.1.1) and the secondary monochromator, positioned on the first axis of the non-dispersive triple axis diffractometry (TAD) setup (described in §4.2). As both monochromators are high quality, double-reflection Si crystals (described in §4.2.1), for the purposes of this simulations chapter, the resultant beam was considered to be perfectly monochromatic. In addition, the low divergence intrinsic to synchrotron undulator X-ray sources allows us to assume the beam is planar at the entrance to the optics hutch (Mocella *et al.*, 2000), so the beam was assumed to be ideally planar and monochromatic, i.e. fully coherent.

The second stage, labelled (*b*) in Figure 5.1, is the beam defining slit, which was varied in the experiments between $0.20 \times 0.20\text{mm}^2$ (vertical \times horizontal) and $0.25 \times 1.50\text{mm}^2$ (v \times h), and for most of the experimental results in the following chapter the beam was $0.25 \times 1.00\text{mm}^2$ (v \times h). This beam size was chosen so that it was sufficiently large to illuminate a sample volume representative of the bulk material, and to achieve sufficient beam intensity. However, despite the relatively large beam size involved, for any single Fraunhofer diffraction pattern simulation we need only consider the transverse coherence lengths, which will be explained further in §5.1.2.

The third stage, labelled (*c*) in Figure 5.1, is the sample. A detailed description of the embedded nanoparticle ensemble morphology and typical size distributions in the range of samples examined in this thesis was presented in §2.2.1. In this chapter we apply the theory presented in chapter 3 to a discussion of the limitations of the first Born and projection approximations for particular nanoparticle sizes and orientations with respect to the beam propagation direction. For this discussion we only consider typical or extreme parameters, whichever is more appropriate to illustrate the applicability of the approximation.

Stage (*d*) in Figure 5.1 is sufficiently in the far field to give the Fraunhofer diffraction pattern from such samples, based on the kinematical X-ray diffraction discussions in chapter 3. Stage (*d*) will be presented in two parts, the first involving a description of how to calculate the Fraunhofer diffraction pattern from a bulk material ensemble of embedded nanoparticles taking into consideration the relative sizes of the illuminated sample volume and the much smaller coherence lengths (§5.1). In the second part (§5.2) we will demonstrate how quantitative size information about the ensemble is encoded in the nanoparticle reconstruction from a simulated diffraction pattern comprised of an incoherent sum of Fraunhofer diffraction patterns. The details of the reconstruction method, based on the iterative hybrid input-output algorithm (HIO),

will also be discussed (§5.2.1).

The fifth stage, labelled (*e*) in Figure 5.1, involves simulations of analyser based reciprocal space mapping (RSM), wherein the roles of the 2nd and 3rd axes (which are coincident but independent), the analyser and detector in our TAD setup, are combined. Simulated and experimentally measured triple axis diffractometry instrumental functions, which were introduced in §4.3.1, are herein compared. In §5.3 we present the results of simulated two dimensional (2D) RSMs of diffraction from ensembles of embedded nanoparticles in a bulk Al-Cu alloy. In these simulations we investigate the effects of nanoparticle size distributions, as well as rotation of the anisotropic Al₂Cu nanoparticles about the optical axis, so that we may interpret the experimental investigations of these properties in chapter 6. These simulation results demonstrate that quantitative information about the bulk material nanoparticle ensemble is obtainable from narrow regions in reciprocal space, or in the limiting case, even from specific 1D scans. Experimentally, this has implications for expediting data collection and thus enabling, for example, the investigation of real-time dynamic changes in the sample, *in situ*, at a time scale defined by a single scan (on the order of 5 minutes). These implications are discussed further in the following chapter.

5.1 Simulation methodology for X-ray diffraction from embedded nanoparticle ensembles

Our discussion of the approach to simulating diffraction from embedded nanoparticle ensembles begins with stage (*c*) as described in the previous section, i.e. considerations of the X-ray interactions with the sample. In the above descriptions of stages (*a*) and (*b*) we explained that the beam is assumed to be plane and monochromatic, and the beam size will play a minor role in the Fraunhofer diffraction patterns from the sample, which will be discussed in §5.1.3.

In §3.1 we described two widely used approximations in X-ray diffraction theory: kinematical diffraction using the first Born approximation, and the projection approximation. In order to develop an appropriate approach to simulating X-ray diffraction from materials that contain embedded nanoparticles, we must ascertain when these approximations are applicable, especially since they greatly simplify simulation and interpretation of experimental data.

The age-hardened Al-Cu samples contain ensembles of embedded Cu or Al₂Cu nanoparticles whose size and size distribution depend on the heat treatment tempera-

ture and time (see chapter 2). Generally, such samples held at higher temperatures for longer periods result in larger nanoprecipitates. The number density of the particles depends on the Cu concentration and ageing conditions. Usually there is a very high number density of small particles if the sample is aged at low temperatures (details in §2.2.2), and there is a trade off between number density and particle size with continued sample ageing. A typical sample investigated by our technique is an 0.65 ± 0.05 mm thick Al-2.0wt% Cu single crystal containing platelet-shaped Al_2Cu nanoparticles (§2.2.1). After heat treatment at 200°C for 48 hours, the nanoparticle diameters qualitatively follow a Boltzmann shaped distribution. The modal (most commonly occurring) particle has a diameter of ~ 370 nm, and a thickness of ~ 6 nm, with the tail of the distribution representing a low number of larger particles. The spatial distribution of the embedded nanoparticles was assumed to be homogeneous, based on 24 transmission electron micrographs,¹ covering a volume of $\sim 12.4 \mu\text{m}^3$, from which the number density was calculated to be ~ 12 particles/ μm^3 . One of these micrographs, viewed along the $\langle 100 \rangle_\alpha$ zone axis, is shown in Figure 5.2. To reiterate from §2.2.1: the Al_2Cu platelets grow along three orthogonal directions, $\langle 100 \rangle_{\text{Al}}$, so two orientations of nanoparticles are visible edge-on in this micrograph. For the following discussion we presume the alignment is such that the optical axis, z , coincides with the $\langle 100 \rangle_\alpha$ zone axis, and the platelet faces are oriented normal to the x_s , y_s , and $z_s = z$ directions, as shown in Figure 5.3.

5.1.1 Limits of the first Born approximation for embedded Al-Cu nanoparticles

Nanoparticles that naturally form embedded in materials often have a refractive index very close to that of their surrounding host matrix, which results in low diffraction and absorption contrast. For the typical sample described above, the refractive index decrement is

$$\Delta\delta = \delta_{\text{Al}_2\text{Cu}} - \delta_{\text{Al}} , \quad (5.1)$$

$$\Delta\mu = \mu_{\text{Al}_2\text{Cu}} - \mu_{\text{Al}} . \quad (5.2)$$

¹The TEM micrograph in Figure 5.2 was provided courtesy of Dr. Brian Gable, then employed by the Department of Materials Engineering at Monash University. The preparation of the samples (as described in §2.2.2 and §2.2.3) was carried out for this particular sample by Dr. Gable and the author, and the statistical analysis of the nanoparticle TEM micrographs was carried out by the author. Other Al-Cu samples were prepared with the help of Dr. Colleen Bettles, also at the Department of Materials Engineering, Monash University.

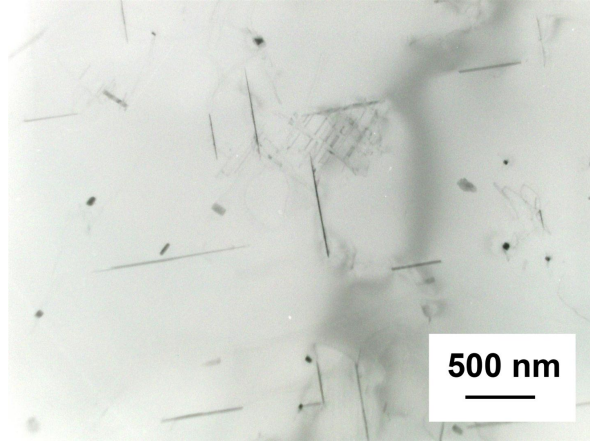


FIGURE 5.2: $\langle 100 \rangle_\alpha$ zone axis TEM micrograph of an Al-2.0wt% Cu sample aged at 200°C for 48 hours. The diameters of the Al₂Cu nanoprecipitates in this sample qualitatively follow a Boltzmann distribution, with a modal diameter of 370nm. This is an example of a typical sample used in the development of the X-ray nano-characterisation technique presented in this thesis. Details about the precipitates seen here were presented in chapter 2. TEM was carried out on a Philips CM20 instrument operated at 200 keV.

For the modal nanoparticles, the accumulated phase shift, ϕ , and attenuation, μ , are (cf. eq. 3.15):

$$\phi = -k \int \Delta\delta dz \approx 5.8 \times 10^{-2}, \quad (5.3)$$

$$\mu = k \int \Delta\beta dz \approx 6.7 \times 10^{-3}, \quad (5.4)$$

where we considered the particle orientations that have their biggest dimension (their ~ 370 nm diameters) aligned along z (lime, labelled (2), and dark blue, labelled (3) in Figure 5.3). Here, the X-ray wavelength $\lambda = 1.0 \text{ \AA}$, $|\Delta\delta| \approx 6.04 \times 10^{-6}$ and $|\Delta\beta| \approx 3.14 \times 10^{-7}$, based on values taken from Stepanov (2008). The use of the first Born approximation is warranted here as for this typical sample $|\phi| \ll 1$ and $|\mu| \ll 1$ (§3.1.1).

5.1.2 Limits of the projection approximation for embedded Al-Cu nanoparticles

In this section we establish the limits of the projection approximation for embedded Al-Cu nanoparticles in various orientations. In §3.1.2 we discussed that the projection approximation may be used if

$$L_{PA} < d \quad (5.5)$$

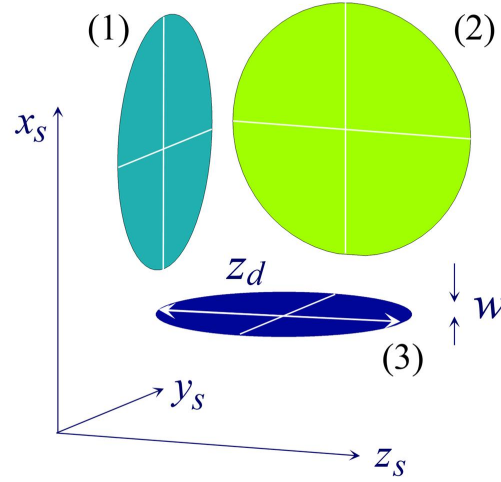


FIGURE 5.3: **Model of three orthogonal Al_2Cu nanoprecipitates.** The approximately platelet-shaped precipitates that naturally grow along three orthogonal directions in an Al-Cu crystal (the $\langle 100 \rangle_{\text{Al}}$ planes) are shown here modelled as idealised platelets with dimensions identified.

where d is now the dimension of the particle transverse to the X-ray beam, and

$$L_{PA} = \sqrt{\frac{\lambda T}{2}}, \quad (5.6)$$

where T is the thickness of the sample in the z direction and λ is the wavelength. This is a reiteration of eq. (3.19). The diffraction plane of the analyser crystal, (x_c, z_c) , is parallel to the sample plane (x_s, z_s) , rotated clockwise by θ_B . The high aspect ratio of the nanoparticles means that they subtend different orientations when rotated about the optical axis, and hence yield orientation-dependent diffraction contrast.

The orientation of nanoparticles that would result in the weakest contrast in the diffraction plane are those with their faces normal to z (and hence with the smallest projected thickness), colored in dark aqua and labelled (1) in Figure 5.3. The projection approximation validity condition (eq. (5.5)) is readily satisfied for the range of wavelengths used in the experiments discussed in this thesis, which was $\lambda \in (0.083\text{--}0.146\text{nm})$. For particle labelled (1) using $\lambda = 0.083\text{nm}$, $T = |w| = 6\text{nm}$ and $d = |z_d| = 370\text{nm}$,

$$L_{PA} = \sqrt{\frac{0.083 \times 6}{2}} \approx 0.5\text{nm} \quad (5.7)$$

and for $\lambda = 0.146\text{nm}$,

$$L_{PA} = \sqrt{\frac{0.146 \times 6}{2}} \approx 0.7\text{nm}, \quad (5.8)$$

which both readily satisfy the projection approximation validity condition.

The highest diffraction contrast in the diffraction plane would be obtained from those nanoparticles that are oriented with their faces normal to the x direction and diameter parallel to z (the blue particle, labeled 3 in Figure 5.3). Now $d = 6\text{nm}$ and $r_z = 370\text{nm}$, so the condition in eq. (5.5) is still satisfied for $\lambda = 0.83\text{\AA}$ where $L_{PA} = 0.4\text{nm}$, and only just satisfied for $\lambda = 1.46\text{\AA}$, as $L_{PA} = 5\text{nm}$. This limits the use of the projection approximation to the projected thickness of approximately a single nanoparticle in this orientation. This result is very restrictive, and needs to be taken into account when simulating diffraction from a large ensemble of embedded nanoparticles in Al-Cu, as discussed in the next section. It also indicates that if simulations based on the projection approximation are to be compared with experimental data then X-ray energies greater than 8 keV should be used.

5.1.3 Simulating Fraunhofer diffraction patterns from large ensembles of weakly diffracting Al-Cu nanoparticles

Having confirmed the validity of the first Born approximation for diffraction from embedded nanoparticles in an Al-Cu alloy, and determined the limits of the projection approximation, let us now consider how that relates to Fraunhofer diffraction from a large ensemble of embedded nanoparticles, labelled stage (d) in Figure 5.1. We can simulate the total diffracted intensity from a large illuminated volume as an incoherent sum of diffracted intensities from individual coherence volumes (defined in §4.1.2), within which the intensities are calculated using the first Born approximation (§3.1.1). Given the restrictions discussed in the previous paragraph, we can either simulate smaller volumes limited in depth by the diameter of a single nanoparticle and use the projection approximation, or simulate the entire coherence volume without applying the projection approximation, both of which are discussed below.

Firstly we consider using the projection approximation. In simulation we can section the sample into slices perpendicular to the z direction, whose thickness is limited to the maximum diameter of a single nanoparticle, i.e. $\Delta z \approx z_d$. The transverse coherence length is dependent upon the source characteristics (see eq. 4.3), and for the purpose of demonstration, we will use a value of $4.6\mu\text{m}$, which corresponds to using a Si(400) monochromator with 10.9 keV X-rays (Table 4.2). Figure 5.4 shows a schematic of the volume of an Al-Cu sample that is illuminated by the X-ray beam. The emphasised region of the sample is bounded in (x_s, y_s) by the transverse coherence length and has depth limited by z_d . The Fraunhofer diffraction pattern

from this emphasised volume is proportional to the 2D Fourier transform (FT) of its transmission function, $t(x_s, y_s)$, as was defined in eq. (3.16).

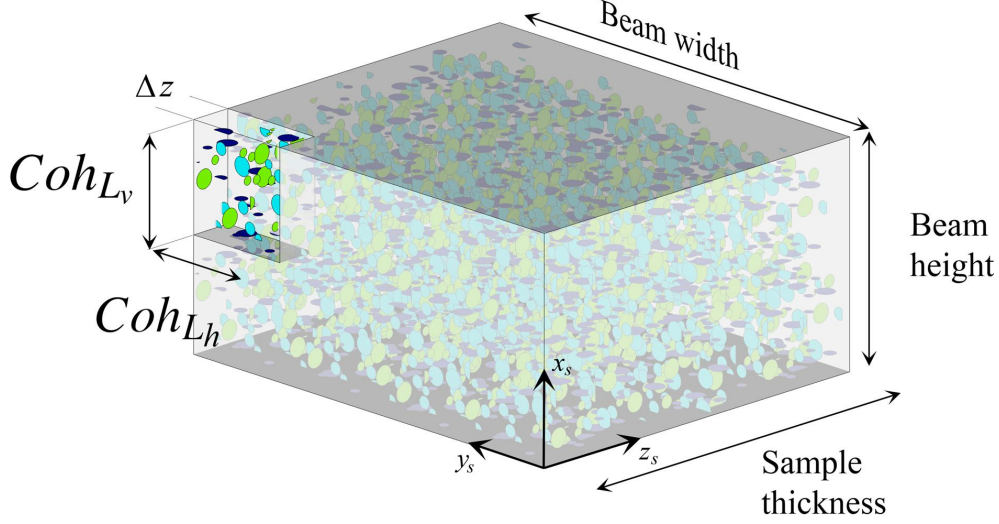


FIGURE 5.4: **Sample volume that contributes coherently to the Fraunhofer diffraction pattern.** The entire illuminated sample volume, encompassing an ensemble of embedded nanoparticles representative of the bulk material, is defined by the beam cross section and sample thickness. The volume defined by the transverse coherence, Coh_L , and approximately the diameter of a single nanoparticle, $\Delta z \approx z_d$ is emphasised. The total Fraunhofer diffraction pattern from the entire illuminated sample volume is comprised of an incoherent sum of Fraunhofer diffraction patterns from the individual regions, as expressed by eq. (5.9).

The resultant 2D Fraunhofer diffraction pattern from the entire illuminated sample volume is an incoherent sum of Fraunhofer diffraction patterns from such volumes, independent of their relative positions in the entire illuminated sample volume:

$$\begin{aligned}
 I(k_x, k_y) &= \sum_{\text{Beam width}} \sum_{\text{Beam height}} \sum_{\text{Sample thickness}} \left| \widetilde{\mathcal{F}}_{\perp} \{t(x_s, y_s)\} \right|^2, \\
 &= \sum_{\text{Beam width}} \sum_{\text{Beam height}} \sum_{j=0}^m \left| \widetilde{\mathcal{F}}_{\perp} \left\{ \int_{z_j}^{z_{j+1}} 1 + ik(-\delta(\mathbf{r}) + i\beta(\mathbf{r})) dz \right\} \right|^2, \quad (5.9)
 \end{aligned}$$

where $\widetilde{\mathcal{F}}_{\perp}$ signifies the 2D Fourier transform (eq. (3.17)), $|z_{j+1} - z_j| = \Delta z \approx z_d$ as shown in Figure 5.4, k is the X-ray wavenumber, $t(x_s, y_s)$ is the transmission function for a weakly diffracting object (eq. (3.15)), and the summations are over the transverse dimensions of the X-ray beam, and the thickness of the sample, i.e. $|z_m - z_0| = \text{sample thickness}$. For such a weakly scattering sample, this is justified. The method of using

summed volumes also proved more practical computationally and was implemented for §5.2.

If the particles are identical and randomly distributed on a 2D plane (which is equivalent to limiting the depth in z to one nanoparticle diameter as just discussed), the diffraction intensity, $I(k_x, k_y)$, would be the product of an individual particle's diffraction pattern and the distribution's statistical expectation (Lipson *et al.*, 1995),

$$I(k_x, k_y) = [N + N^2 \bar{\delta}(k_x = 0, k_y = 0)] \left| \widetilde{\mathcal{F}}_{\perp} \left\{ \int_{z_0}^{z_{ES}} 1 + ik(-\delta(\mathbf{r}) + i\beta(\mathbf{r})) dz \right\} \right|^2 \quad (5.10)$$

where N is the number of particles, $\bar{\delta}$ is a delta function at the origin, and z_0 and z_{ES} are the entrance and exit surfaces of a single nanoparticle, respectively (see Figure 3.2). Thus the signal would be strengthened by the number of particles illuminated (Nikulin *et al.*, 2007). However, naturally grown embedded nanoparticles may not be monodisperse, so this exact expression is not always applicable. For Al-Cu alloys a nearly monodisperse ensemble is achievable if the microstructure consists of very small nanoparticles (i.e. GP zones and the θ'' phase), but the ensemble tends to become polydisperse with further ageing.

Alternatively, the entire coherence volume can be used to calculate the Fraunhofer diffraction pattern, wherein the incoherent sum of diffraction patterns from individual coherence volumes yields

$$I_{\text{CohVol}}(k_x, k_y) = \sum_{\substack{\text{Beam} \\ \text{width}}} \sum_{\substack{\text{Beam} \\ \text{height}}} \sum_{j=0}^m \left| \widetilde{\mathcal{F}}_{\perp} \left\{ \int_{z_j}^{z_{j+1}} [1 + ik(-\delta(\mathbf{r}) + i\beta(\mathbf{r}))] \exp(-iQ_z z') dz \right\} \right|^2, \quad (5.11)$$

where $z_{i+1} - z_i = \Delta z \simeq \text{Coh}_L$. In eq. (5.11) the 3D FT of the scattering potential of the coherence volume is calculated on the surface of the curved Ewald sphere (§3.1.2), up to the chosen angular deviation, determined from the required spatial resolution (cf. §4.2.2).

The assumptions made in the incoherent summation of diffraction patterns from the individual sample volumes, whether using the projection approximation or the longitudinal coherence length (eqs. (5.9) and (5.11), respectively), are that the X-rays diffracted in one volume, $z \in [z_i, z_{i+1}]$, do not interfere with those from another, nor are the X-rays diffracted more than once while propagating through the thickness of the whole sample. For such a weakly diffracting sample (see §5.1.1) this is justified.

It would seem from this approach that a thicker sample, and thus a greater number of similar nanoparticles contributing to the diffraction pattern, is advantageous over a thinner sample. However, we have neglected absorption by the entire sample, which

would exacerbate the low SNR from such weakly diffracting nanoparticles. A simple relationship representing the compromise between the collective diffracting power (i.e. the product of the number of nanoparticles and their individual diffracting power) and the overall beam attenuation due to sample thickness, is given by

$$I \propto N_{\text{particles}} P_{\text{diff}} \exp(-\mu t_{\text{sample}}) \quad (5.12)$$

where $N_{\text{particles}}$ is the number of diffracting particles, P_{diff} is the diffracting power per particle, μ is the linear attenuation coefficient and t_{sample} is the sample thickness. In an ideal sample with a monodisperse, homogeneous nanoparticle ensemble, $N_{\text{particles}} \propto t_{\text{sample}}$, and eq. (5.12) has a profile as shown in Figure 5.5.

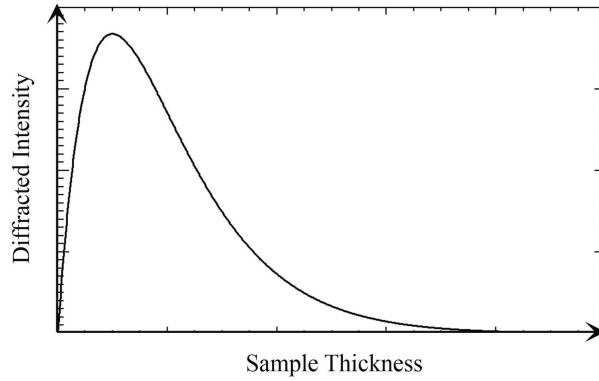


FIGURE 5.5: **X-ray intensity diffracted by a sample with embedded nanoparticles.** In an ideal sample with a monodisperse homogeneous nanoparticle ensemble, the diffracted intensity is proportional to the number of nanoparticles involved in the diffraction and the negative exponent of the sample thickness (i.e. absorption) as in eq. (5.12).

Each Al-Cu sample with a particular microstructure thus has a certain thickness that results in the maximum diffraction signal from the nanoparticles. We will see evidence of this relationship in the experimental RSMs in §6.2. This optimum thickness could be experimentally estimated provided a sufficient number of statistically identical samples (i.e. comprising the same microstructure) of various thicknesses, with identical orientations with respect to the diffraction plane, were available.

If during sample ageing the nanoparticle number density increases (while the sample thickness is constant) then the relationship between $N_{\text{particles}}$ and t_{sample} changes. In this case the optimal thickness remains the same and the diffraction signal from the nanoparticles increases. The ageing process may continue into and beyond the Ostwald ripening stage (see §2.2.2) wherein the number of nanoparticles eventually decreases as the bigger ones grow at the expense of smaller particles. The individual

nanoparticles' diffracting power thus increases due to their increase in volume, and the optimal sample thickness for maximum diffraction contrast again remains unchanged. This means an *in situ*, real-time nanoparticle growth investigation could also be optimised for maximum diffraction contrast.

5.1.4 Simulations of Al-Cu nanoparticle ensembles with various size distributions

We previously discussed that the microstructure in an Al-Cu alloy, i.e. the shape, density, size and spatial distribution of embedded nanoprecipitates, determines its physical properties (§2.2). As the technique being developed in this thesis is aimed at characterisation of such samples by investigating a bulk material sample, it is important to understand what quantitative information about the ensemble we can obtain from the Fraunhofer diffraction patterns of large ensembles of embedded nanoparticles. To this end, the formalism described in the previous section (2D Fraunhofer diffraction patterns obtained by using the projection approximation, as described by eq. (5.9)), was used to simulate Fraunhofer diffraction patterns of large ensembles of Al₂Cu nanoparticles embedded in an Al matrix. The weakly diffracting nanoparticle array corresponding to a sample volume defined by the transverse coherence lengths and the thickness of a single nanoparticle, as highlighted in Figure 5.4, was modelled as a binary object with corresponding refractive indices for the nanoparticles and surrounding matrix. Each sample function was a spatially random distribution of 10–20 orthogonally oriented platelet shaped θ' nanoparticles (§2.2 and Fig. 5.6(a)), whose range of diameters was described by a Gaussian distribution,

$$D = \frac{1}{\sigma \sqrt{2\pi}} \exp \left\{ -\frac{(d_{nano} - S_m)^2}{2\sigma^2} \right\}, \quad (5.13)$$

where d_{nano} is the nanoparticle diameter, S_m is the mean nanoparticle diameter, and σ is the standard deviation. Samples comprised of nanoparticle ensembles with $S_m = 300\text{nm}$ and $S_m = 400\text{nm}$ were simulated, separately, where σ was varied from 1 to 180nm. An example of a simulated 2D array of the projected thickness of embedded Al₂Cu nanoparticles is shown in Figure 5.6, where the ensemble is normally distributed with $S_m = 400\text{ nm}$ and $\sigma = 180\text{nm}$.

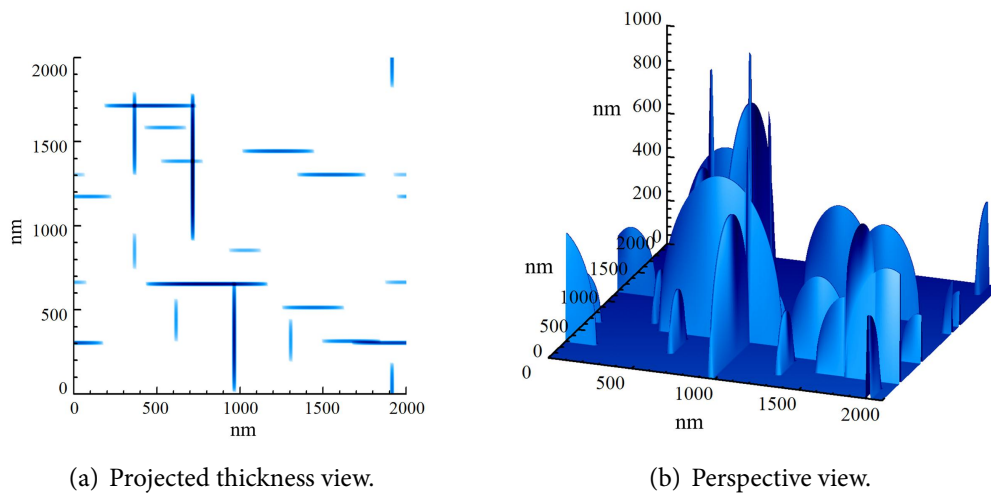


FIGURE 5.6: **Simulated projected thickness of Al_2Cu nanoparticles in an Al-Cu sample.** The ensemble of randomly positioned orthogonal nanoparticles has a mean diameter of $S_m = 400\text{nm}$ and $\sigma = 180\text{nm}$. The Fraunhofer diffraction patterns of 200 such statistically similar arrays were incoherently added to model the Fraunhofer diffraction pattern of a sample volume much greater than a single coherence volume.

5.1.5 Practical considerations for computing Fraunhofer diffraction patterns from large sample volumes

Simulations of the sample and its Fraunhofer diffraction patterns were carried out using IDL 6.4 (ITT Visual Information Solutions). From a practical perspective, the restrictions on array size due to limited random access memory impose a harsh compromise between simulated volume and spatial resolution and/or computing time. The first approach discussed above (eq. (5.9)), using the projected thickness of smaller sample volumes, whose Fraunhofer diffraction patterns are incoherently added, is significantly simpler computationally than the approach without the projection approximation. Including the nanoparticles over the entire longitudinal coherence volume, beyond the applicability of the projection approximation, as described by eq. (5.11), involves the 3D FT of the scattering potential of the object sampled on a curved Ewald sphere (cf. §3.1.2). Computationally this requires 3D double precision complex arrays and nonlinear sampling considerations to account for the Ewald sphere curvature, which is an unnecessary complication in our case since the first Born and projection approximations are indeed applicable.

The 2D FT was numerically implemented using the Fast Fourier Transform (FFT), which is a fast implementation of the Discrete Fourier Transform (Press *et al.*, 2007).

In order to avoid artifacts from the sharp cut-off of the transmission function of the object at the edge of the array, the nanoparticle arrays were simulated with periodic boundary conditions.

We anticipated that it would not be necessary to involve the entire illuminated sample volume in the simulation of Fraunhofer diffraction from such samples when using the projection approximation (as expressed by eq. (5.9)). To demonstrate this, consider an X-ray beam size of $0.10 \times 0.10 \text{ mm}^2$ ($v \times h$). For a sample with a thickness of 0.50 mm this beam illuminates an approximate volume of $5 \times 10^6 \mu\text{m}^3$, which would involve 2.5×10^6 sample sections (assuming a transverse coherence length of $2 \mu\text{m}$ in both x and y , and a maximum nanoparticle diameter of 500 nm). In Figure 5.7 we compare the simulated diffraction pattern from one realisation of a sample section (such as that in Figure 5.6), with diffraction patterns comprising of a normalised incoherent superposition of 10, 200 and 2.5×10^6 Fraunhofer diffraction patterns. Each of the coherent Fraunhofer diffraction patterns was obtained by taking the FT of a 2D transmission function (§3.1.2). The speckle that carries information about the relative positions of the nanoparticles is clearly visible in Figure 5.7(a) where a single model sample was used (such as that shown in Figure 5.6). This speckle is still evident in Figure 5.7(b), which is comprised of an incoherent sum of 10 Fraunhofer diffraction patterns from different realisations of 2D arrangements of the nanoparticles. However, the speckle fluctuations fall to $<1\%$ of the signal (see Figure 5.7(c)) when 200 such Fraunhofer diffraction patterns are incoherently added, and are completely smoothed out when 2.5×10^6 patterns are summed (Figure 5.7(d)).

We confirmed that 200 simulated sample sections is sufficient by demonstrating (in the following section) that simulating the incoherent sum of 2.5×10^6 Fraunhofer diffraction patterns from small ensembles of nanoparticles provides no improvement in the reconstructed nanoparticle profiles nor in convergence of the reconstruction algorithm.

5.2 Nanoparticle reconstructions from simulated Fraunhofer diffraction patterns of polydisperse nanoparticle ensembles

This section describes the second part of simulation stage (d) in Figure 5.1, wherein we present the results of an investigation into the influence of nanoparticle size polydispersity on the Fraunhofer diffraction patterns from large ensembles, and more

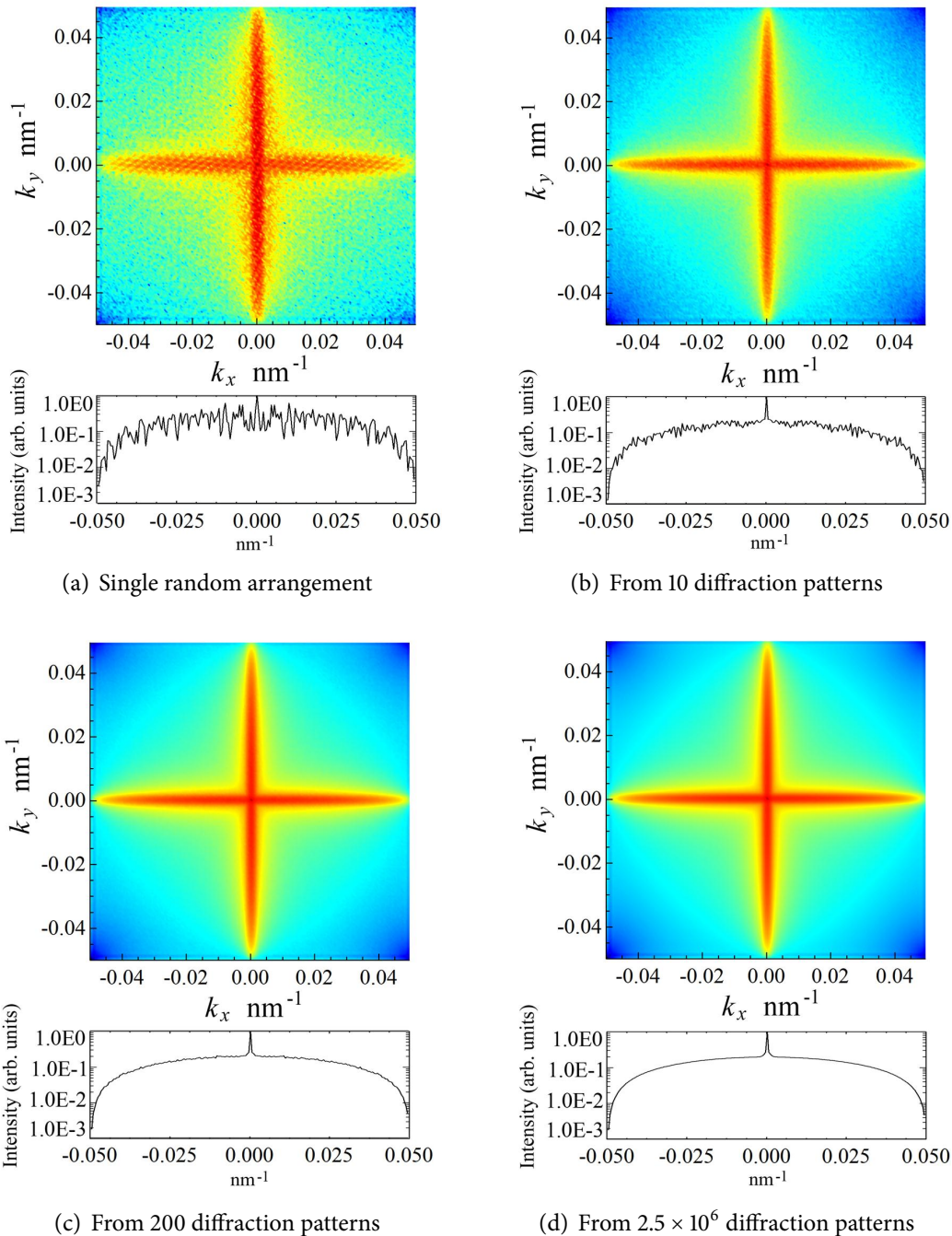


FIGURE 5.7: **Simulated Fraunhofer diffraction patterns from arrays of randomly arranged Al_2Cu nanoparticles.** A single realisation of randomly arranged orthogonal platelet nanoparticles was used for the diffraction pattern in (a), while (b), (c) and (d) are comprised of the incoherent sum of 10, 200 and 2.5×10^6 Fraunhofer diffraction patterns, with corresponding 1D profiles at $k_y = 0$ shown below. The intensities are shown on a log scale. The interparticle interference effects, manifested as speckle in the Fraunhofer diffraction pattern, are smoothed out when a sufficient number of diffraction patterns from random sample section arrays are incoherently added as described by eq. (5.9).

importantly, on the reconstructed nanoparticles. These nanoparticles are iteratively reconstructed from simulated Fraunhofer diffraction patterns from a large sample volume, obtained from the incoherent addition of Fraunhofer diffraction patterns from small sample volumes within which the projection approximation is valid, as was described by eq. (5.9).

5.2.1 The hybrid input-output iterative image reconstruction algorithm

In this section we discuss an iterative image reconstruction method that forms an integral part of the nano-characterisation technique presented in this thesis: the hybrid input-output (HIO) algorithm (Figure 5.8) (Gerchberg and Saxton, 1972; Fienup, 1982).

The Gerchberg and Saxton (1972) algorithm was originally invented to retrieve the phase from two intensity measurements, by iterating between the real-space and Fourier domains while imposing constraints (the measured intensities in each domain). Coherent diffractive imaging (CDI) owes much of its success to the principle of iterative Gerchberg-Saxton phase retrieval algorithm. For the most simple scenario in iterative phase retrieval, the reciprocal space constraint is the square root of the measured intensity. The constraint in real space is a finite support, or a region within which the sample is assumed to exist (i.e. the electron density is positive), surrounded by a zero-density region. Provided the zero-density region is at least twice the size of the support, the phase can be retrieved (Miao *et al.*, 1998). This corresponds to sampling at a spacing finer than the Nyquist frequency, or oversampling (Bates, 1982; Miao *et al.*, 2000). For two and three dimensional diffraction data sets, oversampling need not be double the Nyquist frequency in each dimension (Millane and Stroud, 1997; Miao *et al.*, 1998), as the phase problem is underdetermined by a factor of 2 given the magnitude of a Fourier transform sampled at the Bragg-peak frequency.

Fienup (1978, 1982) generalised and improved the rate of convergence of the original Gerchberg-Saxton algorithm in the HIO algorithm, presented in Figure 5.8. In Figure 5.8 the parameter ξ is a positive constant, $\xi \in (0, 1)$, that governs the level of feedback in the system, and γ represents the set of points at which $g'_k(x, y)$ (the next estimate of the object function) violates the real space constraints, either by being outside the support, or by having a negative value within the support (Miao *et al.*, 1999). In the simpler error reduction algorithm (ER) (Fienup, 1978), the next estimate of the object function, $g_{k+1}(x, y)$, in Figure 5.8 is replaced with

$$g_{k+1}(x, y) = \begin{cases} g'_k(x, y), & (x, y) \notin \gamma \\ 0, & (x, y) \in \gamma, \end{cases} \quad (5.14)$$

and in the input-output (IO) algorithm, the next estimate is

$$g_{k+1}(x, y) = \begin{cases} g_k(x, y), & (x, y) \notin \gamma \\ g_k(x, y) - \xi g'_k(x, y), & (x, y) \in \gamma. \end{cases} \quad (5.15)$$

The progress of the HIO algorithm used in this thesis was monitored through the value of the error, which was defined as

$$\text{Error} = \sqrt{\frac{\sum_{(x,y) \in \gamma} |g'(x, y)|^2}{\sum_{(x,y) \notin \gamma} |g'(x, y)|^2}} \quad (5.16)$$

where the numerator is the sum of the squared values of $g'(x)$ that lie in γ , the set of points where the object-domain constraints are violated, while the denominator is the sum of squared values of $g'(x)$ that do not violate the constraints. A solution was considered to have been found if the error is relatively constant and $\ll 1 \times 10^{-3}$.

The HIO algorithm, or a combination of HIO and ER (for example in [Miao *et al.* \(1998\)](#); [Nakashima *et al.* \(2002\)](#); [Nishino *et al.* \(2003\)](#)), applied to sufficiently oversampled Fraunhofer diffraction data, has proven pivotal in solving the non-crystallographic phase retrieval problem, or image reconstruction, despite being

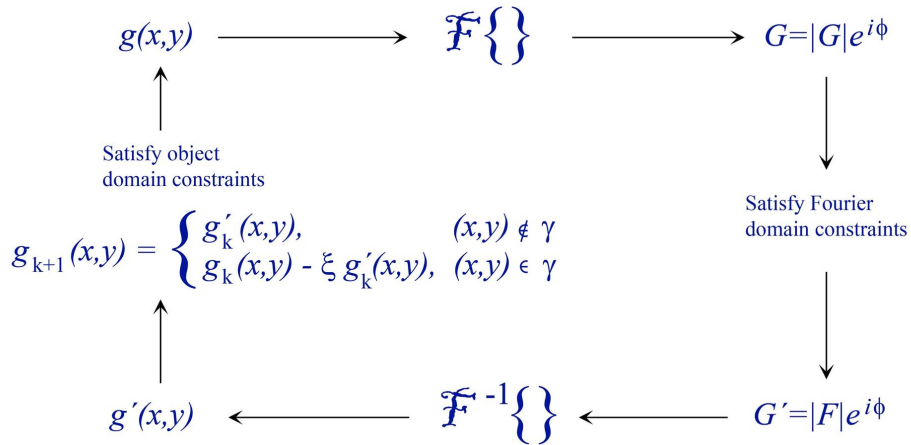


FIGURE 5.8: **Hybrid input-output algorithm.** The HIO algorithm alternates between the real and Fourier domains, imposing constraints that the object must satisfy. In real space, the object is isolated (within a finite support), while in Fourier space, the amplitude must equal the square root of the measured intensity ([Gerchberg and Saxton, 1972](#); [Fienup, 1982](#)).

limited to reconstructing only real, positive functions (Fienup, 1980; Fienup and Kowalczyk, 1990). In CDI this limitation, i.e. the positivity of the imaginary part of complex valued objects, can be used as an internal constraint for image reconstruction (Miao *et al.*, 1998). Reconstruction of a complex-valued object is considerably more difficult, but achievable, given a sufficiently strong support constraint (Fienup, 1987; Pfeifer *et al.*, 2006; Newton *et al.*, 2009).

For optimum algorithm efficiency when using the HIO and related algorithms the support function should be as close as possible to the form and size of the object function (Fienup, 1987). An appropriate initial support function can be calculated from the autocorrelation function² of the diffraction pattern. In one dimension the diameter of the object is half the diameter of the autocorrelation function. However in two dimensions, the exact support can not be determined uniquely from the autocorrelation (Fienup *et al.*, 1982), and so the diameter constraint is not as useful (Fienup, 1982). Marchesini *et al.* (2003) introduced the so-called shrinkwrap algorithm for a dynamic support that uses a threshold value cut-off from the previous estimate of the object to establish the new support, thereby expediting convergence of the algorithm. We explored the use of a shrinkwrap algorithm but our reconstructions showed that the threshold cut-off value (even when using $< 5\%$ of the projected thickness for the support function of the next iteration) strongly affected the reconstructed profiles. The reconstructed diameter was decreased by an inconsistent amount between reconstructions with different threshold cut-off values, thereby introducing ambiguity into the reconstructed nanoparticle profiles. For this reason, the reconstruction results presented in this thesis were obtained using a static support.

5.2.2 Reconstruction results and discussions

We applied the HIO algorithm just described to reconstruct 2D images of Al_2Cu nanoparticles from simulated Fraunhofer diffraction patterns (as shown in §5.1.5) based on Al-Cu samples with microstructures described in §5.1.4. The results presented in this section confirm that it is not necessary to simulate the entire illuminated volume involved in the diffraction, and demonstrate that we can extract quantitative information about the size distribution of the ensemble from the reconstruction.

A comparison of the reconstruction results from Fraunhofer diffraction patterns of 1, 10, 200 and 2.5×10^6 realisations of randomly positioned orthogonal nanoparticles in a $2 \times 2 \mu\text{m}$ array (after 3×10^5 iterations) is shown in Figure 5.9. The sample function

²The autocorrelation of a function is the inverse FT of the magnitude squared of the FT of the function.

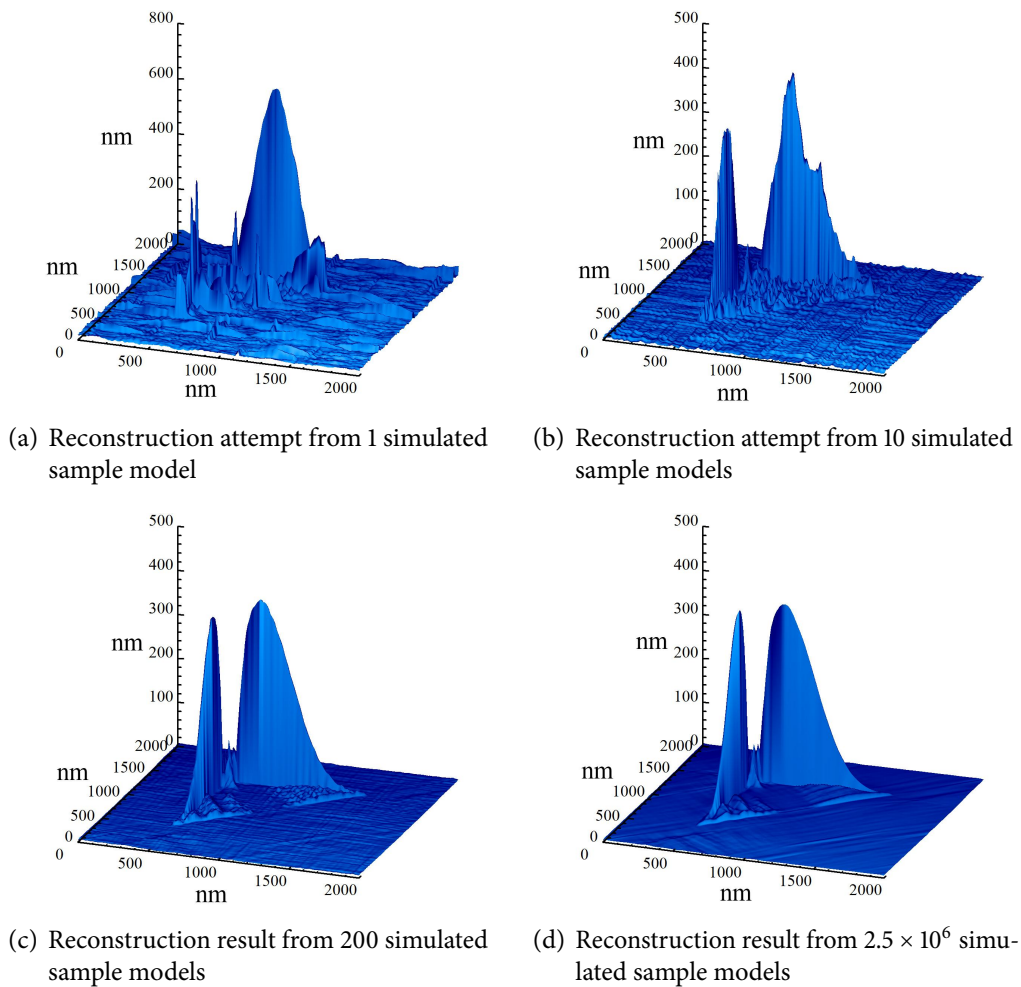


FIGURE 5.9: Reconstruction of Al_2Cu nanoparticles from 1, 10, 200 and 2.5×10^6 model function realisations, after 3×10^5 iterations. The HIO algorithm was applied to simulated Fraunhofer diffraction patterns comprised of an incoherent sum of Fraunhofer diffraction patterns of sample volumes within the coherence volume as described by (eq. 5.9) and as shown in Figure 5.7. The nanoparticle ensemble was normally distributed with $S_m = 400\text{nm}$ and $\sigma = 180\text{nm}$. The reconstruction from 200 model functions in (c) is identical to that from 2.5×10^6 model functions in (d), indicating that the investigation of the effect of polydispersity of the ensemble on the reconstructed nanoparticles does not require the incoherent sum of 2.5×10^6 Fraunhofer diffraction patterns as was suggested in §5.1.5. The two orthogonal reconstructed particles in (c) and (d) were almost identical so their average was used as the final reconstructed nanoparticle profile. The asymmetric elongation of the reconstructed nanoparticle profiles was found to depend quantitatively on the standard deviation of the simulated nanoparticle diameters, indicating that the ensemble nanoparticle size distribution can be extracted from the reconstructed nanoparticle.

for this example was an ensemble with $S_m = 400\text{nm}$ and $\sigma = 180\text{nm}$ (an example of which was shown in Figure 5.6). The reconstruction from 200 sample functions in Figure 5.9(c) is almost identical to that from 2.5×10^6 sample functions in Figure 5.9(d), confirming the expectation discussed in §5.1.5, that the investigation of the effect of polydispersity of the ensemble on the reconstructed nanoparticles does not require the incoherent sum of 2.5×10^6 Fraunhofer diffraction patterns (as was suggested by the arguments made in §5.1.3). The following discussion refers to simulations and reconstructions from 200 sample functions (for each ensemble).

For each normally distributed nanoparticle ensemble (as was described in §5.1.4), two orthogonal platelet nanoparticles were consistently reconstructed from the simulated diffraction patterns. The oversampling condition was always fulfilled (§5.2.1) by using a support whose dimensions were approximately $(S_m + 3\sigma)$ in each direction (as long as somewhere in the convex support the x and y dimensions were of this size). The triangular support used in the example just presented is visible in Figure 5.9. Using a larger support also led to a successful reconstruction, unless the oversampling condition was no longer fulfilled. The relative positions of the two reconstructed nanoparticles varied, generally determined by the size of the support function, where a tighter support function forced the reconstructed nanoparticles to intersect. Using a support much smaller than this led to failure in the convergence of the algorithm as the imposed condition in the object domain (i.e. no electron density outside the support) were no longer appropriate, or in other words, the reconstructed nanoparticle could not fit within the support.

The two orthogonal nanoparticles in the 2D reconstructions were identical (as expected from the simulated sample microstructure) with the exception of a low level of noise, so their profiles were averaged to give an average nanoparticle representative of the ensemble. The reconstruction profiles from a nanoparticle ensemble with $S_m = 400\text{nm}$ and σ between 1 and 180nm are shown in Figure 5.10 (Nikulin *et al.*, 2007).

For the case $S_m = 400\text{nm}$, the reconstructed nanoparticles' increasingly asymmetric profiles are related to the deviation of nanoparticle diameters in the simulated sample via

$$\frac{S_r}{S_m} \approx 1.014 + 0.00127\sigma^{1.332}, \quad (5.17)$$

where S_r is the width of the reconstructed nanoparticle profile, as shown in Figure 5.11(a). These simulations were also carried out for the case $S_m = 300\text{nm}$, where the

resultant relationship was

$$\frac{S_r}{S_m} \approx 1.038 + 0.00158\sigma^{1.331}, \quad (5.18)$$

as shown in Figure 5.11(b).

Thus we have shown how the reconstructed nanoparticle profiles quantitatively depend on the polydispersity of an ensemble. Two sets of normally distributed ensembles of Al_2Cu nanoparticles embedded in an Al matrix were compared, resulting in very similar relationships between the standard deviation and reconstructed nanoparticle size (eqs. (5.17) and (5.18)). These results are potentially very important for the interpretation of reconstructed nanoparticles from experimental diffraction data because they demonstrate that a beam size much larger than a typical coherence volume (even at a third generation synchrotron) does not completely hide size information about a polydisperse ensemble. Indeed we showed that in order to reliably reconstruct nanoparticles whose profiles can be used to quantify the polydispersity we require the incoherent superposition of Fraunhofer diffraction patterns from a sufficient number of small coherence volumes, where sufficiency was based on the interparticle speckle being below 1% of the diffraction signal.

In addition to the presented results, diffraction patterns from a vast number of different sample models were simulated and their average nanoparticles were recon-

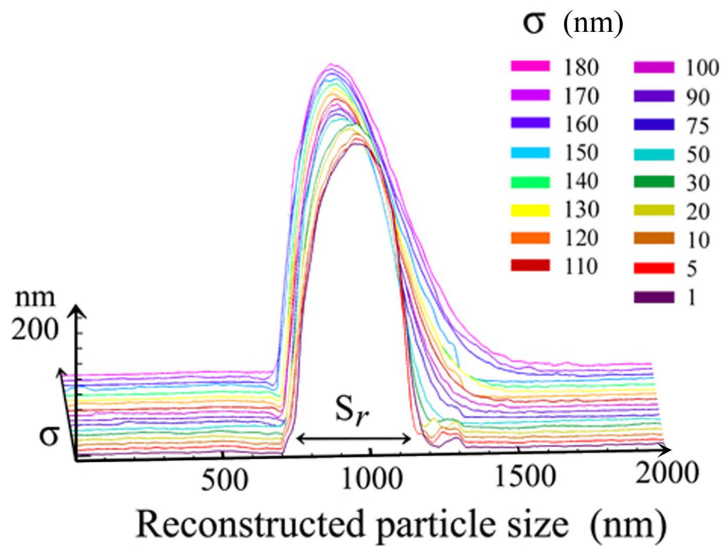


FIGURE 5.10: **Reconstructed nanoparticle profiles from simulated polydisperse Al_2Cu nanoparticle ensembles.** The normally distributed ensembles had $S_m = 400\text{nm}$. The reconstructed nanoparticle size, S_r , taken from the base width, correlates with the standard deviation of the simulated nanoparticle diameters, σ , according to eq. (5.17), as shown in Figure 5.11(a) (Nikulin *et al.*, 2007).

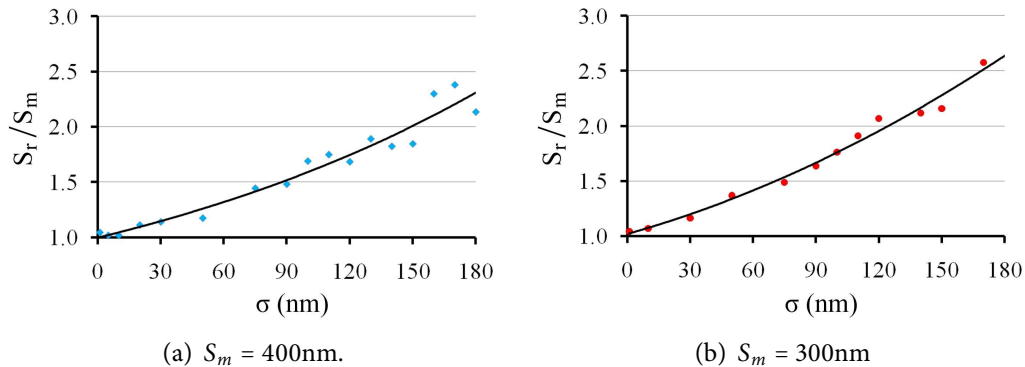


FIGURE 5.11: Ratio of reconstructed nanoparticle diameter tail, S_r , and mean simulated diameter, S_m , vs. standard deviation of diameters, σ .

constructed using the same approach as presented here, wherein we explored periodicity, nanoparticle rotation, and size variations. The convergence of the algorithm was unhindered provided the support function in each case fulfilled the criteria discussed in this section, i.e. that it was sufficiently large to fit the average nanoparticle and yet small enough so that the oversampling condition was fulfilled. When this condition was fulfilled, we found that there was no restriction on the nanoparticle size distributions that could be reliably reconstructed. We also simulated Fraunhofer diffraction patterns from GP zones (single or double layers of pure Cu as compared to Al_2Cu as for the results discussed in this section), wherein the diffraction contrast was greater between the nanoparticles and their surrounding medium, enhancing the signal, but their volume was much smaller. In these instances the average nanoparticles were again readily reconstructed. Sample rotation (particle orientation) did not affect the efficacy of the reconstruction, resulting in correspondingly oriented reconstructed nanoparticles, regardless of the sample model used, which was expected.

Samples with polydisperse nanoparticles that were periodically arranged along one or both axes were also simulated. We found that nanoparticles were rarely reliably reconstructed and the periodicity was always present in the reconstructions in the form of streaks (see Figure 5.12). In Figure 5.12(a) 200 simulated Fraunhofer diffraction patterns were incoherently added, while for the reconstruction in Figure 5.12(b) the diffraction pattern consisted of 10000 sample functions. The increase in the number of models used did not alter the contribution of the periodic signal present in the reconstruction nor improve the reconstructed nanoparticle form. This sensitivity to periodicity may be beneficial if the spatial distribution of the nanoparticles is of primary interest. Conversely, the obvious limitation is that the reconstructed nanopar-

ticle is not likely to be an accurate reconstruction in the presence of well pronounced periodicity in the sample. Although in Al-Cu alloys the microstructure sometimes shows periodicity in small volumes ($< 1\mu\text{m}^3$), the signal from these volumes would not play a significant role compared to the total large volume typically illuminated in our experiments (i.e. $\sim 1.75 \times 10^8\mu\text{m}^3$), so the average reconstructed nanoparticle from experimental results is expected to be accurate.

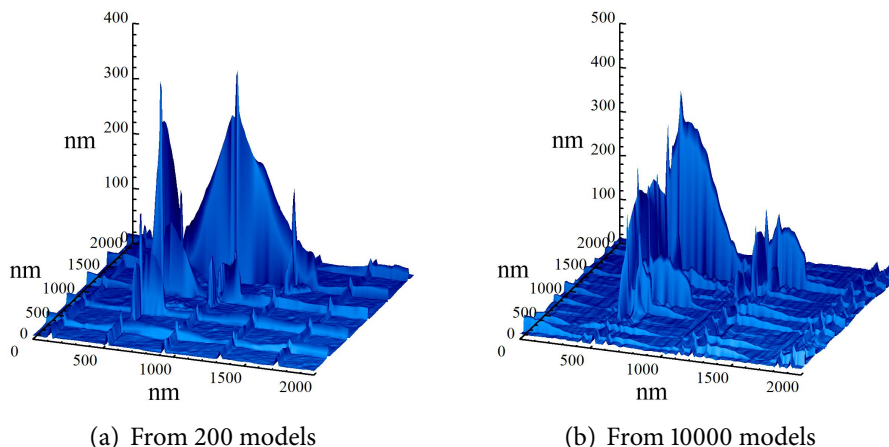


FIGURE 5.12: **Reconstructions from Fraunhofer diffraction of periodically arranged nanoparticles.** In this example the normally distributed ensemble had $S_m = 400\text{nm}$ and $\sigma = 180\text{nm}$. The nanoparticles were arranged periodically in both x_s and y_s , with interparticle spacing of (a) 400nm and (b) various periods (20nm , 30nm , 60nm and 70nm). Streaks from the periodicity are clearly visible and the nanoparticles are not well reconstructed.

We close this section on reconstructions of nanoparticles from simulated Fraunhofer diffraction patterns from large ensembles of embedded nanoparticles with a brief summary of the main results. We discussed how to simulate, and showed an example of, the diffraction pattern of a large sample volume containing weakly diffracting nanoparticles by incoherently superposing a number of Fraunhofer diffraction patterns from volumes within which the projection and first Born approximations are valid. We then demonstrated the consistency of nanoparticle reconstructions from a small number (200) of model realisations involved in the diffraction pattern sum, compared to 2.5×10^6 models, expediting the simulations. We also showed that there was a quantitative relationship between ensemble polydispersity and the reconstructed nanoparticles from such diffraction patterns. We now turn to the next stage in the simulation process, stage (e) in Figure 5.1, involving diffraction from the sample in analyser based reciprocal space maps.

5.3 Simulating analyser based reciprocal space maps

The next stage in the experimental setup (Figure 5.1) is stage (e): analyser based reciprocal space maps of Fraunhofer diffraction from ensembles of weakly diffracting embedded nanoparticles. We described the geometry of reciprocal space mapping in §4.2.2 and in the previous two sections we covered how to model Fraunhofer diffraction from such samples and what information about the ensemble is obtainable from the Fraunhofer diffraction patterns. In this section we present the simulated reciprocal space maps with Fraunhofer diffraction from the sample, wherein we investigate the effects of the size distribution or rotation of the particles about the optical axis, which will enable us to interpret the experimentally measured RSMs presented in the next chapter (§6.2).

5.3.1 Simulating reciprocal space maps with XDC

Reciprocal space maps were simulated using XDC³, a code written for conventional triple crystal diffractometry. XDC calculates a 1D X-ray wavefield diffracted from two ideal crystals in a single-reflection, non-dispersive setting (the sample and analyser in conventional TAD) as a function of their angular positions. The calculation involves solving the Takagi equations (§3.2.2) (Afanasev and Kohn, 1971), with numerical integration as described in the work of Epelboin and Riglet (1979) and Epelboin (1985). XDC can be used to simulate various single scans in reciprocal space, obtained by rotation of either the 2nd or 3rd axis (or both), as was described in Figure 4.3. A 2D RSM is obtained by collating such scans, in a manner that is identical to experimental acquisition of reciprocal space maps (§4.2.2).

The dynamical effects (finite wavelength bandwidth) of the monochromator (the 1st crystal in TAD) are not taken into account in XDC as a planar, monochromatic incident beam is assumed. This high degree of coherence⁴ is not achievable experimentally, nor is it desired as the monochromator wavelength bandwidth plays an

³XDC is a simulation code (written in Fortran) for conventional triple axis diffractometry calculations. It was written by Dr. Timur Gureyev from CSIRO, Australia.

⁴Assuming a planar, monochromator beam in XDC does not simulate complete coherence, as the beam is bounded by the specified length across the surface of the crystals (along x_c), thereby introducing an artificial cut-off. The beam length along x_c was chosen to be $143\mu\text{m}$, corresponding to a beam width of $60\mu\text{m}$ at an incident angle of $\theta_B = 24.765^\circ$ (Si(400) with $\lambda = 1.13747\text{\AA}$). The spatial resolution in the beam was 2nm.

essential role in recording 2D information about the sample, as was discussed in §4.3.2.

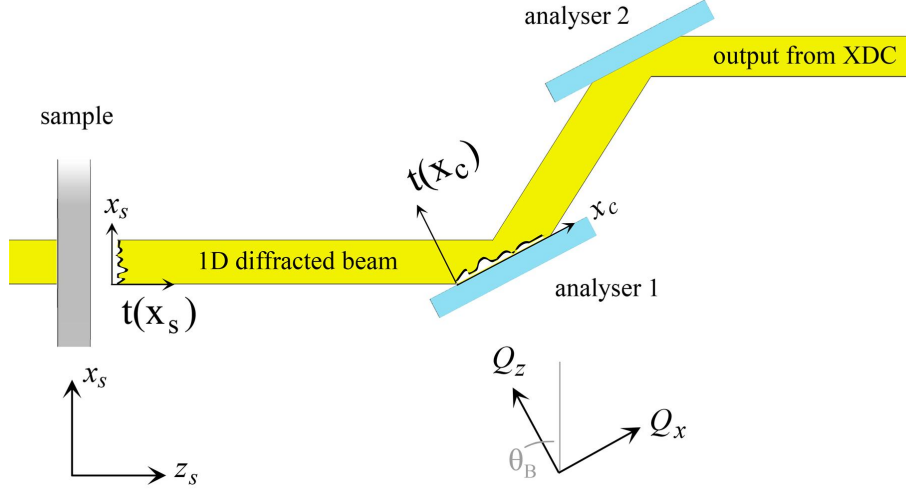


FIGURE 5.13: **Geometry of reciprocal space mapping as simulated by XDC.** A finite 1D plane wave is modulated by the sample and then diffracted from two ideal, semi-infinite crystals in the single reflection, non-dispersive setting. 2D RSMs can be simulated by collating 1D scans as described in Figure 4.8.

The crystalline function of the monochromator is replaced by the sample function from the ensemble of nanoparticles in the form of a 1D transmission function, along x_s , as shown in Figure 5.13. The transmission function of the sample follows the definition in eq. (3.15), where the projection approximation was used, but in this case the sample information in the y direction is omitted. Along the surface of the analyser, x_c , the incident beam is

$$t(x_c) = \frac{t(x_s)}{\sin \theta_B}, \quad (5.19)$$

$$= \frac{1 + ik \int [-\delta(x_s, z_s) + i\beta(x_s, z_s)] dz_s}{\sin \theta_B}. \quad (5.20)$$

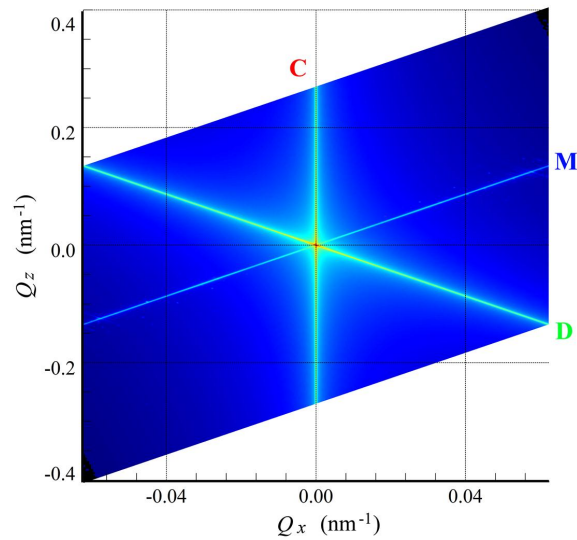
5.3.2 Simulation and measurement of the triple axis diffractometry instrumental function

In the analyser based reciprocal space mapping technique we are developing it is necessary to adequately characterise the effect of the setup before we introduce the sample, which is achieved by simulating and measuring the TAD instrumental function (§4.3.1). In conventional TAD the 2D instrumental profile can be calculated

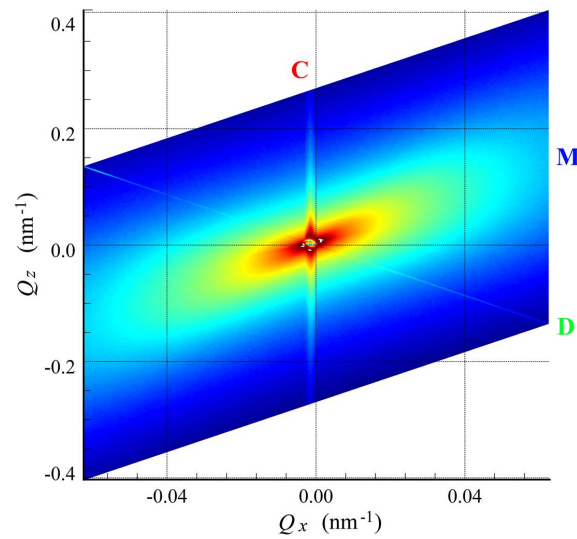
by taking into account the reflectivity of each crystal and the effect of each optical element in the beam path of the triple crystal diffractometer (Zaumseil and Winter, 1982b; Kotsis and Alexandropoulos, 1986; Fewster, 1989; Gartstein *et al.*, 2001). With XDC we calculate the instrumental function by using a plane wave as the input wave instead of the transmission function of the sample. In this case the specified computing length along the surface of the first analyser crystal (along x_c in Figure 5.13) determines the extent of the plane incident wave along x_s , which is equivalent to using an input wavefield the value of which is $(1 + 0i)$ at every point along x_s . As the role of the detector in our TAD setup is replaced by the second analyser crystal in XDC, the detector aperture is not taken into account but is effectively approximated by the angular acceptance of the second Si crystal.

The simulated RSM of the TAD instrumental function calculated with XDC is shown in orthogonal (Q_x, Q_z) coordinates (Figure 5.14(a)), which are related to the angular deviations (from Bragg diffraction positions) of the analyser and detector, α and $\Delta 2\theta$, respectively, via eqs. (4.9) and (4.10). The reciprocal space region that was probed covered a parallelogram, i.e. $Q_x = \pm 0.0622\text{nm}^{-1}$, and for the first scan, $Q_z \in [-0.405, 0.135]\text{nm}^{-1}$, and the last scan (out of 243 in this case), $Q_z \in [-0.135, 0.405]\text{nm}^{-1}$, with steps of 0.00223nm^{-1} along Q_z during scans and steps of 0.00103nm^{-1} along Q_x between scans. The crystal truncation rod is labelled C, and the pseudo peak from crystal 3 in conventional TAD is labelled D. As a result of the omission of the dynamical diffraction of the monochromator in XDC, the monochromator pseudo streak (labelled M) is a delta function, i.e. only one pixel thick.

For comparison with the simulated data, an experimental instrumental function is shown in Figure 5.14(b). It was measured on beamline BL13XU at SPring-8 with a double reflection Si(400) monochromator and single reflection Si(400) analyser crystal. A beam size of $0.25 \times 1.0\text{mm}^2$ ($v \times h$) was used. The experimental setup was described in further detail in §4.1. In the experimental instrumental function (Figure 5.14(b)) the detector streak, inclined at θ_B anti-clockwise from the Q_z axis, is very thin (single pixel), making it difficult to resolve due to large angular steps in α and/or $\Delta 2\theta$ (which were $\alpha_{\text{step}} = 0.008^\circ$ and $\Delta 2\theta_{\text{step}} = 0.016^\circ$). Even slight misalignment of the optics can render this streak invisible. The prominent crystal truncation rod (vertical streak) shows that the RSM is slightly shifted on the Q_x axis, which is due to a slight misalignment of the Bragg position of the analyser. The use of a double reflection monochromator sufficiently suppressed the tails of the monochromator pseudo streak in this RSM to render it invisible (see the discussion on multiple



(a) Simulated TAD instrumental function



(b) Experimentally measured TAD instrumental function

FIGURE 5.14: Simulated and experimentally measured TAD instrumental functions. The X-ray energy was 10.9 keV, and the analyser was a single reflection Si(400) crystal and the beam size was $0.25 \times 1.0 \text{ mm}^2$ ($v \times h$). In the simulations the monochromator pseudo streak, labelled M, is a delta function (except for numerical artifacts that arise from finite steps along the analyser surface), as the simulations do not take into account the wavelength bandwidth of the monochromator. The measured instrumental function shows a very thin detector pseudo streak, labelled D, a wide crystal truncation rod from the analyser, labelled C, and diffuse scattering from air and other effects discussed in the main text.

reflections in §3.2.2). The background intensity is due to air scattering, however its prominence is exaggerated in this RSM due to the detector being saturated in the central region.

As the technique being developed in this thesis is a nanoscale characterisation technique, we are interested in measuring diffraction at high k_x or k_z values, which in a non-Bragg diffracting sample is often a weaker signal. Thus it is more important to choose an incident intensity (beam size) and display range that favours the weaker signals. This choice may lead to saturation in the central region despite the relatively high dynamic range of the detector.

5.3.3 Simulations of RSMs with various nanoparticle size distributions and nanoparticle rotation

In this section we present simulated analyser based RSMs of Fraunhofer diffraction from embedded Al-Cu nanoparticle ensembles. We explore the effect of nanoparticle rotation about the optical axis as well as nanoparticle diameter polydispersity, in order to interpret the experimental RSMs exploring the sensitivity of the technique to nanoparticle presence and orientation, which will be presented in §6.2. First we examine the effect of rotation of the sample about the optical axis on RSMs from a monodisperse system of 250nm mean diameter. Second, we look at the effect of increasing the standard deviation of a polydisperse ensemble for two mean nanoparticle diameters, 250nm and 450nm.

We discussed in §4.3 that the Fraunhofer diffraction from the sample lies with the k_x axis along the monochromator pseudo streak in the RSM. As XDC does not include the effects of the wavelength bandwidth of the monochromator and only considers a 1D input (eq. (5.20)), the signal from the sample modulates only the monochromator pseudo streak and does not carry 2D information about the sample into the RSM in the k_z direction (perpendicular to the monochromator pseudo streak). As a result, only the effective projected nanoparticle diameter along x_s contributes to the diffraction signal along the monochromator pseudo streak. This is equivalent to the projection or Fourier slice theorem we discussed in §3.1.2. For the one dimensional case, the theorem states that the 1D Fourier transform of the projection of the 2D sample function onto the x_s axis is equal to the 1D slice along k_x through the centre of the 2D Fourier transform of the 2D sample function. This is significant because even though the simulations only have a 1D sample function, the diffracted intensity along the monochromator pseudo streak (along k_x) is an appropriate simulation of

the experimental intensities along the streak for the weakly diffracting samples we will examine in chapter 6.

If the initial orientation of the platelet nanoparticles is along the x_s , y_s and z_s axes, as in Figure 5.3, then clockwise rotation about the optical axis by θ_Z results in effective diameters (along x_s) of $d_{\text{eff}(2)} = |S_m \cos(\theta_Z)|$ and $d_{\text{eff}(3)} = |S_m \sin(\theta_Z)|$ for nanoparticles (2) and (3), respectively. In Figure 5.15 the lime and dark blue curves show the effective nanoparticle diameters from nanoparticle (2) and (3), respectively, which contribute simultaneously to the diffracted intensity as a function of rotation about the optical axis.

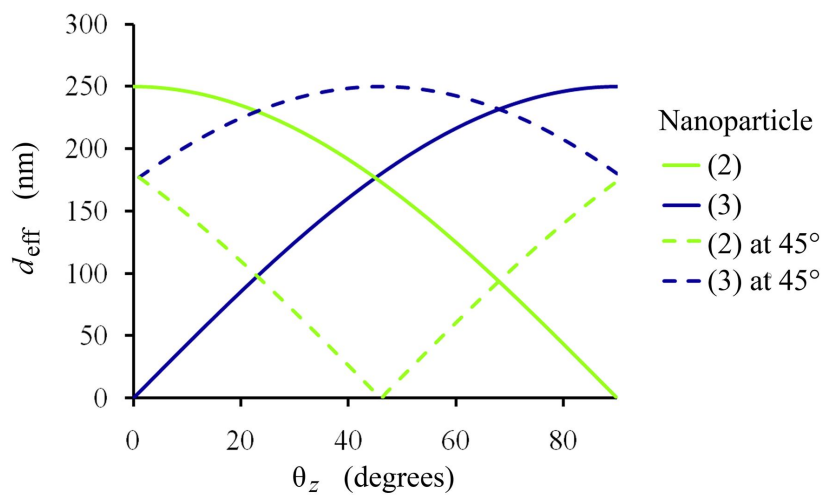


FIGURE 5.15: Effective diameter (projected onto x_s) as a function of the rotation of the sample about the optical axis, z_s . This simple relationship between angle of rotation and effective diameter shows the equivalence of many rotation angles due to the intrinsic symmetry of the habitat planes of two sets of Al-Cu nanoparticles: (2) in (x_s, z_s) and (3) in the (y_s, z_s) plane. The solid lime and dark blue curves show the effective nanoparticle diameter of 250nm particles (labelled (2) and (3) in Figure 5.3 respectively), where both effective diameters contribute to the diffracted intensity simultaneously (but not equally). The dashed curves correspond to the same sample rotated by 45° as will be explored experimentally in the technique feasibility study presented in §6.2.

We will ignore nanoparticle (1) as its diffraction signal is much weaker than that from particles (2) and (3) and rotation about z_s doesn't affect its effective diameter along x_s . This simple geometrical relationship between the azimuthal rotation angle and effective nanoparticle diameters means that many orientations about z_s are equivalent by virtue of the three orthogonal axes of four-fold rotational symmetry of the planes along which the nanoprecipitates form in an Al-Cu alloy (along the orthogonal $\langle 100 \rangle_{\text{Al}}$ family of planes).

The biggest change in the effective nanoparticle diameter during sample rotation leads to the biggest difference in the diffracted intensity along the monochromator pseudo streak. As seen in Figure 5.15, due to the symmetry of the habitat planes of the nanoparticles, the biggest possible change in effective diameter is $\Delta d_{\text{eff}} = S_m / \sqrt{2}$, i.e. perfectly aligned particles with nanoparticles parallel and perpendicular to the diffraction plane for orientation 1, and then rotated by 45° about the optical axis for orientation 2 (Figure 5.16). The sample holder/heater (described in §4.4) was designed to allow rotation of the sample by 45° for this reason.

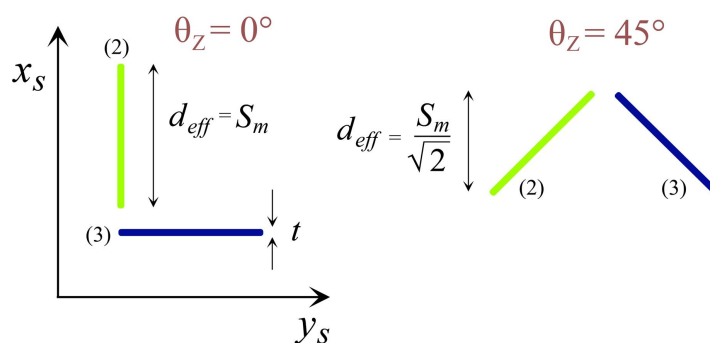


FIGURE 5.16: **Rotation of nanoparticles about the optical axis.** Two orientations – with particles parallel and perpendicular to the diffraction plane, and with both sets of particles at 45° to the diffraction plane.

To investigate the effects of rotation of a sample we simulated RSMs from a monodisperse nanoprecipitate ensemble where $S_m = 250\text{nm}$ with rotation about z_s by $\theta_z = 5, 10, 15, 30,$ and 45 degrees. In Figure 5.17 we show two RSMs corresponding to $\theta_z = 0^\circ$ and $\theta_z = 5^\circ$. The crystal truncation rod from the analyser and pseudo streaks from the second analyser crystal in XDC (Figure 5.13) and the diffraction signal from the sample (along the monochromator pseudo streak) are labelled C, D and M, respectively. The diffracted intensity along the monochromator pseudo streak is the incoherent sum of Airy patterns (the Fourier transform of a circular aperture (Cowley, 1975)), corresponding to the projected nanoparticle profiles in the input of XDC, i.e. the incident beam (eq. (5.20)). For the monodisperse case here, the Airy patterns are identical, which leads to good visibility of diffraction minima and maxima in Figure 5.17(b). This is clearer in Figure 5.18 where the monochromator pseudo streak profiles from the six orientations are compared.

The effective diameters in the ensemble can be found from the first minima in

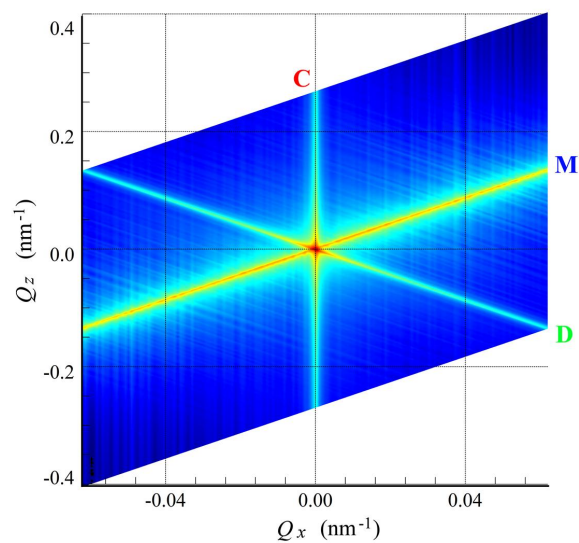
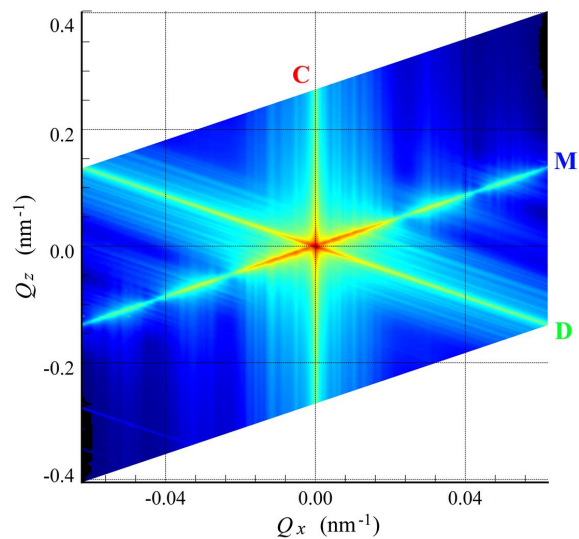
(a) $\theta_Z = 0^\circ$ (b) $\theta_Z = 5^\circ$

FIGURE 5.17: **Simulated 2D RSMs from a monodisperse ensemble of Al-Cu nanoparticles in two orientations.** Both RSMs are from a sample with $S_m = 250\text{nm}$ where (a) has the nanoparticles aligned parallel and perpendicular to the diffraction plane and (b) has the sample rotated by 5° about the optical axis. The 1D input function for XDC primarily affects the monochromator pseudo streak, labelled M, so no 2D information is obtainable from such simulations in the absence of *a priori* knowledge about the nanoparticles. In this case the diffraction profile is an Airy pattern from the effective diameter, d_{eff} , where (a) $d_{\text{eff}} = 250\text{nm}$ and (b) $d_{\text{eff}} = 22\text{nm}$.

the Airy patterns by

$$d_{\text{eff}} \cong \frac{1.22\lambda}{\sin \theta_{\text{mono}}}, \quad (5.21)$$

where θ_{mono} is the deviation of either α or $\Delta 2\theta$ from the Bragg position, since $\alpha = \Delta 2\theta$ along the monochromator pseudo streak.

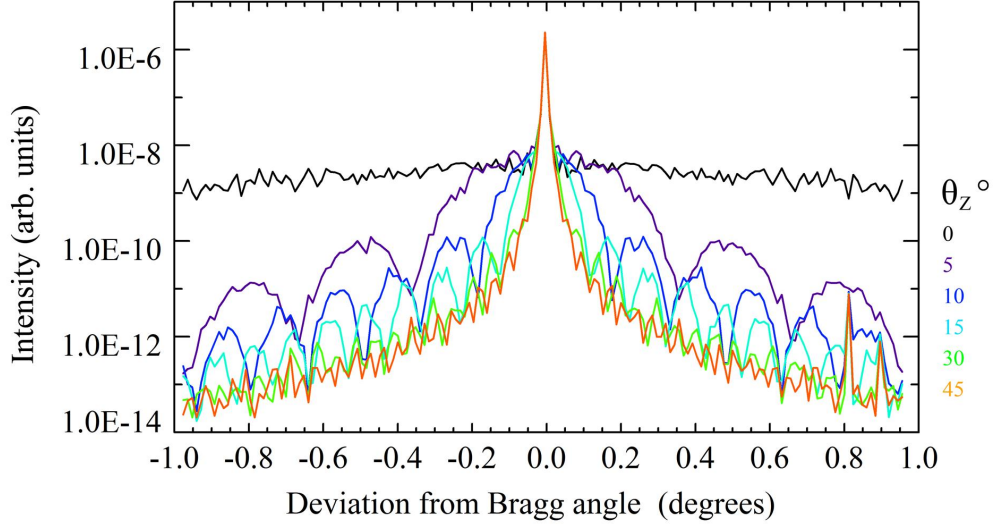


FIGURE 5.18: **Simulated monochromator pseudo streak profiles from various azimuthal orientations of the sample.** The simulated sample had an ensemble of nanoparticles with identical diameters of 250nm, so as to isolate the effects of rotation from that of size deviation. The purple profile corresponds to the monochromator pseudo streak in Figure 5.17(b).

Experimentally the diffracted intensity is proportional to the volume of the scatterer squared. However, in these 2D simulations that are projected into a 1D beam, the intensity depends consequently on the squared projected width of the nanoparticles only. The effective projected width ($\geq 5\text{nm}$) of the nanoparticles follows the complementary relationship to the projected diameter, i.e. when the effective diameter is scaled by the sine, it is scaled by the cosine. This means that as the effective nanoparticle diameter decreases, the projected width increases and the contribution from those particular nanoparticles grows significantly with the projected width. This explains why in the simulated monochromator profiles shown in Figure 5.18 we clearly observe only the Airy patterns corresponding to the smaller effective diameters. For example, when $\theta_z = 5^\circ$ (the purple profile) the effective diameters along x_s of nanoparticles (2) and (3) are 249nm and 22nm, respectively, and we clearly observe the signal from the latter. Interestingly, the intensities in Figure 5.18 are very similar in the central

region ($-0.03^\circ < \theta < 0.03^\circ$) and although there are two sets of orthogonal particles contributing identically to the 45° case (as they have the same effective diameter, d_{eff}), the diffracted intensity does not increase, since the projected nanoparticle width along z_s is at a minimum.

We also investigated the effect of ensemble polydispersity on the monochromator pseudo streak by simulating reciprocal space maps from normally distributed Al-Cu nanoparticle ensembles. Here we present the results from four sets of simulations, where $S_m = 150, 250$ and 450nm with corresponding thicknesses of 2, 4, 5 and 12nm and standard deviations of up to 40% of S_m for each ensembles. To approximate the true form of Al-Cu nanoparticles, the widths of the nanoparticles in each ensemble were normally distributed with the same fractional standard deviation as the diameter.

The simulated monochromator pseudo streaks for the $S_m = 250\text{nm}$ ensembles are shown in Figure 5.19(a) where they have been offset from one another by powers of 10 for clarity. Very similar results were obtained for the $S_m = 150\text{nm}$ case, to which the exact arguments that follow can also be applied. Without loss of generality in our demonstration we include the $S_m = 250$ and 450nm cases.

As the number of nanoparticles in the beam remained relatively constant (~ 360 nanoparticles in a $60\mu\text{m}$ beam along x_s), the intensity of the central region was the same for the various polydisperse ensembles. The intensity profiles are very similar in the simulated angular range, with an increasingly noticeable decline in intensity as σ is increased. This was expected from the sample's idealised orientation whereby the dominant contributor to the diffraction pattern was the width of the nanoparticles. While the first minima (centred at $\sim \pm 1.6^\circ$, from eq. (5.21)) are outside the simulated range, it is nevertheless clear that the intensity decrease in the tails of the red profile ($\sigma = 180\text{nm}$) is due to the contribution of the larger nanoparticles in the polydisperse ensemble since their Airy patterns' first minima is at a smaller diffraction angle. The first minima from the mean diameter in the ensemble are at $\sim \pm 0.03^\circ$, which is visible in Figure 5.19(a) but is not a reliable signal with the chosen angular step size and, more significantly, the level of noise, which is due to rounding errors. In comparison, the simulated monochromator pseudo streak profiles from the $S_m = 450\text{nm}$ ensembles are shown in Figure 5.19(b). The first minima of the monodisperse ensemble (black line) are at $\sim \pm 0.66^\circ$, corresponding to the thickness (12nm) as expected. These results show that diffraction profiles from such ensembles with a standard deviation of $>22\%$ (100nm) inhibit direct evidence of the Airy patterns.

A simple way to overcome the limitation of an insufficient angular range, while keeping the same angular step sizes and experimental data collection times (approx-

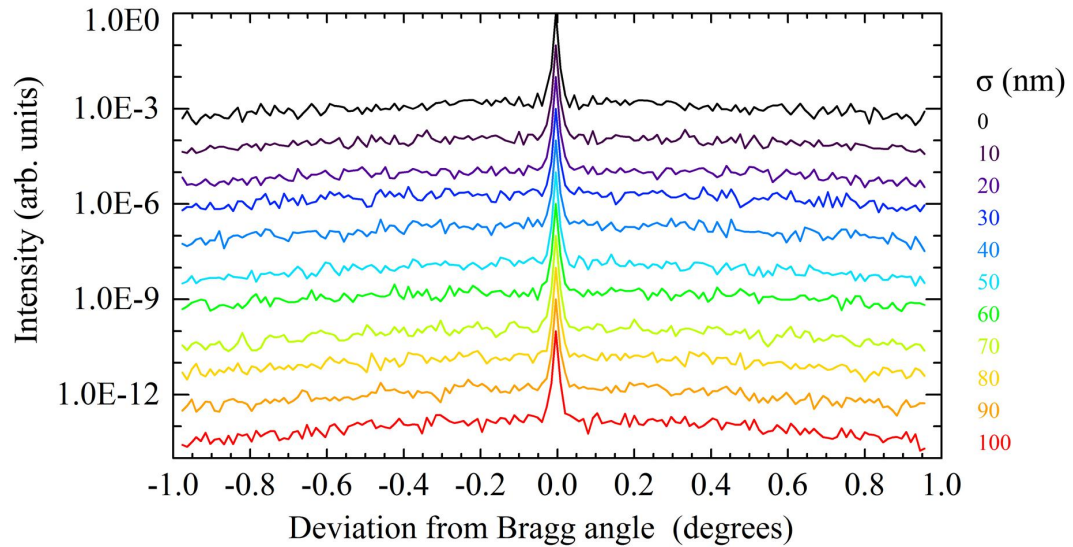
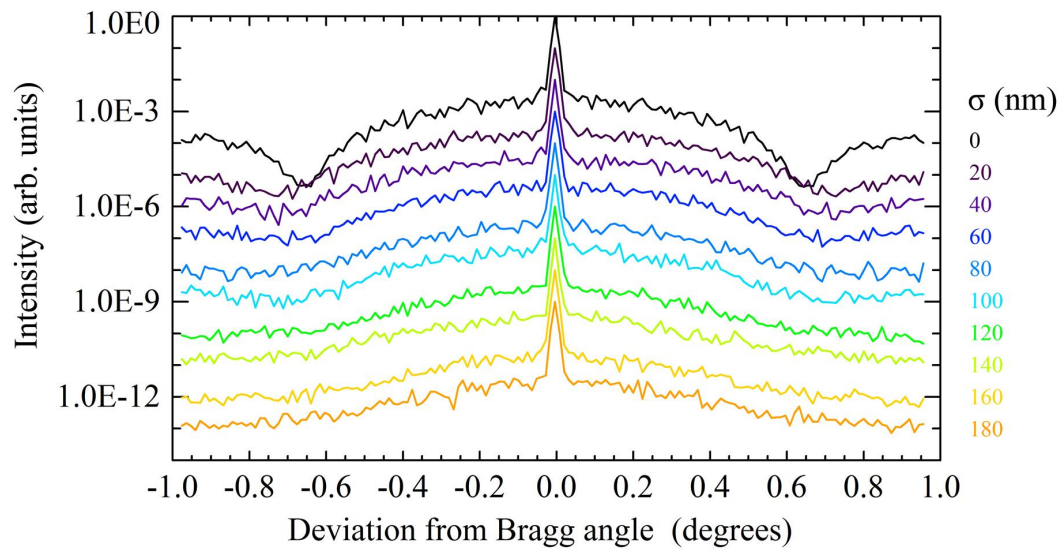
(a) $S_m = 250\text{nm}$ with mean nanoparticle width = 5nm(b) $S_m = 450\text{nm}$ with mean nanoparticle width = 12nm

FIGURE 5.19: **Simulated monochromator pseudo streak profiles from various nanoparticle diameter distributions**, offset from one another for clarity. The simulated samples had ensembles of Al-Cu nanoparticles with (a) $S_m=250\text{nm}$ and (b) $S_m=450\text{nm}$. The nanoparticle widths were normally distributed with the same fractional standard deviation as the diameters. The nanoparticles in all samples were aligned parallel and perpendicular to the diffraction plane, i.e. $\theta_Z = 0^\circ$, whereby the dominant contributor to the diffraction pattern was the width of the nanoparticles. The first minima in (a) are outside the simulated range (at $\sim \pm 1.6^\circ$), hiding the effects of polydispersity. However, the profiles in (b) demonstrate that provided the angular range is sufficient for the first minima to be visible, perfectly aligned samples lend themselves to analysis of polydispersity. In this case the Airy pattern minima are no longer discernible for ensembles with a standard deviation of $>20\%$.

mately 5 minutes per scan) is to introduce a small rotation of the ensemble about the optical axis. This was done for the ensembles with $S_m = 150$, 250 and $S_m = 450$ nm, whose monochromator pseudo streaks are shown in Figure 5.20, where $\theta_Z = 5^\circ$. From these simulations we see the limitation of visibility of Airy pattern minima at standard deviations in the nanoparticle size of approximately 20%.

Figure 5.20(c) shows profiles that differ from simple Airy patterns and the minima and maxima are less clear. The FT of the 1D projected nanoparticle thickness in this case is no longer an Airy pattern so eq. (5.21) is no longer valid. Hence in order to quantitatively analyse the diffraction profile for ensemble size and polydispersity we need to know the form of the nanoparticles and then simulate their diffraction profiles as presented here. In the case of a completely unknown nanoparticle form, a 1D diffraction profile can provide limited quantitative information about at least one dimension of the nanoparticle.

An important observation from these simulation results is that even a very small deviation in alignment of the Al crystallographic axes with the diffraction plane results in a significant change in the diffracted intensity from such anisotropic nanoparticles. Without knowledge of the sample's exact crystallographic orientation it will be difficult to retrieve accurate nanoparticle dimensions from a single diffraction profile. If, however, we record diffraction profiles from two sample orientations with a known relative angle (e.g. 45°), then the problem reduces to solving the following equations for the mean nanoparticle size in the sample, S , and θ_Z ,

$$S|\cos\theta_Z| = \frac{1.22\lambda}{\sin\Delta\alpha_1}, \quad (5.22)$$

$$S|\cos[\theta_Z + 45]| = \frac{1.22\lambda}{\sin\Delta\alpha_2}, \quad (5.23)$$

where S is in nm and θ_Z is the angle between the diffraction plane and the $(001)_{Al}$ plane (particle (2) in Figure 5.16), λ is the wavelength in nm, and $\Delta\alpha_1$ and $\Delta\alpha_2$ are the angles of the first minima in the diffraction profiles from the sample in orientation 1 and 2, respectively. For the orthogonally oriented nanoparticles, particle (3) in Figure 5.16, we need to replace the cosine with sine.

As mentioned briefly in the discussion of Figure 5.19(a), for a monodisperse nanoparticle ensemble with $[100]_{Al}$ parallel to the optical axis, the diffraction profile consists of contributions from two Airy patterns, arising from the diameter of nanoparticle (2) and width of nanoparticle (3). However, in most cases we can only observe one Airy pattern clearly, as measuring the contributions from large diameters requires very high angular resolution. It is experimentally impractical to measure

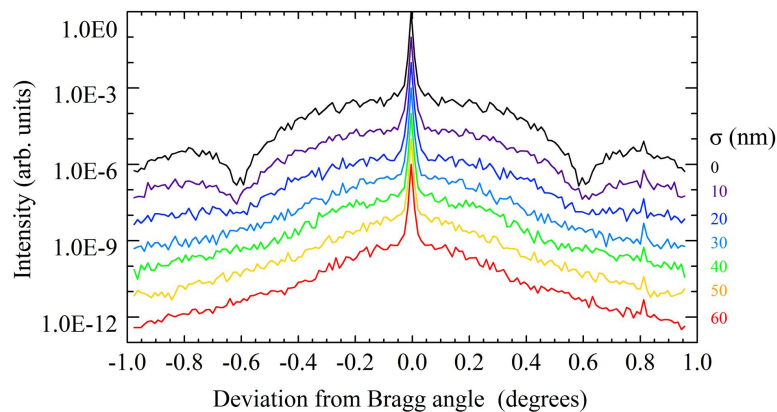
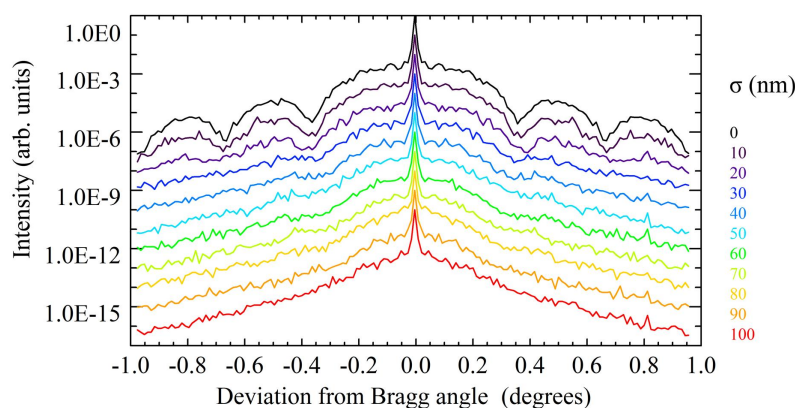
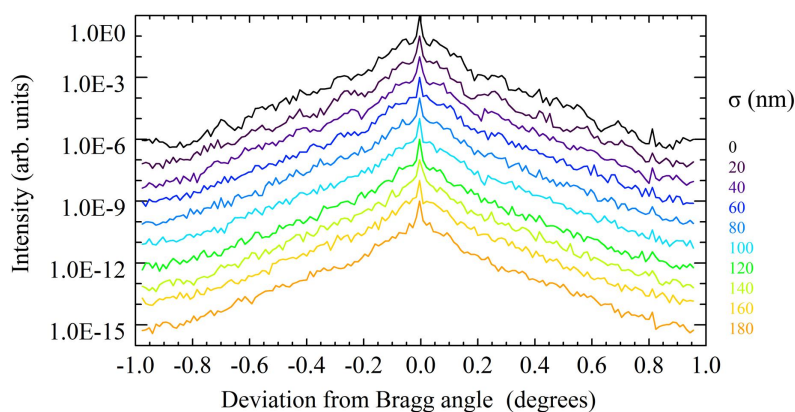
(a) $S_m = 150\text{nm}$ with mean nanoparticle width = 4nm(b) $S_m = 250\text{nm}$ with mean nanoparticle width = 5nm(c) $S_m = 450\text{nm}$ with mean nanoparticle width = 12nm

FIGURE 5.20: **Simulated monochromator pseudo streak profiles from various diameter distributions where $\theta_Z = 5^\circ$.** The simulated samples had ensembles of Al-Cu nanoparticles with (a) $S_m=150\text{nm}$, (b) $S_m=250\text{nm}$ and (c) $S_m=450\text{nm}$. (a) and (b) show that a slightly rotated sample lends itself well to analysis of nanoparticle ensemble polydispersity without the need for very large angular scans, provided S_m and θ_Z are known. However, the (c) profiles are no longer simply Airy patterns as the projected nanoparticle thickness into a 1D function is not a simple form anymore.

both the signal from a large diameter, with high resolution, and the signal from the small width, simultaneously. One could, for example, use a different analyser for different angular resolution, but one would have to prioritise one or the other nanoparticle dimension. In this case when the sample is in orientation 2 ($\theta_z = 45^\circ$) the Airy patterns from nanoparticles (2) and (3) overlap. However, for any other initial orientation of the sample it may be unclear which nanoparticle's Airy pattern is more clearly visible. Equations (5.22) and (5.23) can only be applied if the Airy patterns observed in both orientations of the sample arise from nanoparticles in the same set of crystallographic planes. In this case the complementary version of eq. (5.22) or eq. (5.23) (where cosine is replaced by sine) would yield a more plausible solution for θ_z and S .

These simulations demonstrate that for a polydisperse ensemble with a narrow diameter spread, once S and θ_z are found, the size distribution of the ensemble may be recovered from the visibility of diffraction minima and maxima, as compared in Figure 5.20(b). We also showed that perfectly aligned samples can also lend themselves to analysis of polydispersity provided the angular range of the diffraction data is sufficient for the first minimum (from the nanoparticle width) to be visible.

Another significant outcome from these simulations is that although they are not a comprehensive simulation of the exact setup used in the experimental data collection presented in the next chapter, they do demonstrate that quantitative information about the microstructure (in a bulk material sample containing weakly diffracting embedded nanoparticles) is available from 1D scans in reciprocal space, i.e. along the monochromator pseudo streaks. The benefit of scanning smaller regions in reciprocal space is that time resolved studies with improved time resolution may be carried out, and it would also mean a higher number of samples could be explored given the same experimental beam time.

However, it is still necessary to obtain a complete 2D RSM with a high signal to noise ratio, as well as high angular resolution and range, in order to be able to reconstruct average nanoparticles in the ensemble. An example of where this is required will be shown in §6.2.

5.4 Summary

In this chapter we narrowed the discussion of Fraunhofer diffraction from chapter 3 to the particular case of large ensembles of embedded Al-Cu nanoparticles in a bulk material sized sample. We showed that the first Born approximation is satisfied for

the coherence volumes involved. We also showed that the validity of the projection approximation, which greatly simplifies simulations of diffraction patterns, is limited to very thin sample sections and X-ray energies of >8 keV for the nanoparticle size scales typically used in our experiments. We then presented results of nanoparticle reconstructions from Fraunhofer diffraction patterns of various nanoparticle size distributions, demonstrating that quantitative 1D information regarding the nanoparticle ensemble polydispersity can be extracted from the reconstructions. These simulations demonstrated that a large beam can be used to analyse weakly diffracting embedded nanoparticles.

The last part of this chapter was dedicated to describing simulations of reciprocal space mapping with an analyser crystal. We compared a simulated and experimentally measured instrumental function, highlighting the capabilities and limitations of the idealised simulation approach. Finally, we presented the results of simulations of reciprocal space maps of diffraction from ensembles of Al-Cu nanoparticles in an Al alloy for various size distributions and orientations of the particles with respect to the diffraction plane of the analyser. We showed that it is quite simple to determine the average nanoparticle size in the ensemble and the orientation of the sample with respect to the diffraction plane from the monochromator pseudo streaks in RSMs of two orientations of the sample with a known relative rotation about the optical axis. However, this particular analysis is limited to systems with relatively low polydispersity (a deviation of $\lesssim 20\%$ in normally distributed nanoparticle diameters), as greater deviations concealed the Airy pattern in the diffraction profile. These results emphasise that quantitative information about the ensemble can be extracted directly from small regions in the RSM, which would expedite both static and *in situ* real-time sample investigations.

In the following chapter we present the nano-characterisation technique development as experimentally implemented in three stages. We explore the feasibility of the technique, including its sensitivity to nanoparticle orientation about the optical axis and its ability to study *in situ* real-time nanoparticle growth. We also report on the first experiment to characterise Al-Cu alloys using the techniques simulated here.

Experimental development of an X-ray nanoparticle characterisation technique

6.1 Introduction

In the previous chapter we combined X-ray diffraction theory from chapter 3 and the experimental particulars presented in chapter 4 to describe diffraction from ensembles of embedded nanoparticles. We simulated Fraunhofer diffraction patterns from bulk material sized samples as well as analyser based reciprocal space maps, in which we explored polydispersity and sample rotation.

In this chapter we present the results of a series of experiments, in three stages, in which we implement the reciprocal space mapping technique for the characterisation of embedded nanoparticles. In §6.2 we validate the sensitivity of the new triple axis diffractometry (TAD) technique to the presence and orientation of various size distributions of weakly diffracting nanoparticles in an Al-Cu alloy. The experiment also served to explore a suitable sample thickness for further investigations. The second experiment, presented in §6.3, is an observation of the real-time changes in the diffraction from a variety of Al-Cu alloys during nanoparticle growth, i.e. during *in situ* sample heating. Mono- and polycrystalline samples were used, with different concentrations of copper and ageing temperatures. These results aided the selection of an appropriate sample and heat treatment for the first in-depth, real-time, reciprocal space mapping investigation of *in situ* nanoparticle growth in an Al-Cu alloy. The experiment also led to important improvements in the custom made *in situ* sample heater that were necessary to ensure an accurately controlled, stable sample temperature over the duration of the *in situ* heat treatment. Section 6.4 presents the results from the first *in situ*, real-time X-ray diffraction investigation of the early stages of nanoparticle growth in a bulk material Al-Cu sample containing embedded nanoparticles, using reciprocal space mapping. The time-dependent changes in

one dimensional (1D) diffraction profiles extracted from the reciprocal space maps are shown to be in excellent agreement with simulated profiles based on a semi-quantitative model of local interparticle strain.

6.2 Establishing the sensitivity of the reciprocal space mapping technique to nanoparticle size and orientation: a feasibility study

6.2.1 Introduction

In this section we describe an experiment designed to investigate the sensitivity of the TAD setup to various size distributions of nanoparticles, and to changes in the orientation of the embedded nanoparticles with respect to the diffraction plane of the analyser crystal, as explored in the simulations in §5.3.3. Some results from this section are featured in the publication *Early detection of nanoparticle growth from X-ray reciprocal space mapping*, N. A. Zatsepin, R. A. Dilanian, A. Y. Nikulin, B. M. Gable, B. C. Muddle and O. Sakata, *Appl. Phys. Lett.*, **92** 34101 (2008). This publication is included in the Appendix ([Zatsepin et al., 2008](#)).

6.2.2 Experimental setup and sample details

The experiment was carried out on BL29XU, SPring-8, details of which were presented in §4.1. The TAD setup, as shown in Figure 4.4 and described in §4.2, involved a double reflection, channel-cut Si(400) monochromator, used to select 10.9 keV X-rays, with slits limiting the beam size to $0.25 \times 1.00 \text{mm}^2$ (v×h) for most samples, and $0.20 \times 0.20 \text{mm}^2$ (v×h) for the TAD instrumental function measurements. The analyser was a single reflection Si(400) crystal (refer to §4.2.1) and the detector was a silicon PIN diode (§4.1) with a $0.25 \times 5.00 \text{mm}^2$ (v×h) slit.

The samples were thin discs with diameters of 3mm and thicknesses along the beam propagation direction from $0.60 \pm 0.05 \text{mm}$ to $1.50 \pm 0.05 \text{mm}$, cut from an Al-2.0wt% Cu single-crystal, with the surface parallel to $(100)_{\text{Al}}$. The size of the sample discs was chosen so that samples could easily be prepared for transmission electron microscopy (TEM) subsequently to the X-ray experiments. All samples were subjected to solution heat treating for an hour at 530°C and water quenched, as described in §2.2.

We prepared six samples to explore four different size distributions of embedded nanoparticles, and different sample thicknesses, as listed in Table 6.1. The estimated modal particle diameter was based on heat treatments and previous experience with related samples (Gable, 2006b). These size distributions were chosen to represent four relatively early stages of nanoparticle growth, as understanding the details of these stages are most important for controlling the final microstructure (cf. §2.2). Starting with such small, potentially polydisperse, weakly diffracting embedded nanoparticles presents a challenge as it was unknown whether they would result in any measurable signal.

#	Sample thickness (mm)	Ageing temp. (°C)	Ageing time (hours)	Estimated mean particle diameter, S_m (nm) (Gable, 2006b)
Sample 0	0.65 ± 0.05	120	96	<< 100
Sample 1a	0.73 ± 0.05	150	172	~150
Sample 1b	0.50 ± 0.05	150	172	~150
Sample 2a	0.70 ± 0.05	180	72	~250
Sample 2b	1.50 ± 0.05	180	72	~250
Sample 3a	0.65 ± 0.05	200	48	~350
Sample 3b	1.60 ± 0.05	200	48	~350

TABLE 6.1: List of Al-2.0wt% Cu samples prepared for the feasibility study. Details of various samples prepared for testing the sensitivity of the reciprocal space mapping technique to nanoparticle size, rotation and sample thickness. These samples were cut from a Al-2.0wt% Cu single crystal, with (100)_{Al} parallel to the surface.

6.2.3 Results

The results will be presented by starting with the TAD instrumental function RSM, followed by the sample RSMs and their respective monochromator pseudo streak profiles, each with some discussion. Finally, we discuss the comparison of scaled, symmetrised monochromator pseudo streaks from all samples, and close with general conclusions obtained from this feasibility study.

TAD instrumental function

The TAD instrumental function measured for this particular setup is shown in (Q_x, Q_z) coordinates in Figure 6.1, obtained from $(\alpha, \Delta 2\theta)$ via eqs. (4.9) and (4.10). As with all experimental RSMs presented in this thesis, the intensity has been scaled

against the natural decrease of the current over time, and is displayed on a log scale. This instrumental function has a lower signal to noise ratio (SNR) than that shown in Figure 5.14(b), where we introduced the TAD instrumental function characteristics, since the beam used here was smaller. Qualitatively it is identical, with a thin detector streak and analyser crystal truncation rod, labelled D and C respectively, on a diffuse background. Analyser crystals are never truly perfect, so there is always a diffuse background signal from thermal and point defect diffuse scattering, and dissolved O_2 . There are also parasitic scattering phenomena such as air scattering and contributions from the Beryllium window at the entrance to the synchrotron optics hutch.

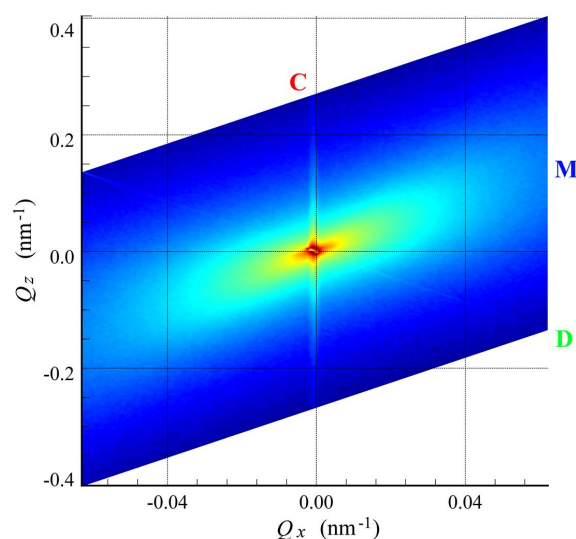


FIGURE 6.1: **Experimental TAD instrumental function**, displayed on a log scale. Reciprocal space map around the Si(400) reflection, showing the analyser's crystal truncation rod (labelled C), monochromator and detector pseudo streaks, labelled M and D, respectively. The beam size at the position of the (absent) sample was $0.20 \times 0.20 \text{ mm}^2$ ($v \times h$).

The limited experimental time at synchrotrons and the sensitivity of the detector meant that the RSMs of the TAD instrumental function were generally measured with shorter exposure times than RSMs with the sample in place, and often with lower resolution, and/or smaller angular range. Qualitatively, this is sufficient in order to ascertain the effects of the instrumental function. However, there is no obvious manner in which to calibrate the RSMs to an identical intensity scale, for a number of reasons. Firstly, in the vicinity of the reciprocal lattice point, i.e. the central region of the RSM, the beam either saturated the detector or its intensity was outside the detector's linear dynamic range (above approximately 5×10^5 photon/sec), even

despite considerable attenuation from the thickest Al-Cu samples (e.g. the thickness of sample 3b was $1.60 \pm 0.05\text{mm}$). Secondly, normalising to the tails of the diffraction peaks, or a region of diffuse scattering away from any particular diffraction streak, may also not be appropriate as the overall scattering and absorption of the sample, which affects entire RSM, is not accurately known.

Sample 0

Sample 0 was an $0.65 \pm 0.05\text{mm}$ thick Al-2.0wt%Cu crystal aged for 96 hours at 120°C . In Figure 2.4 the hardness curve for an Al-2.0wt%Cu crystal artificially aged at 130°C remained relatively flat for over 110 hours. This indicates that precipitation growth after 96 hours is still in the very early stages with a microstructure composed entirely of GP zones that have diameters much smaller than 100nm (see §2.2.1). Since sample 0 was aged at 120°C , its hardness would increase even more slowly than that aged at 130°C , implying that the microstructure in sample 0 was as described, i.e. composed of a large number of GP zones.

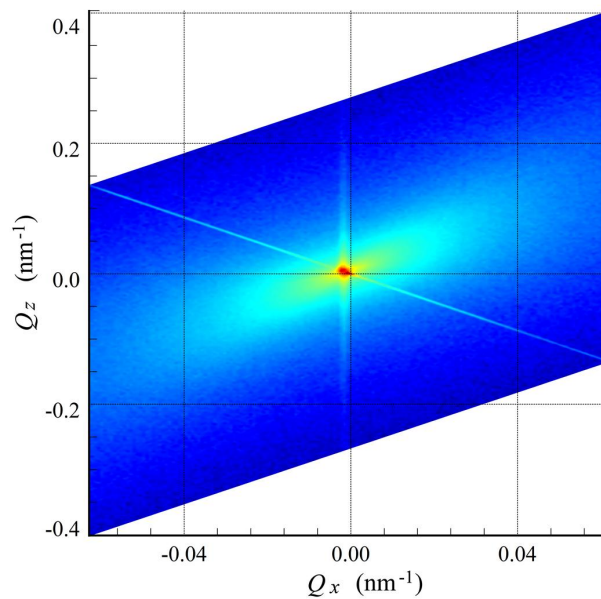


FIGURE 6.2: **Experimental RSM from sample 0** ($0.65 \pm 0.05\text{mm}$ thick, $S_m \ll 100\text{nm}$), displayed on a log scale. The angular ranges were $\alpha = \pm 0.966^\circ$, $\Delta 2\theta = \pm 1.932^\circ$, with steps of 0.012° and 0.024° respectively. The beam size was $0.25 \times 1.00\text{mm}^2$ (v×h).

As discussed in §4.3.2, Fraunhofer diffraction from the sample is expected to be most prominent along the monochromator pseudo streak, where $\alpha = \Delta 2\theta$. The

monochromator pseudo streaks from the instrumental function and from the RSM of sample 0, with the intensity of the latter scaled by 12, are compared in Figure 6.3. The intensity of the diffraction profile from sample 0 is lower than without the sample due to absorption, but the central regions ($\alpha = (-0.1, 0.1)$) can not be reliably compared as the instrumental function's profile extends beyond the linear dynamic range of the detector, as mentioned earlier. The agreement between the scaled monochromator pseudo streak profile from sample 0 (dashed blue line) and the instrumental function profile indicates the lack of a significant diffraction signal from the nanoparticles in the sample. The GP zones are simply too small and too weakly diffracting to result in a measurable diffraction signal.

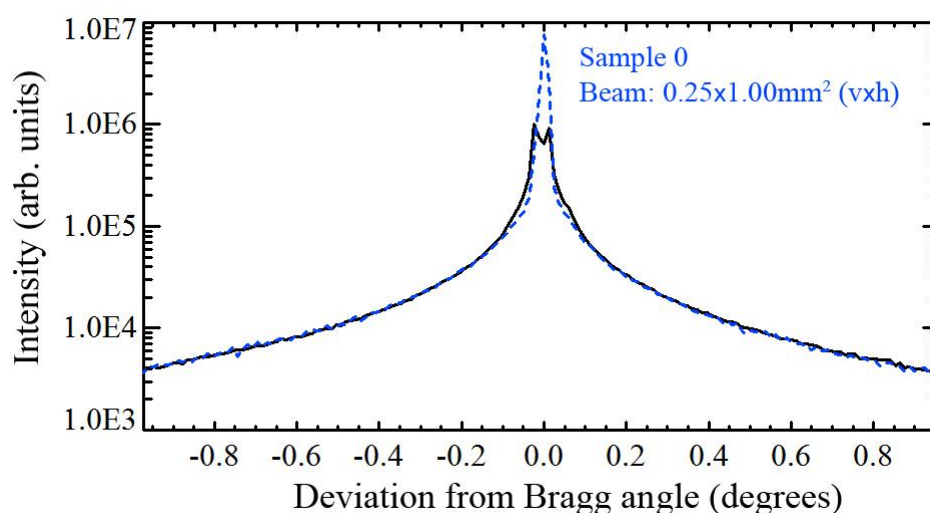


FIGURE 6.3: Experimental monochromator pseudo streaks from the TAD instrumental function (solid black line) and sample 0 (dashed blue line). Sample 0 was 0.65 ± 0.05 mm thick, with $S_m \ll 100$ nm, and the beam size was 0.25×1.00 mm² (v × h). The sample's monochromator pseudo streak's intensity was scaled by 12 to facilitate comparison with the instrumental function, showing that they are almost identical. The central point of the TAD instrumental function indicates saturation of the detector.

Samples 1a and 1b

Samples 1a and 1b were 0.73 ± 0.05 mm and 0.50 ± 0.05 mm thick Al-2.0wt%Cu crystals, respectively, aged for 172 hours at 150°C, yielding an estimated mean nanoparticle diameter of ~ 150 nm. The RSM collected from sample 1a (0.73 ± 0.05 mm) was obtained with a beam size of 0.20×0.20 mm² (v × h), shown in Figure 6.4(a), while for the RSM

from sample 1b ($0.50 \pm 0.05\text{mm}$), in Figure 6.4(b), a beam size of $0.25 \times 1.00\text{mm}^2$ ($v \times h$) was used. All other experimental parameters were identical.

Despite an improved SNR due to the increase in beam cross section by a factor of 6.25 and decrease in sample thickness by $0.23 \pm 0.10\text{mm}$ for sample 1b, no significant diffraction signal from the sample was evident in either RSM, as evident in Figure 6.5. Again, we attribute this to insufficient diffracting volume, as the estimated average nanoparticle diameter was 150nm.

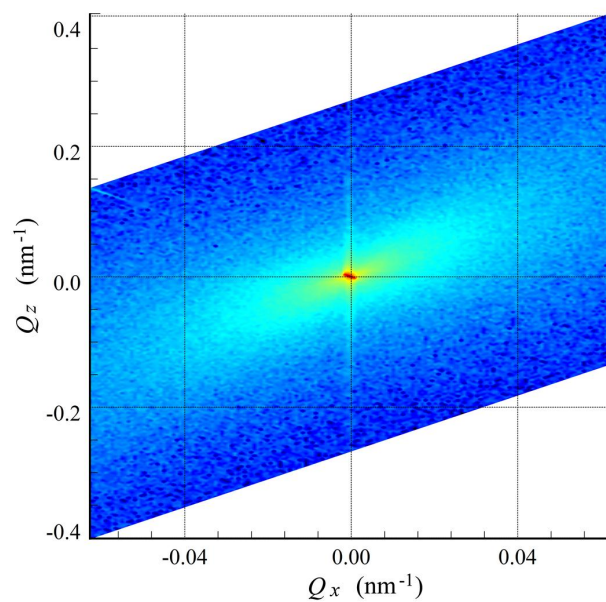
Sample 2a

Sample 2a was an $0.70 \pm 0.05\text{mm}$ thick Al-2.0wt% Cu crystal, aged for 72 hours at 180°C , yielding an estimated $S_m \approx 250\text{nm}$. RSMs were collected for two orientations of sample 2a as shown in Figure 6.6. The measurements were then repeated with a smaller beam to test for consistency, with results shown in Figure 6.7. One orientation of the sample was with $(100)_{\text{Al}}$ and $(010)_{\text{Al}}$ planes (§2.2) parallel and perpendicular to the diffraction plane of the analyser, in order to maximise the diffraction contrast due to the high aspect ratio (diameter to thickness) of the nanoplatelets. For the second orientation the sample was rotated by 45° about the optical axis. The effective diameter of platelets in both planes in orientation 2 was then, ideally, $S_m / \sqrt{2}$ (where S_m is the mean diameter as in Figure 5.16), and the equivalent contribution from both crystallographic planes at 45° to the diffraction plane was expected to enhance the total diffraction signal (§5.3.3).

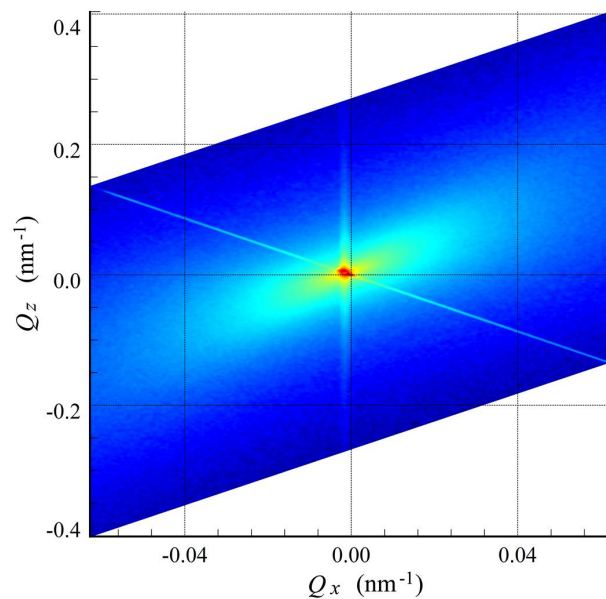
The repeated measurements used a smaller beam, i.e. $0.25 \times 0.20\text{mm}^2$ ($v \times h$) for Figure 6.7 compared to $0.25 \times 1.00\text{mm}^2$ ($v \times h$) for Figure 6.6. The detector pseudo streak is mostly unresolvable in Figure 6.7(b), due to the streak's characteristic thinness and possible drift in the setup during the overall scan duration. It is difficult to make a qualitative comparison between the two beam sizes directly from the RSMs due to the decrease in the SNR, so the four monochromator pseudo streaks, measured with two beam sizes for each sample orientation, are compared in Figure 6.8.

The Fraunhofer diffraction pattern from a real electron density distribution has twofold rotational symmetry (Bracewell, 2000). As a result, we expected to see a symmetric diffraction profile representing the Fourier transform (FT) of the effective nanoparticle diameters along the x_s axis akin to our simulations in §5.3.3.

In Figure 6.6(a) it is evident that sample 2a in orientation 1 has given rise to a streak along the monochromator pseudo streak direction. In orientation 2, where the nanoprecipitates were at $\pm 45^\circ$ to the diffraction plane, the monochromator pseudo streak (Figure 6.6(b)) was shortened in the positive Q_x direction, while being markedly



(a) Sample 1a. The beam size was $0.20 \times 0.20 \text{mm}^2$ ($v \times h$).



(b) Sample 1b. The beam size was $0.25 \times 1.00 \text{mm}^2$ ($v \times h$).

FIGURE 6.4: **Experimental RSMs of sample 1a** ($0.73 \pm 0.05 \text{mm}$ thick, $S_m \approx 150 \text{nm}$) **and sample 1b** ($0.50 \pm 0.05 \text{mm}$ thick, $S_m \approx 150 \text{nm}$) **using different beam sizes**, displayed on a log scale. The angular ranges were $\alpha = \pm 0.966^\circ$, $\Delta 2\theta = \pm 1.932^\circ$, with steps of 0.012° and 0.024° respectively.

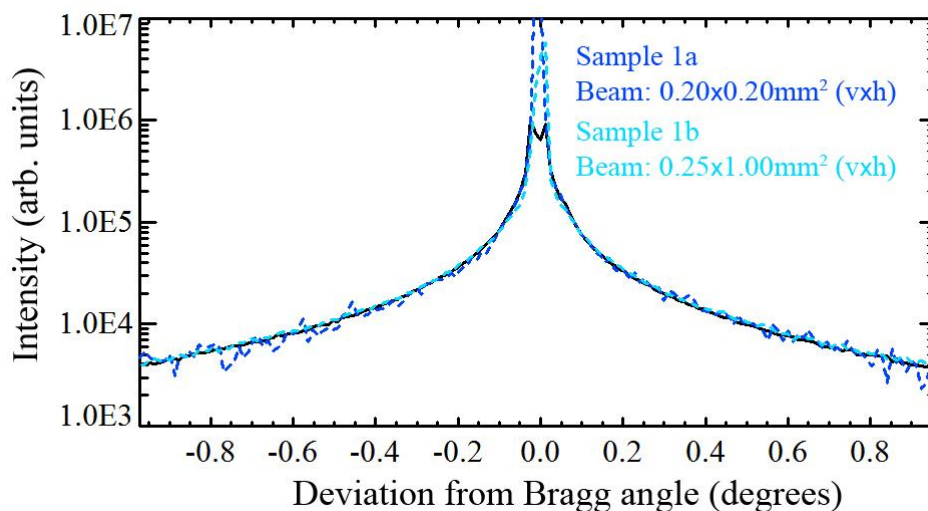
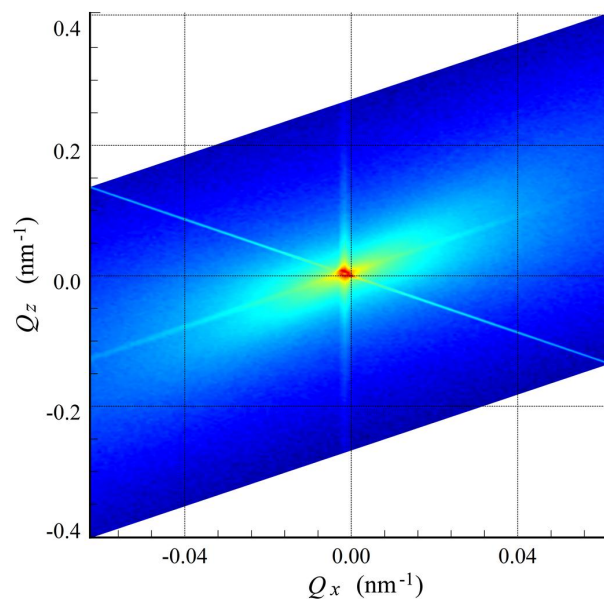


FIGURE 6.5: Experimental monochromator pseudo streaks from the TAD instrumental function (solid black line), sample 1a (dashed blue line) and sample 1b (dashed cyan line). Sample 1a was 0.73 ± 0.05 mm thick, with $S_m \approx 150$ nm, and the beam size was 0.20×0.20 mm² (v×h), while sample 1b was 0.50 ± 0.05 mm thick, with $S_m \approx 150$ nm, and the beam size was 0.25×1.00 mm² (v×h). The dashed blue and cyan profiles, from sample 1a and 1b, have been scaled by 62.5 and 9, respectively, to facilitate comparison with the instrumental function profile.

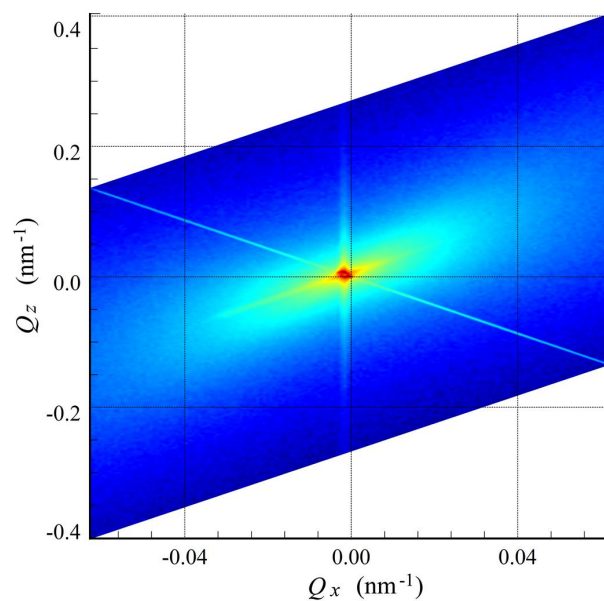
diminished in intensity in the negative Q_x direction. This is more clearly shown in Figure 6.8 where the monochromator pseudo streaks from the instrumental function and both orientations of sample 2a are compared.

In Figure 6.8 we compare the scans from each orientation, separately, where the intensity of the monochromator pseudo streaks measured with the smaller beam has been scaled ($\times 56$) and boxcar averaged (over 3 pixels), while those measured with the bigger beam were scaled by 8. The excellent agreement between the profiles for orientation 2, in particular, demonstrate the reproducibility of the results (Figure 6.8(b)). The weak asymmetry between scans from orientation 1 (Figure 6.8(a)) may be due to a number of reasons, which will be discussed in §6.2.5.

Recall that the simulated monochromator pseudo streak diffraction profiles from azimuthal rotation of sample 2a (in §5.3.3, where a monodisperse diameter distribution was assumed) showed that given a perfect initial alignment of the $(010)_{Al}$ plane with the Q_z axis, the greatest difference in the diffraction profile was visible for a 45° rotation about the optical axis. Even slight rotation of the sample forces the monochromator pseudo streak tail's intensity to decrease significantly (see Figure 5.18). If orientation 1 was with $(010)_{Al}$ at 5° from the Q_z axis, and orientation 2

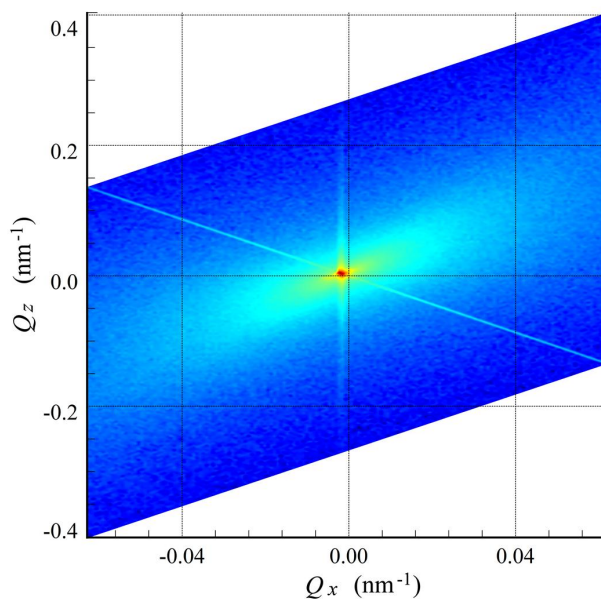


(a) Sample 2a in orientation 1. Beam size = $0.25 \times 1.00 \text{mm}^2$ (v×h).

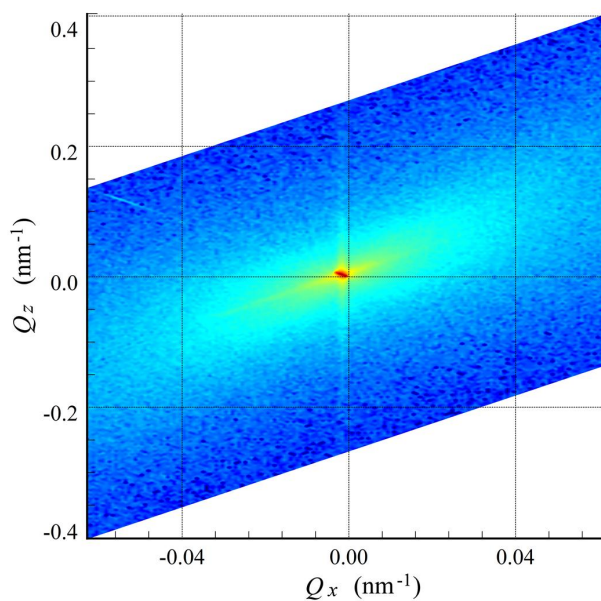


(b) Sample 2a in orientation 2. Beam size = $0.25 \times 1.00 \text{mm}^2$ (v×h).

FIGURE 6.6: **Experimental RSMs of sample 2a** ($0.70 \pm 0.05 \text{mm}$ thick, $S_m \approx 250 \text{nm}$) **in two orientations**, displayed on a log scale. The angular ranges were $\alpha = \pm 0.966^\circ$ and $\Delta 2\theta = \pm 1.932^\circ$, with steps of 0.012° and 0.024° respectively. The second orientation (b) is at 45° relative to the first (a).

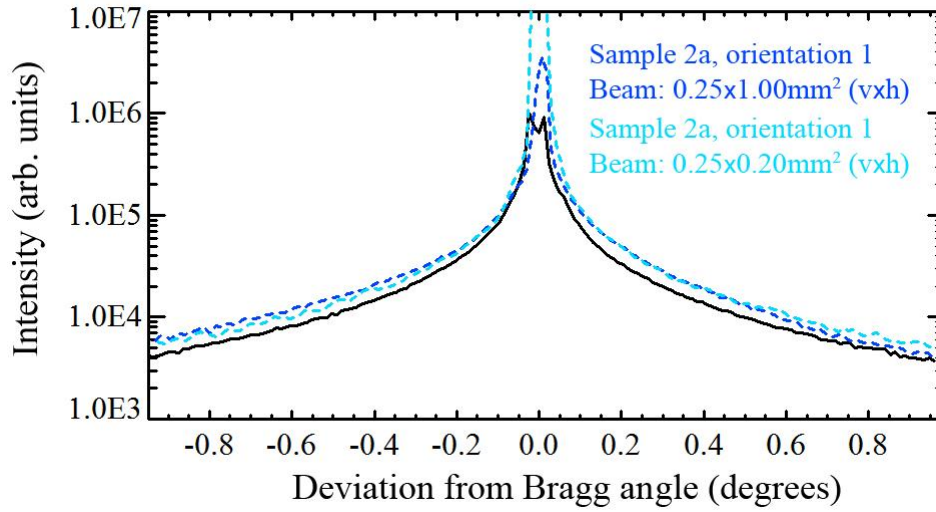


(a) Sample 2a in orientation 1. Beam size = $0.25 \times 0.20 \text{mm}^2$ (v×h).

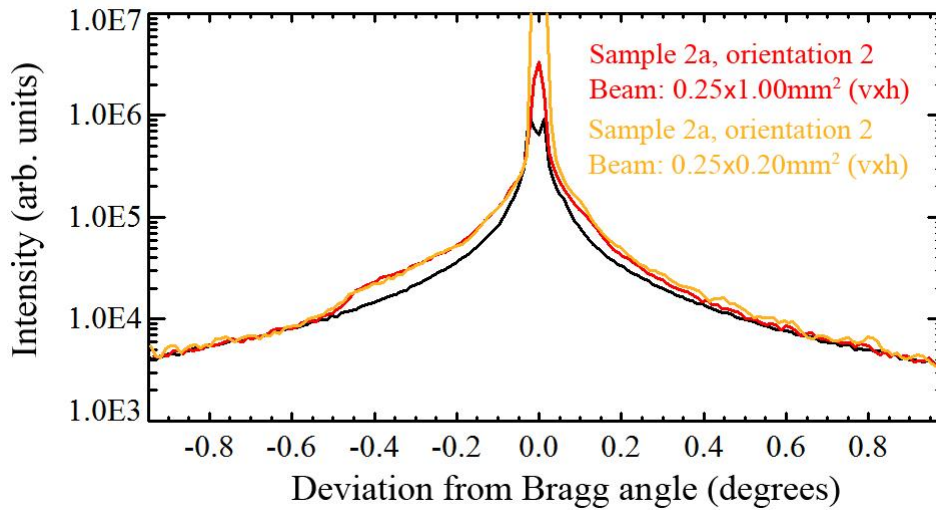


(b) Sample 2a in orientation 2. Beam size = $0.25 \times 0.20 \text{mm}^2$ (v×h).

FIGURE 6.7: Experimental RSMs of sample 2a ($0.70 \pm 0.05 \text{mm}$ thick, $S_m \approx 250 \text{nm}$) in two orientations, using a smaller beam than in Figure 6.6, displayed on a log scale. The angular ranges were $\alpha = \pm 0.966^\circ$, $\Delta 2\theta = \pm 1.932^\circ$, with steps of 0.012° and 0.024° respectively. The second orientation is at 45° relative to the first.



(a) Sample 2a in orientation 1.



(b) Sample 2a in orientation 2.

FIGURE 6.8: **Experimental monochromator pseudo streak profiles from sample 2a** ($0.70 \pm 0.05\text{mm}$ thick, with $S_m \approx 250\text{nm}$) **in two orientations and with two different beam sizes**. The dashed blue line in (a) and solid red line in (b) were scaled by 8 for comparison with the monochromator pseudo streak from the TAD instrumental function (solid black line). The dashed cyan line in (a) and the solid orange line in (b) are from the RSMs obtained with a smaller beam ($0.25 \times 0.20\text{mm}^2$ ($v \times h$)) than the blue and red profiles ($0.25 \times 1.00\text{mm}^2$ ($v \times h$)), so for this comparison the intensities have been scaled by 56 and a boxcar smoothing function has been applied. The second orientation is at 45° relative to the first. The excellent agreement between the monochromator pseudo streaks from the sample in the second orientation, i.e. the solid red and orange lines in (b), in particular, demonstrates the reproducibility of the experimental results obtained with this technique.

had $(010)_{\text{Al}}$ at 50° from the Q_z axis, the difference between the two would not be as significant. We previously discussed (and showed in Figure 5.15) that the three-axis symmetry of the nanoparticle habitat planes results in a high degree of redundancy in the rotation about the optical axis. Suppose the misorientation in this experiment was precisely $\theta_z = \pm 22.5^\circ$, then a rotation of the sample about the optical axis by 45° into orientation 2 ($\theta_z = \pm 67.5^\circ$) would result in identical effective diameters from the complementary orthogonal nanoparticle orientation (see Figure 5.15), since $250 \sin 22.5^\circ = 250 \cos 67.5^\circ$, and no change would be observed along the monochromator pseudo streak. Any other initial misorientation of θ_z would result in some intermediate visibility of the changes in the diffraction profile when the sample is rotated by 45° .

It is most likely that the alignment of the nano-platelets in this experiment was not exactly parallel and perpendicular to the analyser crystal's diffraction plane as initially assumed, for the following reasons. Firstly, it is probable that the surface of the sample was not ideally parallel to $(100)_{\text{Al}}$, despite being cut with an accuracy of $<1^\circ$ (§2.2.3). The careful mechanical grinding/thinning of samples 1, 2, and 3 for this experiment was performed manually with extra fine grade sandpaper (P1200), which may have easily exacerbated this misalignment. Secondly, retaining ideal alignment of the thin specimens (3mm wide discs) in the mini sample holder, sandwiched between the platinum foil separating the flat brass layers (Figure 4.12) is very difficult when manually inserting the sample. Thirdly, the sample itself may not have perfectly parallel surfaces, the platinum foil may be curved, and the brass mini sample holder may also have slightly unparallel surfaces. Also, when the sample-sandwich is positioned in the heater it too may not be perfectly aligned with its face normal to the beam. The unavoidable, unquantifiable, compounded effect of the possible causes of nanoparticle misalignment ambiguates quantitative analysis of monochromator pseudo streaks, especially since the nanoparticle distribution may be polydisperse.

Sample 2b

RSMs collected from sample 2b, a thicker version of sample 2a, are shown in Figure 6.9. The increased thickness of the sample ($1.50 \pm 0.05\text{mm}$ compared to $0.70 \pm 0.05\text{mm}$ for sample 2a) meant the number of nanoparticles involved in the diffraction was more than doubled, but the attenuation by the Al matrix also increased. Theoretically, the $0.70 \pm 0.05\text{mm}$ thick Al-2.0wt% Cu discs resulted in $\sim 1.07\%$ transmission of incident intensity, while the $1.50 \pm 0.05\text{mm}$ Al-2.0wt% Cu resulted in only $\sim 0.006\%$ intensity transmission. Hence despite using an X-ray source of extremely high brilliance (§4.1)

the low number of particles (which ideally increases linearly with sample thickness) was insufficient to yield a high SNR.

The small beam size ($0.20 \times 0.50 \text{mm}^2$ ($v \times h$)) used to measure the RSM of sample 2b in orientation 1, as shown in Figure 6.9(a), rendered the detector pseudo streak unresolvable, due to both the low intensity and the streak's characteristic thinness (cf. §5.3). For the RSM of sample 2b in orientation 2 (Figure 6.9(b)), the beam size was enlarged to $0.25 \times 1.50 \text{mm}^2$ ($v \times h$), so the detector streak is more evident, and the SNR is higher so the noise fluctuations are less significant.

The monochromator pseudo streak profiles from sample 2b are compared with the instrumental function monochromator streak in Figure 6.10. For easier comparison with the instrumental function, both profiles have been scaled (by 2.5×10^3) and boxcar smoothed (3 pixels), and displayed in the same figure. The peak intensity from sample 2b in orientation 2 (solid red line) is higher than for orientation 1 (dashed blue line) due to the increase in beam size by a factor of 3.75.

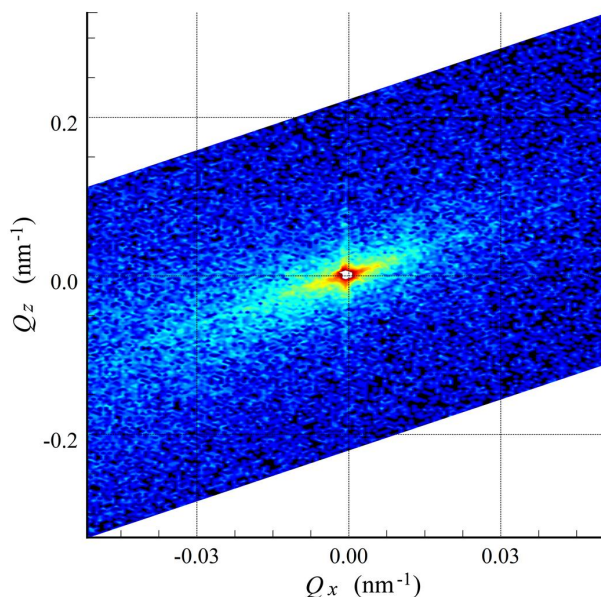
Both diffraction profiles (dashed blue and solid red) manifest approximately symmetric intensity modulations in the region ($\alpha = \Delta 2\theta$) $\in (-0.1^\circ, 0.1^\circ)$, manifesting a similar shape to an Airy pattern. Ignoring diffraction from those particles with their flat faces normal to the optical axis (as they are too thin to cause a measurable signal), there should ideally be a contribution from each of the two nanoparticle orientations (2) and (3) in Figure 5.3, as was discussed at the end of §5.3.3. In that section we also discussed how to obtain the mean nanoparticle diameter, S , and the angle between $(100)_{\text{Al}}$ and the diffraction plane, θ_Z , from the diffraction profiles of two sample orientations with a known relative angle (eqs. (5.22) and (5.22)).

For orientation 1 (dashed blue line), where the nanoparticles were perpendicular and parallel to the diffraction plane, the first minima are at $\sim \pm 0.03^\circ$, which according to eq. (5.21) correspond to an effective nanoparticle diameter of $\sim 265 \text{nm}$. For orientation 2 (solid red line), rotated by 45° about the optical axis relative to the first orientation, the first minima are at $\sim \pm 0.04^\circ$, yielding an effective diameter of $\sim 200 \text{nm}$. In measuring only one Airy pattern for each sample orientation, ambiguity arises from the lack of knowledge about which particle, (2) or (3) in Figure 5.3, the pattern corresponds to. Hence from orientation 1 of the sample, eq. (5.22) could take the form of either

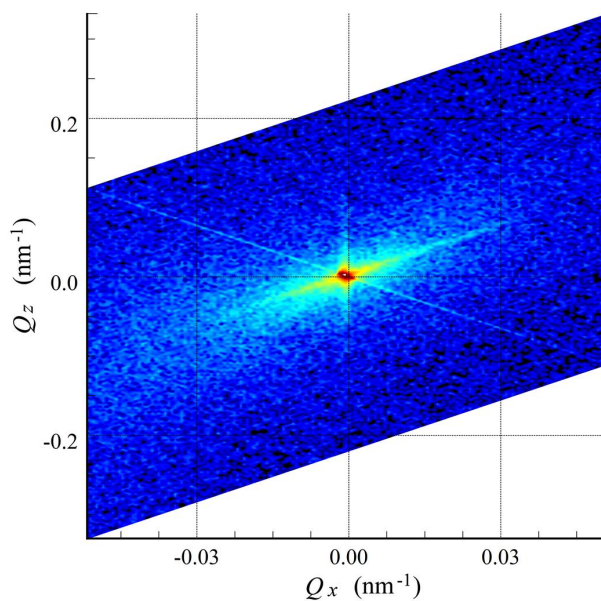
$$S|\cos \theta_Z| \approx 265, \quad (6.1)$$

or

$$S|\sin \theta_Z| \approx 265, \quad (6.2)$$



(a) Sample 2b, orientation 1. The beam size was $0.20 \times 0.50 \text{mm}^2$ (v×h).



(b) Sample 2b, orientation 2. The beam size was $0.25 \times 1.50 \text{mm}^2$ (v×h).

FIGURE 6.9: **Experimental RSMs from sample 2b** ($1.50 \pm 0.05 \text{mm}$ thick, $S_m \approx 250 \text{nm}$) **in two orientations**, displayed on a log scale. The angular ranges were $\alpha = \pm 0.795^\circ$, $\Delta 2\theta = \pm 1.59^\circ$, with steps of 0.01° and 0.02° respectively, and half the range for the instrumental function. The second orientation is at 45° relative to the first.

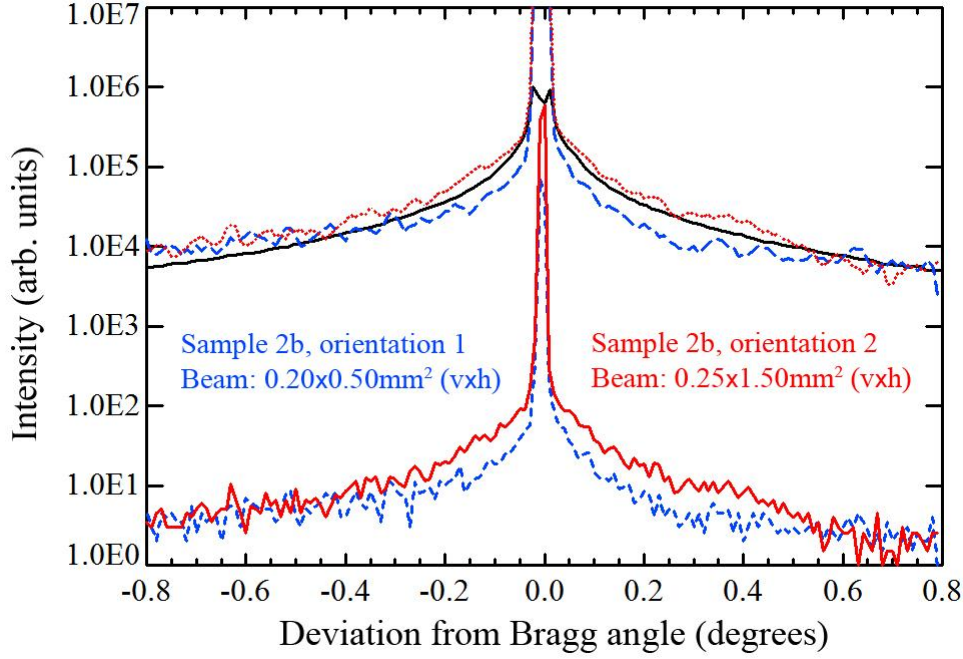


FIGURE 6.10: Experimental monochromator pseudo streaks from the TAD instrumental function (solid black line), sample 2b in orientation 1 (dashed blue line) and orientation 2 (solid red line). Sample 2b was $1.50 \pm 0.05\text{mm}$ thick, with $S_m \approx 250\text{nm}$, and the beam size was $0.20 \times 0.50\text{mm}^2$ (v×h) for orientation 1 and $0.25 \times 1.50\text{mm}^2$ (v×h) for orientation 2. The long-dashed blue profile and dotted red profile have been scaled by 2.5×10^3 from the correspondingly colored profiles from sample 2b, and smoothed by boxcar averaging over 3 pixels to facilitate comparison with the instrumental function profile.

while from orientation 2 of the sample, eq. (5.23) could take the form

$$S |\cos[\theta_Z + 45]| \approx 199, \quad (6.3)$$

or

$$S |\sin[\theta_Z + 45]| \approx 199, \quad (6.4)$$

leading to four possible combinations of eqs. (5.22) and (5.23). Three of these combinations result in $S \approx 265.5\text{nm}$, with $\theta_Z \approx \pm 3.5^\circ$, while the combination of eq. (6.2) and eq. (6.3) leads to $S \approx 607.1\text{nm}$ and $\theta_Z \approx 25.9^\circ$. Based on this, and our initial estimate that sample 2b was prepared with an average nanoparticle diameter of $\sim 250\text{nm}$, we choose $S \approx 265.5\text{nm}$ and $\theta_Z \approx \pm 3.5^\circ$ as the most reasonable solution.

It is important to note, however, that the intensity minima on which these values depend were single points in the measured diffraction profile, at very small angular deviations from the Bragg conditions, so they are not very accurate. In addition,

care must be taken with such noisy data to not misinterpret the noise fluctuations as a diffraction signal from the nanoparticles. If the intention was to base the characterisation solely on the monochromator pseudo streak, then the analysis would obviously benefit from a much more accurate measurement of the intensity at very small angular deviations, which are readily obtainable with the TAD setup. However, it would be impractical to measure the entire two dimensional (2D) RSM with such angular precision.

Sample 3a

Sample 3a was an 0.65 ± 0.05 mm thick Al-2.0wt% Cu crystal, aged for 48 hours at 200°C , yielding an estimated $S_m \approx 350$ nm. RSMs from sample 3a (Figure 6.11) were measured with slightly higher angular precision (and hence a higher sampling frequency) than that for samples 1 and 2, i.e. $\alpha_{\text{step}} = 0.008^\circ$, compared to $\alpha_{\text{step}} = 0.012^\circ$ and the beam size was 0.25×1.00 mm² (v×h).

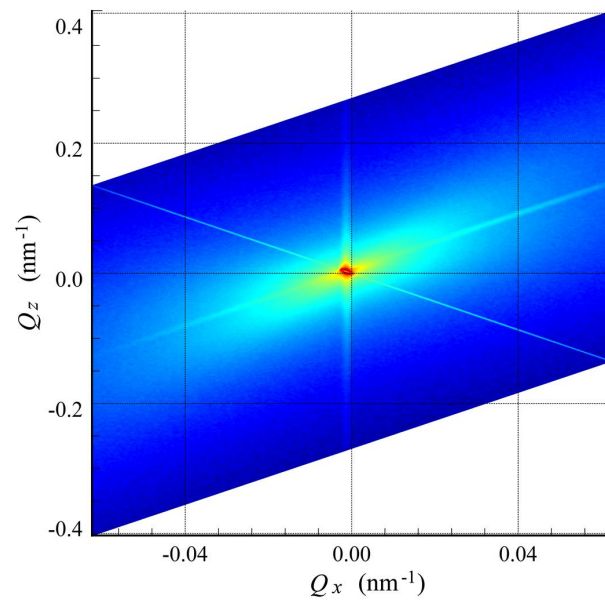
For clarity, the monochromator pseudo streak profiles are compared in Figure 6.12. We observe the same qualitative effect as for the rotation of sample 2a (Figure 6.8(b)), i.e. the diffracted intensity profile from the second orientation decreased overall, and was shortened in the negative Q_x direction, again manifesting weak asymmetry. This is easier to see in the comparison of the instrumental function (solid black line) and the scaled (by 7.5) diffraction profile from sample 3a in orientation 2 (solid red line). The shoulder drops off at $\sim -0.44^\circ$, while for sample 2a it was at $\sim -0.47^\circ$. It is not certain exactly what is causing this particular profile, but possible reasons for such asymmetry will be discussed below, in §6.2.5.

Sample 3b

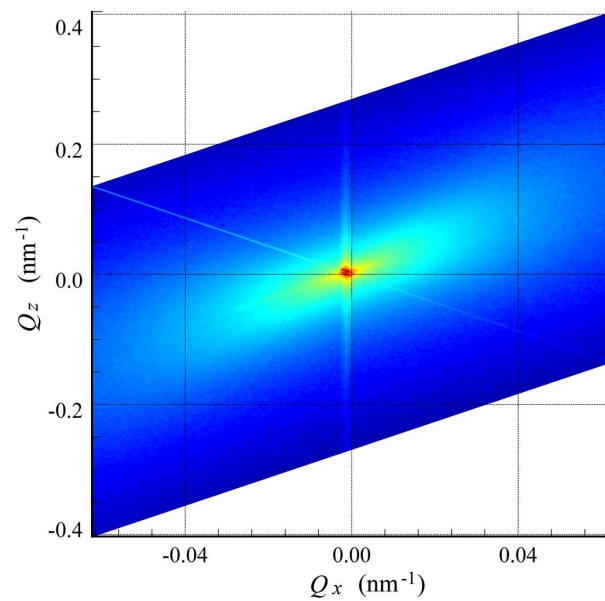
Sample 3b was 1.60 ± 0.05 mm thick with an estimated $S_m \approx 350$ nm, aged at 200°C for 48 hours. The RSM for sample 3b in Figure 6.13 was collected with the same beam size as for sample 3a (0.25×1.00 mm² (v×h)). We expected the increased number of nanoparticles in the beam to provide sufficient diffracting volume for a stronger signal to be seen than for sample 3a or 2a.

In Figure 6.14 the monochromator pseudo streak profile from sample 3b in orientation 1 is compared to the profile from sample 2b (since they have a similar thickness but different nanoparticle size distributions), and to the profile from sample 3a (as they have the same nanoparticle size distribution but different sample thicknesses).

An Al-2.0wt% Cu specimen that underwent the same heat treatment as samples



(a) Sample 3a, orientation 1.



(b) Sample 3a, orientation 2.

FIGURE 6.11: **Experimental RSMs from sample 3a** ($0.65 \pm 0.05\text{mm}$ thick, $S_m \approx 350\text{nm}$) **in two orientations**, displayed on a log scale. The angular ranges were $\alpha = \pm 0.968^\circ$, $\Delta 2\theta = \pm 1.936^\circ$, with steps of 0.008° and 0.016° , respectively. The beam size was $0.25 \times 1.00\text{mm}^2$ ($v \times h$).

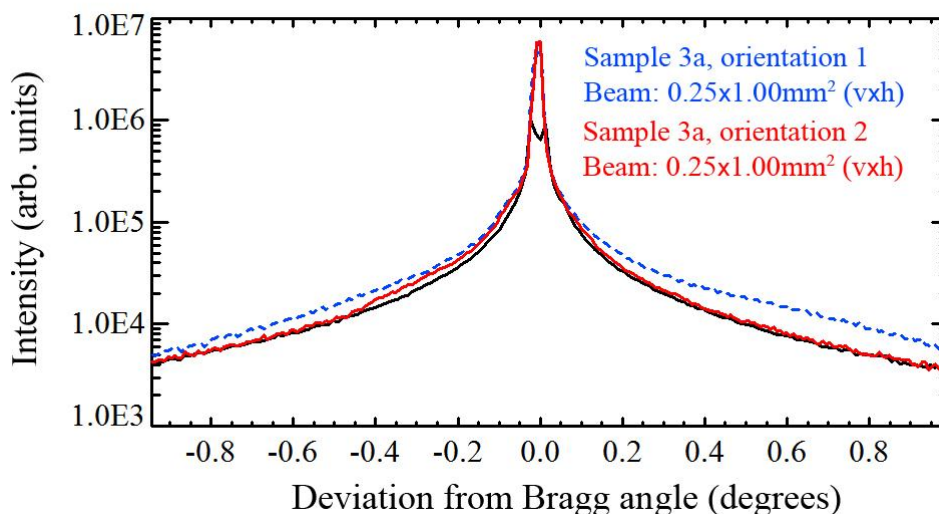


FIGURE 6.12: **Experimental monochromator pseudo streaks from the TAD instrumental function (solid black line), sample 3a in orientation 1 (dashed blue line) and orientation 2 (solid red line).** Sample 3a was $0.65 \pm 0.05\text{mm}$ thick, with $S_m \approx 350\text{nm}$, and the beam size was $0.25 \times 1.00\text{mm}^2$ (v \times h). The monochromator pseudo streak intensities from the sample have been scaled by 7.5 and smoothed by boxcar averaging over 3 pixels to facilitate comparison with the instrumental function profile. The asymmetry in the red profile is very similar to that seen from sample 2a in the same orientation (i.e. the solid red and orange profiles in Figure 6.8(b)).

3a and 3b was analysed by TEM (carried out on a Philips CM20 instrument operated at 200 keV) for nanoparticle number density and size distribution. From 24 micrographs, the nanoparticle number density was estimated to be ~ 12 particles/ μm^3 . The nanoparticle diameter distribution calculated from these TEM micrographs indicated a distribution of nanoparticle diameters that qualitatively followed a Boltzmann distribution, with a modal nanoparticle diameter of $\sim 370\text{nm}$.

It appears that in this case, since the thickness of the sample theoretically results in $\sim 0.003\%$ intensity transmission, once again the SNR was too low, despite the increase in nanoparticle size (compared to sample 2b, which at $1.50 \pm 0.05\text{mm}$ was similar in thickness, with an estimated nanoparticle mean diameter of 250nm).

We will compare the symmetrised and scaled monochromator pseudo streaks from all the samples in the discussion following the reconstruction section below.

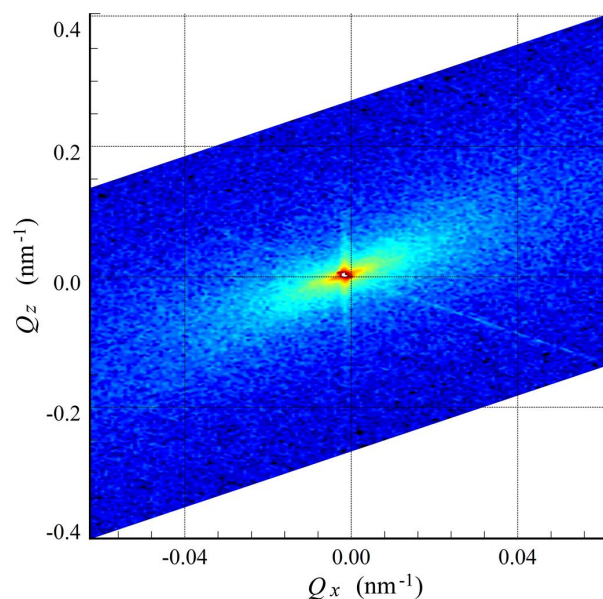


FIGURE 6.13: Experimental RSM from sample 3b ($1.60 \pm 0.05\text{mm}$ thick, $S_m \approx 350\text{ nm}$), displayed on a log scale. The angular ranges were $\alpha = \pm 0.966^\circ$, $\Delta 2\theta = \pm 1.932^\circ$, with steps of 0.012° and 0.024° respectively. The beam size was $0.25 \times 1.00\text{mm}^2$ ($v \times h$).

6.2.4 Nanoparticle reconstruction

As proof of concept, we present the reconstruction of an average nanoparticle, representative of the illuminated ensemble, from an experimentally measured RSM presented in the above section. This particular nanoparticle reconstruction was carried out by Dr. Ruben Dilanian, then at the School of Physics, Monash University.

The phase retrieval or image reconstruction algorithm used here was the hybrid input-output (HIO) algorithm presented in §5.2.1. This algorithm has previously been shown to successfully reconstruct a 2D image of a modal Al_2O_3 nanoparticle in an amorphous matrix, from experimental Fraunhofer diffraction data (Dilanian and Nikulin, 2005), where the authors employed a triple axis diffractometry setup identical to that used in this thesis. In this earlier work *a priori* knowledge about the spherical symmetry of the particle lead to a pseudo-3D reconstruction (Dilanian and Nikulin, 2005).

The measured RSM from sample 2a ($0.70 \pm 0.05\text{mm}$ thick) in orientation 1 (Figure 6.6(a)) was best suited to enable a reconstruction due to several factors: the sample contained a sufficient number of nanoparticles of suitably large size (estimated $S_m \approx 250\text{nm}$), to yield a significant SNR despite absorption, wherein the beam was large enough to encompass a sufficient number of said nanoparticles ($0.25 \times 1.00\text{mm}^2$

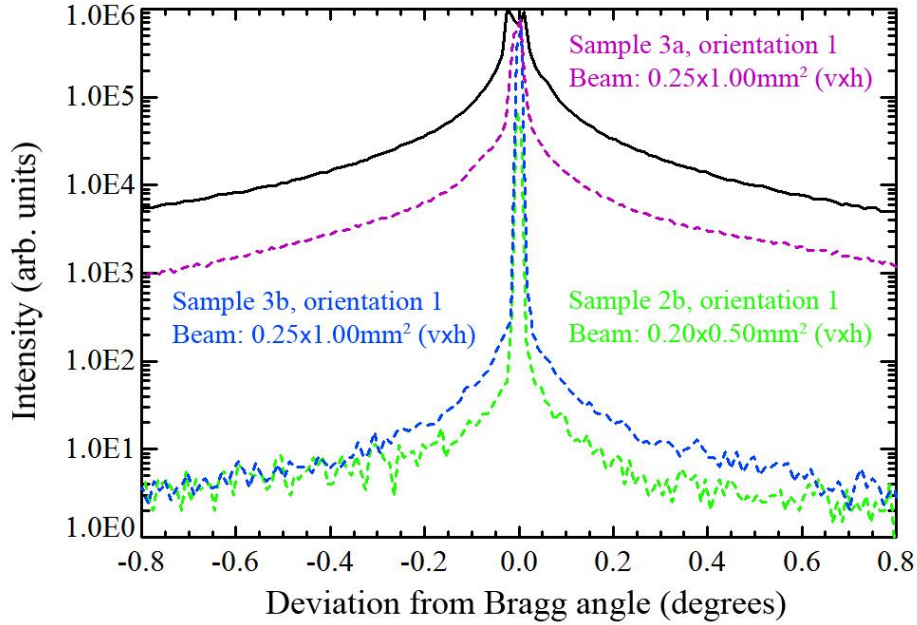


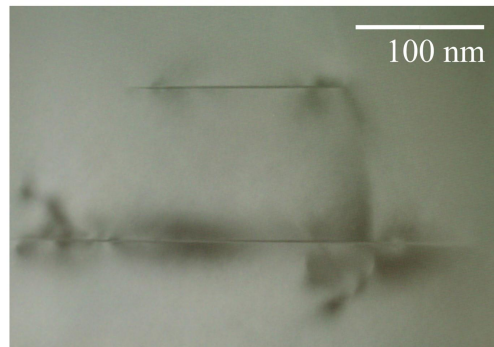
FIGURE 6.14: **Experimental RSMs from 2b (dashed green line), 3a (dashed purple line with higher intensity) and sample 3b (dashed blue line) in orientation 1.** All three samples were in orientation 1, i.e. they were assumed to be oriented with $(010)_{Al}$ and $(001)_{Al}$ at $0/90^\circ$ to the diffraction plane. Samples 2b, 3a and 3b were $1.50 \pm 0.05\text{mm}$, $0.65 \pm 0.05\text{mm}$ and $1.60 \pm 0.05\text{mm}$ thick Al-2.0wt% Cu, respectively. The beam sizes were $0.20 \times 0.50\text{mm}^2$ ($v \times h$) for sample 2b and $0.25 \times 1.00\text{mm}^2$ ($v \times h$) for samples 3a and 3b.

($v \times h$)). However, the reconstruction attempts from measured RSMs of sample 2a in orientation 2 and in both orientations but with a smaller beam (Figures 6.6(b) and 6.7) were not successful as the algorithm could not converge on a solution. We believe the unsuccessful reconstruction attempts are due to a very low SNR, strong contributions from the instrumental function which were difficult to remove and from the saturated pixels and/or non linear response of the detector in the low momentum transfer (central regions) of the diffraction patterns.

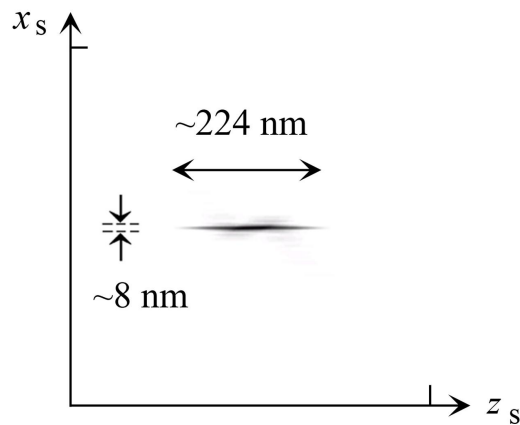
A modal nanoparticle, representative of the ensemble is shown in Figure 6.15(b). Using the conventional Fraunhofer diffraction relationship to obtain the spatial resolution (eq. (4.11)) (Nikulin *et al.*, 2004; Dilanian and Nikulin, 2005)

$$\Delta x \approx \frac{\lambda}{\Delta\Theta}, \quad (6.5)$$

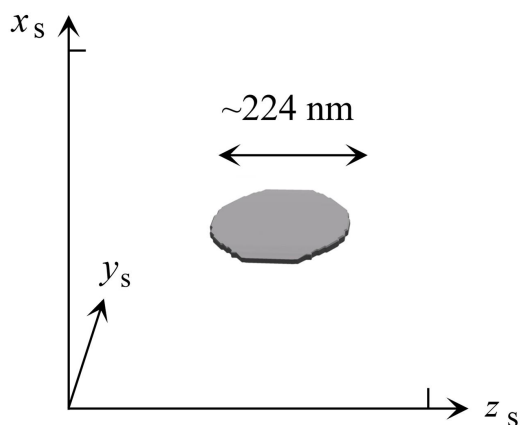
where $\Delta\Theta$ is the total angular range of the experimental data, yields $\Delta x = 3.4\text{nm}$. This gives the reconstructed nanoparticle a diameter of $\sim 224\text{nm}$, and thickness of $\sim 8\text{nm}$ (Zatsepin *et al.*, 2008). Based on *a priori* knowledge about the symmetry of



(a) $\langle 100 \rangle_\alpha$ zone axis TEM micrograph of two typical nanoparticles, seen edge on, from sample 2a. TEM was carried out on a Philips CM20 instrument operated at 200 keV.



(b) 2D image of the projected thickness of an experimentally reconstructed modal nanoparticle.



(c) 3D rendering of an experimentally reconstructed modal nanoparticle based on *a priori* knowledge of its symmetry.

FIGURE 6.15: Reconstruction of a modal nanoparticle from an RSM of sample 2a in orientation 1 compared to a TEM micrograph. Sample 2a was an 0.70 ± 0.05 thick Al-2.0wt% Cu specimen, heat treated at 180°C for 72 hours. An HIO iterative image reconstruction algorithm (described in §5.2.1) was used to reconstruct the modal nanoparticle from the RSM shown in Figure 6.6. A transmission electron micrograph of two typical nanoparticles in the sample is shown for comparison.

the nanoparticles, a 3D realisation of the reconstruction is shown in Figure 6.15(c). A TEM micrograph of two random particles in sample 2a is shown in Figure 6.15(a) for comparison.

6.2.5 Further discussions and conclusions

Consider now the symmetrised monochromator pseudo streak profiles from all the presented RSMs, scaled to facilitate comparison with the instrumental function (Figure 6.16). To symmetrise the profiles, each one was averaged with a copy of itself reversed in the angular deviation (i.e. α or $\Delta 2\theta$).

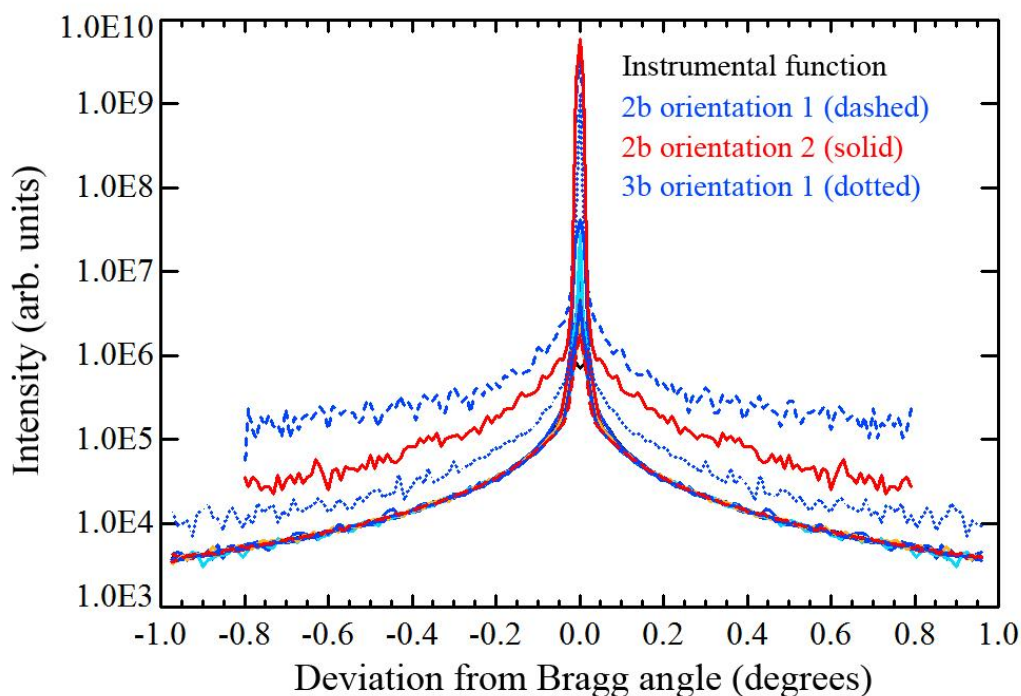


FIGURE 6.16: Comparison of symmetrised experimental monochromator pseudo streaks from the TAD instrumental function and Al-2.0wt% Cu samples of various thickness and with different microstructures. The instrumental function RSM was shown in Figure 6.1, and the sample RSMs were shown throughout §6.2. These diffraction profiles have been symmetrised and scaled to facilitate comparison. The similarity of the symmetrised profiles emphasises that the diffraction signal from the different nanoparticle ensembles is very weak, and that asymmetry in the diffracted intensity plays a very important role.

To reiterate, the monochromator pseudo streak profiles from such weakly diffracting nanoparticles were expected to be symmetric because the Fraunhofer diffraction

pattern from a real electron density distribution has twofold rotational symmetry (Bracewell, 2000). However, the profiles from sample 2a in orientation 2, and both orientations of samples 2b, 3a and 3b all show slight asymmetry, as seen in Figures 6.8(b), 6.10, 6.12 and 6.14, respectively. The profiles from sample 2a in orientation 2 with two different beam sizes show the same asymmetry, which is also very similar to that of sample 3b in orientation 2, i.e. a shoulder-like profile that drops off at $\sim -0.44^\circ$ (sample 2a) and $\sim -0.47^\circ$ (sample 3a). The other asymmetric profiles have tails with slightly different inclination and/or various small peaks, all of which are effects that have not been seen in simulations.

The agreement between the symmetrised monochromator pseudo streak profiles from the samples and that from the instrumental function in Figure 6.16 emphasises that most of the signal from the samples was contained in the asymmetry. This can not be said of the profiles from sample 2b in orientation 1 (dashed blue line), 2b in orientation 2 (solid red line) and 3b in orientation 1 (dotted blue line), which have been scaled slightly higher than the rest of the profiles for clarity. These particular profiles have already been discussed above, in their respective sections.

The presence of asymmetry in the diffraction profile may indicate the presence of strain in the sample (Vartanyants *et al.*, 2000; Robinson and Miao, 2004; Newton *et al.*, 2009) and can be modelled as an imaginary electron density component. In §2.2.1 we discussed that coherent nanoprecipitates (the GP zones, comprised of pure Cu) and semi-coherent Al₂Cu and Al₃Cu nanoprecipitates are surrounded by strain fields in the host Al matrix, which may be the source of this asymmetry in the diffraction profiles. Since the strain fields are dynamic during nanoparticle growth, one would expect the asymmetry to change in real time, during *in situ* sample ageing. This effect was made use of in the second stage of the experimental development of our technique, where we carried out an essential preliminary study of diffraction changes during the *in situ* ageing of various Al-Cu alloys. Also, it is from this perspective of strain dynamics in the sample that we will analyse the data from the *in situ*, real-time nanoparticle growth experiment presented in §6.4. However, since strain fields surrounding the nanoparticles were not considered for the static case presented in this section nor in the simulations presented in the previous chapter, they would make an interesting direction for further work.

In the idealised, normally distributed platelet nanoparticle ensembles simulated in §5.3.3 we showed that the Airy pattern minima were no longer visible when the standard deviation of the nanoparticle diameters was $\gtrsim 20\%$. We presume that most of the samples investigated in this experiment had a wide nanoparticle diameter

distribution and thus did not result in intensity minima in the monochromator pseudo streaks. From TEM micrographs of Al-Cu alloys (such as in Figure 2.5) it appears that the polydispersity may surpass this limitation for ensembles of θ' phase particles that have diameters of ~ 100 to ~ 500 nm (§2.2.1). However, we must reiterate from §1.1.1 and §2.2.2 that due to the nature of destructive sample preparation for TEM analysis, requiring $< \sim 0.3 \mu\text{m}$ thick sample sections, the platelet-shaped nanoparticle diameters measured from TEM micrographs are often chords and not actual diameters. Thus it is difficult to calculate the standard deviation of the nanoparticle ensemble in one of our samples from TEM micrographs. However, polydispersity does not affect the ability of the iterative algorithm to reconstruct an average nanoparticle, as was shown in §5.2 and §6.2.4.

Let us consider the significance of observing diffraction pattern changes from rotation of the sample about the optical axis. When measuring diffraction patterns from the entire illuminated sample volume in direct space (with a pixel array detector, for example), the incoherent addition of diffracted X-ray distributions produces a continuous, diffuse intensity distribution, akin to that seen in small angle X-ray scattering (refer to §1.1.4). The mean size of the particles can be estimated, but the particle shape can not be readily and uniquely reconstructed as the phases of waves diffracted from different parts of the object cannot be retrieved from the intensity pattern in this case (van der Veen and Pfeiffer, 2004; Nikulin *et al.*, 2007; Nikulin, A.Y. and Dilanian, R.A. and Gable, B.M. and Muddle, B.C. and Hester, J.R. and Ishikawa, T. and Yang, P. and Moser, H.O., 2008). To invert the diffraction pattern, as is performed in CDI, the nanoparticles of interest need to be isolated and ensured to be within a volume smaller than the coherence volume, thus avoiding this incoherent addition of diffracted intensities from uncorrelated sample sections (see §1.1.4). We reiterate that weakly diffracting embedded nanoparticles such as the Cu and Al₂Cu nanoparticles in Al-Cu alloys are too small in volume and too similar to the surrounding matrix to diffract a detectable amount, to be measured by current CDI type methods. More importantly, as we are seeking a bulk material characterisation, the necessary volume for statistical analysis is far beyond current coherence volumes.

This brings us to one of the main advantages of the TAD based technique we are developing for characterising nanoparticles. Since the FT is insensitive to object shift, the distribution of diffracted X-rays from identical nanoparticles is identical regardless of their position in the matrix. Thus despite the low diffraction contrast and the small size of individual nanoparticles resulting a low diffraction power, detectable intensities result from the superposition of diffraction from a large ensemble of similar

particles, which increases the SNR by approximately the number of nanoparticles illuminated by the beam, as in eq. (5.10) (Nikulin *et al.*, 2007).

In order to attempt a more quantitative analysis of such data in comparison to the idealised simulated results in §5.3.3, the experimental RSM from each sample needs to be measured with identical parameters such as sample thickness and beam size. The beam size and attenuators (if present) must ensure that the detector response is linear over the entire dynamic range of the X-ray intensities in the RSM (or has a calibrated one-to-one response over the necessary dynamic range), so as to enable meaningful normalisation between the samples and avoid saturation effects as seen in our results.

Analysis based on fitting would involve four contributions: the direct, transmitted beam, a diffuse background, the monochromator pseudo streak and Fraunhofer diffraction from the sample itself. The direct, transmitted beam's intensity depends on absorption by the sample and air absorption and scatter, which is constant for both cases, with and without the sample. However, the thickness of the sample is not precisely known at the position illuminated by the X-rays and as mentioned earlier, the detector was often saturated in the central region of the RSM, which further complicates the fit. The diffuse background and monochromator pseudo streak would ideally be obtained from the TAD instrumental function RSM. Parameters that affect the contribution to the RSM of the Fraunhofer diffraction from the sample include the number, size, exact composition and orientation of particles. It was not the purpose of the technique being developed to attempt to fit the monochromator pseudo streaks with this multitude of parameters, but rather to demonstrate the sensitivity of the technique to ensembles of weakly diffracting nanoparticles and the ability to reconstruct a nanoparticle representative of the ensemble directly from the RSM.

We have shown that although a 2D RSM is necessary for reconstructions, it may be possible to obtain quantitative information about the ensemble from the monochromator pseudo streak. It may not be ideal to scan solely along the monochromator pseudo streak as the RSM may be misaligned even a little, but a small 2D region, such as a thin parallelogram along the monochromator pseudo streak, could be recorded with a longer exposure time. The longer exposure time would increase the SNR of the diffraction from the nanoparticles, which proved critical to the attainability of reconstructions from experimental RSMs (cf. §6.2.4), and to identifying intensity minima (in the Airy patterns, for example) along the monochromator pseudo streaks. Measuring diffraction data with higher angular resolution along the monochroma-

tor pseudo streak than those obtained here would also provide optimal sampling for obtaining size information about the ensemble, especially for larger diameters (cf. §5.3). In addition, probing a smaller region in reciprocal space would allow the investigation of diffraction changes over time scales on the order of a single 1D scan, i.e. ~5 minutes. In comparison, an entire 2D scan often requires 8–10 hours (less for instrumental function measurements, taken with shorter exposure time per datum point) (cf. §4.2.2). One could, in theory, optimise the setup to observe even faster nanoparticle growth dynamics in a particular sample by only measuring the intensity changes at one particular point in reciprocal space, once the setup was calibrated.

6.2.6 Summary

In this feasibility study we explored the sensitivity of reciprocal space mapping with an analyser to samples of varying thickness and containing different nanoparticle size distributions. We confirmed that 10.9 keV X-rays are sufficiently penetrative to observe a diffraction signal from a very sparse ensemble of weakly diffracting Al-Cu nanoparticles in their natural state (e.g. ~ 12 particles/ μm^3), embedded in an Al matrix. The samples were sufficiently thick to represent the bulk material nanoplatelet distribution ($0.50\text{--}1.60 \pm 0.05\text{mm}$), and results did not disagree with the expected compromise between the total diffracting volume and beam attenuation, as expressed by eq. (5.12). Indeed, despite the limited particle density and scale, and the sparseness of the distribution, the present X-ray optics and beam dimensions allowed diffraction data to be collected from a very large total population of dispersed nanoparticles.

Of the four size distributions with average nanoplatelet diameters of $\ll 100\text{nm}$, $\sim 150\text{nm}$, $\sim 250\text{nm}$ and $\sim 370\text{nm}$, we were able to observe diffraction effects from the two latter diameter distributions. For those samples containing nanoplatelets with diameters of 250nm and 370nm , a sample thickness of $1.50\text{--}1.60 \pm 0.05\text{mm}$ (samples 2b and 3b) showed too much attenuation and a low SNR, so quantitative analysis of the profiles was inconclusive. However, RSMs recorded from two orientations about the optical axis for thin versions of these two samples (i.e. samples 2a and 3a) showed consistent qualitative effects along the monochromator pseudo streak, demonstrating the sensitivity of the technique to the orientation of the nanoparticles with respect to the diffraction plane. We then showed that nanoparticle reconstruction is possible from a 2D RSM obtained with our setup, provided the instrumental function does not dominate the RSM. We also discussed how quantitative information about the ensemble can be obtained from the monochromator pseudo streak alone, enabling the measurement of diffraction changes (such as asymmetry in the diffraction profiles)

from nanoparticle growth on the order of minutes. This dynamic effect is discussed in the following two experimental stages.

6.3 A phenomenological study of diffraction changes during *in situ* nanoparticle growth using triple axis diffractometry

6.3.1 Introduction

In age hardenable materials, such as Al-Cu alloys, the nucleation and the initial growth stages of nanoparticles strongly influence the resultant microstructure, which in turn determines the material's physical properties such as strength and plastic behaviour (for more details see §2.2). In this experiment we investigated the practicalities of probing these early stages of nanoparticle growth with our TAD based technique.

We sought to determine appropriate experimental parameters for performing a real-time, *in situ* nanoparticle growth investigation by determining the influence of the concentration of Cu in Al, which significantly affects the growth patterns of ensembles of Al-Cu particles (§2.2), and the corresponding ageing temperatures that display measurable changes on a time scale suitable for real-time, *in situ* investigations.

Although the physical origin of the asymmetry observed in the monochromator pseudo streak profiles in the previous section is not certain, it is expected that strain fields in the alloy during the early nano-precipitation stages would affect the observed asymmetry. Based on this premise, we measured changes in the diffracted intensities during the *in situ* growth of nanoparticles in various mono- and polycrystalline Al-Cu alloy samples, at different artificial ageing temperatures. As mentioned in §5.3.3, the data collection time of this technique is currently a limitation to exploring processes faster than a few minutes, however a large number of standard heat treatments for such nanomaterials involves slow nanoparticle formation and growth, making it quite suitable for such investigations. The *in situ*, real-time experiment carried out as a result of outcomes made in this and the previous study (that will be presented in §6.4) was performed at a brighter source to minimise RSM collection time.

6.3.2 Experimental setup and sample details

This experiment was carried out at the ANBF, BL20B of the Photon Factory, the details of which were presented in §4.1. We examined the use of two X-ray energies. First,

we tested an X-ray energy of 8.5 keV, which is close to the Cu $K_{\alpha 1}$ transition energy of 8.05 keV, to see if potential future *in situ* real-time investigations on such samples could be carried out with an in-house rotating anode X-ray source. At this energy the advantageous vacuum capability of the "BigDiff" was used to avoid significant air scatter and hence increase the SNR. The secondary monochromator was a symmetric, double reflection Si(111) crystal (§4.2.1). This lower order reflection was chosen over Si(400) in the previous experiments (carried out with a brighter X-ray source) so as to increase the flux on the sample.

The X-ray energy was later increased to 15 keV with the expectation that it would improve the diffraction contrast between the embedded nanoparticles and the Al matrix since the difference of the absorptive part of their refractive indices, i.e. $|\beta_{\text{Al}} - \beta_{\text{Al}_2\text{Cu}}|$ (cf. eq. (3.3)), increases by a factor of ~ 5 compared to 8.5 keV. The higher energy beam also reduced parasitic air scattering to a level that did not require vacuum conditions. In this case the secondary monochromator was set to the Si(333) reflection.

The beam size was set to $0.40 \times 0.20 \text{ mm}^2$ ($v \times h$) by a pair of crossed slits upstream of the sample, for both X-rays energies and all samples. The analyser was a Si(111) single reflection crystal, and the detector was a Radicon scintillation counter (§4.1.1).

The samples examined are listed in Table 6.2. Having noted from results in §6.2 that samples with thicknesses greater than $\sim 0.70 \text{ mm}$ were too highly absorbing, the samples in this experiment were prepared with thicknesses of $0.41\text{--}0.65 \pm 0.05 \text{ mm}$. Sample S5 underwent artificial ageing for 6 hours at 200°C in an air oven, prior to *in situ* heating in the "BigDiff" for 20 hours.

#	Al- x Cu (% wt)	Al surface plane	Mono/poly crystalline	Sample thickness (mm)	Ageing Temp ($^\circ\text{C}$)	Ageing time (Hours)	X-ray Energy (keV)
# S1	4.7	(111) _{Al}	mono	0.60 ± 0.05	220	7	8.5
# S2	2.0	N/A	poly	0.45 ± 0.05	250	20	8.5
# S3	2.0	(100) _{Al}	mono	0.65 ± 0.05	~ 30	2.5	8.5
# S4	4.0	N/A	poly	0.38 ± 0.02	200	10	15.0
# S5	2.0	(100) _{Al}	mono	0.65 ± 0.05	200	6+20	15.0

TABLE 6.2: **Sample details and their respective heating treatments.** With limited experimental time it was necessary to explore as many possible microstructural and heating scenarios as possible, to find suitable candidates for *in situ*, real-time X-ray studies. Sample S5 underwent artificial ageing for 6 hours at 200°C prior to *in situ* heating during the experiment for 20 hours. All other times correspond to *in situ* heating only.

While the samples underwent *in situ* artificial ageing, as detailed in Table 6.2, we measured a series of 1D $\theta/2\theta$ scans centred on the points $(\alpha_0, \Delta 2\theta) = (\pm 0.05, 0)^\circ$ where α and $\Delta 2\theta$ are deviations of the analyser and detector from their respective Bragg conditions, which corresponds to $(Q_x, Q_z) = (\pm 0.0028, 0.0000)\text{nm}^{-1}$ for both energies (see Figure 6.17). The angular range of the scans was $\alpha = \pm 0.4^\circ$, $\Delta 2\theta = \pm 0.8^\circ$, with step sizes 0.008° and 0.016° respectively, which corresponds to $Q_z \in (-0.093, 0.093)\text{nm}^{-1}$ for the 8.5 keV case and $Q_z \in (-0.167, 0.167)\text{nm}^{-1}$ for the 15 keV case.

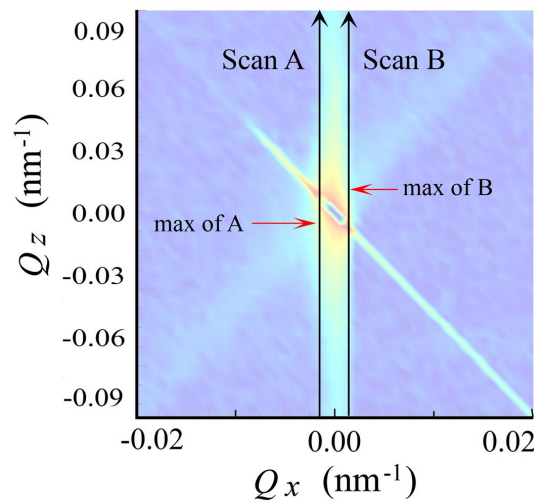


FIGURE 6.17: **Reciprocal space geometry of 1D scans recorded during *in situ* nanoparticle growth investigations in various Al-Cu alloys.** The 2D experimental RSM is provided solely as a guide. Scan A corresponds to a $\theta/2\theta$ scan over $\alpha = \pm 0.4^\circ$, $\Delta 2\theta = \pm 0.8^\circ$, with the analyser offset at $\alpha_0 = -0.05^\circ$ ($Q_x = 0.0028\text{nm}^{-1}$). Scan B covers the same $\theta/2\theta$ range as scan A, but with the analyser offset at $\alpha_0 = +0.05^\circ$ ($Q_x = 0.0028\text{nm}^{-1}$). The range of the 1D scans in Q_z was $\pm 0.093\text{nm}^{-1}$ as shown here for the 8.5 keV case, and $Q_z \pm 0.167\text{nm}^{-1}$ for the 15 keV case.

The intensities at the points along the scans (labelled A and B in Figure 6.17) that intersected the monochromator pseudo streak were compared, i.e. their ratio was used as a measure of asymmetry in the diffraction pattern due to *in situ* nanoparticle growth. As we were interested in the qualitative nature of the asymmetry of the maxima of scan A and scan B, the different Q_z ranges for the two X-ray energies were inconsequential. We anticipated that the position $\alpha = \pm 0.05^\circ$ would show similar asymmetries to those observed in the monochromator pseudo peaks presented in §6.2. A secondary reason for choosing this position was that it is sufficiently close to the central part of the diffraction pattern to have a high intensity without being

saturated. Thirdly, to minimise the time between scans so as to form an accurate picture of *in situ* heating induced changes, the relatively slow movement of the high precision α goniometer necessitated small movements of the analyser.

6.3.3 Results and discussions

We found that the ratio of the maxima of the A_{scan} at $\alpha_0 = -0.05^\circ$ and B_{scan} at $\alpha_0 = +0.05^\circ$ (Figure 6.17) changed as a function of ageing time. As we were interested in the qualitative nature of the curves over time, the general gradients of the relative intensity curves were made positive and arbitrarily set to zero at $t = 0$, for easier qualitative comparison of their gradients (Figure 6.18).

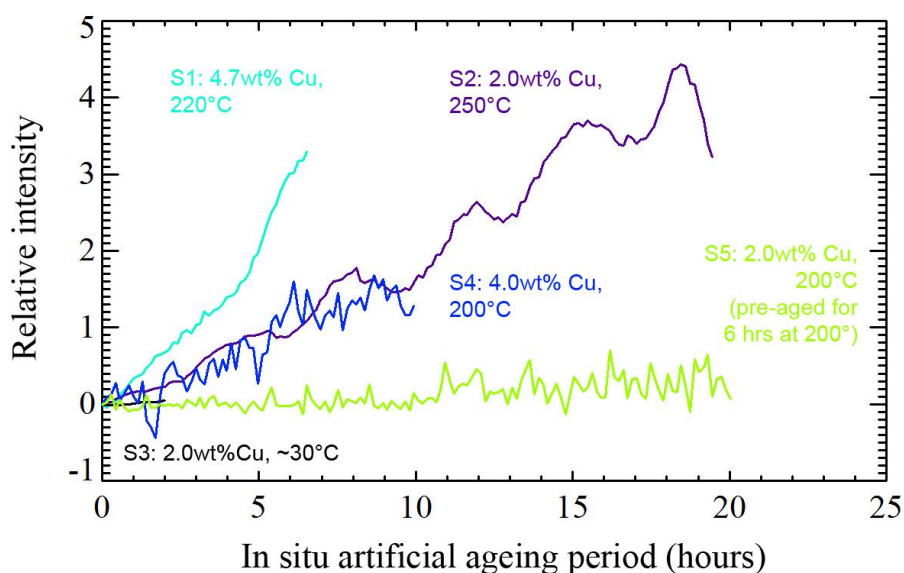


FIGURE 6.18: **Experimental results of a preliminary *in situ* nanoparticle growth X-ray diffraction investigation of Al-Cu samples.** The samples investigated were listed in Table 6.2. The relative intensities of the maxima of 1D $\theta/2\theta$ scans at $\alpha = \pm 0.05^\circ$ are shown on a linear scale, for various heating temperatures. Interestingly, the asymmetric behaviour of the intensity maxima qualitatively correlated with hardness curves for similar heat treatments and Cu concentrations. In addition to demonstrating the ability to measure *in situ*, real-time changes in the X-ray diffraction from the nucleating and growing nanoparticles, this experiment aided in the design of a rigorous *in situ*, real-time investigation.

The obvious trend in Figure 6.18 is that higher Cu concentrations and higher ageing temperatures result in a greater magnitude of the change in the relative intensity gradient with time, or in other words more rapid changes in the diffracted intensities.

Qualitatively, these results are well correlated to hardness curves for Al-Cu alloys of similar Cu concentrations and similar ageing temperatures, repeated from Figure 2.4 but with a linear time scale in Figure 6.19.

As expected from our understanding of the driving forces for nanoparticle growth in artificially aged Al-Cu alloys, the most rapid diffraction changes were observed for sample S1, which contained the highest concentration of Cu investigated (4.7wt%) and was aged at a relatively high temperature of 220°C. In Figure 6.19 the light blue line shows the hardness of an Al-4.5wt% Cu sample aged at 220°C, so the slightly higher concentration of Cu in S1 would result in an even more steep rise in hardness, i.e. even more rapid dynamics. By the end of the 7 hour *in situ* heat treatment of S1 there was some loss of vacuum in the "BigDiff" (which is not actively pumped during data acquisition to avoid vibration) and so it is possible that the increased parasitic air scatter may have affected the results towards the latter half of the heat treatment, but the overall rapid increase in asymmetry in comparison to other samples was assumed to be unaffected.

Interestingly, sample S2 and S4 showed similar relative intensity gradients despite their different Cu concentrations and ageing temperatures. Sample S2, a polycrystalline Al-2.0wt% Cu alloy, was aged at 250°C, while sample S4 was a polycrystalline Al-4.0wt% Cu alloy aged at 200°C. It appears that although the higher concentration of Cu in S4 leads to a faster increase in alloy hardness (Figure 6.19), the higher ageing temperature for S2 compensates for its lower Cu concentration. We can interpolate the hardness curves in Figure 6.19 for an Al-4.0wt% Cu alloy treated at 190°C (dark red line) and that treated at 220°C (dark blue line) to estimate the hardness curve for an ageing temperature of 200°C for a sample with the same Cu concentration.

Sample S3 (black line in Figure 6.18) was aged naturally, i.e. the intensities were measured without intentional heating of the sample. The temperature of the sample during the scans was slightly higher than ambient room temperature, i.e. $30 \pm 5^\circ\text{C}$, due to heating by the incident X-ray beam. The unvarying relative intensities were expected from the knowledge that nanoparticle growth during natural ageing is very slow. It is possible that some diffraction changes could be observed from natural ageing promptly following the solution heat treatment and quenching, but in this case the sample was kept at room temperature for weeks so no rapid dynamics were expected.

Sample S5, which was pre-aged at 200°C for 6 hours in an air oven, also did not show significant changes in the relative intensities (lime line in Figure 6.18). It appears that since the sample was kept at room temperature for a few hours following the

pre-ageing treatment, further artificial ageing *in situ* did not affect the monochromator pseudo streak intensities in the same way as those samples without pre-ageing. This too implies that the most dynamic changes in an Al-Cu alloy would be in the period closely following solution heat treatment and quenching, when the Cu is in supersaturated solid solution.

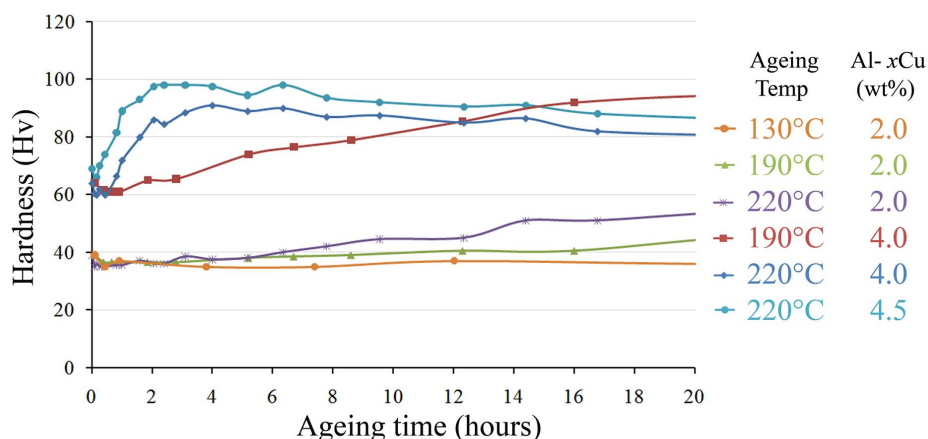


FIGURE 6.19: Al-Cu hardness curves for Cu concentrations and heat treatments similar to samples S1-S5 (Gable, 2006a).

We can not rule out the possibility that samples S3 and S5 may have resulted in interesting dynamic changes in 2D scans as our scans were only one dimensional. However, we can say with certainty that higher Cu concentrations and ageing temperatures do result in faster dynamics and easily measurable intensity asymmetry. Such treatments and samples (e.g. S1, S2 or S4) would thus lend themselves well to *in situ* real-time investigation with our setup without further experimental technique development. Indeed, we can infer that for similar materials that depend on embedded nanoparticle ensembles for their physical properties, hardness curves are a simple qualitative, albeit crude, way of predicting the suitability of samples for real-time nanoparticle growth investigations with our technique, provided they have not undergone previous artificial ageing.

It is possible that in the 15 keV case, the use of a secondary monochromator with a different reflection to the primary beamline monochromator (in a wavelength dispersive setup), resulted in an asymmetric rocking curve, which could also lead to asymmetry in the diffraction pattern. This asymmetry was not simulated as it is not expected from the Fraunhofer diffraction pattern of a symmetric particle, nor were diffuse scattering and dispersive monochromators incorporated. However, the

relative intensities at A and B would still be a qualitative measure of dynamic changes in the sample.

The results of the feasibility study presented in §6.2 regarding a suitable sample thickness for Al-Cu alloys were also confirmed in this study as we saw a significant diffraction signal from all samples using sample thicknesses of $0.41\text{--}0.65 \pm 0.05\text{mm}$, despite the lower brilliance of the bending magnet source compared to the third generation synchrotron undulator source used in the previous experimental stage (refer to §4.1.1 and Table 4.1).

As a secondary outcome of this study, we improved the custom made sample heater's temperature stability and enabled its remote control. During this experiment, the heater was incapable of maintaining a temperature of 250°C throughout multiple long scans, seemingly due to deterioration of the Nichrome heating element. We modified the design to electronically (automatically) supply a constant current and potential to the wire, regardless of its resistance changing with heat and/or further deterioration. These significant changes were made prior to the following experiment, in which we carried out the first rigorous *in situ* real-time investigation of the dynamic changes in RSM of diffraction from embedded nanoparticles in an Al-Cu alloy during nanoparticle formation and early stages of growth.

In conclusion, this preliminary investigation of real-time X-ray diffraction changes during *in situ* Al-Cu nanoparticle growth confirmed our expectations that higher Cu concentration and ageing temperature affects the dynamics in the diffracted intensities faster. The results led to a deeper, qualitative understanding of suitable samples and heat treatments for more thorough future real-time, *in situ* studies, such as the one presented in the following section.

6.4 In situ reciprocal space mapping of the initial stages of nanoparticle growth in an Al-Cu alloy

6.4.1 Introduction

We present an experimental demonstration of analyser based, reciprocal space mapping of real-time, *in situ* nanoparticle growth in an Al-Cu alloy. A phenomenological analysis of the data is presented, involving simulations of the effects of clustering and dynamic strain in early stages of nanoparticle growth, which are very well corre-

lated with the measured diffraction profiles during the heating of the sample. This section embodies an important step towards non-destructive, *in situ*, bulk material investigations of large ensembles of weakly diffracting nanoparticles.

Such investigations are imperative for the understanding, and ultimately the control, of nanomaterial properties governed by the ensemble of embedded nanoparticles.

The work presented in this section has been published in *Real-time in situ nanoclustering during initial stages of artificial ageing of Al-Cu alloys*, N. A. Zatsepin, R. A. Dilanian, A. Y. Nikulin, X. Gao, B. C. Muddle, V. N. Matveev and O. Sakata, *J. Appl. Phys.*, **107** 24303 (2010), included in the Appendix (Zatsepin *et al.*, 2010).

In §6.2 we showed that with an X-ray energy of 10.9 keV, diffraction effects from weakly diffracting Al₂Cu nanoparticles with $\gtrsim 150$ nm diameters, were visible for samples with thicknesses of ~ 0.73 mm. We then showed in §6.3 that *in situ*, real-time nanoparticle growth investigations on similar samples could be carried out with our technique. Sample thicknesses of $(0.38-0.65)\pm 0.05$ mm were explored but the main parameters affecting changes in the diffraction pattern during *in situ* ageing of the sample were the temperature and Cu concentration. The X-ray energy, Cu concentration, artificial ageing temperature and sample thickness for the experiment presented in this section, discussed in §6.4.2, were chosen based on these results.

6.4.2 Experimental setup and sample details

The experiment was carried out on beamline BL13XU, at SPring-8 (§4.1). An energy of 12.4 keV was used, selected by double-crystal Si 400 monochromator and then spatially collimated by a crossed pair of 0.20×0.40 mm² (v \times h) slits (§4.2). The analyser was a double-reflection Si(400) crystal (§4.2.1) to ensure high angular resolution and decrease artifacts that may result from high analyser tails (§4.3.1). The vertical slit in front of the scintillation counter was 200μ m in width, chosen as a compromise between sufficient intensity to lower data collection time and high angular resolution.

Based on the outcomes of the previous two sections, a 0.60 ± 0.05 mm thick Al-4.0wt% Cu single crystal, grown with the Al(111) parallel to the surface, was chosen as the sample for this experiment. The thickness was thinner than the approximate 0.73mm visibility threshold found in §6.2 to lessen the absorption from the extra Cu present in this sample (4 wt% compared to 2 wt%).

In preparation, the sample was solution treated in order to dissolve any nano-precipitates contained in the Al-Cu sample prior to carrying out the *in situ* heat treatment (as described in §2.2). However, the sample was unavoidably kept at room temperature for a week prior to the *in situ* heat treatment, which allowed the earliest

stage of nano-precipitation (GP zones) to nucleate naturally (as discussed in §2.2). An annealing temperature of 220°C was chosen based on the results of the experiments in §6.2, supported by the high gradient of the hardness curve for an Al-4.0wt% Cu sample heated at 220°C, implying that microstructural changes will occur at a rate that suits our time scale of real-time studies.

The growth process of the embedded nanoparticles was monitored during a series of ageing treatments at 220°C. In order to measure the 2D RSM with the sample in a relatively static state, it was rapidly cooled to room temperature by an attached copper heat sink after each ageing period. The *in situ* artificial ageing was then continued and RSM collection was repeated after a total of 35, 48, 55, 75, 95, 115, and 136 minutes.

During the *in situ* sample heating, single $\alpha/\Delta 2\theta$ scans were collected at analyser positions of $\alpha = \pm 0.04^\circ$, in order to keep track of any rapid changes in the diffracted intensity. The angular range of these 1D scans was $\alpha = \pm 0.355^\circ$, with step sizes of 0.01° in α and 0.02° in $\Delta 2\theta$. The RSM was comprised of $\alpha/\Delta 2\theta$ scans with shifts of α in between, over the range of $\alpha = \pm 0.355^\circ$ and $\Delta 2\theta = \pm 0.710^\circ$, with 0.01° and 0.02° step sizes, respectively, probing a rectangle in (Q_x, Q_z) coordinates (§4.2.2) that covers the range $Q_x \in (-0.0314, 0.0316)\text{nm}^{-1}$ and $Q_z \in (-0.0798, 0.0792)\text{nm}^{-1}$. The measured RSMs are shown in Figures 6.20 and 6.21.

As discussed in §6.2.3, perfect alignment of the main optical axis with $[100]_{\text{Al}}$ is virtually impossible due to the difficulties of maintaining the alignment during handling of the small specimens. However since there are three orthogonal axes of four-fold rotational symmetry of the planes along which the nanoprecipitates form, X-rays incident along the $[111]_{\text{Al}}$ direction ensures at least one of the directions of strain, and the FT of at least one of the orthogonal sets of nanoprecipitates, intercepts the Ewald Sphere. Hence the sample was aligned with $[111]_{\text{Al}}$ perpendicular to the beam, and its orientation was constant throughout the experiment.

6.4.3 Results and analysis

Two dimensional RSMs of diffraction from various stages of *in situ* nanoparticle nucleation and growth in the Al-Cu sample are shown in Figures 6.20, which includes the RSM collected prior to *in situ* heating, and the RSMs collected after 35, 48, and 55 minutes of sample heating. Figure 6.21 shows RSMs collected after 75, 95, 115 and 136 minutes of *in situ* sample heating.

From the results of the preliminary *in situ* experiment presented in §6.3, we expected the real-time, *in situ* changes in the diffraction pattern to be most prominent along the monochromator pseudo streak. However, the asymmetric diffraction profile

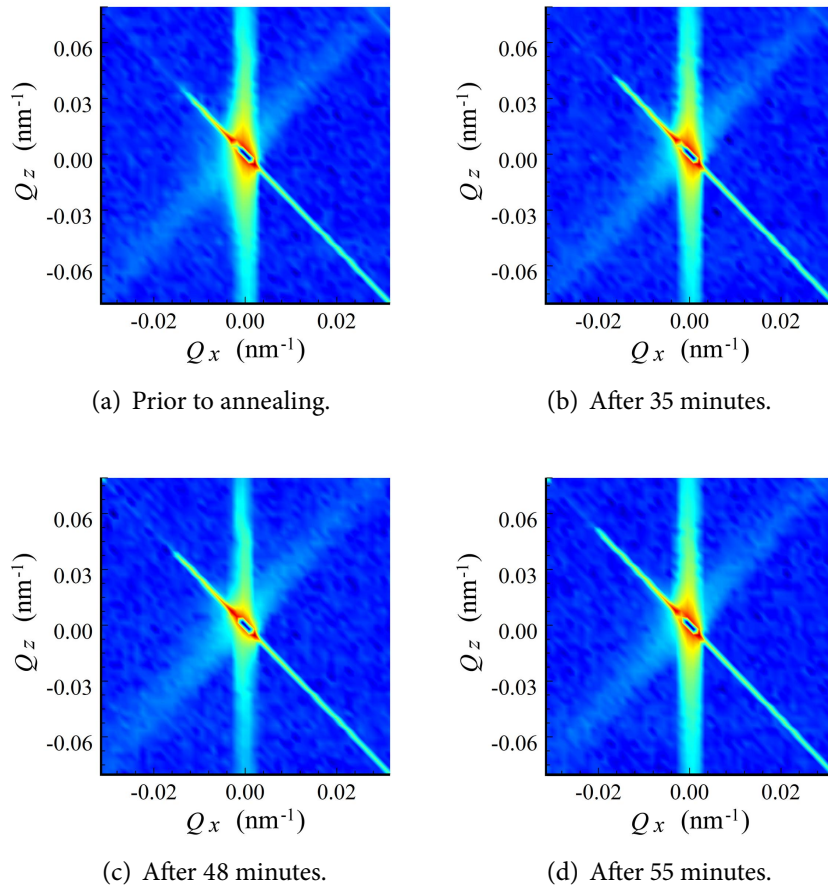


FIGURE 6.20: **Experimental RSMs collected during the *in situ*, real-time nanoparticle growth in an Al₁₁₁-4.0wt% Cu single crystal.** 5-8 of 8 The intensities are displayed on a log scale. The thermodynamically irreversible nature of carefully controlled microstructure growth (see chapter 2 for details) allowed *in situ* heat treatments to be paused while the 2D RSMs were collected. Results 1-4 of 8.

in the direction of the detector pseudo streak is instead clearly visible in the 2D reciprocal space map shown in Figure 6.22. In this figure we define the parameter $\varepsilon(t)$, which we will show to be directly dependent on the gradient of electron density along the optical axis in the analysis that follows.

Figure 6.23 shows the variation of this intensity profile during the ageing treatment at 220°C, as a function of angular deviation of the detector, $\Delta 2\theta$. Of note is the well-pronounced asymmetric form of the intensity profile at the initial stage and throughout the ageing treatment. During the heat treatment the $\Delta 2\theta < 0$ side tail of the intensity profile started to rise and form a shoulder-like shape. The length ε of this “shoulder” (cf. Figure 6.22) increased with ageing time, reaching a maximum value of

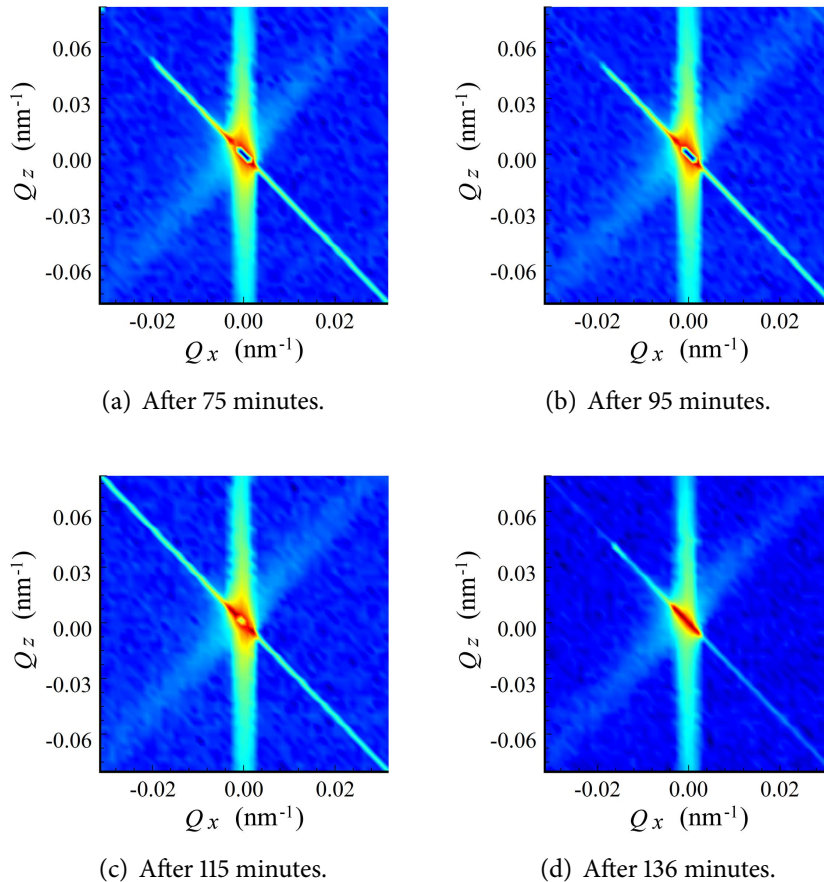


FIGURE 6.21: **Experimental RSMs collected during the *in situ*, real-time nanoparticle growth in an Al₁₁₁-4.0wt% Cu single crystal. Part 2 of 2.** The intensities are displayed on a log scale. The thermodynamically irreversible nature of carefully controlled microstructure growth (see chapter 2 for details) allowed *in situ* heat treatments to be paused while the 2D RSMs were collected. Results 5-8 of 8.

$\varepsilon_{max} \sim 0.28^\circ$ after around 95 minutes of artificial ageing, and then decreased slightly (Figure 6.24). However, further ageing resulted in the intensity profile abruptly changing into an almost symmetrical shape apart from the addition of a single diffraction peak at an angular deviation of $\Delta\theta \sim 0.22^\circ$.

In order to understand these interesting effects, we propose the following phenomenological interpretation. Let us consider the diffracted intensity profile using the conventional concept of a form-factor function (Guinier, 1952). The intensity diffracted from a sample containing nanoscale particles or clusters can be represented as a product of the diffracted amplitude of the analyser and the form-factor function of the sample (Aristov *et al.*, 1991). Generally, the intensity detected through the

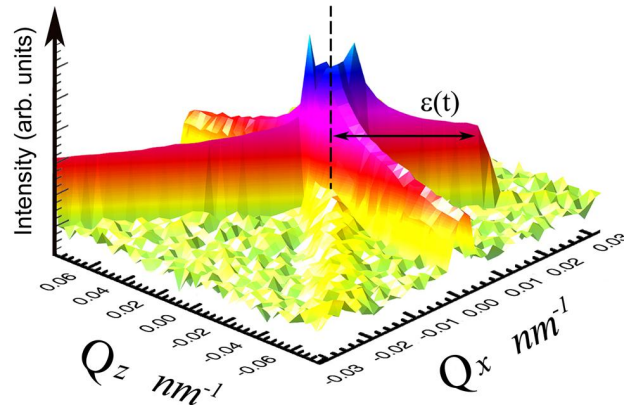


FIGURE 6.22: **Experimental RSM from an Al-4.0wt% Cu sample annealed at 220°C for 75 minutes.** The asymmetric intensity profile (diagonally) is emphasised in this view (displayed on a log scale), with the order parameter of strain field modulation, $\epsilon(t)$, labelled. The Q_x and Q_z axes have been inverted in this Figure compared to Figures 6.20 and 6.21.

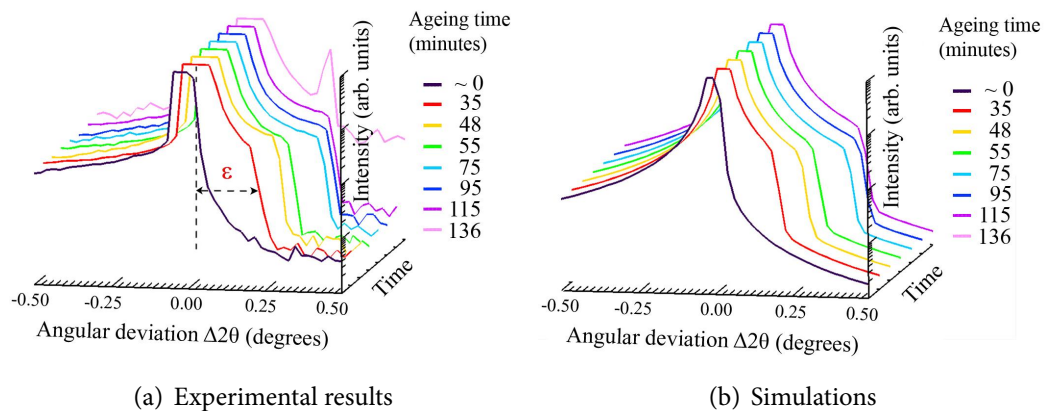


FIGURE 6.23: **Time dependent variation of the intensity profile along the ($\alpha = 0$, $\Delta 2\theta$) direction of the 2D X-ray diffraction data,** as shown in Figure 6.22 during the ageing treatment of an Al-4.0wt% Cu sample at 220°C.

presented experimental technique can be expressed by the following convolution integral:

$$I(Q) \sim \left| \int_{-\infty}^{\infty} \tilde{G}(Q) \cdot R(Q+W) dW \right|^2, \quad (6.6)$$

where Q is the scattering vector, and $\tilde{G}(Q)$ and $R(Q)$ are the FTs of the transmission functions of the object (§3.1.1) and the analyser, respectively (Afanas'ev and Kohn, 1971; Dilanian and Nikulin, 2005; Zatsepin *et al.*, 2010).

The intensity profile along the ($\alpha = 0, \Delta 2\theta$) direction of the 2D diffraction pattern in Figure 6.22 can be well approximated by a product of 1D scattering amplitude of the analyser, $R(Q)$, and the 1D form-factor function, $G(Q)$, the shape of which depends on the structure heterogeneity of the sample, and characterises variables such as strain, defect clusters and nanoparticles:

$$I_{1D}(Q, t) \approx |R_0(Q, t)|^2 \sim |G(Q, t) \cdot R(Q)|^2, \quad (6.7)$$

where $R_0(Q, t)$ is the resultant diffraction amplitude. Approximating the analyser as a perfect semi-infinite, non absorbing crystal, its complex diffraction amplitude $R(Q)$ can be expressed as

$$R(Q) = \frac{1}{2} \left(\delta(Q) - \frac{1}{i\pi Q} \right), \quad (6.8)$$

where δ is the Dirac delta function (Nikulin and Steinfeld, 2004). Note that eq. (6.8) is simply the FT of a Heaviside step function.

In the first Born approximation (§3.1.1, (Born and Wolf, 1999)) the function $G(Q, t)$ can be written as

$$G(Q) \sim \int_{-\infty}^{\infty} \rho'(r, t) \exp(iQz) dz, \quad (6.9)$$

where

$$\rho'(r, t) = \frac{1}{\rho_0(r)} \frac{\partial \rho_P(r, t)}{\partial z}, \quad (6.10)$$

ρ is the electron density, and z is the direction normal to the surface of the object (Bataillou *et al.*, 2003). The electron density can be expressed as a sum of the electron density of the Al matrix, ρ_0 , which is constant, and the electron density of the Al-Cu clusters, ρ_P , i.e.

$$\rho(r, t) = \rho_0(r) + \rho_P(r, t), \quad (6.11)$$

with normalised electron density $\tilde{\rho}$ defined as

$$\tilde{\rho}(r, t) = \frac{\rho(r, t)}{\rho_0(r)} = 1 + \frac{\rho_P(r, t)}{\rho_0(r)}. \quad (6.12)$$

According to [Aristov *et al.* \(1991\)](#), eq. (6.9) can be expressed as:

$$\int_{-\infty}^{\infty} \rho'(r, t) \exp(iQz) dz \sim 1 + \frac{2}{\pi} \arctan(f(Q, t)), \quad (6.13)$$

where

$$f(Q, t) = b_0 \cdot (Q + \varepsilon(t)), \quad (6.14)$$

so as a result, the aforementioned angular "shoulder" length ε is directly dependent on $\partial \rho_p(r, t) / \partial z$. Thus the intensity profile can be expressed as a function of Q and t (for $Q \neq 0$):

$$\begin{aligned} I_{1D}(Q) &\sim |G(Q) \cdot R(Q)|^2 \\ &\sim \left| \frac{b_1}{Q} + \frac{b_2}{Q} \cdot \arctan[b_0(Q + \varepsilon(t))] \right|^2 \\ &= |R_1(Q, t) + R_2(Q, t)|^2, \end{aligned} \quad (6.15)$$

with parameters $b_0 = 8.5 \times 10^3$, $b_1 = 5.0$, and $b_2 = 3.0 \times 10^2$. Simulated intensity profiles based on eq. (6.15) shown in Figure 6.23(b) are in good agreement with experimental intensity profiles, shown in Figure 6.23.¹

The first term in eq. (6.15), $R_1(Q, t)$, represents the shape of the scattering amplitude of the crystal analyser, while the second term, $R_2(Q, t)$, carries information about the microstructure transformations in the sample during the ageing treatment. We suggest that the shape of $R_2(Q, t)$ can be explained by the specific nature of point defect distribution, such as vacancies, Cu atoms, *etc.*, throughout the crystal lattice of the Al matrix. The lack of long-range spatial correlation, in the case of an almost random distribution of defects at the initial stage of the ageing treatment, leads to formation of a broad diffusion peak, which can be anisotropic in reciprocal space ([Krivoglaz, 1996](#)). At the microscopic level, this can be expressed as long-period modulation of the lattice strain field. It is evident from the experimental results that further treatment leads to the redistribution of point defects and the formation of nanoscale clusters (precipitates). The grouping of point defects into clusters, coherent precipitates, or other organised structures, changes the strain field (by decreasing the period of strain field modulation) and results in a redistribution of scattering intensity profile (i.e. the appearance and elongation of the "shoulder", ε) ([Krivoglaz, 1996](#)). From this perspective, the $\varepsilon(t)$ function (Figure 6.24) can be used as an order parameter of the field modulation.

We hypothesise that further growth and clustering of nanoprecipitates leads to further localization of the strain field in short-range regions and to depletion

¹These diffraction profiles were simulated by the author.

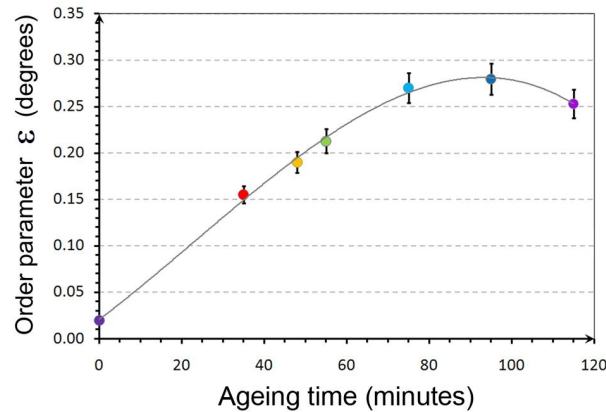


FIGURE 6.24: Strain field modulation parameter, ϵ , as a function of time, t .

of Cu atoms in the Al matrix, as discussed in chapter 2. We conjecture that the intermittent annealing resulted in a higher number density of precipitates, with a resultant smaller size (and narrow spread of sizes) than would otherwise be reached if artificial ageing was continuous for the equivalent period. In an earlier study on a similar alloy (Nikulin *et al.*, 2007; Nikulin, A.Y. and Dilanian, R.A. and Gable, B.M. and Muddle, B.C. and Hester, J.R. and Ishikawa, T. and Yang, P. and Moser, H.O., 2008), simulations and 3D nanoparticle reconstructions indicated that the modal nanoparticles are the most significant contributor to the diffraction pattern collected with a similar experimental setup. Thus the angular position of the additional peak, which becomes visible at 136 minutes of ageing (Figure 6.23(a)), corresponds to the modal size of the precipitates (Nikulin *et al.*, 2007; Zatsepin *et al.*, 2008). Considering that the X-ray propagation direction is parallel to $[111]_{\text{Al}}$, while the precipitates grow along the $\{100\}_{\text{Al}}$ planes (chapter 2), the effective mean precipitate size (calculated from $\lambda/\epsilon_{\text{final}} \sim 26.0\text{nm}$, where λ is the X-ray wavelength), multiplied by the interplanar spacing $\sqrt{h^2 + k^2 + l^2} = \sqrt{3}$, results in an actual mean precipitate size of 45nm. Figure 6.25 shows transmission electron micrographs of the sample subsequent to the final stage of annealing. Amid the myriad of smaller nanoparticles, clusters of coarser Al_3Cu precipitates are starting to form (Figure 6.25(a)). Figure 6.25(b) shows the modal size of the locally homogeneous Cu nanoparticle phase precipitates (§2.2) to be just under 50nm in diameter, with very low variation, which is comparable to the size determined from our diffraction data.

From a materials engineering perspective, it is still too early to assert consummate knowledge of the entire clustering mechanism, despite extensive interdisciplinary studies on precipitation behavior in Al-Cu alloys (Kanadani and Sakakibara, 1989;

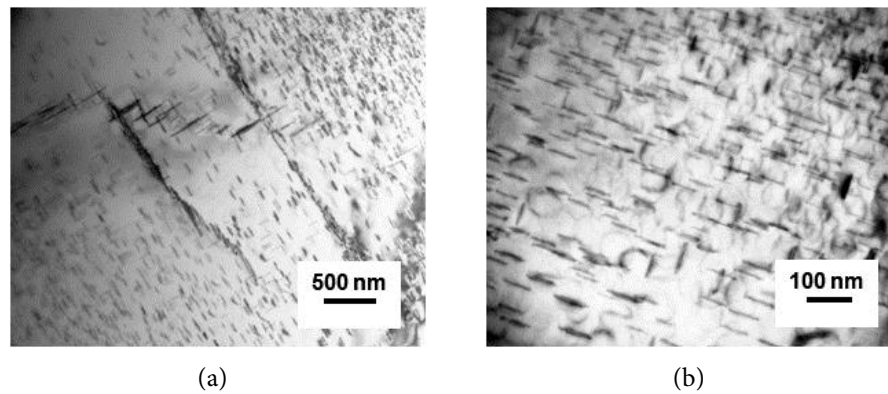


FIGURE 6.25: $\langle 100 \rangle_{\alpha}$ zone axis TEM micrographs of an Al-4.0wt% Cu sample, after 6 periods of ageing at 220°C for a total of 136 minutes. (a) Shows an isolated cluster of coarser θ' precipitates among hundreds of smaller θ'' precipitates. (b) Shows the modal θ'' precipitate size to be just under 50nm. TEM was carried out on a Philips CM20 instrument operated at 200 keV.

Barlat and Liu, 1998; Son *et al.*, 2005; Esmaili and Lloyd, 2006). A more thorough exposition would require absolute understanding of the interaction of the strain fields across the whole volume subjected to experimental investigation (an incredibly complex problem). There is no known method that can directly observe the migration of individual Cu atoms within their host matrix or quantitatively distinguish strain fields in bulk materials. Investigations of the redistribution of individual solute atoms in order to assemble into clusters and precipitates can only be theoretical or a numerical simulation, as performed by Wolverton (1999) and Wang *et al.* (2005), for example. However, such precise, localised simulations, which focus on individual atoms, require one to make the fallible assumption that the results are representative of the bulk material. The analysis presented here illustrates that bulk-material studies on the nanometer scale do not necessitate distinguishing individual Cu atoms in order to investigate nucleation and strain dynamics. The sample used herein was a very high quality aluminium single crystal, which, due to the absence of defects, justifies the assumption of an initially homogeneous solid solution across the large volume of sample illuminated by the X-rays ($\sim 0.20 \times 0.40 \times 0.70 \text{mm}^3$). Thus our analysis, involving a strain order parameter to model ensemble averaged strain dynamics, is an appropriate approach for a bulk material investigation. The widespread homogeneity in particle dimensions was also supported by the transmission electron micrograph obtained subsequent to the *in situ* annealing (Figure 6.25).

It has been shown that HIO-like algorithms are capable of reconstructing a complex object, including strain in a nanocrystal, (Fienup, 1987; Pfeifer *et al.*, 2006;

Newton *et al.*, 2009), provided sufficiently strong support constraints are applied. However, it is difficult to establish an appropriate support size for iterative reconstructions as the strains are not confined to a nanoparticle but rather, they extend far into the Al matrix, beyond the dimensions of the early precipitates. The reciprocal space resolution of the 50×50 step RSMs measured in this experiment defined a real space range of 794nm along x and 314nm along z . In the best case scenario, oversampling would be sufficient for a reconstruction if the area of the support was at most half the entire area, and the reconstructed average strain distributions would have to fit within the support. The purpose of this experiment was to demonstrate the possibility of investigating *in situ* diffraction effects from the very early stages of the growth of weakly diffracting nanoparticles, so it was not expected that the relatively low angular resolution RSMs would serve as a basis for nanoparticle reconstruction.

6.4.4 Conclusions

In summary, this experiment represents the first *in situ*, real-time X-ray investigation of the nanoparticle growth in an Al-Cu sample representative of the bulk material. We developed a semi-quantitative analysis of dynamic local strain transformations surrounding the precipitates at the earliest stages of their formation. A simple but justifiable interpretation of the diffraction data identified dynamic changes in the strain field that can be characterized by an order parameter, allowing one to qualitatively explain the unusual behavior of intensity profiles during the ageing treatment of Al-Cu alloys. This innovative work warrants further study in order to establish a more quantitative characterisation method for *in situ* precipitate nucleation and kinetics, and suggestion for such work are presented in the next chapter. Nonetheless, the experimental technique presented here had been demonstrated to allow real-time, *in situ*, non-destructive analysis of a large 3D volume of material, with sufficient resolution to resolve nanoparticles.

Combined with the ability to record high angular and spatial resolution reciprocal space maps from weakly diffracting embedded nanoparticle ensembles (as shown in §6.2) we have demonstrated that the TAD technique developed in this thesis is capable of static and real-time characterisation of bulk material samples.

6.5 Summary

This chapter presented three stages in the experimental development of our analyser based, reciprocal space mapping technique for the characterisation of samples containing ensembles of weakly diffracting, embedded nanoparticles. In the feasibility study we explored various nanoparticle size distributions and sample thicknesses. We confirmed predictions from simulations in the previous chapter, that the sample information is concentrated on the monochromator pseudo streaks. Although the polydispersity and imprecisely known sample alignment complicated the analysis of the experimental monochromator streaks directly, a successful nanoparticle reconstruction from a 2D reciprocal space map demonstrated that quantitative information about the weakly diffracting ensemble is obtainable with our technique. We then examined the practicalities of recording real-time diffraction data from Al-Cu alloys at early stages of nanoparticle growth, enabling the first TAD based X-ray diffraction study of *in situ*, real-time nanoparticle formation in an Al-Cu alloy to be carried out. The interesting results obtained in the final experiment, made possible by the sample and experimental parameters tested by the preliminary investigations, were analysed in the context of a semi-quantitative model of local interparticle strain, with excellent agreement between simulation and experiment. Limitations and suggested future development of our nanoparticle characterisation technique are included in the following chapter.

Conclusions

7.1 Overview

We have presented the first stages in the development of a novel technique for the non-destructive, bulk material characterisation of nanomaterials that contain weakly diffracting, embedded nanoparticles. Current widespread and emerging techniques for nanoscale material imaging and characterisation were critically reviewed with respect to the potential of embedded nanoparticle characterisation in Chapter 1. We asserted that a non-crystallographic X-ray characterisation method, such as analyser based, reciprocal space mapping, has distinct benefits due to the high penetration of, and resolution attainable with, hard X-rays in the 8–15 keV range.

The primary advantages of the analyser based, reciprocal space mapping technique are its sensitivity to low diffraction contrast, ability to encompass a large volume (up to several cubic millimetres) and deliver high resolution reconstructions of modal nanoprecipitates, representative of the ensemble, without the need for a tomographic approach. The measurement of diffracted intensity in reciprocal space with a counting detector provides the necessary high dynamic range and very high resolution (we showed a reconstruction in chapter 6 with 8 nm resolution), provided the sample remains unchanged over exposure times on the order of a few hours or more. This also allows us to use a large beam (e.g. up to $0.25 \times 1.50 \text{ mm}^2$ (v×h)) to explore sample volumes representative of the bulk material ($\sim 0.60 \text{ mm}^3$). The technique's robustness is highlighted by its lack of strong dependence on the X-ray coherence volume and experimental optics stability.

The technique has been demonstrated for *in situ* characterisation of the nanoparticle formation and growth in Al-Cu alloys, a typical example of a material class that draws its physical properties from the size, shape and distribution of naturally forming embedded nanoparticles. The morphology of these nanoparticles, along with

particulars of nanoparticle nucleation and growth kinetics were presented in chapter 2. A thorough understanding of the microstructure in this technologically important family of samples was necessary for the development and validation of such a novel technique.

We established an appropriate description of kinematic diffraction from large ensembles of weakly diffracting nanoparticles embedded in a matrix, as well as the necessary aspects of X-ray dynamical diffraction theory to encompass the pertinent role of high quality monochromator and analyser crystals (chapter 3). We then devised a corresponding simulation methodology by considering the limits of the first Born and projection approximations for the Al-Cu nanoparticles in particular. We simulated Fraunhofer diffraction and reciprocal space maps from nanoparticle ensembles in different orientations and with varying degrees of polydispersity (chapter 5). In these simulations we quantified the correlation between the size distribution of an ensemble of nanoparticles and the average nanoparticle size iteratively reconstructed from the Fraunhofer diffraction patterns of numerous such ensembles. We also demonstrated that using a beam with dimensions on the order of typical coherence volumes (even at third generation synchrotrons) is insufficient for a successful nanoparticle reconstruction from a spatially random distribution of such nanoparticles. We also showed how the average nanoparticle size and orientation can be determined directly from the 1D monochromator pseudo streaks in the reciprocal space maps from two sample orientations (with a known relative angle).

Exploiting the high brilliance of synchrotron X-rays, we validated the sensitivity of the technique to embedded nanoparticles and their crystallographic orientation in chapter 6. Despite the very low number density of the weakly diffracting nanoparticles in those particular samples, we successfully reconstructed, in three dimensions, a nanoparticle representative of the ensemble, using limited *a priori* knowledge about the symmetry of the particle.

Practical considerations for the design of an *in situ*, real time X-ray diffraction investigation of the initial growth dynamics of embedded nanoparticles in a bulk material sample were explored in a demonstration experiment. Finally, we presented the first, real-time, *in situ* X-ray diffraction investigation of the nanoscale precipitates during the early stages of artificial ageing of Al-Cu alloys. A model of specific, dynamic local strain transformations in the host Al matrix was used to semi-quantitatively explain the unusual behavior of experimental diffracted intensity profiles, supported by very well correlated simulations.

7.2 Limitations of this study and suggested future work

7.2.1 Extensions of the technique to laboratory X-ray sources

The success of the presented technique in addressing the problem of bulk material nanoparticle ensemble characterisation suggests further development is warranted. In order to generalise and make practicable its promised capabilities, the technique would be preferred on laboratory sources. Indeed, in terms of convenience, general accessibility and the cost of synchrotron beamline use, laboratory X-ray sources are preferable to synchrotrons for such investigations. We can infer that the technique does not require modification to be adapted to an incoherent X-ray source such as a rotating anode as the technique does not require a high degree of experimental optics stability nor coherence volume. Such investigations have begun with a rotating anode X-ray source at the School of Physics at Monash University.

A significant limitation of reciprocal space mapping with an analyser crystal is the data collection time, limited by available photon flux. A single reciprocal space map (RSM) on a 162×162 grid required 8–10 hours at a high-brilliance undulator beamline at SPring-8, and would require even longer at the Photon Factory. Fortunately the technique does not suffer from the effects of mechanical instabilities on the micron scale, even lateral or vertical vibrations of the analyser are tolerated provided the beam is diffracted entirely into the detector aperture. However, the thermal stability of the analyser may start to play a role for longer scans. Extended experimental time would require a reliable method of monitoring the incident flux in order to meaningfully normalise the RSM.

The increased beam divergence of a laboratory X-ray source, in comparison to a synchrotron X-ray source, would decrease the achievable angular resolution in experimental data. To retain the same high angular resolution in the RSMs measured in a laboratory as that in the RSMs presented in this thesis, a second analyser crystal would be needed downstream of the first analyser. The significant loss of flux concomitant with the use of the second analyser crystal could be overcome with a larger beam or thorough elimination of parasitic scattering. Fortunately, the statistical homogeneity of the samples allows us to illuminate a much larger region with the expected signal magnification approximately proportional to the number of particles illuminated. This setup would be more accurately simulated by XDC, the dynamical

diffraction code for conventional triple crystal diffractometry that was used in the simulations presented in chapters 5. The X-ray diffractometer at the School of Physics at Monash University is also currently being developed to include a double analyser setup for further development of this work.

7.2.2 Suggested further development of the method for simulating two dimensional RSMs

There are a number of sample and experimental aspects that have significant effects on the measured data. In this thesis we have made progress in understanding some of these well, but for a fully comprehensive picture of experimentally measured diffraction data we need to further develop the simulation methods.

We need to establish a more comprehensive method for simulating the two dimensional (2D) RSMs than the one presented in this thesis as it only involved one dimensional (1D) sample data in the RSMs. This 1D approach was shown to be suitable for samples and experimental conditions where the first Born and projection approximations are valid. However, quantitative information about the sample could only be obtained from the 1D data with sufficient *a priori* knowledge, e.g. the alignment of at least one sample axis. However, for randomly orientation embedded nanoparticle systems we would like to be able to simulate the true three dimensional (3D) nature of the diffraction process, including both the elastic scattering in the sample and the dynamical diffraction in the analyser. Here we suggest an approach to simulating 2D RSMs containing 2D Fraunhofer diffraction from the sample and discuss the implications of the finite acceptance of the analyser in two dimensions.

Under the first Born approximation we can consider the instrumental function and the sample's Fraunhofer diffraction as independent (incoherent) contributions to the RSM. The steps for the suggested approach to 2D RSMs are as follows: 1. Calculate the 2D Fraunhofer diffraction pattern (in the (x_s, z_s) plane) of a 3D sample containing an embedded ensemble of nanoparticles, with intensities weighted by the reflectivity of the monochromator; 2. Rotate this by θ_B anticlockwise to align (k_x) with the monochromator pseudo streak in the (Q_x, Q_z) coordinates of the analyser crystal; 3. Calculate the resultant X-ray wavefield, which is an incoherent sum of the incident wave (in this case the instrumental function) and the diffracted component (the monochromator-reflectivity-weighted Fraunhofer diffraction pattern). The instrumental function can again be calculated using XDC. In addition, nanoparticle reconstruction methods should be developed from such simulated data, including a

deconvolution of the instrumental function if the sample's diffraction signal is too weak.

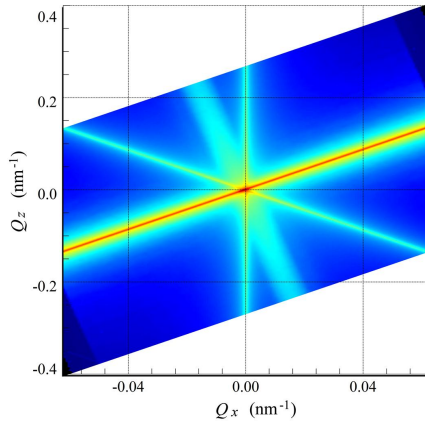
For the purpose of demonstration we present a number of examples of such simulations exploring 2D aspects in Figure 7.1. The second orientation in each set is at 45° about the optical axis relative to the first orientation. The simulated sample contained an ensemble of Al_2Cu nanoplatelets (in Al) with normally distributed diameters where the mean diameter, $S_m = 250\text{nm}$, and the standard deviation, $\sigma = 50\text{nm}$.

The strong diffraction signal along the monochromator pseudo streak, particularly in Figures 7.1(a) and 7.1(b), is expected from the idealised alignment. The much weaker signal parallel to k_z remains the same in both RSMs since the nanoparticles that give rise to it do not change their orientation with respect to the diffraction plane of the analyser. In Figure 7.1(c) and 7.1(d) the sample is slightly misaligned with respect to the beam, i.e. $\theta_X = 5^\circ$, $\theta_Y = -5^\circ$, $\theta_Z = 5^\circ$ and for orientation 2, $\theta_Z = 50^\circ$, which represents a plausible experimental scenario. The obvious difference between these RSMs and those from the perfectly aligned sample once again emphasises the technique's high sensitivity to sample orientation, which we discussed at length in the previous two chapters. In Figure 7.1(e) and 7.1(f), the sample orientation was chosen at random, where the realisation shown has $\theta_X = 31^\circ$, $\theta_Y = 5^\circ$, $\theta_Z = 28^\circ$ and $\theta_Z = 73^\circ$ for orientation 2. While these 2D RSMs show significant differences, their monochromator pseudo streaks (compared in Figure 7.2) are generally very similar. Thus some *a priori* knowledge about sample orientation is necessary in order to analyse 1D diffraction results in the manner discussed in §5.3.3, and to optimise the data collection.

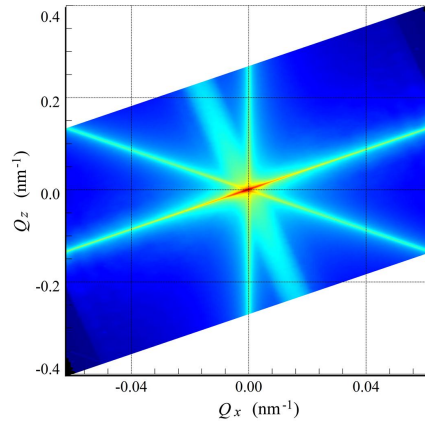
In such simulations it would be necessary to quantitatively justify the strength of the contribution to the RSM made by the sample's Fraunhofer diffraction pattern by considering the total diffracting volume, which depends on the nanoparticle number density, sample thickness and beam size.

7.2.3 Implications of the 2D diffraction plane of the analyser

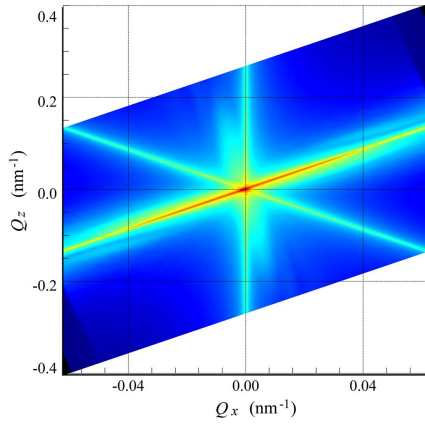
In relation to step 1 from the previous discussion, we need to also consider the following. Since the analyser is sensitive to diffraction only in the (k_x, k_z) plane of the sample, we need to consider how diffracted X-rays with a non-zero k_y component affect the measured intensity. In the experiments undertaken, the detector collimating



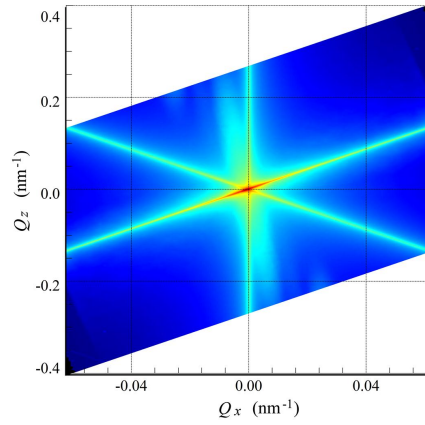
(a) Orientation 1: perfect alignment;
 $\theta_X = 0^\circ, \theta_Y = 0^\circ, \theta_Z = 0^\circ$



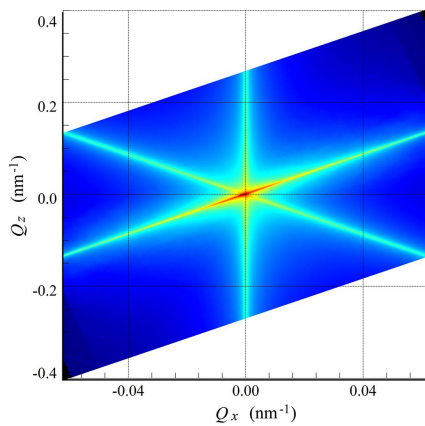
(b) Orientation 2: perfect alignment with
 $\Delta\theta_Z = 45^\circ; \theta_X = 0^\circ, \theta_Y = 0^\circ, \theta_Z = 45^\circ$.



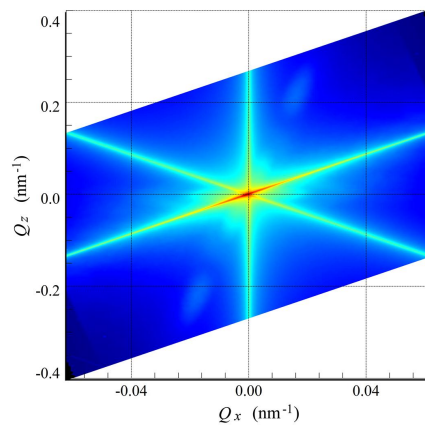
(c) Orientation 1: slightly misaligned;
 $\theta_X = 5^\circ, \theta_Y = -5^\circ, \theta_Z = 5^\circ$



(d) Orientation 2: slightly misaligned with
 $\Delta\theta_Z = 45^\circ; \theta_X = 5^\circ, \theta_Y = -5^\circ, \theta_Z = 50^\circ$



(e) Orientation 1: random orientation;
 $\theta_X = 31^\circ, \theta_Y = 5^\circ, \theta_Z = 28^\circ$



(f) Orientation 2: random orientation with
 $\Delta\theta_Z = 45^\circ; \theta_X = 31^\circ, \theta_Y = 5^\circ, \theta_Z = 73^\circ$

FIGURE 7.1: **Simulated RSMs with 2D sample functions from nanoparticle ensembles in various orientations**, shown on a log scale. The sample was an array of platelet Al_2Cu nanoparticles with $S_m = 250\text{nm}$ and $\sigma = 50\text{nm}$. Orientation 2 was at 45° about the optical axis relative to orientation 1 for comparison with RSMs in previous chapters. The strongest sample signal is expectedly along the monochromator pseudo streak but substantial diffraction effects are visible in the k_z direction. The monochromator pseudo streaks from (e) and (f) are compared in Figure 7.2.

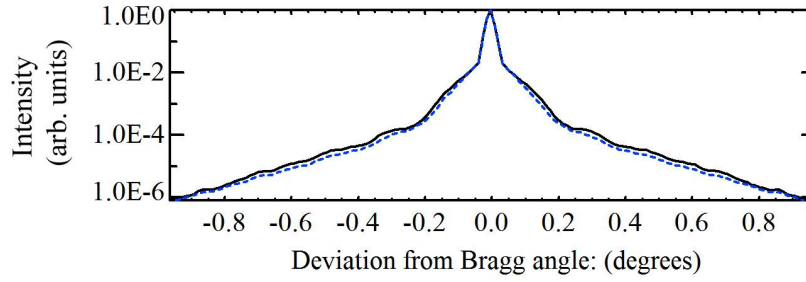


FIGURE 7.2: **Simulated monochromator pseudo streaks from Figure 7.1(e) and 7.1(f) compared.** The platelet nanoparticles were rotated by 31° , 5° and 73° about the x_s , y_s and z_s axes, respectively. Orientation 1 (dashed blue line) and 2, with the sample oriented at $\theta_Z = 45^\circ$ relative to orientation 1 (solid black line) are generally very similar while substantial differences are evident in the simulated 2D RSMs (Figures 7.1(e) and 7.1(f)) demonstrating the benefits of a 2D simulation method to explore all possible sample orientations.

slit perpendicular to the diffraction plane was either very wide ($\sim 5\text{mm}$) or omitted altogether, such that the acceptance window greatly exceeded the scattered wavefield. The $\pm k_y$ range imposed by the reflectivity of the analyser crystal thus served as the only limitation.

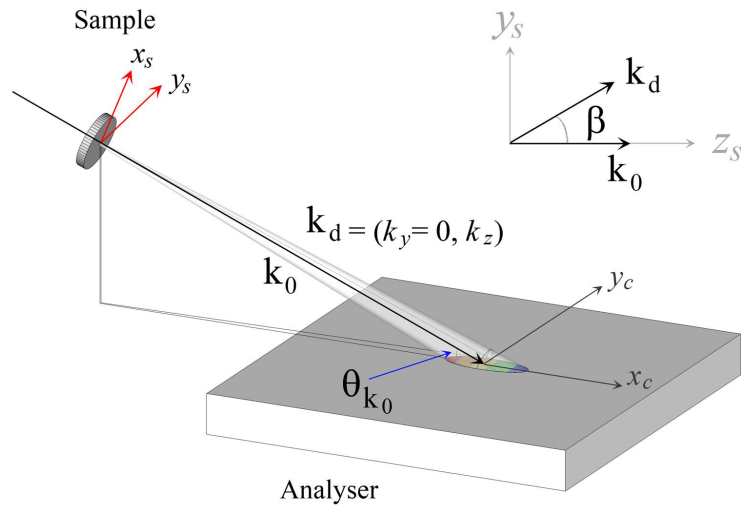
The schematic in Figure 7.3(a) shows the diverging beam (diffracted X-rays) emerging from the sample (exaggerated for clarity), incident on the analyser crystal. Consider the magnification of the surface of the analyser crystal for figure 7.3(a), in Figure 7.3(b). The coordinates (x_s, y_s) correspond to the vertical and horizontal directions in the sample, (x_c, y_c) correspond to the coordinate system parallel to the surface of the analyser crystal (we only consider symmetric Bragg reflections), and the analyser is rotated about the y_c axis, rendering it insensitive to diffraction in that direction.

X-rays diffracted in the y_s (k_y) direction, labeled k_d in Figure 7.3(b), have a smaller incident angle, θ_{k_d} , compared to the direct beam, θ_{k_0} , i.e. $\theta_{k_d} = \theta_{k_0} - \omega$. The angular decrement ω is related to the diffraction angle in the k_y direction, β , by

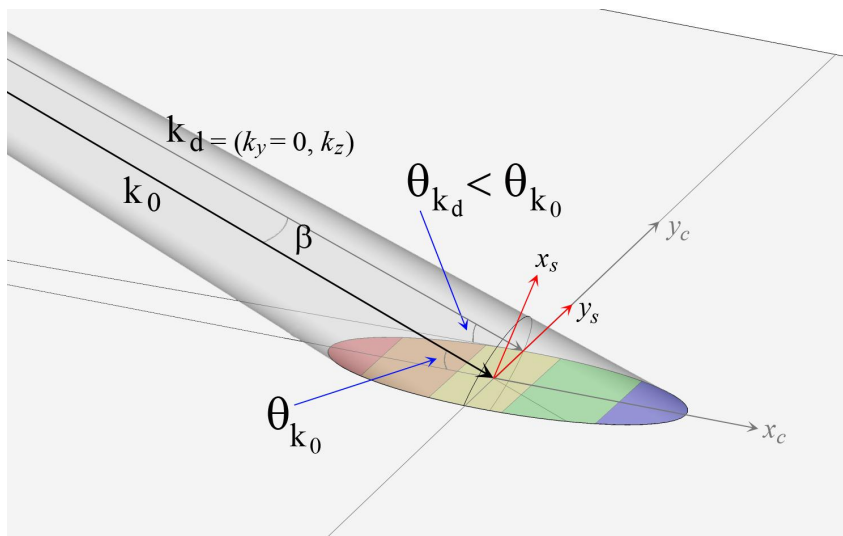
$$\omega = \theta_{k_0} - \arctan \left[\cos \left(2 \arcsin \left[\frac{1}{2} \beta \sec(\theta_{k_0}) \right] \right) \tan(\theta_{k_0}) \right]. \quad (7.1)$$

Incidentally, for $\beta < \pi/4$, eq. (7.1) gives the same result as eq. 4 in Nesterets *et al.* (2004), where the deviation from θ_{k_0} of incident angle of the y-diverted beam, ω , is related to the divergence in the y direction, β , by (Pinsker, 1978)

$$\omega = \frac{\beta^2}{2} \tan(\theta_{k_0}). \quad (7.2)$$



(a) Schematic of X-ray beam diffracted by the sample, incident on the analyser crystal. The colors of the intersection of the beam with the analyser surface correspond to their x diffracted components.



(b) Magnification of 7.3(a) with angles labelled as discussed in the section on the resolution function.

FIGURE 7.3: Incident X-ray beam on the analyser. X-rays diffraction by the sample with a non-zero k_y component are incident on the analyser at slightly smaller angles than the direct beam, \mathbf{k}_0 , limiting the amount of y deviated X-ray beam that reaches the detector with appreciable intensity.

For a perfectly aligned high quality analyser crystal, these X-rays will contribute significantly to the measured intensity if their incident angle is within $\pm\delta_{os}$ of θ_B , where δ_{os} is half the Darwin width of the analyser's rocking curve defined in eq. (3.35), with typical values shown in Table 4.2.

Using 1.13747\AA X-rays incident on a Si(400) analyser crystal results in $\omega = \delta_{os} = 2.26''/2$ (Stepanov, 2008), which limits β to $\pm 1005''$ according to eq. (7.1). A simulated 3D Fourier transform of an N^3 array of nanoparticles, where $N = 200$ sampled at $\Delta y = 10\text{nm}$ increments, renders the step size Δk_y as $5 \times 10^{-4}\text{nm}^{-1}$, which corresponds to a diffraction angle of $\sim 57\ \mu\text{rad}$ or $11.7''$. For this particular array size and sampling rate, the incoherent superposition of k_y -diffracted X-rays would thus involve 172 pixels, i.e. $1005/11.7 \approx 86$ pixels about $(k_x, k_z) = (0, 0)$, covering the range $k_y \in (\pm 0.043\text{nm}^{-1})$.

In Figure 7.4 we compare the Fraunhofer diffraction pattern in the (k_x, k_z) plane at $k_y = 0$ with that comprised of a projection in reciprocal space of the Fraunhofer diffraction patterns where $k_y \in (\pm 0.043\text{nm}^{-1})$. These simulations are comprised of incoherent diffraction patterns from 500 realisations of spatially randomly distributed Al_2Cu nanoparticles in a $2 \times 2 \times 2\ \mu\text{m}^3$ volume. The nanoparticles in this example were aligned perfectly with the diffraction plane for orientation 1 and with $\theta_z = 45^\circ$ for orientation 2.

For orientation 1 there was a slight decrease of interference fringes and an increase in overall intensity, as expected (compared Figure 7.4(c) to 7.4(a)). However, the significance of the contribution from y -diffracted X-rays is particularly well pronounced in comparing the $(k_y = 0)$ diffraction pattern in Figure 7.4(b) with that from $k_y \in (\pm 0.043\text{nm}^{-1})$ in Figure 7.4(d), both from the sample in orientation 2. In the latter, the diffraction signal along k_x arising from the rotated nanoparticles' facets is dominant, while it is relatively weak in the single diffraction pattern at $k_y = 0$. It is thus clear that 3D effects play a significant role in the diffraction pattern obtained by our technique and so should be incorporated into future simulations and reconstructions.

The cumulative effect of the aspects we have discussed, including sample alignment, polydispersity, the need for considering the 3D nature of diffraction and, as discussed in §6.2.4, an insufficient signal-to-noise ratio in real data, appears to be stagnation of the reconstruction algorithm. Attempts at reconstructing nanoparticles from either set of simulations (Figures 7.1 and 7.4) using the iterative method described in §5.2.1 have not been successful, thus warranting further reconstruction technique development for simulations. However, reconstructions from experimental data have shown good agreement with expected nanoparticle microstructures (e.g. in §6.2.4). Improvements in the reconstruction approach for future simulated and

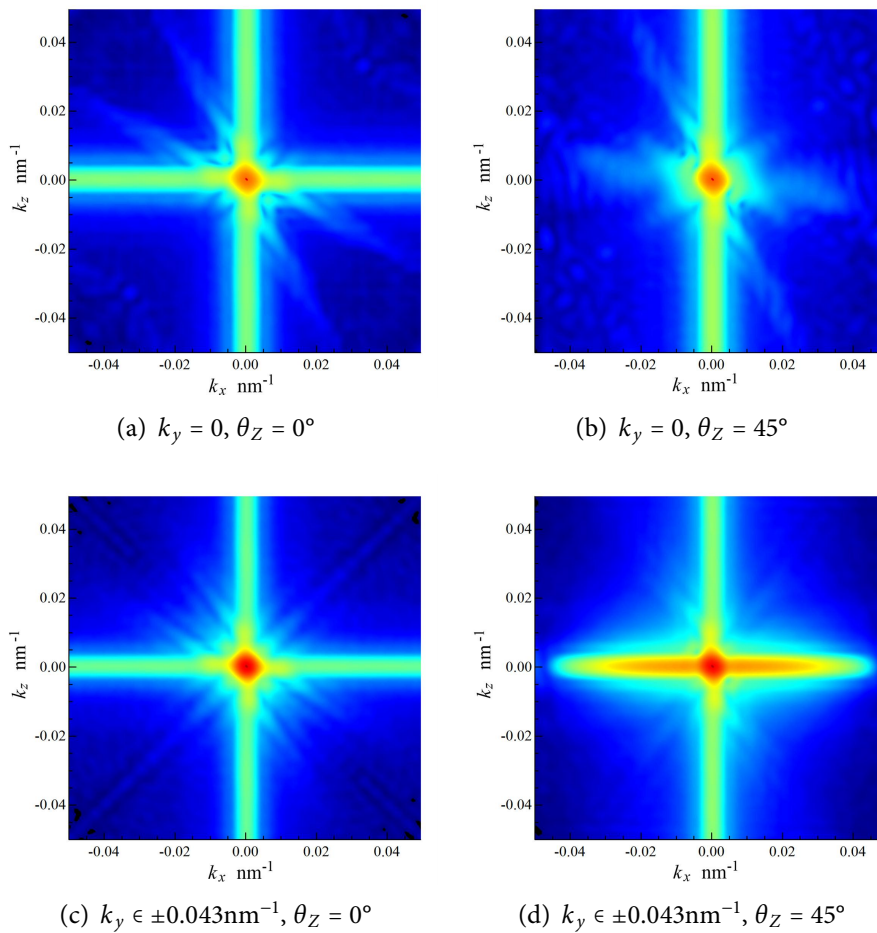


FIGURE 7.4: **Fraunhofer diffraction patterns from 3D nanoparticle ensembles**, shown on a log scale. The 2D diffraction pattern in the (k_x, k_z) plane at $k_y = 0$ is compared with the incoherent sum of 172 (k_x, k_z) diffraction patterns covering the range $k_y \in (\pm 0.043 \text{ nm}^{-1})$. The significance of considering the 3D nature of the interaction of the diffracted beam and the analyser's reflectivity is emphasised by the difference between (b) and (d).

experimental data should include additional constraints to ensure convergence. An example of a useful restrictive condition is the shrinkwrap algorithm (Marchesini *et al.*, 2003), which has been shown to be successful with nanoparticle reconstructions from similar experimental data (cf. §5.2.1), some of which is presented below.

7.2.4 Current work on nanoparticle reconstruction based on outcomes discussed in the thesis

A number of further experiments were carried out as a result of the technique methodology developed in this thesis. These experiments were based on our outcomes and confirmations of the suitability of source characteristics and experimental parameters such as beam size, X-ray energy and scan ranges, as well as sample particulars such as thickness, Cu concentration and preparation procedures. Ongoing related work at Monash University includes further development of nanoparticle image reconstruction from RSMs collected from similar and identical samples to those used herein. Some promising reconstruction results are shown in Figures 7.5 (Pelliccia *et al.*, 2010). We will discuss these results in outline only as they do not form part of the author's contribution to the technique.

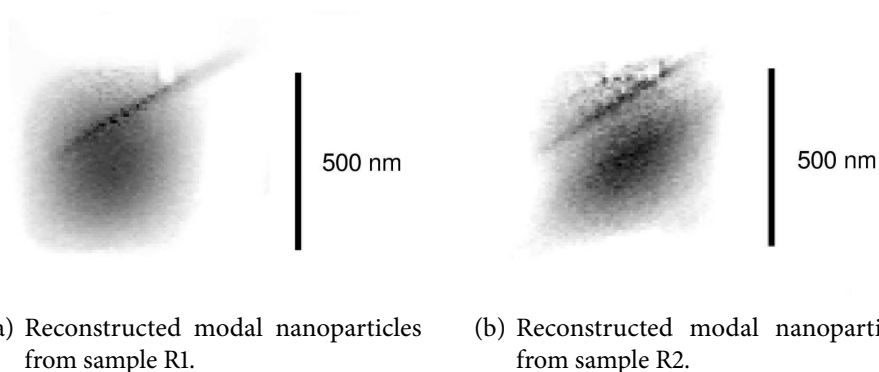


FIGURE 7.5: **Reconstructed nanoparticles from experimental RSMs.** Both Al-4.0wt% Cu samples were $\lesssim 0.30$ mm thick along the beam, artificially aged at 220° for 8.5 hours. The microstructure is shown in the transmission electron micrograph in Figure 7.6. The reconstruction results are relatively consistent for the two samples that were prepared identically but were in slightly different orientations. Data from Pelliccia *et al.* (2010) used with permission.

These nanoparticles were reconstructed using a combination of the hybrid input output (HIO) algorithm used in this thesis and the error reduction (ER) algorithm, as well as a dynamic support (the shrinkwrap algorithm) (see §5.2.1 for details).

The spatial resolution in the reconstructions was 12 nm (Figure 7.5), which strongly affected the thickness of the reconstructed nanoparticles.

In our exploration of the threshold of nanoparticle detectability in these types of samples (§6.2), we discussed that a thinner sample is beneficial due to less attenuation by the Al matrix, while a higher number of nanoparticles would, naturally, result in a stronger signal. Hence the Al-4.0wt% Cu sample with a thickness of $\lesssim 0.30\text{mm}$ along the direction of X-ray beam propagation, which were used for the experiments discussed by Pelliccia *et al.* (2010), provided a sufficiently high nanoparticle number density (due to the high concentration of Cu), while beam attenuation was decreased in comparison to our thicker samples. These samples were aged at 220° for 8.5 hours resulting in the microstructure shown in the transmission electron micrographs in Figure 7.6. The beam size was set to $0.10 \times 1.00\text{mm}^2$ (v

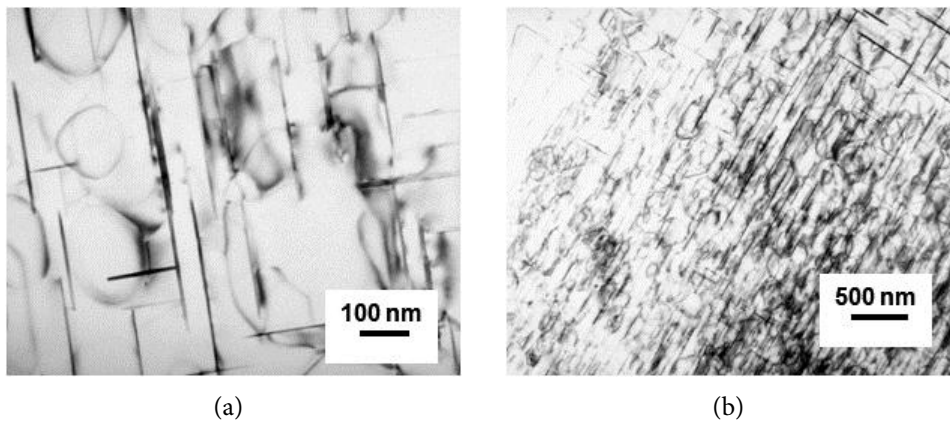


FIGURE 7.6: $\langle 100 \rangle_\alpha$ zone axis transmission electron micrograph of Al-4.0wt% Cu aged at 220° for 8.5 hours. The dimensions of the reconstructed nanoparticles in Figure 7.5 are in good agreement with those shown here. TEM was carried out on a Philips CM20 instrument operated at 200 keV.

Repeated attempts to reconstruct nanoparticles using the shrinkwrap algorithm, starting with random phase distributions, resulted in very similar reconstructions. The consistent convergence of the reconstructed nanoparticle shape lends credibility to the reconstruction despite our demonstrated sensitivity to nanoparticle orientation in both simulation and experimental data. The reproducibility and consistency shows that despite the non unique nature of the reconstructions, which require *a priori* knowledge about the sample to interpret appropriately, these results are very promising.

An interesting question remains, which concerns the contribution to the diffraction pattern of nanoparticles significantly larger than the majority of nanoparticles in the ensemble. The reconstructions from simulated Fraunhofer diffraction patterns of normally distributed polydisperse Al₂Cu nanoparticles in §5.2.2 showed that the reconstructed nanoparticle profile was asymmetric with a tail-like effect (Figure 5.10). However, the nanoparticle distributions are naturally closer to Boltzmann distribution curves than a true Gaussian distribution, wherein the modal and average nanoparticle diameters are no longer the same. It would thus be interesting to simulate other polydisperse systems (including Boltzmann distributions and bimodal distributions) in addition to the normally distributed ones as presented in this work, in order to more confidently interpret the nanoparticle reconstruction results from future experimental data.

7.2.5 Retrospective considerations regarding the samples

We showed in this thesis that relatively quantitative information can be obtained about the nanoparticle ensemble in a sample representative of the bulk material, relatively quickly (on the order of ~5 minutes). Thus the technique developed in this thesis could be supplementary to other nanoparticle characterisation techniques. For example transmission electron microscopy may provide some information about the microstructure; our technique may then be implemented to analyse, on the bulk material scale, the embedded weakly diffracting nanoparticle ensemble. It can even be used for *in situ*, real-time nanoparticle growth studies, although it requires optimisation for each particular nanoparticle system.

In §5.3 and §6.2 we discussed how the alignment of the nanoparticles with respect to the diffraction plane affects the diffraction patterns. We assumed that one set of nanoparticles were positioned with their faces consistently perpendicular to the optical axis and discussed rotation about the optical axis. It was shown in simulations that from two orientations with a known relative angle we could calculate the mean nanoparticle diameter and orientation of the sample (provided the ensemble was not too polydisperse) from the diffraction profile along the monochromator pseudo streak. We also discussed the possible contributions to the misalignment of the nanoparticles during sample preparation. This alignment problem could be overcome by using a sample holder with at least two degrees of freedom: rotation about the x_s and z_s axes, i.e. the vertical sample axis and the optical axis, preferably automated and with high precision.

Further experiments and simulations are also needed to establish more quanti-

tatively the relationship between diffraction signal (due to size and number density of nanoparticles) and overall thickness of the sample. Secondly, in hindsight, the number of degrees of freedom (parameters) in the microstructure of Al-Cu alloys proved too high even for the rigorous, quantitative feasibility studies presented herein. Even such a relatively "simple" light metal alloy does not have a guaranteed embedded nanoparticle shape or size distribution, with unnecessary complexities of nanoparticle nucleation and kinetics. If a monodisperse, well characterised ensemble of nanoprecipitates was available, it would be a more suitable candidate for quantitative development of the technique. However, it is precisely the lack of a characterisation method that could ensure or confirm the designed characteristics of a bulk material sample that inspired and instigated the research in the first place. A well characterised 2D nanoscale grid could be a good candidate, however in order to validate the technique's ability to characterise ensembles of polydisperse nanoparticles, the previous argument still stands.

In order to investigate real time, *in situ* nucleation and growth of precipitates in complex samples, an accurate model of the dynamic changes in the sample needs to be formulated. For example, in Al-Cu alloys, when the Cu is in supersaturated solid solution (and assumed to be homogeneous), optically the refractive index of the sample is a weighted mixture of the two elements. In essence, as the nanoparticles begin to nucleate, the crystal lattices of clusters and earliest forms of precipitates (pure Cu) are well aligned with the Al matrix, and are thus surrounded by lattice strain that extend much further into the lattice than the particle's size. The lattice strain can be modelled as a variation in the electron density, making the early precipitates continuous rather than discrete 3D volumes with Cu refractive index, in the simulations. As the nanoprecipitates grow, at some not strictly defined stage, their empirical composition becomes Al_3Cu , which would need to be included in the simulations. Eventually, the experimental approach could be extended to *in situ*, real-time investigations of the effects of stress/pressure on materials, which also significantly affect the microstructure (by preferential growth directions, for example).

7.3 Summary

A critical review of the limitations of current nanoscale imaging techniques was presented with a view to highlight the lack of a technique that is capable, alone, of non-destructive, high resolution characterisation of materials with embedded ensembles of weakly diffracting nanoparticles. The emerging analyser based, reciprocal

space mapping technique presented has been shown to be capable of reconstructions of nanoparticles representative of the ensemble with nanometer scale resolution. The essential details of the experimental setup, theoretical approach to simulations and preparation of samples were presented. The technique, though early in its development, boasts the capability of *in situ* investigations of nanoparticle formation and early stages of nanoparticle growth. The technique is also readily extendible to incoherent sources, with the potential to make high resolution, bulk material analysis with laboratory X-ray sources readily achievable.

Bibliography

- Afanas'ev, A.M., Aleksandrov, P.A., Imamov, R.M., Lomov, A.A., and Zavyalova, A.A. Diffraction scattering at angles far from the Bragg angle and the structure of thin subsurface layers. *Acta Cryst. A* **40**(4) 352–355 (1984). (Cited on pages 15 and 59.)
- Afanas'ev, A.M. and Fanchenko, S.S. On the X-ray analysis of thin subsurface layers. Bicrystal diffraction analogues. *Acta Cryst. A* **44**(1) 25–33 (1988). (Cited on page 15.)
- Afanas'ev, A.M. and Kohn, V.G. Dynamical theory of x-ray diffraction in crystals with defects. *Acta Cryst. A* **27**(5) 421–430 (1971). (Cited on pages 43, 47, 93 and 148.)
- Alani, R. and Pan, M. In situ transmission electron microscopy studies and real-time digital imaging. *J. Microsc.* **203**(1) 128–133 (2001). (Cited on pages 4 and 20.)
- Alexandropoulos, N.G. and Kotsis, K.T. Use of kinematical diffraction in x-ray topography. *J. Appl. Cryst.* **18**(6) 509–512 (1985). (Cited on page 59.)
- Als-Nielsen, J. and McMorrow, D. *Elements of Modern X-ray Physics*. Wiley, New York (2001). (Cited on page 8.)
- ANBF. Australian National Beamline Facility (ANBF) (2009). Available from: www.synchrotron.org.au/index.php/aussynbeamlines/external-beamlines. (Cited on page 53.)
- Aristov, V., Kuznetsov, S., Nikulin, A., and Snigirev, A. X-ray diagnostics of 2D strain profiles in semiconductor crystals. *Semicond. Sci. Technol.* **7** A168–A170 (1992). (Cited on page 13.)
- Aristov, V.V., Goureev, T.E., Nikulin, A.Y., and Snigirev, A.A. X-ray diagnostics of the elastic stress gradient in crystals. *Phys. Stat. Sol. A* **127**(1) 33–42 (1991). (Cited on pages 146 and 149.)
- Attwood, D.T. *Soft X-Rays and Extreme Ultraviolet Radiation: Principles and Applications*. Cambridge University Press, Cambridge (2000). (Cited on pages 32, 36, 50, 55 and 57.)
- Authier, A. *Dynamical Theory of X-Ray Diffraction*. Oxford University Press, Oxford (2003). (Cited on pages 40, 42, 43, 44, 45, 46, 51, 52, 57 and 59.)
- Ballabriga, R., Campbell, M., Heijne, E., Llopart, X., and Tlustos, L. The Medipix3 prototype, a pixel readout chip working in single photon counting mode with improved spectrometric performance. In *IEEE Nuclear Science Symposium Conference Record*, volume 6 (2006). (Cited on page 11.)

- Bamler, R. Can one see the Ewald sphere? *Appl. Opt.* **27**(10) 2012–2016 (1988). (Cited on page 39.)
- Bárcena, M. and Koster, A.J. Electron tomography in life science. *Semin. Cell Dev. Biol.* **20**(8) (2009). (Cited on page 4.)
- Barlat, F. and Liu, J. Precipitate-induced anisotropy in binary Al-Cu alloys. *Mater. Sci. Eng. A* **257**(1) 47–61 (1998). (Cited on pages 21 and 151.)
- Barnea, Z., Creagh, D.C., David, T.J., Garrett, R.F., Janky, S., Stevenson, A.W., and Wilkins, S.W. The Australian diffractometer at the Photon Factory. *Rev. Sci. Instrum.* **63**(1) 1069–1072 (1992). (Cited on page 53.)
- Bastow, T.J. and Celotto, S. Clustering and formation of nano-precipitates in dilute aluminium and magnesium alloys. *Mater. Sci. Eng. C* **23**(6-8) 757–762 (2003). (Cited on page 20.)
- Bataillou, B., Moriceau, H., and Rieutord, F. Direct inversion of interfacial reflectivity data using the patterson function. *J. Appl. Cryst.* **36**(6) 1352–1355 (2003). (Cited on page 148.)
- Bates, R.H.T. Fourier phase problems are uniquely soluble in more than one dimension: I: underlying theory. *Optik (Stuttgart)* **61** 247–262 (1982). (Cited on page 85.)
- BL-20B. Multipurpose monochromatic and white beam hard x-ray station (Australian National Beamline Facility) (2000). Available from: anbf2.kek.jp/spec2.html. (Cited on page 53.)
- BL13XU Outline. BL13XU: Surface and Interface Structures (2010). Available at: www.spring8.or.jp/wkg/BL13XU/instrument/lang-en/INS-0000000394/instrument_summary_view. (Cited on page 53.)
- BL29XU Outline. BL29XU: RIKEN Coherent X-ray Optics (2010). Available at: www.spring8.or.jp/wkg/BL29XU/instrument/lang-en/INS-0000000348/instrument_summary_view. (Cited on page 53.)
- Bonse, U. and Hart, M. An x-ray interferometer. *Appl. Phys. Lett.* **6**(8) 155–156 (1965). (Cited on pages 7 and 63.)
- Bonse, U. X-ray imaging: past and present. In S.R. Stock, editor, *Developments in X-Ray Tomography VI*, volume 7078. Proc. SPIE (2008). (Cited on page 5.)
- Borchardt-Ott, W. and Gould, R.O. *Crystallography*. Springer Verlag, Berlin (1995). (Cited on page 5.)
- Born, M. and Wolf, E. *Principles of Optics: Electromagnetic Theory of Propagation, Interference and Diffraction of Light*. Cambridge University Press, Cambridge, 7th edition (1999). (Cited on pages 32, 33, 35, 36, 38, 60 and 148.)

- Bowen, D.K. and Tanner, B.K. *High Resolution X-ray Diffractometry and Topography*. Taylor & Francis Ltd, London (1998). (Cited on page 13.)
- Bracewell, R.N. *The Fourier Transform and its Applications*. McGraw-Hill, New York, 3rd edition (2000). (Cited on pages 37, 115 and 132.)
- Bragg, W.H. The reflection of X-rays by crystals. (II.). *Proc. R. Soc. London, Ser. A* **89**(610) 246–248 (1913a). (Cited on pages 5 and 41.)
- Bragg, W.L. The structure of some crystals as indicated by their diffraction of X-rays. *Proc. R. Soc. London, Ser. A* **89**(610) 248–277 (1913b). (Cited on pages 5 and 41.)
- Bragg, W.L. *The Development of X-ray Analysis*. Bell, London (1975). (Cited on page 5.)
- Brumberger, H. *Modern Aspects of Small-Angle Scattering*, volume 451 of *Series C: Mathematical and Physical Sciences*. Kluwer Academic Publishers, Netherlands (1993). (Cited on page 8.)
- Bubakova, R. and Szmíd, Z. Proton bombardment damage in silicon. *Phys. Stat. Sol. B* **8** 105–114 (1965). (Cited on page 13.)
- Burge, R.E., Fiddy, M.A., Greenaway, A.H., and Ross, G. The phase problem. *Proc. R. Soc. London, Ser. A* **350**(1661) 191–212 (1976). (Cited on page 15.)
- Chapman, D., Thomlinson, W., Johnston, R.E., Washburn, D., Pisano, E., Gmur, N., Zhong, Z., Menk, R., Arfelli, F., and Sayers, D. Diffraction enhanced x-ray imaging. *Phys. Med. Biol.* **42**(11) 2015–2025 (1997). (Cited on page 7.)
- Chapman, H.N. Phase-retrieval X-ray microscopy by Wigner-distribution deconvolution. *Ultramicroscopy* **66**(3-4) (1996). (Cited on page 11.)
- Chapman, H.N., Barty, A., Bogan, M.J., Boutet, S., Frank, M., Hau-Riege, S.P., Marchesini, S., Woods, B.W., Bajt, S., Benner, W.H., London, R.A., Plonjes, E., Kuhlmann, M., Treusch, R., Dusterer, S., Tschentscher, T., Schneider, J.R., Spiller, E., Moller, T., Bostedt, C., Hoener, M., Shapiro, D.A., Hodgson, K.O., van der Spoel, D., Burmeister, F., Bergh, M., Caleman, C., Huldt, G., Seibert, M.M., Maia, F.R.N.C., Lee, R.W., Szoke, A., Timneanu, N., and Hajdu, J. Femtosecond diffractive imaging with a soft-x-ray free-electron laser. *Nat. Phys.* **2**(12) 839–843 (2006). (Cited on pages 10 and 12.)
- Chapman, H. X-ray imaging beyond the limits. *Nat. Mater.* **8**(4) 299–301 (2009). (Cited on page 12.)
- Chen, J.H., Costan, E., van Huis, M.A., Xu, Q., and Zandbergen, H.W. Atomic pillar-based nanoprecipitates strengthen AlMgSi alloys. *Science* **312**(5772) 416–419 (2006). (Cited on pages 4 and 20.)
- Cloetens, P., Barrett, R., Baruchel, J., Guigay, J., and Schlenker, M. Phase objects in

- synchrotron radiation hard x-ray imaging. *J. Phys. D* **29** 133–146 (1996). (Cited on page 7.)
- Cohen, H.A., Schmid, M.F., and Chiu, W. Estimates of validity of projection approximation for three-dimensional reconstructions at high resolution. *Ultramicroscopy* **14**(3) 219–226 (1984). (Cited on page 39.)
- Cowley, J.M. *Diffraction Physics*. North Holland Publishing Company, Amsterdam (1975). (Cited on pages 4, 36, 40 and 99.)
- Creagh, D.C., Foran, G.J., Cookson, D.J., Garrett, R.F., and Johnson, F. An eight-position capillary sample spinning stage for the diffractometer at BL20B at the Photon Factory. *J. Synchrotron Radiat.* **5** 823–825 (1998). (Cited on page 53.)
- Cruickshank, D.W.J., Juretschke, H.J., and Kato, N. *P. P. Ewald and his Dynamical Theory of X-ray Diffraction*, volume 50. Oxford University Press, New York, 2nd edition (1996). (Cited on page 42.)
- Czeczor, S., Löchte, L., Gottstein, G., Staron, P., and Kampmann, R. Growth kinetics of Guinier-Preston-zones in Al-4wt%Cu studied by small-angle neutron scattering and transmission electron microscopy. *Phys. Stat. Sol. A* **182**(2) 631–639 (2000). (Cited on page 9.)
- Darahanau, A.V., Nikulin, A.Y., Dilanian, R.A., and Muddle, B.C. Nano-resolution profiling of micro-structures using quantitative x-ray phase retrieval from fraunhofer diffraction data. *Phys. Lett. A* **335**(5–6) 494–498 (2005). (Cited on page 15.)
- Darahanau, A.V., Nikulin, A.Y., Dilanian, R.A., Muddle, B.C., Souvorov, A., Nishino, Y., and Ishikawa, T. X-ray diffraction profiling of metal-metal interfaces at the nanoscale. *Phys. Rev. B* **75**(7) 075416 (2007). (Cited on pages 15 and 16.)
- Darwin, C.G. The theory of x-ray reflection. *Philos. Mag.* **27** (1914a). (Cited on page 43.)
- Darwin, C.G. The theory of x-ray reflection. Part II. *Philos. Mag.* **27** 675–690 (1914b). (Cited on page 43.)
- Davis, T.J., Gureyev, T.E., Gao, D., Stevenson, A.W., and Wilkins, S.W. X-ray image contrast from a simple phase object. *Phys. Rev. Lett.* **74**(16) 3173–3176 (1995a). (Cited on page 7.)
- Davis, T., Gao, D., Gureyev, T., Stevenson, A., and Wilkins, S. Phase-contrast imaging of weakly absorbing materials using hard X-rays. *Nature* **373**(6515) 595–598 (1995b). (Cited on page 7.)
- Demtröder, W. *Laser Spectroscopy: Basic Concepts and Instrumentation*. Springer Verlag, New York, 3rd edition (2003). (Cited on page 56.)
- DeRosier, D.J. Correction of high-resolution data for curvature of the ewald sphere.

- Ultramicroscopy* **81**(2) 83–98 (2000). (Cited on page 39.)
- Deschamps, A., David, L., Nicolas, M., Bley, F., Livet, F., Séguéla, R., Simon, J.P., Vigier, G., and Werenskiold, J.C. Recent developments in small-angle x-ray scattering for the study of metals and polymers. *Adv. Eng. Mater.* **3**(8) 579–586 (2001). (Cited on page 7.)
- Deschamps, A., Dumont, D., Lae, L., and Bley, F. Use of small-angle x-ray scattering for the characterisation of precipitates in Aluminium alloys. *Mater. Sci. Forum* **519-521** 1349–1354 (2006). (Cited on pages 9 and 20.)
- Dilanian, R.A. and Nikulin, A.Y. X-ray diffraction imaging of Al₂O₃ nanoparticles embedded in an amorphous matrix. *Appl. Phys. Lett.* **87** 161904 (2005). (Cited on pages 12, 128, 129 and 148.)
- DuMond, J.W.M. Theory of the use of more than two successive X-ray crystal reflections to obtain increased resolving power. *Phys. Rev.* **52** 872–883 (1937). (Cited on page 63.)
- EIGER. The EIGER project (2009). Available at: pilatus.web.psi.ch/eiger.htm. (Cited on page 11.)
- Eisebitt, S., Luning, J., Schlotter, W.F., Lorgen, M., Hellwig, O., Eberhardt, W., and Stohr, J. Lensless imaging of magnetic nanostructures by x-ray spectro-holography. *Nature* **432**(7019) 885–888 (2004). (Cited on page 11.)
- Eisenberger, P., Alexandropoulos, N.G., and Platzman, P.M. X-ray Brillouin scattering. *Phys. Rev. Lett.* **28**(23) 1519–1522 (1972). (Cited on page 13.)
- Epelboin, Y. Simulation of x-ray topographs. *Mater. Sci. Eng. A* **73** 1–43 (1985). (Cited on page 93.)
- Epelboin, Y. and Riglet, P. Boundary conditions in the numerical integration of takagi-taupin equations. application to the Laue and Bragg cases. *Phys. Stat. Sol. A* **54**(2) 547–556 (1979). (Cited on page 93.)
- Erni, R., Rossell, M.D., Kisielowski, C., and Dahmen, U. Atomic-resolution imaging with a sub-50-pm electron probe. *Phys. Rev. Lett.* **102**(9) 096101 (2009). (Cited on page 4.)
- Esmacili, S. and Lloyd, D.J. The role of copper in the precipitation kinetics of 6000 series Al alloys. *Mater. Sci. Forum* **519-521** 169–176 (2006). (Cited on pages 21 and 151.)
- Esmacili, S., Poole, W.J., and Lloyd, D.J. *Advances in the Metallurgy of Aluminum Alloys*. ASM International, Ohio (2001). (Cited on page 20.)
- Ewald, P.P. Optics of crystals. *Ann. Phys.-Berlin* **354**(1) 1–38 (1916). (Cited on page 43.)
- Ewald, P.P. Zur Begründung der Kristalloptik: III.Röntgenstrahlen. *Ann. Phys.-Berlin*

- 359(24) 519–597 (1917). (Cited on page 43.)
- Ewald, P.P., editor. *Fifty Years of X-ray Diffraction*. Springer, Oosthoek, Utrecht (1962). (Cited on page 42.)
- Ewald, P.P. Introduction to the dynamical theory of X-ray diffraction. *Acta Cryst. A* **25**(1) 103–108 (1969). (Cited on page 43.)
- Eymery, J., Favre-Nicolin, V., Froberg, L., and Samuelson, L. X-ray measurements of the strain and shape of dielectric/metallic wrap-gated inas nanowires. *Appl. Phys. Lett.* **94**(13) 131911–3 (2009). (Cited on page 8.)
- Faulkner, H.M.L. and Rodenburg, J.M. Movable aperture lensless transmission microscopy: A novel phase retrieval algorithm. *Phys. Rev. Lett.* **93** (2004). (Cited on page 11.)
- Feigin, L.A. and Svergun, D.I. *Structure Analysis by Small-Angle X-ray and Neutron Scattering*. Plenum Press, New York (1987). (Cited on page 8.)
- Fewster, P.F. A high-resolution multiple-crystal multiple-reflection diffractometer. *J. Appl. Cryst.* **22**(1) 64–69 (1989). (Cited on pages 13 and 95.)
- Fewster, P.F. Combining high-resolution X-ray diffractometry and topography. *J. Appl. Cryst.* **24**(2) 178–183 (1991). (Cited on page 64.)
- Fewster, P.F. X-ray diffraction from low-dimensional structures. *Semicond. Sci. Technol.* **8**(11) 1915–1934 (1993). (Cited on page 13.)
- Fienup, J.R. Reconstruction of an object from the modulus of its Fourier transform. *Opt. Lett.* **3**(1) 27–29 (1978). (Cited on page 85.)
- Fienup, J.R. Iterative method applied to image reconstruction and to computer-generated holograms. *Opt. Eng.* **19** 297–305 (1980). (Cited on page 87.)
- Fienup, J.R. Phase retrieval algorithm: a comparison. *Appl. Opt.* **21**(15) 2758–2769 (1982). (Cited on pages 10, 85, 86 and 87.)
- Fienup, J.R. Reconstruction of a complex-valued object from the modulus of its Fourier transform using a support constraint. *J. Opt. Soc. Am.* **4**(1) 118–123 (1987). (Cited on pages 87 and 151.)
- Fienup, J.R., Crimmins, T.R., and Holsztynski, W. Reconstruction of the support of an object from the support of its autocorrelation. *J. Opt. Soc. Am.* **72** 610–624 (1982). (Cited on page 87.)
- Fienup, J.R. and Kowalczyk, A.M. Phase retrieval for a complex-valued object by using a low-resolution image. *J. Opt. Soc. Am. A* **7** 450–458 (1990). (Cited on page 87.)
- Förster, E., Goetz, K., and Zaumseil, P. Double crystal diffractometry for the characterization of targets for laser fusion experiments. *Krist. Tech.* **15**(8) 937–945 (1980).

- (Cited on page 7.)
- Förster, S., Timmann, A., Konrad, M., Schellbach, C., Meyer, A., Funari, S.S., Mulvaney, P., and Knott, R. Scattering curves of ordered mesoscopic materials. *J. Phys. Chem. B* **109**(4) 1347–1360 (2005). (Cited on page 8.)
- Fourme, R. and Hendrickson, W.A. *Synchrotron Radiation and Biophysics*, pages 156–175. Ellis Horwood Ltd, Chichester (1990). (Cited on page 6.)
- Fratzl, P., Langmayr, F., and Paris, O. Evaluation of 3D small-angle scattering from non-spherical particles in single crystals. *J. Appl. Cryst.* **26**(6) 820–826 (1993). (Cited on page 8.)
- Fratzl, P. Small-angle scattering in materials science - a short review of applications in alloys, ceramics and composite materials. *J. Appl. Cryst.* **36**(3 Part 1) 397–404 (2003). (Cited on page 7.)
- Fribourg, G., Deschamps, A., and Bréchet, Y. Precipitation strengthening in AA7449 aluminium alloy: understanding the relationship between microstructure, yield strength and strain hardening. *Mater. Sci. Forum* **519-521** 991–996 (2006). (Cited on page 9.)
- Gable, B. Al-Cu hardness peaks (2006a). Private communication. (Cited on pages [vii](#), [24](#), [26](#) and [141](#).)
- Gable, B. Private communication (2006b). (Cited on page [111](#).)
- Gabor, D. A new microscopic principle. *Nature* **161**(4098) 777–778 (1948). (Cited on page 7.)
- Gartstein, E., Mandelbrot, M., and Mogilyanski, D. Instrumental origin effects in triple-axis diffraction. *J. Phys. D* **34** A57–A63 (2001). (Cited on pages [62](#) and [95](#).)
- Gerchberg, R.W. and Saxton, W.O. A practical algorithm for the determination of phase from image and diffraction plane pictures. *Optik (Stuttgart)* **35** 237–246 (1972). (Cited on pages [10](#), [85](#) and [86](#).)
- Gerold, V. On the structures of Guinier-Preston zones in Al-Cu alloys. *Scr. Metall.* **22** 927–932 (1988). (Cited on page [23](#).)
- Glatter, O. and Kratky, O. *Small Angle X-Ray Scattering*. Academic Press Inc., London (1982). (Cited on page 7.)
- Goodman, J.W. *Introduction to Fourier Optics*. Roberts & Company Publishers, Colorado, USA, 3rd edition (2005). (Cited on page [32](#).)
- Goudeau, P., Fontaine, A., Naudon, A., and Williams, C.E. Anomalous small-angle scattering in metallurgy: a feasibility experiment with an Al-Zn alloy. *J. Appl. Cryst.* **19**(1) 19–24 (1986). (Cited on page 8.)
- Goureev, T.E., Nikulin, A.Y., and Petrashen, P.V. X-ray diagnostics of 2D deformation

- profiles in crystals with periodically distorted near-surface region. *Phys. Stat. Sol. A* **130**(2) 263–271 (1992). (Cited on page 15.)
- Grundmann. Atomic structure based simulation of x-ray scattering from strained superlattices. *Phys. Stat. Sol. B* **218**(2) 417–423 (2000). (Cited on page 47.)
- Guinier, A. Structure of age-hardened aluminium-copper alloys. *Nature* **142** 569–570 (1938). (Cited on page 21.)
- Guinier, A. *X-ray Crystallographic Technology*. Hilger and Watts, Hilger Division, London (1952). (Cited on pages 9, 41 and 146.)
- Guinier, A., Fournet, G., Walker, C.B., and Yudowitch, K.L. *Small-Angle Scattering of X-rays*. Wiley, New York (1955). (Cited on page 7.)
- Gureyev, T.E., Davis, T.J., Pogany, A., Mayo, S.C., and Wilkins, S.W. Optical phase retrieval by use of first Born-and Rytov-type approximations. *Appl. Opt.* **43**(12) 2418–2430 (2004). (Cited on page 35.)
- Hansen, S. and Pedersen, J.S. A comparison of three different methods for analysing small-angle scattering data. *J. Appl. Cryst.* **24**(5) 541–548 (1991). (Cited on page 8.)
- Hart, M. Review Lecture: Ten Years of X-Ray Interferometry. *Proceedings of the Royal Society of London. Series A, Mathematical and Physical Sciences* **346**(1644) 1–22 (1975). (Cited on page 7.)
- Härtwig, J. Hierarchy of dynamical theories of x-ray diffraction for deformed and perfect crystals. *J. Phys. D* **34** A70–A77 (2001). (Cited on page 47.)
- Hatch, J.E. *Aluminium: Structure and Physical Metallurgy*. ASM International, Metal Park, Ohio (1998). (Cited on pages 20 and 27.)
- Haubold, H.G. and Martinsen, D. Structure determination of self-interstitials and investigation of vacancy clustering in copper by diffuse x-ray scattering. *J. Nucl. Mater.* **69-70** (1978). (Cited on page 13.)
- Haubold, H.G., Wang, X.H., Jungbluth, H., Goerigk, G., and Schilling, W. In situ anomalous small-angle X-ray scattering and X-ray absorption near-edge structure investigation of catalyst structures and reactions. *J. Mol. Struct.* **383**(1-3) 283–289 (1996). (Cited on page 8.)
- Helliwell, J.R. *Macromolecular Crystallography with Synchrotron Radiation*. Cambridge University Press, Cambridge (2005). (Cited on page 5.)
- Hendrickson, W.A. Determination of macromolecular structures from anomalous diffraction of synchrotron radiation. *Science* **254**(5028) 51–58 (1991). (Cited on page 6.)
- Henrich, B., Bergamaschi, A., Broennimann, C., Dinapoli, R., Eikenberry, E., Johnson, I., Kobas, M., Kraft, P., Mozzanica, A., and Schmitt, B. PILATUS: a single photon

- counting pixel detector for X-ray applications. *Nucl. Instrum. Methods Phys. Res., Sect. A* **607**(1) 247–249 (2009). (Cited on page 11.)
- Hirsch, P.B., Howie, A., and Whelan, M.J. A kinematical theory of diffraction contrast of electron transmission microscope images of dislocations and other defects. *Philos. Trans. R. Soc. London, Ser. A* **252**(1017) 499–529 (1960). (Cited on page 39.)
- Hirth, S.M., Marshall, G.J., Court, S.A., and Lloyd, D.J. Effects of Si on the aging behaviour and formability of aluminium alloys based on AA6016. *Mater. Sci. Eng. A* **319** 452–456 (2001). (Cited on page 20.)
- Hornbogen, E. Investigation by means of the electron microscope of precipitation in Al-Cu solid solutions. Part 3. The diagram for the formation of nuclei in Al-Cu alloys. *Aluminum* **43**(3) 163–166 (1967). (Cited on page 25.)
- Huang, W.J., Zuo, J.M., Jiang, B., Kwon, K.W., and Shim, M. Sub-angstrom-resolution diffractive imaging of single nanocrystals. *Nat. Phys.* **5**(2) 129–133 (2009). (Cited on page 4.)
- Iida, A. and Kohra, K. Separate measurements of dynamical and kinematical x-ray diffraction from perfect and surface damaged single crystals with a triple crystal diffractometer. *Jpn. J. Appl. Phys.* **17**(5) 963–964 (1978). (Cited on page 13.)
- Iida, A. and Kohra, K. Separate measurements of dynamical and kinematical x-ray diffraction from silicon crystals with a triple crystal diffractometer. *Phys. Stat. Sol. A* **51**(2) 533–542 (1979). (Cited on pages 13, 59, 60, 62 and 63.)
- Ingal, V.N. and Beliaevskaya, E.A. X-ray plane-wave topography observation of the phase contrast from a non-crystalline object. *J. Phys. D* **28**(11) 2314–2317 (1995). (Cited on page 7.)
- Iwata, K. and Nagata, R. Calculation of refractive index distribution from interferograms using the Born and Rytov's approximation. *Jpn. J. Appl. Phys.* **14**(Supplement 14-1) 379–384 (1975). (Cited on page 38.)
- Jenkins, R. and Snyder, R.L. *Introduction to X-Ray Powder Diffractometry*. John Wiley and Sons, New York (1996). (Cited on page 6.)
- Juul Jensen, D., Lauridsen, E.M., Margulies, L., Poulsen, H.F., Schmidt, S., Sørensen, H.O., and Vaughan, G.B.M. X-ray microscopy in four dimensions. *Mater. Today* **9**(1-2) 18–25 (2006). (Cited on page 10.)
- Kanadani, T. and Sakakibara, A. Short-range clustering in dilute Al-Cu alloy. *Phys. Stat. Sol. A* **114**(1) K197–K199 (1989). (Cited on pages 21 and 150.)
- Khachaturyan, A.G. *Theory of Structural Transformations in Solids*. John Wiley & Sons, New York (1983). (Cited on page 23.)
- Kim, K.J. Characteristics of synchrotron radiation. In *X-ray data booklet, 2nd edition*.

- Lawrence Berkeley National Laboratory, Berkeley, CA (2001). (Cited on pages 50, 51, 54 and 57.)
- Kirian, R., Wang, X., Weierstall, U., Schmidt, K., Spence, J., Hunter, M., Fromme, P., White, T., Chapman, H., and Holton, J. Femtosecond protein nanocrystallography – data analysis methods. *Opt. Express* **18**(6) 5713–5723 (2010). (Cited on page 12.)
- Kirz, J., Jacobsen, C., and Howells, M. Soft x-ray microscopes and their biological applications. *Q. Rev. Biophys.* **28**(01) 33–130 (1995). (Cited on page 10.)
- Kohmura, Y., Nishino, Y., Ishikawa, T., and Miao, J. Effect of distorted illumination waves on coherent diffraction microscopy. *J. Appl. Phys.* **98**(12) 123105–6 (2005). (Cited on page 10.)
- Konno, T.J., Kawasaki, M., and Hiraga, K. Characterization of Guinier-Preston zones by high-angle annular detector dark-field scanning transmission electron microscopy. *JEOL News* **36E** (2001). (Cited on pages 21 and 23.)
- Kotsis, K.T. and Alexandropoulos, N.G. Diffraction pattern near the Bragg angle for an asymmetrically cut crystal. *J. Appl. Cryst.* **19**(6) 473–476 (1986). (Cited on page 95.)
- Kotsis, K.T. and Alexandropoulos, N.G. A source of spurious peaks in a multi-crystal x-ray spectrometer. *J. Phys. E* **20**(1) 74–76 (1987). (Cited on page 62.)
- Kou, S. *Welding Metallurgy*. John Wiley and Sons, New York, 2nd edition (2003). (Cited on page 21.)
- Kress, R. *Linear Integral Equations*. Springer Verlag, New York, 2nd edition (1999). (Cited on page 5.)
- Krivoglaz, M. *Diffuse Scattering of X-Rays and Neutrons by Fluctuations*. Springer, Berlin (1996). (Cited on page 149.)
- Lambard, J. and Zemb, T. A triple-axis Bonse-Hart camera used for high-resolution small-angle scattering. *J. Appl. Cryst.* **24**(5) 555–561 (1991). (Cited on page 17.)
- Larson, B.C. and Schmatz, W. Huang diffuse scattering from dislocation loops and cobalt precipitates in copper. *Phys. Rev. B* **10**(6) 2307–2314 (1974). (Cited on page 13.)
- Larson, B.C. and Schmatz, W. Huang diffuse scattering from dislocation loops. *Phys. Stat. Sol. B* **99**(1) 267–275 (1980). (Cited on page 13.)
- Larson, B.C., Yang, W., Ice, G.E., Budai, J.D., and Tischler, J.Z. Three-dimensional x-ray structural microscopy with submicrometre resolution. *Nature* **415**(6874) 887–890 (2002). (Cited on page 10.)
- Lazzari, R., Renaud, G., Revenant, C., Jupille, J., and Borensztein, Y. Adhesion of growing nanoparticles at a glance: Surface differential reflectivity spectroscopy and

- grazing incidence small angle x-ray scattering. *Phys. Rev. B* **79**(12) 125428–8 (2009). (Cited on page 8.)
- Leith, E. and Upatnieks, J. Reconstructed wavefronts and communication theory. *J. Opt. Soc. Am.* **52**(10) 1123–1130 (1962). (Cited on page 7.)
- Leith, E. and Upatnieks, J. Wavefront reconstruction with continuous-tone objects. *J. Opt. Soc. Am.* **53**(12) 1377–1381 (1963). (Cited on page 7.)
- Leith, E. and Upatnieks, J. Wavefront reconstruction with diffused illumination and three-dimensional objects. *J. Opt. Soc. Am.* **54**(11) 1295–1301 (1964). (Cited on page 7.)
- Lipson, S.G., Lipson, H., and Tannhauser, D.S. *Optical Physics*. Cambridge University Press, Cambridge, 3rd edition (1995). (Cited on page 79.)
- Liu, J. Scanning transmission electron microscopy and its application to the study of nanoparticles and nanoparticle systems. *J. Electron Microsc.* **54**(3) 251–278 (2005). (Cited on page 4.)
- Lloyd, D.J. Aluminum alloys used in automotive skin sheet. In D.S. Wilkinson and W.J. Poole, editors, *Advances in Industrial Materials*, volume 1101, pages 3–17. The Metallurgical Society of CIM, Montreal, Canada (1998). (Cited on page 20.)
- Lokker, J.P., van der Pers, N.M., Verbruggen, A.H., Janssen, G., Jongste, J.F., and Radelaar, S. Localized stress near and the thermal expansion of Al₂Cu precipitates in an Al thin film matrix. *J. Appl. Phys.* **87**(2) 682–688 (2000). (Cited on page 20.)
- Marchal, J., Tartoni, N., and Nave, C. Synchrotron applications of pixel and strip detectors at Diamond Light Source. *Nucl. Instrum. Methods Phys. Res., Sect. A* **604**(1-2) 123–126 (2009). (Cited on page 12.)
- Marchesini, S., He, H., Chapman, H.N., Noy, A., Hau-Riege, S.P., Howells, M.R., Weierstall, U., and Spence, J.C.H. X-ray imaging reconstruction from the diffraction pattern alone. *Phys. Rev. B* **68** 1401011–1401014 (2003). (Cited on pages 87 and 165.)
- Marlaud, T., Baroux, B., Deschamps, A., Chemin, J.L., and Hénon, C. Understanding the compromise between strength and exfoliation corrosion in high strength 7000 alloys. *Mater. Sci. Forum* **519-521** 455–460 (2006). (Cited on page 9.)
- Martin, J.W. *Precipitation Hardening*. Pergamon Press, Oxford (1968). (Cited on pages 20, 21 and 27.)
- Materlik, G., Sparks, C.J., and Fischer, K. *Resonant Anomalous X-ray Scattering: Theory and Applications*. Elsevier Science, North-Holland, Amsterdam (1994). (Cited on page 8.)
- Matsubara, E. and Cohen, J.B. Local atomic arrangements in the solid solution Al-1.7 at.% Cu at 793 deg K. *Acta Metall.* **31**(12) 2129–2135 (1983). (Cited on page 21.)

- McNulty, I., Kirz, J., Jacobsen, C., Anderson, E.H., Howells, M.R., and Kern, D.P. High-resolution imaging by Fourier transform x-ray holography. *Science* **256**(5059) 1009–1012 (1992). (Cited on page 11.)
- Merica, P.D., Waltenberg, R.G., and Freeman, J.R. Constitution and metallography of aluminium and its light alloys with copper and with magnesium. *Sci. Pap. Bur. Stand. (U.S.)* **15**(347) 105 (1919a). (Cited on page 20.)
- Merica, P.D., Waltenberg, R.G., and Freeman, J.R. Constitution and metallography of aluminum and its light alloys with copper and with magnesium. *Trans. Am. Inst. Min. Metall. Eng.* **LXIV** 3–25 (1921). (Cited on page 20.)
- Merica, P.D., Waltenberg, R.G., and Scott, H. Heat treatment of duralumin. *Bull. Am. Inst. Metall. Eng.* **150** 913–949 (1919b). (Cited on page 20.)
- Merica, P.D., Waltenberg, R.G., and Scott, H. Heat treatment of duralumin. *Sci. Pap. Bur. Stand. (U.S.)* **15** 271 (1919c). (Cited on page 20.)
- Miao, J., Charalambous, P., Kirz, J., and Sayre, D. Extending the methodology of x-ray crystallography to allow imaging of micrometre-sized non-crystalline specimens. *Nature* **400** 342–344 (1999). (Cited on pages 10, 12 and 85.)
- Miao, J., Ishikawa, T., Johnson, B., Anderson, E.H., Lai, B., and Hodgson, K.O. High resolution 3D x-ray diffraction microscopy. *Phys. Rev. Lett.* **89**(8) 0883031–0883034 (2002). (Cited on page 10.)
- Miao, J., Kirz, J., and Sayre, D. The oversampling phasing method. *Acta Cryst. D* **56** 1312–1315 (2000). (Cited on page 85.)
- Miao, J., Sayre, D., and Chapman, H.N. Phase retrieval from the magnitude of the Fourier transforms of nonperiodic objects. *J. Opt. Soc. Am. A* **15**(6) 1662–1669 (1998). (Cited on pages 10, 85, 86 and 87.)
- Miao, J., Chen, C.C., Song, C., Nishino, Y., Kohmura, Y., Ishikawa, T., Ramunno-Johnson, D., Lee, T.K., and Risbud, S.H. Three-dimensional GaN-Ga₂O₃ core shell structure revealed by x-ray diffraction microscopy. *Phys. Rev. Lett.* **97**(21) 215503 (2006). (Cited on page 10.)
- Miao, J., Hodgson, K.O., Ishikawa, T., Larabell, C.A., LeGros, M.A., and Nishino, Y. Imaging whole Escherichia coli bacteria by using single-particle x-ray diffraction. *PNAS* **100**(1) 110–112 (2003). (Cited on page 10.)
- Midgley, P.A. Electron tomography for materials science. *Microsc. Microanal.* **13**(S02) 912–913 (2007). (Cited on page 4.)
- Millane, R.P. Phase retrieval in crystallography and optics. *J. Opt. Soc. Am.* **A7** (1990). (Cited on page 10.)
- Millane, R.P. and Stroud, W.J. Reconstructing symmetric images from their under-

- sampled Fourier intensities. *J. Opt. Soc. Am. A* **14**(3) 568–579 (1997). (Cited on page 85.)
- Mills, D.M., Helliwell, J.R., Kwick, A., Ohta, T., Robinson, I.A., and Authier, A. Brightness, spectral brightness or brilliance - Report of the Working Group on Synchrotron Radiation Nomenclature. *J. Synchrotron Radiat.* **12**(3) 385 (2005). (Cited on page 57.)
- Mocella, V., Epelboin, Y., and Guigay, J.P. X-ray dynamical diffraction: the concept of a locally plane wave. *Acta Cryst. A* **56**(3) 308–316 (2000). (Cited on pages 56 and 72.)
- Moser, H.O. A Guided Survey of Synchrotron Radiation Sources. In A. Chao, H. Moser, and Z. Zhao, editors, *Accelerator Physics, Technology and Applications: Selected Lectures of OCPA International Accelerator School 2002, Singapore*, pages 35–51. World Scientific, Singapore (2004). (Cited on page 51.)
- Muddle, B.C. and Nie, J.F. Nucleation-mediated structural refinement and aluminum alloy design. *Mater. Sci. Forum* **519-521** 191–196 (2006). (Cited on pages 9 and 20.)
- Mueller, R.K., Kaveh, M., and Iverson, R.D. A new approach to acoustic tomography using diffraction techniques. In A.F. Metherell, editor, *Acoustic Imaging*, volume 8, pages 615–628. Plenum Press, New York (1980). (Cited on page 38.)
- Müller, S., Wang, L.W., Zunger, A., and Wolverton, C. Coherent phase stability in Al-Zn and Al-Cu fcc alloys: The role of the instability of fcc Zn. *Phys. Rev. B* **60**(24) 16448–16462 (1999). (Cited on page 20.)
- Murray, J.L. The aluminium-copper system. *Int. Mater. Rev.* **30** 211–233 (1985). (Cited on pages 21 and 23.)
- Nakashima, Y., Hattori, M., and Komatsu, S. Phase retrieval microscope based on photon image detection. *Jpn. J. Appl. Phys.* **41**(Part 1, No. 7B) 4809–4812 (2002). (Cited on page 86.)
- Nellist, P.D., McCallum, B.C., and Rodenburg, J.M. Resolution beyond the ‘information limit’ in transmission electron microscopy. *Nature* **374**(6523) 630–632 (1995). (Cited on page 11.)
- Nellist, P.D. and Rodenburg, J.M. Electron ptychography. I. Experimental demonstration beyond the conventional resolution limits. *Acta Cryst. A* **54**(1) 49–60 (1998). (Cited on page 11.)
- Nesterets, Y.I., Gureyev, T.E., Paganin, D., Pavlov, K.M., and Wilkins, S.W. Quantitative diffraction-enhanced x-ray imaging of weak objects. *J. Phys. D* **37** 1262–1274 (2004). (Cited on page 161.)
- Neutze, R., Wouts, R., van der Spoel, D., Weckert, E., and Hajdu, J. Potential for

- biomolecular imaging with femtosecond X-ray pulses. *Nature* **406**(6797) 752–757 (2000). (Cited on page 12.)
- Newton, M.C., Leake, S.J., Harder, R., and Robinson, I.K. Three-dimensional imaging of strain in a single ZnO nanorod. *Nat. Mater.* **9**(2) 120–124 (2009). (Cited on pages 87, 132 and 152.)
- Nieto-Vesperinas, M. *Scattering and Diffraction in Physical Optics*. Wiley (1991). (Cited on page 32.)
- Nikulin, A.Y. Inversion in X-ray diffraction: Zeros of the complex diffraction amplitude. *Physica B* **252**(4) 319–329 (1998a). (Cited on page 15.)
- Nikulin, A.Y. Phase-retrieval x-ray diffractometry: a tool for unambiguous characterization of crystalline materials. *Recent Res. Devel. Appl. Phys.* **1** 1–21 (1998b). (Cited on page 15.)
- Nikulin, A.Y. Uniqueness of the complex diffraction amplitude in x-ray Bragg diffraction. *Phys. Rev. B* **57**(18) 11178–11183 (1998c). (Cited on page 15.)
- Nikulin, A.Y., Darahanau, A.V., Horney, R., and Ishikawa, T. High-resolution x-ray diffraction imaging of non-Bragg diffracting materials using phase retrieval x-ray diffractometry (PRXRD) technique. *Physica B* **349**(1-4) 281–295 (2004). (Cited on page 129.)
- Nikulin, A.Y., Dilanian, R.A., Zatsepin, N.A., Gable, B.M., Muddle, B.C., Souvorov, A.Y., Nishino, Y., and Ishikawa, T. 3-D x-ray diffraction imaging with nanoscale resolution using incoherent radiation. *Nano Lett.* **7**(5) 1246–1250 (2007). (Cited on pages 65, 79, 89, 90, 133, 134, 150 and 195.)
- Nikulin, A.Y., Sakata, O., Hashizume, H., and Petrashen, P.V. Mapping of two-dimensional lattice distortions in silicon crystals at submicrometer resolution from x-ray rocking-curve data. *J. Appl. Cryst.* **27**(3) 338–344 (1994). (Cited on page 15.)
- Nikulin, A.Y., Siu, K., Davis, J.R., and Usher, B.F. On a possibility of high-resolution characterization of InGaAs/GaAs multilayers using phase-retrieval x-ray diffractometry technique. *J. Phys. D* **33**(20) 2521–2526 (2000). (Cited on page 15.)
- Nikulin, A.Y., Siu, K., Davis, J.R., Zaumseil, P., Souvorov, A.Y., and Freund, A. Application of the phase-retrieval x-ray diffractometry to an ultra-high spatial resolution mapping of SiGe films near the absorption edge of Ge. *Phys. Stat. Sol. A* **184**(1) 145–155 (2001). (Cited on page 15.)
- Nikulin, A.Y. and Steinfeld, R. X-ray Bragg diffraction profiles from unstrained layered single-crystal structures: theoretical considerations, simulation and reconstruction using phase-retrieval x-ray diffractometry. *Thin Solid Films* **467**(1-2) 28–35 (2004).

(Cited on page 148.)

- Nikulin, A.Y., Stevenson, A.W., and Hashizume, H. Model-independent determination of the strain distribution for a $\text{Si}_{0.9}\text{Ge}_{0.1}\text{Si}$ superlattice using x-ray diffractometry data. *Phys. Rev. B* **53**(13) 8277–8282 (1996a). (Cited on page 15.)
- Nikulin, A.Y., Stevenson, A.W., Hashizume, H., Cookson, D., Hobler, G., and Wilkins, S.W. Model-independent determination of 2D strain distribution in ion-implanted silicon crystals from x-ray diffraction data. *Semicond. Sci. Technol* **12** 350–354 (1997a). (Cited on page 15.)
- Nikulin, A.Y., Stevenson, A.W., Hashizume, H., Wilkins, S.W., Cookson, D., Foran, G., and Garrett, R.F. High-resolution triple-crystal x-ray diffraction experiments performed at the Australian National Beamline Facility on a silicon sample with lateral periodic superstructure. *J. Appl. Cryst.* **28**(1) 57–60 (1995a). (Cited on page 15.)
- Nikulin, A.Y., Stevenson, A.W., Wilkins, S.W., Hashizume, H., and Cookson, D. High-resolution mapping of two-dimensional lattice distortions in ion-implanted crystals from x-ray diffractometry data. *J. Appl. Cryst.* **28** 803–811 (1995b). (Cited on page 15.)
- Nikulin, A.Y., Zaumseil, P., and Petrashen, P.V. Unambiguous determination of crystal-lattice strains in epitaxially grown SiGe/Si multilayers. *J. Appl. Phys.* **80** 6683–6688 (1996b). (Cited on page 15.)
- Nikulin, A.Y., Zaumseil, P., and Petrashen, P.V. The characterization of SiGe/Si multilayers via an unambiguous solution of the inverse problem in x-ray Bragg diffraction. *J. Phys. D* **30**(17) 2373–2378 (1997b). (Cited on page 15.)
- Nikulin, A.Y. and Dilanian, R.A. and Gable, B.M. and Muddle, B.C. and Hester, J.R. and Ishikawa, T. and Yang, P. and Moser, H.O. Nondestructive three-dimensional x-ray diffraction imaging of nanoscale particles. *Adv. Synchrotron Radiat.* **1**(02) 207–220 (2008). (Cited on pages 133 and 150.)
- Nishino, Y., Miao, J., and Ishikawa, T. Image reconstruction of nanostructured non-periodic objects only from oversampled hard x-ray diffraction intensities. *Phys. Rev. B* **68** (2003). (Cited on pages 12 and 86.)
- Nugent, K.A. Coherent methods in the x-ray sciences. *Adv. Phys.* **59**(1) (2009). (Cited on pages 10, 11 and 12.)
- Odén, M., Rogström, L., Knutsson, A., Ternner, M.R., Hedström, P., Almer, J., and Ilavsky, J. In situ small-angle x-ray scattering study of nanostructure evolution during decomposition of arc evaporated *tialn* coatings. *Appl. Phys. Lett.* **94**(5) 053114 (2009). (Cited on page 8.)

- Ogata, K. *Modern Control Engineering*. Prentice Hall, Upper Saddle River, NJ, 3rd edition (2009). (Cited on page 68.)
- Paganin, D.M. *Coherent X-ray Optics*. Oxford University Press, New York (2006). (Cited on pages 32, 35, 36 and 37.)
- Parrini, L. and Schaller, R. Origin of θ'' relaxation in reinforced and unreinforced Al-Cu alloys. *Phys. Stat. Sol. A* **155**(1) 51–62 (1996). (Cited on page 24.)
- Pauling, L. *The Nature of the Chemical Bond and the Structure of Molecules and Crystals: An Introduction to Modern Structural Chemistry*. Cornell University Press, New York, 3rd edition (1946). (Cited on page 5.)
- Pelliccia, A., Nikulin, A.Y., Muddle, B.C., and Sakata, O. X-ray diffraction imaging of embedded nanoparticles with sub-10nm resolution (2010). Submitted. (Cited on pages 165 and 166.)
- Petrashen', P.V. and Chukhovskii, F.N. Restoration of the phase of an x-ray wave diffracted in a single-crystal layered structure. *Sov. Phys. Dokl.* **34** 957 (1989). (Cited on page 15.)
- Pfeifer, M.A., Williams, G.J., Vartanyants, I.A., Harder, R., and Robinson, I.K. Three-dimensional mapping of a deformation field inside a nanocrystal. *Nature* **442** 63–66 (2006). (Cited on pages 10, 12, 87 and 151.)
- Pick, M.A., Bickmann, K., Pofahl, E., Zwill, K., and Wenzl, H. A new automatic triple-crystal X-ray diffractometer for the precision measurement of intensity distribution of Bragg diffraction and Huang scattering. *J. Appl. Cryst.* **10**(6) 450–457 (1977). (Cited on page 13.)
- Pietsch, U., Holý, V., and Baumbach, T. *High-Resolution X-ray Scattering: From Thin Films to Lateral Nanostructures*. Springer Verlag, New York, 2nd edition (2004). (Cited on page 62.)
- Pinsker, Z.G. *Dynamical Scattering of X-rays in Crystals*. Springer Verlag, Berlin (1978). (Cited on pages 43 and 161.)
- Podorov, S.G., Faleev, N.N., Pavlov, K.M., Paganin, D.M., Stepanov, S.A., and Förster, E. A new approach to wide-angle dynamical X-ray diffraction by deformed crystals. *J. Appl. Cryst.* **39**(5) 652–655 (2006). (Cited on page 47.)
- Press, W., Teukolsky, S., Vetterling, W., and Flannery, B. *Numerical Recipes: The Art of Scientific Computing*. Cambridge University Press, New York, 3rd edition (2007). (Cited on pages 37 and 82.)
- Preston, G.D. The diffraction of x-rays by age-hardening aluminium copper alloys. *Proc. R. Soc. London, Ser. A* **167**(931) 526–538 (1938a). (Cited on page 7.)
- Preston, G.D. Structure of age-hardened aluminium-copper alloys. *Nature* **142** 570

- (1938b). (Cited on page 21.)
- Putnam, C.D., Hammel, M., Hura, G.L., and Tainer, J.A. X-ray solution scattering (SAXS) combined with crystallography and computation: defining accurate macromolecular structures, conformations and assemblies in solution. *Q. Rev. Biophys.* **40**(03) 191–285 (2007). (Cited on page 7.)
- Ramos, A., Tchoubar, D., and Pons, C.H. Surfaces of Cd(S, Se) nanoparticles by small-angle x-ray scattering. *J. Appl. Cryst.* **29**(4) 346–352 (1996). (Cited on page 8.)
- Ravi, C., Wolverton, C., and Ozolins, V. Prediction metastable phase boundaries in Al-Cu alloys from first-principles calculations of free energies: The role of atomic vibrations. *Europhys. Lett.* **73**(5) 719–725 (2006). (Cited on pages 22 and 23.)
- Renaud, G., Lazzari, R., Revenant, C., Barbier, A., Noblet, M., Ulrich, O., Leroy, F., Jupille, J., Borensztein, Y., Henry, C.R., Deville, J.P., Scheurer, F., Mane-Mane, J., and Fruchart, O. Real-time monitoring of growing nanoparticles. *Science* **300**(5624) 1416–1419 (2003). (Cited on page 8.)
- Revenant, C., Renaud, G., Lazzari, R., and Jupille, J. Defect-pinned nucleation, growth, and dynamic coalescence of Ag islands on MgO(001): An in situ grazing-incidence small-angle x-ray scattering study. *Phys. Rev. B* **79**(23) 235424–10 (2009). (Cited on page 8.)
- Robinson, I.K. Crystal truncation rods and surface roughness. *Phys. Rev. B* **33**(6) 3830–3836 (1986). (Cited on pages 42 and 62.)
- Robinson, I.K. and Miao, J. Three-dimensional coherent X-ray diffraction microscopy. *MRS Bull.* **29**(3) 177–181 (2004). (Cited on page 132.)
- Robinson, I.K., Vartanyants, I.A., Williams, G.J., Pfeifer, M.A., and Pitney, J.A. Reconstruction of the shapes of gold nanocrystals using coherent x-ray diffraction. *Phys. Rev. Lett.* **87** (2001). (Cited on page 10.)
- Rodenburg, J.M. and Bates, R.H.T. The theory of super-resolution electron microscopy via Wigner-distribution deconvolution. *Philos. Trans. R. Soc. London, Ser. A* **339**(1655) 521–553 (1992). (Cited on page 11.)
- Rodenburg, J.M. and Faulkner, H.M.L. A phase retrieval algorithm for shifting illumination. *Appl. Phys. Lett.* **85**(20) 4795–4797 (2004). (Cited on page 11.)
- Rodenburg, J.M., Hurst, A.C., and Cullis, A.G. Transmission microscopy without lenses for objects of unlimited size. *Ultramicroscopy* **107**(2-3) (2007). (Cited on page 11.)
- Russell, K.C. and Aaronson, H.I. Sequences of precipitate nucleation. *J. Mater. Sci.* **10**(11) 1991–1999 (1975). (Cited on pages 22 and 25.)

- Russell, K. Nucleation in solids: the induction and steady state effects. *Adv. Colloid Interface Sci.* **13**(3-4) 205–318 (1980). (Cited on page 25.)
- Rytov, S.M. Diffraction of light by ultrasonic waves. *Izv. Akad. Nauk SSSR* (2) 223–259 (1937). (Cited on page 38.)
- Sakamoto, N., Harada, M., and Hashimoto, T. In situ and time-resolved SAXS studies of Pd nanoparticle formation in a template of block copolymer microdomain structures. *Macromolecules* **39**(3) 1116–1124 (2006). (Cited on page 8.)
- Sakanaka, S., Asaoka, S., Cheng, W.X., Haga, K., Harada, K., T. Honda, M.I., Kasuga, T., Kobayashi, Y., Maezawa, H., Mishina, A., Mitsunashi, T., Miyajima, T., Miyauchi, H., Nagahashi, S., Nogami, T., Obina, T., Pak, C., Sasaki, H., Sato, Y., Shioya, T., Tadano, M., Takahashi, T., Tanimoto, Y., Tsuchiya, K., Uchiyama, T., Ueda, A., Umemori, K., Yamamoto, S., Ieiri, T., Isagawa, S., Kageyama, T., Kikuchi, M., Kudo, K., Nakamura, T.T., Nakanishi, H., Oide, K., Ono, M., Ozaki, T., Sakai, H., Sakamoto, Y., Takasaki, S., Tejima, M., and Yoshimoto, S. Status of the Photon Factory. In *Proceedings of Asian Particle Accelerator Conference (APAC 07)*, pages 142–144. Indore, India (2007). (Cited on page 52.)
- Saldin, D.K., Poon, H.C., Shneerson, V.L., Howells, M., Chapman, H.N., Kirian, R.A., Schmidt, K.E., and Spence, J.C.H. Beyond small-angle x-ray scattering: Exploiting angular correlations. *Phys. Rev. B* **81**(17) 174105 (2010). (Cited on page 8.)
- Sayre, D. Some implications of a theorem due to Shannon. *Acta Cryst.* **5** 843 (1952). (Cited on page 10.)
- Sayre, D., Chapman, H.N., and Miao, J. On the extendibility of x-ray crystallography to non-crystals. *Acta Cryst. A* **54**(2) 232–239 (1998). (Cited on page 10.)
- Schmid, G. *Nanoparticles: From Theory to Application*. Wiley VCH, Weinheim (2004). (Cited on page 3.)
- Schmidbauer, M. *X-ray Diffuse Scattering from Self-Organized Mesoscopic Semiconductor Structures*. Springer Verlag, Berlin (2004). (Cited on pages 41 and 43.)
- Sequeira, A.D., Pedersen, J.S., and Kostorz, G. The anisotropy of metallic systems - analysis of small angle scattering data. In H. Brumberger, editor, *Modern Aspects of Small Angle Scattering*, page 273. Kluwer Academic Publishers Group (1995). (Cited on page 10.)
- Shapiro, D., Thibault, P., Beetz, T., Elser, V., Howells, M., Jacobsen, C., Kirz, J., Lima, E., Miao, H., Neiman, A.M., and Sayre, D. Biological imaging by soft x-ray diffraction microscopy. *PNAS* **102**(43) 15343–15346 (2005). (Cited on page 10.)
- Shinohara, Y., Kawasaki, N., Ueno, S., Kobayashi, I., Nakajima, M., and Amemiya, Y. Observation of the transient rotator phase of *n*-hexadecane in emulsified droplets

- with time-resolved two-dimensional small- and wide-angle x-ray scattering. *Phys. Rev. Lett.* **94**(9) (2005). (Cited on page 8.)
- Siu, K., Nikulin, A.Y., Tamasaku, K., and Ishikawa, T. An application of phase retrieval x-ray diffractometry to refraction/small-angle scattering data. *J. Phys. D* **34** 2912–2917 (2001a). (Cited on page 15.)
- Siu, K., Nikulin, A.Y., Tamasaku, K., and Ishikawa, T. X-ray phase retrieval in high-resolution refraction data from amorphous materials. *Appl. Phys. Lett.* **79**(13) 2112–2114 (2001b). (Cited on page 15.)
- Siu, K.K.W., Nikulin, A.Y., Wells, P., Harvey, E., Bigault, T., Freund, A.K., and Ishikawa, T. Unambiguous x-ray phase retrieval from Fraunhofer diffraction data. *J. Appl. Phys.* **93** 5161 (2003). (Cited on page 15.)
- Smith, R. and Sandland, G.E. An accurate method of determining the hardness of metals, with particular reference to those of a high degree of hardness. *Proc. Instn. Mech. Engrs* **1** 623–641 (1922). (Cited on page 26.)
- Snigirev, A., Snigireva, I., Kohn, V., Kuznetsov, S., and Schelokov, I. On the possibilities of x-ray phase contrast microimaging by coherent high-energy synchrotron radiation. *Review of Scientific Instruments* **66**(12) 5486–5492 (1995). (Cited on page 7.)
- Somenkov, V., Tklich, A., and Shil'stein, S. Refraction contrast in x-ray introscopy. *Sov. Phys. Tech. Phys.* **36**(11) 1309–1311 (1991). (Cited on page 7.)
- Son, S., Takeda, M., Mitome, M., Bando, Y., and Endo, T. Precipitation behavior of an Al-Cu alloy during isothermal aging at low temperatures. *Mater. Lett.* **59**(6) 629–632 (2005). (Cited on page 151.)
- Spence, J.C.H. Diffractive (lensless) imaging. In P.W. Hawkes and J.C.H. Spence, editors, *Science of Microscopy*, volume 1, chapter 19, pages 1196–1227. Springer, New York (2007). (Cited on pages 12, 37 and 39.)
- SPring-8 Features. SPring-8 Features (2010). Available at: www.spring8.or.jp/en/about_us/whats_sr/sp8_features. (Cited on pages 51 and 53.)
- Starke Jr., E. and Staley, J. Application of modern aluminum alloys to aircraft. *Progress in Aerospace Sciences* **32**(2-3) 131–172 (1996). Cited By (since 1996) 92. (Cited on pages 20, 24 and 26.)
- Stepanov, S.A. X-ray dynamical diffraction data on the web (2008). Available at: sergey.gmca.aps.anl.gov/. (Cited on pages 52, 59, 75 and 163.)
- Svergun, D.I. Mathematical methods in small-angle scattering data analysis. *J. Appl. Cryst.* **24**(5) 485–492 (1991). (Cited on page 8.)
- Takagi, S. Dynamical theory of diffraction applicable to crystals with any kind of

- small distortion. *Acta Cryst.* **15**(12) 1311–1312 (1962). (Cited on pages 43 and 47.)
- Takagi, S. A dynamical theory of diffraction for a distorted crystal. *J. Phys. Soc. Jpn.* **26** 1239–1253 (1969). (Cited on page 43.)
- Taupin, D. Théorie dynamique de la diffraction des rayons x par les cristaux déformés. *Bull. Soc. Franc. Miner. Crist.* **87** 469–511 (1964). (Cited on pages 43 and 47.)
- Thiyagarajan, P. Characterization of materials of industrial importance using small-angle scattering techniques. *J. Appl. Cryst.* **36**(3 Part 1) 373–380 (2003). (Cited on page 8.)
- van der Veen, J.F. and Pfeiffer, F. Coherent x-ray scattering. *J. Phys. Condens. Matter* **16** 5003–5030 (2004). (Cited on pages 10 and 133.)
- Vartanyants, I.A., Ern, C., Donner, W., Dosch, H., and Caliebe, W. Strain profiles in epitaxial films from x-ray Bragg diffraction phases. *Appl. Phys. Lett.* **77** 3929–3931 (2000). (Cited on page 132.)
- Vartanyants, I.A., Robinson, I.K., Onken, J.D., Pfeifer, M.A., Williams, G.J., Pfeiffer, F., Metzger, H., Zhong, Z., and Bauer, G. Coherent x-ray diffraction from quantum dots. *Phys. Rev. B* **71**(24) (2005). (Cited on page 10.)
- von Laue, M. Die dynamische Theorie der Röntgenstrahlinterferenzen in neuer Form. *Ergreb. Exakt. Naturwiss.* **10** 133–158 (1931). (Cited on page 43.)
- von Laue, M. *Röntgenstrahl-Interferenzen*. Akademische Verlagsgesellschaft, Frankfurt am Main (1960). (Cited on pages 40 and 43.)
- Wagner, H.D. Nanocomposites: Paving the way to stronger materials. *Nat. Nanotechnol.* **2**(12) 742–744 (2007). (Cited on page 3.)
- Wang, J., Wolverton, C., Müller, S., Liu, Z.K., and Chen, L.Q. First-principles growth kinetics and morphological evolution of Cu nanoscale particles in Al. *Acta Mater.* **53**(9) 2759–2764 (2005). (Cited on page 151.)
- Wang, S.Q., Schneider, M., Ye, H.Q., and Gottstein, G. First-principles study of the formation of Guinier-Preston zones in Al-Cu alloys. *Scr. Mater.* **51**(7) (2004). (Cited on page 23.)
- Warren, B.E. *X-ray Diffraction*. Addison-Wesley Pub. Co, Reading (1969). (Cited on page 36.)
- Wilkins, S., Gureyev, T., Gao, D., Pogany, A., and Stevenson, A. Phase-contrast imaging using polychromatic hard x-rays. *Nature* **384**(6607) 335–338 (1996). (Cited on page 7.)
- Williams, C.E., May, R.P., and Guinier, A. Small-Angle Scattering of X-Rays and Neutrons. In E. Lifshin, editor, *X-ray Characterization of Materials*, chapter 4, pages 211–254. Wiley VCH, Weinheim, Germany (1999). (Cited on page 7.)

- Williams, D.B. and Carter, C.B. *Transmission Electron Microscopy: a Textbook for Materials Science*. Springer Verlag, New York, 2nd edition (2009). (Cited on page 4.)
- Williams, G.J., Pfeifer, M.A., Vartanyants, I.A., and Robinson, I.K. Three-dimensional imaging of microstructure in Au nanocrystals. *Phys. Rev. Lett.* **90** 175501 (2003). (Cited on pages 10 and 12.)
- Williams, J.C. and Starke, E.A. Progress in structural materials for aerospace systems. *Acta Mater.* **51**(19) 5775–5799 (2003). (Cited on page 20.)
- Wilm, A. Physikalisch-metallurgische Untersuchungen über magnesiumhaltige Aluminiumlegierungen. *Metallurgie* **8** 225–227 (1911). (Cited on page 20.)
- Wolf, E. Three-dimensional structure determination of semi-transparent objects from holographic data. *Opt. Commun.* **1**(4) 153–156 (1969). (Cited on pages 37 and 38.)
- Wolf, M., DeRosier, D.J., and Grigorieff, N. Ewald sphere correction for single-particle electron microscopy. *Ultramicroscopy* **106**(4-5) 376–382 (2006). (Cited on page 39.)
- Wolverton, C. First-principles prediction of equilibrium precipitate shapes in Al-Cu alloys. *Philos. Mag. Lett.* **79**(9) 683–690 (1999). (Cited on pages 22, 23, 24 and 151.)
- Wolverton, C. First-principles theory of 250 000-atom coherent alloy microstructure. *Modell. Simul. Mater. Sci. Eng.* **8**(3) 323–333 (2000). (Cited on page 21.)
- Yefanov, O.M., Zozulya, A.V., Vartanyants, I.A., Stangl, J., Mocuta, C., Metzger, T.H., Bauer, G., Boeck, T., and Schmidbauer, M. Coherent diffraction tomography of nanoislands from grazing-incidence small-angle x-ray scattering. *Appl. Phys. Lett.* **94**(12) 123104–3 (2009). (Cited on page 8.)
- Zachariasen, W.H. *Theory of X-Ray Diffraction in Crystals*. John Wiley, New York (1945). (Cited on pages 5 and 40.)
- Zandbergen, H.W. Structure determination of Mg₅Si₆ particles in Al by dynamic electron diffraction studies. *Science* **277** 1221–1225 (1997). (Cited on page 23.)
- Zatsepin, N.A., Dilanian, R.A., Nikulin, A.Y., Gable, B.M., Muddle, B.C., and Sakata, O. Early detection of nanoparticle growth from x-ray reciprocal space mapping. *Appl. Phys. Lett.* **92** 034101 (2008). (Cited on pages 55, 110, 129, 150 and 195.)
- Zatsepin, N.A., Dilanian, R.A., Nikulin, A.Y., Gao, X., Muddle, B.C., Matveev, V.N., and Sakata, O. Real-time in situ nanoclustering during initial stages of artificial aging of Al-Cu alloys. *J. Appl. Phys.* **107** 024303 (2010). (Cited on pages 21, 56, 143, 148 and 195.)
- Zaumseil, P. and Winter, U. Triple crystal diffractometer investigations of imperfections in silicon crystals with Laue-case diffraction. *Phys. Stat. Sol. A* **73** 455–466 (1982a). (Cited on page 13.)

- Zaumseil, P. and Winter, U. Triple crystal diffractometer investigations of silicon crystals with different collimator-analyzer arrangements. *Phys. Stat. Sol. A* **70** 497–505 (1982b). (Cited on pages [13](#), [63](#) and [95](#).)
- Zaumseil, P. and Winter, U. Characterization of boron implanted silicon by x-ray triple crystal diffractometry. *Phys. Stat. Sol. A* **120** 67–75 (1990). (Cited on page [13](#).)
- Zaumseil, P., Winter, U., Vartanyants, I.A., and Kharitonov, I.Y. Comparison between two x-ray methods for deformation profile determination. *Phys. Stat. Sol. A* **121** K149–153 (1990). (Cited on page [13](#).)
- Zhuang, Y., Stangl, J., Darhuber, A.A., Bauer, G., Mikulík, P., Holý, V., Darowski, N., and Pietsch, U. X-ray diffraction from quantum wires and quantum dots. *J. Mater. Sci.: Mat. in Electr.* **10**(3) 215–221 (1999). (Cited on page [4](#).)
- Zickler, G.A., Eidenberger, E., Leitner, H., Stergar, E., Clemens, H., Staron, P., Lippmann, T., and Schreyer, A. In-situ small-angle x-ray scattering study of the precipitation behavior in a Fe-25at.%Co–9at.%Mo alloy. *Mater. Charact.* **59**(12) 1809–1813 (2008). (Cited on page [8](#).)
- Zuo, J.M., Vartanyants, I.A., Gao, M., Zhang, R., and Nagahara, L.A. Atomic resolution imaging of a carbon nanotube from diffraction intensities. *Science* **300**(5624) 1419–1421 (2003). (Cited on page [4](#).)

List of Abbreviations

ANBF	Australian National Beamline Facility
CCD	Charged-coupled device
CDI	Coherent diffractive imaging
CSIRO	Commonwealth Scientific and Industrial Research Organisation
CTR	Crystal truncation rod
DCD	Double crystal diffractometry
ER	Error reduction
FDT	Fourier diffraction theorem
FFT	Fast Fourier transform
FT	Fourier transform
FWHM	Full width at half-maximum
GISAXS	Grazing incidence small angle X-ray scattering
GP	Guinier-Preston
HIO	Hybrid input-output
IO	Input-output
MAD	Multi-wavelength anomalous dispersion
PC	Phase contrast
PRXRD	Phase retrieval X-ray diffractometry
RMS	Root-mean-square
RSM	Reciprocal space map

SANS	Small angle neutron scattering
SAXS	Small angle X-ray scattering
SNR	Signal to noise ratio
STEM	Scanning transmission electron microscopy
TAD	Triple axis diffractometry
TCD	Triple crystal diffractometry
TEM	Transmission electron microscopy
XDC	X-ray diffraction calculations - a simulation code for conventional triple axis diffractometry, written by Dr. Timur Gureyev



Publications arising from this thesis

This appendix contains the following journal papers, based on the work undertaken during the PhD.

N. A. Zatsepin, R. A. Dilanian, A. Y. Nikulin, S. Gao, B. C. Muddle, V. N. Matveev and O. Sakata, *Real-time in situ nanoclustering during initial stages of artificial aging of Al-Cu alloys*. J. Appl. Phys. **107** 024303(1–6), (2010). Reprinted with permission from [Zatsepin et al. \(2010\)](#). Copyright 2010, American Institute of Physics.

N. A. Zatsepin, R. A. Dilanian, A. Y. Nikulin, B. M. Gable, B. C. Muddle, and O. Sakata. *Early detection of nanoparticle growth from x-ray reciprocal space mapping*. Appl. Phys. Lett. **92** (3) 034101(1–3), (2008). Also published in the Virtual Journal of Nanoscale Science and Technology, **17** (5) (2008). Reprinted with permission from [Zatsepin et al. \(2008\)](#). Copyright 2008, American Institute of Physics.

A. Y. Nikulin, R. A. Dilanian, **N. A. Zatsepin**, B. M. Gable, B. C. Muddle, A. Y. Souvorov, Y. Nishino, and T. Ishikawa. *3-D X-ray diffraction imaging of nanoparticles using incoherent radiation*. Nano Letters **7** (5) 1246, (2007). Reprinted with permission from [Nikulin et al. \(2007\)](#). Copyright 2007, American Chemical Society.

Conference proceedings

N. A. Zatsepin, R. A. Dilanian, A. Y. Nikulin, B. M. Gable, B. C. Muddle, and O. Sakata, *Towards in situ X-ray diffraction imaging at the nanometer scale*, Proc. SPIE, Vol. **7042**, 70420F, 2008.

A. Y. Nikulin, R. A. Dilanian, **N. A. Zatsepin**, and B. C. Muddle, *Three-dimensional x-ray diffraction nanoscopy*, Proc. SPIE, Vol. **7042**, 70420H, 2008.

Conference talks

N. A. Zatsepin, A. Y. Nikulin, R. A. Dilanian, B. C. Muddle, O. Sakata, *Advances in real-time x-ray diffraction in-situ nanoscopy*. X-ray Micro and Nanoprobes (XMNP 2009), Palinuro, Italy, June 2009.

N. A. Zatsepin, R. A. Dilanian, A. Y. Nikulin, B. M. Gable, B. C. Muddle, and O. Sakata, *Toward in situ x-ray diffraction imaging at the nanometer scale*. SPIE Optics and Photonics: Symposium on NanoScience and Engineering, San Diego, CA, August 2008.

Conference contributions

N. A. Zatsepin, R. A. Dilanian, A. Y. Nikulin, B. M. Gable, B. C. Muddle, and O. Sakata, *Early Detection of Nanoparticle Growth by High Resolution X-ray Diffractometry*. IUMRS - International Conference on Electronic Materials, Sydney, Australia, July 2008. (Poster)

A. Nikulin, A. Darahanau, **N. Zatsepin**, R. Dilanian, B. Muddle, A. Souvorov, O. Sakata, *3D X-Ray Diffraction Nanoscopy: In Situ Non-Destructive Imaging of Dispersed Nano-Particles, Cracks and Metal-Metal Interfaces*. IUMRS- International Conference on Electronic Materials, Sydney, Australia, July 2008. (Presented by A. Nikulin)

B. C. Muddle, R. Dilanian, **N. Zatsepin**, A. Y. Nikulin, *Non-Destructive 3-D X-Ray Diffraction Imaging at the Nanoscale*. 2008 TMS Annual Meeting & Exhibition, Symposium 3-Dimensional Materials Science Presentation, in the session titled "Modeling and Characterization across Length Scales III", New Orleans, LA, March 2008. (Presented by B. C. Muddle)